

**REACTOR PHYSICS STUDIES IN THE  
GCFR PHASE-II CRITICAL ASSEMBLY**

**edited by**

**R. B. Pond**



U of C-AUA-USERDA

---

**ARGONNE NATIONAL LABORATORY, ARGONNE, ILLINOIS**

**Prepared for the U. S. ENERGY RESEARCH  
AND DEVELOPMENT ADMINISTRATION  
under Contract W-31-109-Eng-38**

The facilities of Argonne National Laboratory are owned by the United States Government. Under the terms of a contract (W-31-109-Eng-38) between the U. S. Energy Research and Development Administration, Argonne Universities Association and The University of Chicago, the University employs the staff and operates the Laboratory in accordance with policies and programs formulated, approved and reviewed by the Association.

#### MEMBERS OF ARGONNE UNIVERSITIES ASSOCIATION

The University of Arizona	Kansas State University	The Ohio State University
Carnegie-Mellon University	The University of Kansas	Ohio University
Case Western Reserve University	Loyola University	The Pennsylvania State University
The University of Chicago	Marquette University	Purdue University
University of Cincinnati	Michigan State University	Saint Louis University
Illinois Institute of Technology	The University of Michigan	Southern Illinois University
University of Illinois	University of Minnesota	The University of Texas at Austin
Indiana University	University of Missouri	Washington University
Iowa State University	Northwestern University	Wayne State University
The University of Iowa	University of Notre Dame	The University of Wisconsin

#### NOTICE

This report was prepared as an account of work sponsored by the United States Government. Neither the United States nor the United States Energy Research and Development Administration, nor any of their employees, nor any of their contractors, subcontractors, or their employees, makes any warranty, express or implied, or assumes any legal liability or responsibility for the accuracy, completeness or usefulness of any information, apparatus, product or process disclosed, or represents that its use would not infringe privately-owned rights. Mention of commercial products, their manufacturers, or their suppliers in this publication does not imply or connote approval or disapproval of the product by Argonne National Laboratory or the U. S. Energy Research and Development Administration.

Printed in the United States of America  
Available from  
National Technical Information Service  
U. S. Department of Commerce  
5285 Port Royal Road  
Springfield, Virginia 22161  
Price: Printed Copy \$6.75; Microfiche \$3.00

---

ANL-76-108

---

ARGONNE NATIONAL LABORATORY  
9700 South Cass Avenue  
Argonne, Illinois 60439

REACTOR PHYSICS STUDIES IN THE  
GCFR PHASE-II CRITICAL ASSEMBLY

edited by

R. B. Pond\*

Applied Physics Division

September 1976

\*The work reported represents the efforts of the following persons:  
E. F. Bennett, S. K. Bhattacharyya, M. M. Bretscher, R. G. Bucher,  
R. J. Cornella, K. E. Freese, E. F. Groh, J. A. Morman, I. K. Olson,  
R. B. Pond, W. R. Robinson, D. M. Smith, D. C. Wade, and T. J. Yule.



## TABLE OF CONTENTS

<u>No.</u>	<u>Title</u>	<u>Page</u>
I.	INTRODUCTION . . . . .	2
A.	Description of the ZPR-GCFR Phase-II Assembly . . . . .	2
B.	Operational Measurements and Assembly Parameters . . . . .	4
C.	Reflector Worth . . . . .	4
II.	CALCULATIONAL MODELS . . . . .	5
A.	Broad-Group Cross-Sections . . . . .	5
B.	Benoist Anisotropic Diffusion Coefficients . . . . .	7
C.	The RZ Model . . . . .	8
D.	The XY Model . . . . .	10
III.	SMALL-SAMPLE REACTIVITY WORTH MEASUREMENTS . . . . .	10
A.	Introduction . . . . .	10
B.	Reactor Configurations . . . . .	11
1.	Central and radial worth measurements in the unreflected assembly . . . . .	11
2.	Axial worth measurements in the unreflected assembly . . .	11
3.	Central worth measurements in the reflected assembly . . .	11
C.	Experimental Method and Equipment . . . . .	12
1.	Oscillator . . . . .	12
2.	Samples . . . . .	12
3.	Fine autorod . . . . .	12
D.	Calculational Methods . . . . .	13
E.	Reactivity Worth Results . . . . .	13
1.	Unreflected assembly central worths . . . . .	13
2.	Reflected assembly central worths . . . . .	14
3.	Unreflected assembly axial and radial worths . . . . .	14

# TABLE OF CONTENTS

<u>No.</u>	<u>Title</u>	<u>Page</u>
F.	Discussion of Reactivity Worth Results. . . . .	14
1.	Central worths in the unreflected assembly. . . . .	14
2.	Central worths in the reflected assembly. . . . .	15
3.	Radial and axial worths in the unreflected assembly . . . .	16
IV.	REACTIVITY WORTH OF HELIUM . . . . .	16
A.	Introduction . . . . .	16
B.	Experimental Technique . . . . .	16
C.	Experimental Equipment . . . . .	16
D.	Results and Analysis . . . . .	17
E.	Central Worth of Air . . . . .	19
V.	$^{238}\text{U}$ DOPPLER EFFECT MEASUREMENT. . . . .	20
A.	Introduction . . . . .	20
B.	Experimental Measurements. . . . .	21
C.	Calculational Model. . . . .	22
1.	Perturbation formulation . . . . .	22
2.	Cross-section preparation. . . . .	23
3.	Doppler difference cross-sections. . . . .	24
4.	Flux ratios. . . . .	24
D.	Discussion of Results. . . . .	25
VI.	CENTRAL REACTION RATES AND UNIT-CELL MEASUREMENTS. . . . .	26
A.	Introduction . . . . .	26
B.	Central Rate Measurements. . . . .	26
1.	Experimental technique . . . . .	26
2.	Data reduction and results . . . . .	27

# TABLE OF CONTENTS

<u>No.</u>	<u>Title</u>	<u>Page</u>
C.	Unit-Cell Measurements . . . . .	27
1.	Experimental technique . . . . .	27
2.	Data reduction . . . . .	28
3.	Normalization . . . . .	28
4.	Stainless steel corrections to capture rates . . . . .	29
5.	Unit-cell reaction rates . . . . .	29
6.	Results . . . . .	31
D.	Calculations . . . . .	31
VII.	REACTION RATE DISTRIBUTIONS . . . . .	32
A.	Introduction . . . . .	32
B.	Reaction Rate Distributions . . . . .	33
1.	Radial traverses . . . . .	33
2.	Axial traverses . . . . .	33
3.	Uranium-oxide pin zone traverse . . . . .	34
C.	Foil Data Reduction . . . . .	34
1.	Fission rates . . . . .	34
2.	Capture rates . . . . .	34
3.	Unit cell and stainless steel corrections and normalization . . . . .	34
D.	Calculational Procedures . . . . .	35
E.	Results . . . . .	35
VIII.	MEASUREMENT OF ABSORPTION-TO-FISSION RATIOS AND THE CENTRAL- POINT BREEDING RATIO . . . . .	36
A.	Introduction . . . . .	36
B.	Reactivity-Reaction Rate Method . . . . .	36
C.	Measured Quantities . . . . .	38

# TABLE OF CONTENTS

<u>No.</u>	<u>Title</u>	<u>Page</u>
	D. Calculated Quantities . . . . .	39
	E. Perturbation Denominator Measurements . . . . .	39
	F. Absorption-to-Fission Ratios. . . . .	40
	G. Central-Point Breeding Ratio. . . . .	41
	H. Summary . . . . .	41
IX.	GCFR CONTROL ROD WORTHS . . . . .	41
X.	CENTRAL SPECTRUM MEASUREMENT. . . . .	42
XI.	KINETIC PARAMETER VERIFICATION. . . . .	43
XII.	REFERENCES. . . . .	47



## LIST OF FIGURES

<u>No.</u>	<u>Title</u>	<u>Page</u>
I- 1.	Unit-Cell Structure of the Core and Axial Blanket. . . . .	50
I- 2.	Unit-Cell Structure of the Radial Blanket. . . . .	50
I- 3.	Unit-Cell Structure of the Axial and Radial Reflectors . . . .	50
I- 4.	Stationary-Half Type-1 Drawer Loading Master for the Core and Axial Blanket. . . . .	51
I- 5.	Stationary-Half Type-2 Drawer Loading Master for the Core and Axial Blanket. . . . .	51
I- 6.	Stationary-Half Type-3 Drawer Loading Master for the Core and Axial Blanket. . . . .	52
I- 7.	Stationary-Half 24 in.-Section Drawer Loading Master for the Radial Blanket . . . . .	52
I- 8.	Stationary-Half 12 in.-Section Drawer Loading Master for the Radial Blanket . . . . .	53
I- 9.	Unreflected Reference Configuration. . . . .	54
I-10.	Reflected Reference Configuration. . . . .	55
I-11.	Sketch of the Unreflected Critical Reference Assembly. . . . .	55
I-12.	Sketch of the Reflected Critical Reference Assembly. . . . .	56
II- 1.	RZ Unreflected Calculational Model . . . . .	57
II- 2.	RZ Reflected Calculational Model . . . . .	58
II- 3.	XY Unreflected Calculational Model . . . . .	59
II- 4.	XY Reflected Calculational Model . . . . .	59
III- 1.	Unreflected Reactor Configuration for the Small-Sample Central and Radial Reactivity Worth Measurements . . . . .	60
III- 2.	Unreflected Reactor Configuration for the Small-Sample Axial Reactivity Worth Measurements. . . . .	60
III- 3.	Reflected Reactor Configuration for the Small-Sample Central Reactivity Worth Measurements. . . . .	61
III- 4.	Radial Traverse of MB-10 ( $^{239}\text{Pu}$ ) . . . . .	62
III- 5.	Radial Traverse of MB-21 ( $^{235}\text{U}$ ). . . . .	62

# LIST OF FIGURES

<u>No.</u>	<u>Title</u>	<u>Page</u>
III- 6.	Radial Traverse of MB-25 ( $^{238}\text{U}$ ) . . . . .	63
III- 7.	Radial Traverse of $\text{CH}_2(\text{F})$ -4 (Polyethylene Foam). . . . .	63
III- 8.	Radial Traverse of Li-15 ( $^6\text{Li}$ ) . . . . .	64
III- 9.	Radial Traverse of 304 SST . . . . .	64
III-10.	Axial Traverse of MB-10 ( $^{239}\text{Pu}$ ) . . . . .	65
III-11.	Axial Traverse of Pu-240-2D ( $^{240}\text{PuO}_2$ ) . . . . .	65
III-12.	Axial Traverse of MB-25 ( $^{238}\text{U}$ ) . . . . .	66
III-13.	Axial Traverse of $\text{UO}_2$ -1 ( $^{238}\text{UO}_2$ ) . . . . .	66
III-14.	Axial Traverse of $\text{CH}_2(\text{F})$ -4 (Polyethylene Foam) . . . . .	67
III-15.	Axial Traverse of 304 SST. . . . .	67
IV- 1.	Measured Net Worth of the Helium Samples . . . . .	68
IV- 2.	Graph of the Calculated Real and Adjoint Fluxes and the ENDF/B-IV He Elastic Scattering Cross-Section . . . . .	68
V- 1.	$^{238}\text{U}$ Doppler Effect Measurement Configuration. . . . .	69
V- 2.	Doppler Effect for Samples N-1, MT-1, and $\text{UO}_2$ . . . . .	69
V- 3.	Doppler Effect per Kilogram of $^{238}\text{U}$ . . . . .	70
V- 4.	Cross Sectional View of the Oscillator Drawer and Doppler Capsule. . . . .	70
VI- 1.	Core Configuration for Reaction Rate Measurements. . . . .	71
VI- 2.	Fission Chamber Position Within Stationary-Half Type-1 Core Drawer. . . . .	71
VI- 3.	Aluminum Foil Holders. . . . .	72
VI- 4.	Linear Least-Squares Fits Used to Derive Stainless Steel Correction Factors for Capture Rates . . . . .	72
VI- 5.	Intra-Cell Plutonium Fission Rates in the Core Region. . . . .	73
VI- 6.	Intra-Cell Enriched Uranium Fission Rates in the Core Region. . . . .	74

# LIST OF FIGURES

<u>No.</u>	<u>Title</u>	<u>Page</u>
VI- 7.	Intra-Cell Enriched Uranium Fission Rates in the Axial Blanket Region . . . . .	75
VI- 8.	Intra-Cell Enriched Uranium Fission Rates in the Radial Blanket Region . . . . .	76
VI- 9.	Intra-Cell Depleted Uranium Fission Rates in the Core Region . . . . .	77
VI-10.	Intra-Cell Depleted Uranium Fission Rates in the Axial Blanket Region . . . . .	78
VI-11.	Intra-Cell Depleted Uranium Fission Rates in the Radial Blanket Region . . . . .	79
VI-12.	Intra-Cell Depleted Uranium Capture Rates in the Core Region . . . . .	79
VI-13	Intra-Cell Depleted Uranium Capture Rates in the Axial Blanket Region . . . . .	80
VI-14.	Intra-Cell Depleted Uranium Capture Rates in the Radial Blanket Region . . . . .	81
VI-15.	Example of Interpolated Curve Used to Determine the $^{238}\text{U}$ Capture Rate in a Fuel Plate . . . . .	81
VII- 1.	Movable-Half Axial Blanket Pin Zone. . . . .	82
VII- 2.	Location of Enriched and Depleted Uranium Foils Within Selected Rods of the Pin Zone . . . . .	82
VII- 3.	$^{239}\text{Pu}$ Radial Fission Rate Distribution, Unreflected Assembly . . . . .	83
VII- 4.	$^{235}\text{U}$ Radial Fission Rate Distribution, Unreflected Assembly . . . . .	83
VII- 5.	$^{238}\text{U}$ Radial Fission Rate Distribution, Unreflected Assembly . . . . .	84
VII- 6.	$^{238}\text{U}$ Radial Capture Rate Distribution, Unreflected Assembly . . . . .	84
VII- 7.	$^{235}\text{U}$ Radial Fission Rate Distribution, Reflected Assembly . . . . .	85
VII- 8.	$^{238}\text{U}$ Radial Fission Rate Distribution, Reflected Assembly . . . . .	85

# LIST OF FIGURES

<u>No.</u>	<u>Title</u>	<u>Page</u>
VII- 9.	$^{238}\text{U}$ Radial Capture Rate Distribution, Reflected Assembly. . . . .	86
VII-10.	$^{239}\text{Pu}$ Axial Fission Rate Distribution, Unreflected Assembly. . . . .	86
VII-11.	$^{235}\text{U}$ Axial Fission Rate Distribution, Unreflected Assembly. . . . .	87
VII-12.	$^{238}\text{U}$ Axial Fission Rate Distribution, Unreflected Assembly. . . . .	88
VII-13.	$^{238}\text{U}$ Axial Capture Rate Distribution, Unreflected Assembly. . . . .	89
VII-14.	$^{235}\text{U}$ Axial Fission Rate Distribution, Reflected Assembly. . . . .	90
VII-15.	$^{238}\text{U}$ Axial Fission Rate Distribution, Reflected Assembly. . . . .	90
VII-16.	$^{238}\text{U}$ Axial Capture Rate Distribution, Reflected Assembly. . . . .	91
IX- 1.	Drawer Loading for the Type-2 Core Composition and the GCFR Control Rod Compositions . . . . .	91
X- 1.	Spectrum Measurement Central-Drawer Loading . . . . .	92
X- 2.	Measured and Calculated Spectra at the Center of the GCFR Phase-II Core. . . . .	93
X- 3.	Measured and Calculated Spectra at the Center of the GCFR Phase-I Core . . . . .	94
X- 4.	Broad-Group Calculated Spectra for GCFR Phase-I and -II Cores . . . . .	95
X- 5.	Broad-Group Measured Spectra for GCFR Phase-I and -II Cores . . . . .	96
X- 6.	Broad-Group Measured and Calculated Spectra at the Center of the GCFR Phase-II Core. . . . .	97
X- 7.	Broad-Group Measured and Calculated Spectra at the Center of the GCFR Phase-I Core . . . . .	98
XI- 1.	$\beta\text{D/S}$ vs Subcriticality. . . . .	98

# LIST OF TABLES

<u>No.</u>	<u>Title</u>	<u>Page</u>
I- 1.	Composition Void Volume Fractions . . . . .	99
I- 2.	Composition Average Atom Densities. . . . .	99
I- 3.	Reference Configuration Dimensions. . . . .	100
I- 4.	Summary of Measurements and Parameters. . . . .	101
I- 5.	Location and Worth of ZPR-9 Fuel and <sup>10</sup> B Rods . . . . .	102
I- 6.	Delayed Neutron Fractions and Effective Decay Constants for the Reference Configurations. . . . .	103
I- 7.	Decay Constants . . . . .	104
I- 8.	Reactivity Worths of Steps Toward the Establishment of the Axial and Radial Stainless Steel Reflector . . . . .	104
II- 1.	Energy Structure of the 29-Group Cross-Section Set. . . . .	105
II- 2.	Cross-Sections Generated. . . . .	105
II- 3.	Benoist Anisotropic Diffusion-Coefficient Multipliers . . . . .	106
II- 4.	With-Streaming Neutron Balance from RZ Calculations . . . . .	106
III- 1.	Sample Description. . . . .	107
III- 2.	Sample Composition. . . . .	108
III- 3.	Results of FAR Calibrations . . . . .	109
III- 4.	Experimental Small-Sample Central Reactivity Worths in the Unreflected Assembly. . . . .	109
III- 5.	Calculated Small-Sample Central Reactivity Worths in the Unreflected Assembly with Comparison to Experimental Worths. . . . .	110
III- 6.	Calculated and Experimental Isotopic or Elemental Central Reactivity Worths in the Unreflected Assembly . . . . .	111
III- 7.	Experimental Small-Sample Central Reactivity Worths in the Reflected Assembly. . . . .	112
III- 8.	Calculated and Experimental Small-Sample Central Reactivity Worths in the Reflected Assembly with Comparison to Unreflected Results. . . . .	113

# LIST OF TABLES

<u>No.</u>	<u>Title</u>	<u>Page</u>
III- 9.	Isotopic Central Reactivity Worths in the Reflected Assembly with Comparison to Unreflected Results. . . . .	113
III-10.	Experimental Small-Sample Radial Reactivity Worth Traverses in the Unreflected Assembly. . . . .	114
III-11.	Experimental Small-Sample Axial Reactivity Worth Traverses in the Unreflected Assembly. . . . .	115
III-12.	Comparison of the C/E Values for Isotopic Central Worths in the GCFR Phase-I Assembly and the GCFR Phase-II Unreflected Assembly. . . . .	116
IV- 1.	Concentrations and Central Worths of the Helium and Sample Impurities. . . . .	116
IV- 2.	Experimental and Calculated Worths of the Helium Samples . . .	116
V- 1.	Description of Doppler Samples . . . . .	117
V- 2.	Doppler Effect Worth Measurements. . . . .	117
V- 3.	Summary of Experimental Doppler Results. . . . .	117
V- 4.	Unit-Cell Specifications for the Doppler Calculations. . . . .	118
V- 5.	Composition Atom Densities Used in the Doppler Calculations. .	118
V- 6.	One-Dimensional Diffusion Theory Models for Generating Regional Fluxes. . . . .	119
V- 7.	Doppler Difference $^{238}\text{U}$ Group Capture Cross-Sections . . . . .	119
V- 8.	Integral-Transport Theory Real and Adjoint Flux Ratios . . . . .	120
V- 9.	Summary of $^{238}\text{U}$ Doppler Effect Calculations. . . . .	120
VI- 1.	Measured Reaction Rates at Matrix Location S-23/22 . . . . .	121
VI- 2.	Mass and Composition of Fission Counter Sources. . . . .	121
VI- 3.	Measured and Calculated Central Reaction Rate Ratios . . . . .	122
VI- 4.	Description of Activation Foils. . . . .	122
VI- 5.	Relative Depleted Uranium Capture Rates Used to Derive Stainless Steel Correction Factors . . . . .	123
VI- 6.	Relative Unit-Cell Reaction Rates, Core Region, Row 22, 0-2 Inches . . . . .	123

# LIST OF TABLES

<u>No.</u>	<u>Title</u>	<u>Page</u>
VI- 7.	Relative Unit-Cell Reaction Rates, Core Region, Row 22, 22-24 Inches. . . . .	124
VI- 8.	Relative Unit-Cell Reaction Rates, Core Region, Row 33, 0-2 Inches. . . . .	124
VI- 9.	Relative Unit-Cell Reaction Rates, Axial Blanket Region, Row 22, 24-26 Inches. . . . .	125
VI-10.	Relative Unit-Cell Reaction Rates, Axial Blanket Region, Row 22, 34-36 Inches. . . . .	125
VI-11.	Relative Unit-Cell Reaction Rates, Radial Blanket Region, 0-2 Inches. . . . .	126
VI-12.	Comparison of Integrating Foil Results with Linear Integration of Circular Foil Results for Selected U <sub>3</sub> O <sub>8</sub> Plates . . . . .	127
VI-13.	<sup>238</sup> U Capture Rate Ratios of Plate-Averaged-to-Surface- Foil-Averaged and to Center-Foil-Averaged . . . . .	127
VI-14.	Cell-Average to Mapping-Foil Ratios . . . . .	128
VI-15.	Unit-Cell Mapping Foil Reaction Rates, Normalized to Absolute Fission Counter Results. . . . .	128
VI-16.	Normalization Factors and Axial Correction Factors for Unit-Cell Data. . . . .	129
VI-17.	Cell-Averaged Reaction Rates at Unit-Cell Locations . . . . .	129
VI-18.	Measured and Calculated Cell-Averaged Reaction Rate Ratios. . . . .	130
VII- 1.	Normalized Experimental Radial Reaction Rate Data . . . . .	131
VII- 2.	Normalized Calculated Radial Reaction Rate Data . . . . .	131
VII- 3.	Normalized Experimental Axial <sup>238</sup> U Reaction Rate Data . . . . .	132
VII- 4.	Normalized Experimental Axial Fission Rate Data . . . . .	132
VII- 5.	Normalized Calculated Axial Reaction Rate Data. . . . .	133
VIII- 1.	Absolute Reaction Rate Measurements . . . . .	133
VIII- 2.	Reactivity Worth Measurements . . . . .	134
VIII- 3.	<sup>252</sup> Cf Worth Measurements and Calculations . . . . .	135

# LIST OF TABLES

<u>No.</u>	<u>Title</u>	<u>Page</u>
VIII- 4.	Spectrum-Averaged Calculated Quantities. . . . .	135
VIII- 5.	Unnormalized Perturbation Denominator. . . . .	136
VIII- 6.	Normalized Perturbation Denominator. . . . .	136
VIII- 7.	Thin-Sample $(1 + \bar{\alpha})$ Values . . . . .	136
VIII- 8.	Errors in $(1 + \bar{\alpha})$ from Uncertainties in Measured Quantities . . . . .	136
VIII- 9.	Error Sensitivities. . . . .	137
VIII-10.	Central-Point Breeding Ratio Measurement . . . . .	137
IX- 1.	Average Atom Densities for Control Rod Compositions. . . . .	138
IX- 2.	GCFR Control Rod Worths. . . . .	138
X- 1.	Measured Central Neutron Spectrum. . . . .	139



REACTOR PHYSICS STUDIES IN THE  
GCFR PHASE-II CRITICAL ASSEMBLY

Edited by

R. B. Pond

ABSTRACT

The reactor physics studies performed in the gas cooled fast reactor (GCFR) mockup on ZPR-9 are covered. This critical assembly, designated Phase II in the GCFR program, had a single zone  $\text{PuO}_2\text{-UO}_2$  core composition and  $\text{UO}_2$  radial and axial blankets. The assembly was built both with and without radial and axial stainless steel reflectors.

The program included the following measurements: small-sample reactivity worths of reactor constituent materials (including helium);  $^{238}\text{U}$  Doppler effect; uranium and plutonium reaction rate distributions; thorium, uranium, and plutonium  $\alpha$  and reactor kinetics.

Analysis of the measurements used ENDF/B-IV nuclear data; anisotropic diffusion coefficients were used to account for neutron streaming effects. Comparison of measurements and calculations to GCFR Phase I are also made.

# REACTOR PHYSICS STUDIES IN THE GCFR PHASE-II CRITICAL ASSEMBLY

Edited by

R. B. Pond

## I. INTRODUCTION

The GCFR Phase-II assembly was the second in a series of critical assemblies in support of the gas cooled fast reactor design and was designated Assembly 29 on ZPR-9 at Argonne. The purpose of this phase of the program was to further characterize some of the important physics parameters of the GCFR design and to establish a reference for subsequent zone-core assemblies leading eventually to the engineering-mockup-critical assembly of the GCFR demonstration plant.

The Phase-II assembly was built with and without a surrounding solid stainless steel reflector. The purpose of the reflector was to provide a clean benchmark assembly in which neutron-leakage effects could be adequately described by calculational techniques. Without the reflector it was found that neutron leakage affected predictions of in-core physics measurements depending upon the calculational model used to represent the ZPR stainless steel matrix, reactor bed and reactor knees that surround the GCFR assembly.

In this report a detailed description of the Phase-II unreflected and reflected assemblies are given together with the physics measurement results and analyses. Included are results of ZPR-9 operational measurements, spectrum measurements, reactivity worth measurements (Doppler, helium, small-sample), GCFR control rod worths, reaction rates, point conversion ratio measurements and kinetics parameter measurements. The calculational data base used during the Phase-II program and relevant data comparisons to the Phase-I program<sup>1</sup> are also presented.

### A. Description of the ZPR-GCFR Phase-II Assembly

The ZPR-GCFR Phase-II assembly has a unit-cell structure that is derived from the Phase-I structure with a decrease in the void fraction from ~52 to 42 v/o in the core and axial blanket regions. The core and axial blanket compositions are 3-drawer unit cells with a platelet loading pattern repeating itself four times in each unit cell. The repeating pattern is identical to the Phase-I pattern except that one column of 1/2 in. void has been removed from the Phase-II pattern. Apart from the ZPR drawer and matrix tube structure, the platelet loading translates into a 3/4-drawer unit cell. The radial blanket is a 1-drawer unit cell and is identical to the Phase-I composition with a void fraction of ~37 v/o. Figures I-1 and -2 are diagrams of the unit cells for the core, axial blanket, and radial blanket compositions including representations of the matrix tube, drawer and platelet loading. Figure I-3 is a diagram of the unit cells of the radial and axial reflector compositions. The compositions are similar except the axial reflector stainless steel was placed directly in the matrix tube without a drawer. Table I-1 summarizes the void fractions of the various Phase-II compositions.

Included in the above void fractions of the GCFR Phase-II compositions is a built-in 3.90 v/o void fraction due to ZPR-9 drawer and matrix tube clearance specifications. The remainder of the void fraction is simulated in each composition with void devices made from 15 mil-thick 304 stainless steel formed into 1/8 and 1/4 in.-wide by 2 in.-high trays. These trays are welded together to form the 1/4 and 1/2 in. open-ended void frames within the compositions shown in Figs. I-1 and -2. In perspective, a column of 1/8 and 1/4 in. trays contributes 4.59 and 9.80 v/o respectively, to the void fraction of a drawer composition. For example, in the radial reflector (Fig. I-2) the combination of two columns of 1/4 in. trays (1/2 in.-void frame) plus two columns of 1/8 in. trays (1/4 in.-void frame) plus one column of 1/8 in. trays plus the built-in void fraction (3.90 v/o) sum to an ~37 v/o void fraction.

Figures I-4 to -8 are the drawer master loadings for the stationary-half; movable-half drawer masters would be mirror images of the stationary-half masters. Figures I-4, -5, and -6 show respectively, the Type -1, -2, and -3 drawer masters for the 3-drawer unit cell of the core and axial blanket compositions. In each 36 in. drawer, 24 in. of the core and the 12 in. axial blanket are shown. Figures I-7 and -8 show respectively, the unit cell of the 36 in.-long radial blanket with the first 24 in. in a 24 in.-long drawer and the last 12 in. in an effective 12 in.-long drawer. The radial and axial reflectors were respectively 36 and 6 in. long in each reactor half. With these drawer loadings the effective height in ZPR-9 of the GCFR Phase-II core is 48 in. The axial blanket is 12 in. on each end of the core and is followed by a 6 in.-long axial reflector. The radial blanket and reflector extended a full 72 in. Table I-2 tabulates average atom densities for the GCFR Phase-II compositions. Each drawer type in the core and axial blanket as well as the unit-cell compositions for the core, blankets and reflectors are separately tabulated.

Figures I-9 and -10 show the critical (unreflected and reflected) reference configurations established for the GCFR Phase-II assembly in ZPR-9. These figures show a midplane view of the stationary-half of ZPR-9. The movable-half configuration is a mirror image of the stationary-half. The placement of the core thermocouples (T) and the locations of the ZPR-9 operational dual purpose  $^{10}\text{B}$  blades and fuel rods are also shown in the figures. Except for the six fuel rod locations denoted by S (stationary-half only) or M (movable-half only), the thermocouples and the control and safety rods are also symmetric about the midplane. The drawer type loaded in each vertical matrix column in the core and axial blanket regions are indicated by numbers 1, 2, or 3. The number of matrix tubes of each composition and the effective cylindrical radius of each region are shown in Table I-3.

Figures I-11 and -12 are sketches of the reference configurations giving the dimensions of the various regions. The axial dimensions in the core and radial reflector regions include the 32 mil-front edge thickness of the drawer and the two 32 mil-front edge thicknesses of the two drawers holding the radial blanket composition. An additional 344 mils is included in the radial blanket dimension which results from the physical separation of the 24 and 12 in. sections of the blanket composition. The 282 mil separation of the axial blanket and reflector compositions is also indicated in Fig. I-12. (The calculational models for these configurations assumed that these small voids were filled with either radial blanket or axial reflector composition.)

## B. Operational Measurements and Assembly Parameters

A summary of several operational measurements and calculated assembly parameters for the unreflected and reflected reference configurations are shown in Table I-4. The table includes measured reactivity coefficients, composition exchange worths, assembly critical masses, ZPR-9 rod worths, calculated kinetics parameters, eigenvalues and reactivity conversion factors.

## C. Reflector Worth

The 6 in.-long axial reflector was formed by inserting two  $1 \times 2 \times 6$  in. stainless steel blocks directly into the matrix tubes behind nearly all of the core/axial blanket locations. The dual purpose control rod locations were left unchanged and only one  $1 \times 2 \times 6$  in. block was added behind the six thermocouple locations. The axial reflector was not included behind the radial blanket region. The radial reflector was formed by adding two complete rings of drawers encircling the existing radial blanket region. The half-height of the radial reflector was 36 in. in the form of stainless steel blocks loaded into stainless steel drawers and then into the matrix tubes. The inclusion of the stainless steel drawers in the radial reflector accounts for the slight difference in the average atom densities for the radial and axial reflectors as shown in Table I-2.

To compensate for the positive reactivity effect of adding the reflector, core-edge drawers were exchanged for radial blanket drawers. The steps toward establishing the reference reflected assembly are shown in Table I-8. All reactivity data were corrected to 25°C using a temperature coefficient of  $-2.19 \pm 0.03$  Ih/°C. The small reactivity effect of  $^{241}\text{Pu}$  decay was neglected in correcting the measurements to the reference loading.

Subcritical measurements were made using the rod-drop inverse-kinetics technique and the GCFR Phase-II unreflected kinetics parameters of Table I-6. (The reactivity results were insensitive to whether reflected or unreflected assembly kinetic parameter sets were used.) Excess reactivity measurements were made using a calibrated ZPR-9 (fuel) control rod.

Since the addition of the radial and axial reflector was simultaneously accomplished with the removal of fuel at the edge of the core, a clean measurement of the reflector worth was not possible. The reactivity worth of fuel at the core edge is different for the reference unreflected assembly than for the reference reflected assembly due to slightly differing radii and the effect of the reflector.

Using the fuel worth at the edge of the core for the reference unreflected Phase-II assembly ( $31.24 \pm 0.16$  Ih/kg), the clean critical, zero-excess reactivity, fissile material loading is reduced from 622.74 kg with 112.6 Ih excess to 619.14 kg with 0 Ih excess. Similarly, using the edge fuel worth for the reference reflected Phase-II assembly ( $33.36 \pm 0.22$  Ih/kg), the clean critical, zero-excess reactivity, fissile material loading is reduced from 590.78 kg with 66.4 Ih excess to 588.79 kg with 0 Ih excess. Hence, the difference in critical mass, 30.35 kg, taken at 33.36 Ih/kg gives the inferred worth of the reflector as  $1012.5 \pm 6.7$  Ih.

Alternatively, the worth of the reflector may be thought of as the excess reactivity of the reference reflected assembly minus the excess reactivity of the reference unreflected assembly plus the worth of the edge fuel removed to compensate for the addition of the reflector, i. e.,

$$66.4 \text{ Ih} - 112.6 \text{ Ih} + (31.96 \text{ kg})(33.36 \text{ Ih/kg}) = 1020.0 \pm 25.0 \text{ Ih}.$$

The slight difference in the two methods may be ascribed to the difference in edge-fuel worth of various combinations of Type-1, Type-2, and Type-3 core drawers. The average fuel worths for the two reference configurations, 31.24 Ih/kg and 33.36 Ih/kg, were determined by replacing equal numbers of Type-1, -2, and -3 core drawers with radial blanket drawers whereas the actual combination of drawers removed to compensate for the reflector was eight Type 1, sixteen Type 2, and eight Type 3. The uranium-oxide content of these three types of drawers differs slightly and the plutonium content of the Type-1 and -3 drawers is not exactly one-half that of the Type-2 drawer. The actual worth of the drawers removed, therefore, may not be the same as that determined using the average worth per kilogram for the 31.96 kg of fissile material removed. The worth of the stainless steel reflector by either method, however, is about the same within experimental uncertainties.

The calculated worth of the axial and radial stainless steel reflector is 1133.7 Ih which is the difference in reactivity of the as-built reflected assembly configuration and the same assembly configuration (core and blanket regions) without the reflector.

## II. CALCULATIONAL MODELS

The calculational models created for the post analysis of the GCFR Phase-II experiments are based on 29-group diffusion theory with Benoist anisotropic diffusion coefficients. Both a half-height RZ model and a half-plane XY model were generated for the reference (unreflected and reflected) experimental configurations. The space and energy independent transverse buckling of the XY model was chosen so that the XY and RZ models produced the same eigenvalue.

The cross-sections were based on the ENDF/B-IV data and were processed through the ETOE-II/MC<sup>2</sup>-2/SDX broad-group cross-section generation codes.<sup>2,3,4</sup> Spatial and energy self-shielding were accounted for.

### A. Broad-Group Cross-Sections

The 29 broad-group cross-section set generated for GCFR Phase-II was based on the ENDF/B-IV evaluated nuclear data file and was processed through the ETOE-II/MC<sup>2</sup>-2/SDX code system. The 29-group structure was the same as used for Phase I and spanned the energy range for 14.191 MeV through thermal with the energy and lethargy mesh shown in Table II-1. (The thermal group cross-sections were ENDF/B-III rather than ENDF/B-IV data.)

The neutron spatial and energy self-shielding produced by the plate unit-cell structure was accounted for by use of the SDX cell homogenization code. The 226-group base library used in SDX was generated by MC<sup>2</sup>-2 for the critically-buckled, homogenized GCFR Phase-I core configuration. (Since the  $k_{\infty}$  of the Phase-I and -II unit cells is nearly the same, little error is in-

troduced by the use of the Phase-I base library.) The unit-cell average broad-group  $\sigma$  was generated in SDX using an inconsistent P1 spatial and energy collapse.<sup>r</sup>

Cross-sections for nine unit-cell types were generated. The nine compositions were: (See Figs. I-1 and -2)

- a. core 3-drawer unit cell,
- b. core Type 1,
- c. core Type 2,
- d. core Type 3,
- e. radial blanket 1-drawer unit cell,
- f. axial blanket 3-drawer unit cell,
- g. axial blanket Type 1,
- h. axial blanket Type 2, and
- i. axial blanket Type 3.

Code limitations necessitated an approximation in modeling the core and axial blanket 3-drawer unit cells. The nonsymmetric four subunit cells in the three drawers (see Fig. I-1) constituted too large a cell for solution in SDX. The four subunit cells in the three drawers (each having a drawer and matrix tube interface at a different place within the cell) was modeled by a single 3/4-drawer platelet unit cell plus stainless steel interface regions in every position at which an interface occurred in any of the actual cells. This model approximates the spatial and resonance energy self-shielding in the four distinct subunit cells of the 3-drawer unit cell.

Four types of cross-sections were generated:

- a. "Shielded" cross-sections which include the effects of plate spatial self-shielding and resonance energy self-shielding in such a way that cell average reaction rates are correctly predicted using a diffusion theory model in which the unit-cell composition is homogenized.
- b. "Detector" cross-sections which do not include the plate spatial self-shielding effects and which correctly predict infinitely dilute, spatially homogeneous detector reaction rates in the diffusion theory model.
- c. "Plate" cross-sections for use in the generation of Benoist anisotropic diffusion coefficients.
- d. "Trace element" cross-sections generated for infinitely dilute, spatially uniform isotopes not present in the cell composition. These are the same as "detector" cross-sections.

Seven sets of broad-group cross-sections were generated by collapsing over fine (226) group spectral characteristics of several locations in the core:

- a. asymptotic core (A),
- b. core near radial blanket (B),
- c. core near axial blanket (C),
- d. radial blanket near core (D),
- e. asymptotic radial blanket (E),
- f. axial blanket near core (F), and
- g. asymptotic axial blanket (G).

The letters refer to the spectrum collapse regions indicated in Fig. II-1.

Not all cross-section types were generated for the seven spectra or for the nine unit cells; Table II-2 indicates which cross-sections were generated. Cross-sections for the reflector and matrix tube compositions were not generated; instead, unit-cell detector type cross-sections generated for the asymptotic radial and axial blanket compositions were used for these compositions. The radial reflector and matrix tube compositions of Fig. II-2 used the spectrum region-E radial blanket cross-sections and the axial reflector used the spectrum region-G axial blanket cross-sections.

#### B. Benoist Anisotropic Diffusion Coefficients

Neutron streaming in the air-filled "void slots" used in the ZPR mock-up to represent the GCFR coolant channels was modeled by introducing anisotropic diffusion coefficients into the diffusion theory calculations. Benoist "multipliers" were used such that the anisotropic diffusion coefficients were obtained as the product of the Benoist multiplier and the normal, isotropic, diffusion coefficient,  $1/3\Sigma_{tr}$ . For the directions parallel to the void slots:

$$D_{||} = M_{||}/3\Sigma_{tr}$$

while for the direction perpendicular to the slots:

$$D_{\perp} = M_{\perp}/3\Sigma_{tr}$$

In the RZ model the parallel and perpendicular results were averaged for use in the R direction:

$$D_R = (M_{\perp} + M_{||})/6\Sigma_{tr}$$

The 29-group multipliers,  $M_{\perp}$  and  $M_{||}$ , were generated for three unit cells:

- a. core 3-drawer unit cell,
- b. axial blanket 3-drawer unit cell, and
- c. radial blanket unit cell

using the Benoist formula:

$$\frac{M_k}{(\Sigma_{tr})_{cell}} = \frac{\sum_i \sum_j V_i \phi_i \frac{1}{(\Sigma_{tr})_i} P_{ij,k}}{\sum_i V_i \phi_i}$$

Here  $V_i$ ,  $\phi_i$ , and  $(\Sigma_{tr})_i$  are respectively the width, average flux, and macroscopic transport cross-section in plate  $i$  of the cell, and

$$P_{ij,k} = \frac{3(\Sigma_{tr})_j}{V_i} \int_{V_j} d\vec{r} \int_{V_i} d\vec{r}' \frac{e^{-\Sigma|\vec{r} - \vec{r}'|}}{4\pi|\vec{r} - \vec{r}'|^2} \Omega_k^2$$

is the directional probability that source neutrons in plate  $i$  suffer their first collision in region  $j$ . Here  $\Omega_k$  is the direction cosine, and  $k = ||$  or  $k = \perp$ .

The radial blanket unit-cell model is shown in Fig. I-2. Due to code limitations the 3-drawer unit cells for the core and axial blanket were approximated. For the core cell, the model consisted of a symmetric cell extending from the middle of the first  $U_3O_8$  plate and the left half of the first  $U_3O_8$  plate in drawer Type-1 was moved to the right side of drawer Type-3 in the approximate cell. (With the void slots squeezed out, such a cell is indeed symmetric.) The geometry of the axial blanket cell model coincided with that of the core cell.

The plate number densities were generated with the assumption that all plates were stretched to the full 2.175 in. height of the matrix tube. The stainless steel from the matrix tube top and bottom, drawer bottom, cladding ends, etc. was smeared into the one-dimensional plates of the model (including the void slots) according to area fraction. This procedure causes the values of  $M_k$  from the one-dimensional calculation to agree with a more realistic two-dimensional result.

In the formula for  $M_k$ , the flux was taken to be flat. This was an excellent approximation. Table II-3 lists the values of  $M_{||}$  and  $M_{\perp}$ .

### C. The RZ Model

The reference unreflected experimental configuration as cylindricalized and shown in Fig. I-11 was represented by the RZ model shown in Fig. II-1. A mesh spacing of  $\sim 2$  cm was used in both the R and Z directions. Twenty



centimeters of homogenized matrix tube composition surrounded the blankets, and logarithmic boundary conditions (extrapolation distance =  $0.71 \lambda_{tr}$ ) were used on the external surfaces.

The compositions were those given in Table I-2 except that the trace elements Cu, P, S, and Co were lumped into the iron and C, Si, and Al were lumped into the oxygen. The 3-drawer core composition was used in regions COREA, COREB and COREC, and the outer radius of region COREB was chosen to match the area of the part of the core shown in Fig. I-9 which contains an integral number of 3-drawer unit cells. The same was true in the axial blanket. The fragmented cells at the core/radial blanket interface were put into the region named EDGE2 and EDGE5.

The constant-composition domains (core, axial blanket, and radial blanket) were subdivided into the various regions shown in Fig. II-1 to facilitate the use of cross-sections collapsed over the corresponding spectra.

The reference reflected experimental configuration as cylindricalized and shown in Fig. I-12 was represented by the RZ model shown in Fig. II-2. The unreflected and reflected model prescriptions were similar except that only ten centimeters of homogenized matrix tube composition surrounded the reflectors, and the EDGE2 and EDGE5 regions were absent in the reflected model since the core contained exactly an integral number of 3-drawer unit cells.

The Benoist anisotropic diffusion-coefficient multipliers of Table II-3 were used in the appropriate compositions. The homogenized matrix tube region used isotropic diffusion coefficients. This was a good approximation in the radial region due to the absence of streaming paths but was probably poor in the axial region. Isotropic coefficients were also used for the reflector regions. Table I-4 summarizes the kinetics parameters generated in the RZ with-streaming calculations for the unreflected and reflected reference configurations.

Table II-4 summarizes the neutron balance from the calculations which included streaming. The eigenvalues produced by RZ calculations with and without Benoist diffusion coefficients indicate that neutron streaming reduces the eigenvalues more than 1.5%. The effect of the reflector on neutron leakage is to reduce the unreflected configuration blanket-leakage probability from  $\sim 22$  to 11%. If the homogenized matrix tube composition is also included, the leakage probability is reduced from 11.18 to 11.13% with an axial/radial leakage split of 26.10/73.90%. With the  $\sim 8\%$  radial-leakage probability, reflection from the ZPR bed and knees can be expected. The equivalent radius of the bed and knees that surround the reflected configuration is about 124 cm compared to a radial reflector radius of 96 cm. There is, therefore, about 28 cm of matrix tube composition separating the reflector and the reactor structure.

While the reflector reduces the unreflected configuration leakage by a factor of two, it is probable that reflection from the reactor structure will occur and the calculational model will underpredict the reflector spectrum. Based upon the calculated reduction in leakage for the as-built thickness of the axial and radial stainless steel reflector, the axial and radial leakages are reduced, respectively, approximately 0.06% and 0.66% per centimeter of reflector thickness.

#### D. The XY Model

The reference unreflected and reflected experimental configurations as shown in Figs. I-9 and -10 were represented by the planar XY models shown in Figs. II-3 and -4. A half-plane model was required to accommodate the loading asymmetry in the X direction (e.g. matrix location 13/21 is filled with a Type-3 drawer while a Type-1 drawer is opposite it in matrix location 13/25).

The mesh spacing was taken as 2.76 cm (two mesh points per drawer) in both the X and Y dimensions. Homogenized matrix tube composition was represented as surrounding the blanket exterior (22 cm) in the unreflected configuration and surrounding the reflector exterior (11 cm) in the reflected configuration. Logarithmic boundary conditions were used on the exterior surfaces. Space and energy independent transverse bucklings were chosen to force the XY eigenvalues to match the RZ eigenvalues.

The compositions are shown in Table I-2 except that, as with the RZ model, the trace elements were lumped with iron and oxygen. The same radial compositions as used in the RZ model were used in the XY model. Compositions of drawer Types 1, 2, and 3 were used as appropriate for the fragmented cells at the core/blanket interface. The Benoist anisotropic diffusion-coefficient multipliers of Table II-3 were used as:

$$D_X = M_{\perp} / 3\Sigma_{tr}$$

$$D_Y = M_{||} / 3\Sigma_{tr}$$

Isotropic coefficients were used in the reflector and homogenized matrix tube regions.

### III. SMALL-SAMPLE REACTIVITY WORTH MEASUREMENTS

#### A. Introduction

Small-sample reactivity worth measurements were made in both the unreflected and reflected versions of the GCFR Phase-II assembly. The purpose of these measurements were (1) to obtain direct determinations of central, radial, and axial reactivity worths of important materials in the GCFR program, (2) for comparison to calculations, and (3) for purposes of normalization to other phases of the GCFR program.

Three separate sets of measurements, using the sample-oscillation reactivity-difference technique, were conducted. The first two sets were central and radial traverse worth measurements, and axial traverse worth measurements in the unreflected GCFR Phase-II assembly. The configurations for these two measurements differed in sample oscillator location and reactivity adjustment compensation for the oscillator relocation. The third set of measurements were central worth measurements in the GCFR Phase-II reflected assembly.

## B. Reactor Configurations

### 1. Central and radial worth measurements in the unreflected assembly

Modifications to the basic configuration included: (1) the insertion hole for the radial sample changer traverse tube, (2) the installation of the FAR, and (3) core/radial blanket boundary reactivity adjustments.

The insertion hole was  $\sim 2.86$  cm in diameter located in the stationary-half, 4.45 cm from the core midplane and extended along matrix row 23 from column 21 (near the center of the core) to column 37 (outer edge of the radial blanket). The autorod was installed in matrix position S/M-23/14 and core/radial blanket boundary adjustments to attain a suitable excess reactivity were made by replacing blanket composition with core composition at matrix positions S/M-16/15, -30/15, -33/19, -13/27, -16/31, and -30/31. This configuration, with a measured excess reactivity of  $\sim 76$  Ih, is shown in Fig. III-1.

### 2. Axial worth measurements in the unreflected assembly

Modifications to the basic GCFR Phase-II configuration for the axial measurements included: (1) the removal of the central fuel drawers in S/M-23/23 to permit installation of the axial sample changer traverse tube, (2) the removal of fuel drawers and replacement with the FAR in S/M-23/14, (3) the loading of Type-2 drawers in S/M-23/13 to compensate for the fuel removed in S/M-23/14, and (4) the core/radial blanket boundary adjustments to attain a suitable excess. These adjustments were made by replacing blanket material with core material at matrix locations S/M-19/13, -27/13, -13/19, -33/19, -13/27, -33/27, -17/32, -29/32, -9/33, and -27/33. This configuration, shown in Fig. III-2, had a measured excess of  $\sim 84$  Ih.

### 3. Central worth measurements in the reflected assembly

For these measurements the basic configuration was the GCFR Phase-II reflected assembly. This configuration was the same as the GCFR Phase-II unreflected assembly configuration with the addition of a stainless steel axial and radial reflector and the adjustment of the core/radial blanket boundary to attain a suitable excess.

Modifications to this basic configuration for the central worth measurements included: (1) the insertion hole in the stationary-half row 23, columns 21 through 39 for the radial sample changer traverse tube, (2) installation of the FAR in S/M-23/14 and the loading of Type-2 drawers in S/M-23/13, and (3) core/radial blanket boundary adjustments to attain a suitable excess. These adjustments made at matrix locations S/M-16/15, -30/15, -32/18, -14/28, -16/31, and -30/31 resulted in an estimated excess of  $\sim 125$  Ih. This configuration is shown in Fig. III-3.

## C. Experimental Method and Equipment

### 1. Oscillator

The reactivity worth measurements were made by monitoring the reactivity change determined by the change in the position of a calibrated autorod while pneumatically oscillating an encapsulated sample radially in and out of the assembly with the sample changer. The autorod consisted of an autorod drawer, a 5/8 in.-thick tapered polyethylene blade that extended axially, completely through the core and axial blankets, a servo-control system, and a rod position potentiometer. The sample changer consisted of a turret containing eight sample positions which could be remotely selected from the control room and a double walled stainless steel traverse tube. The radial position of the traverse tube was remotely adjustable from the control room allowing a sample capsule to be pneumatically injected into a prescribed radial position in the assembly.

Three compensated ion chambers connected in parallel and located above the movable-half of the reactor continuously monitored the neutron population as the servo-control system positioned the autorod to maintain a constant current from these chambers. The output signal of the rod position potentiometer along with the sample capsule position signal (sample-in or -out) from the sample changer were digitized and transmitted to digital scalars interfaced with an on-line computer where the autorod position vs. sample capsule position information was accumulated. The reactivity worth of the sample capsule was determined from the change in position of the calibrated autorod for each sample-in and -out cycle.

Data was accumulated for several sample-in and -out cycles for each sample, and the method of Bennett and Long<sup>5</sup> was used to analyze the data so as to eliminate the effect of linear drift caused by the GCFR Phase-II temperature coefficient of reactivity. This reactivity drift was being compensated for by the autorod and therefore had to be accounted for during the sample worth measurements.

The axial traverses were performed by mounting the sample changer behind the stationary-half of the reactor with the stainless steel traverse tube inserted axially in matrix location 23/23. Otherwise the method of accumulation of radial and axial data was identical.

### 2. Samples

The samples used in these measurements are described in detail in Tables III-1 and -2. Reactivity worth measurements of sample capsules and empty capsules (both types contained in stainless steel sample-changer capsule holders) were performed. The reactivity worth of the empty capsule was subtracted from the worth of the sample capsule to yield the worth of the sample.

### 3. Fine autorod

The principal method of determining the integral and differential worth of the FAR, based upon inverse kinetics, was developed by Cohn et al.<sup>6</sup> An on-line computer data acquisition system was used to record the outputs of the FAR position potentiometer and the reactor flux level. During one second

sampling intervals, the computer recorded the flux level and the rod position simultaneously while the autorod was oscillated-in and -out of the core. A least-squares fitting method was used to fit the rod position to the associated reactivities using a multi-order orthogonal polynomial fitting function. Reactivities were calculated using inverse kinetics and the condensed versions of the unreflected assembly delayed neutron parameters of Table I-6.

The FAR was calibrated separately for each of the three sets of small-sample measurements using calibration parameters from the first through the seventh order. The uniformity of the results, however, demonstrated that parameters beyond the first-order were not significant. The first-order results of the total FAR worth for the three calibrations are listed in Table III-3.

#### D. Calculational Methods

The reactivity worths were calculated by first-order perturbation theory from a 29-group diffusion theory model of the GCFR Phase-II assembly. A half-height RZ model of the unreflected reference configuration was used for the axial and central worth calculations, while a half-plane XY model was used for the radial worth calculations. The space and energy independent transverse buckling of the XY model was chosen so that the XY and RZ models produced the same eigenvalue. Cross-sections were based on the ENDF/B-IV. The conversion factor used for the unreflected RZ model calculations was 975 lh per percent reactivity.

The reactivity worth calculations for the GCFR Phase-II reflected configuration were performed identically to the unreflected calculations using the RZ model of the reference reflected configuration. The pre-analysis reactivity conversion factor of 972 lh per percent reactivity for the GCFR Phase-II reflected assembly was used in determining the calculated worths. The post-analysis reactivity conversion factor of 972 lh per percent reactivity produced no change in the calculated worth results.

The calculated central worths for both the unreflected and reflected configurations were determined at the first mesh interval of the RZ calculational model which was  $z = 1.02$  cm from the axial midplane of the reactor. Since the sample insertion tube was offset from the axial midplane by  $z = 4.45$  cm a slight discrepancy existed between the "central" positions of the calculated and experimental worths. Interpolation of the isotopic calculated axial worths between the second ( $z = 3.06$  cm) and third ( $z = 5.10$  cm) mesh intervals produced calculated worths at 4.45 cm. Comparison of the calculated results at  $z = 1.02$  cm and  $z = 4.45$  cm indicates the ratio of results at  $z = 1.02$  cm to results at  $z = 4.45$  cm is  $\sim 1.01$ . No corrections for these different  $Z$  values have been made in the reported data. The effect of the sample tube being offset by 4.45 cm for the radial worth measurements was explicitly taken into account in the XY calculations by the specification of the appropriate transverse integration height in the perturbation calculations.

#### E. Reactivity Worth Results

##### 1. Unreflected assembly central worths

Table III-4 contains the results of the small-sample central worth measurements in the GCFR Phase-II unreflected assembly. Table III-5 contains

the calculated small-sample results along with the C/E ratios. Table III-5 also includes sample-size correction factors computed using the PIT code.<sup>8</sup> No sample-size effect correction factors have been applied to any of the reported data. These factors are reported to demonstrate that fissile and fertile material worths are not a strong function of sample size for the sample masses used in this experiment.

Calculated and experimental isotopic central worths along with their C/E ratios are reported in Table III-6. The experimental isotopic worths were determined by solving the simultaneous equations relating isotopic worths to sample worths, i.e.

$$\sum_i M_{ij} \rho_i = \rho_j$$

where  $m_{ij}$  is the mass fraction of isotope  $i$  in sample  $j$ , and  $\rho$  is the reactivity worth of isotope  $i$  or sample  $j$ . The sample worths of samples of smallest mass were used for cases where more than one sample size was measured. No sample-size effect correction was otherwise made.

## 2. Reflected assembly central worths

Tables III-7 to -9 contain the experimental and calculated results and the C/E ratios for the small sample and isotopic worth determinations in the GCFR Phase-II reflected assembly. The ratios of the reflected to unreflected assembly results for both the small samples and isotopes are also included.

## 3. Unreflected assembly axial and radial worths

Tables III-10 and -11 contain the experimental results for the radial and axial worth traverses in the GCFR Phase-II unreflected assembly. A comparison of calculated and experimental results are graphically compared in Figs. III-4 to -15. Figures III-4 to -9 compare the relative experimental and calculated radial reactivity worths, each normalized to unity at the center, as a function of radius at  $z = 0$ . Figures III-10 to -15 compare the relative axial reactivity worths as a function of axial distance from the assembly midplane at  $r = 0$ . No sample-size effect corrections were applied to any of the data.

## F. Discussion of Reactivity Worth Results

For the most part the relative results of the small-sample reactivity worth measurements and calculations for GCFR Phase II compare closely to Phase-I. All the basic data has been presented in this report as it was in the Phase-I report without any adjustments for sample-size effects. Calculated sample-size effect correction factors were obtained for the heavy material samples and are tabulated in Table III-5 to demonstrate that sample-size effects for these samples are small ( $\pm 1$  to 2%).

### 1. Central worths in the unreflected assembly

While both composite sample worth results (Tables III-4 and -5) and isotopic worths evaluated from the experimental sample data (Table III-6) are reported, the isotopic results provide a clearer insight into the behavior

of the real and adjoint spectra. The C/E values for the heavy isotopes and strong absorbers are in general less than for Phase I (~7%). The light scattering material worths are poorly predicted again with the worths of the hydrogenous materials predicted to be negative while being measured as positive. This discrepancy can again be attributed to the sensitivity of the calculations of the real and adjoint spectra upon errors in the cross-sections and approximations in the processing codes.

Two adjustments to the C/E values were made to further compare the Phase-I and Phase-II results. In Table III-12 the normal C/E values have been shown for the various isotopes along with "adjusted" values. The first adjustment was made by multiplying all the normal C/E values by the C/E for the perturbation denominator which was determined (see Section VIII) to be  $0.850 \pm 0.014$ . The second adjustment method consisted of dividing the normal C/E values by the C/E value of  $^{239}\text{Pu}$ .

The adjusted values so obtained should give an indication of the C/E for the perturbation numerator. If it is assumed that the discrepancy between experiment and calculation for the  $^{239}\text{Pu}$  worth is caused entirely by the perturbation denominator evaluation, the two adjustments should be equivalent. Table III-12 shows they differ by about 3%. Normal and "adjusted" C/E values for Phase I are also listed in Table III-12 for comparison.

A comparison of the  $^{239}\text{Pu}$  adjusted C/E values for Phase I to those of Phase II shows good agreement for the heavy isotopes and  $^{10}\text{B}$ . This indicates that the 7% difference between the Phase-I and Phase-II normal C/E values that was mentioned previously was probably caused by inexact determinations of the calculated perturbation denominators for either or both Phase-I and -II calculations. An exception to the good agreement was the  $^{241}\text{Pu}$  isotope. A partial explanation for this disagreement is the relatively high uncertainty (~8%) in the  $^{241}\text{Pu}$  experimental result for Phase I.

The difference of about 7% in the Phase-I and Phase-II C/E values adjusted by the measured perturbation denominators for each phase can be attributed to the uncertainties in the measured and calculated perturbation denominators for each phase. The isotopes with the most significant discrepancies in their  $^{239}\text{Pu}$  adjusted C/E values are  $^{238}\text{U}$  and  $^{10}\text{B}$ . Similar discrepancies were noted in the Phase-I results.

## 2. Central worths in the reflected assembly

Reactivity worth measurements of several small samples at the center of the Phase-II reflected assembly are presented and compared to central worths in the unreflected assembly in Tables III-7 and -8. Very little difference between the results for the two assemblies is to be noted. The ratios of the reflected to unreflected results is slightly positive for the experimental results and slightly negative for the calculated results. Isotopic results, evaluated from the composite sample data, are reported in Table III-9. The reflected to unreflected ratios for the isotopic data agree generally with the composite sample data. The unreflected to reflected calculated perturbation denominator ratio of 0.9909 indicated that very little change in the results was expected.

### 3. Radial and axial worths in the unreflected assembly

Radial worth traverses (see Table III-10 and Figs. III-4 to -9) are in general agreement with Phase-I results. Normalized experimental and calculated results show good agreement for the heavy materials ( $^{239}\text{Pu}$ ,  $^{235}\text{U}$ , and  $^{238}\text{U}$ ), rather poor agreement for 304 SST, and almost total disagreement for the hydrogenous material, polyethylene foam, including misprediction of the sign of the worth. A light absorber containing predominantly  $^6\text{Li}$  demonstrated excellent agreement between experimental and calculated results.

Axial worth traverses of several materials resulted in similar worth profiles as the radial measurements. Again good agreement between normalized experimental and calculated results was demonstrated for the heavy materials including  $^{239}\text{Pu}$ ,  $^{240}\text{Pu}$ ,  $^{238}\text{U}$ , and  $^{238}\text{UO}_2$  with poor agreement for 304 SST. The sign of the polyethylene foam worth was totally mispredicted.

## IV. REACTIVITY WORTH OF HELIUM

### A. Introduction

The reactivity worth of helium was measured at the center of the GCFR Phase-II unreflected assembly. These measurements, the first of their kind in ZPR-9, were intended to provide experimental and calculational data to be used to predict the loss-of-coolant accident for the GCFR safety analysis. The experimental technique, analogous to that used for Doppler and axial small-sample reactivity worth measurements, was based on the accurate measurement of the worth of pressurized cylinders of helium.

### B. Experimental Technique

The experimental procedure consisted of measuring the reactivity worth of the sample cylinder relative to an air-filled reference cylinder by alternately positioning the sample and reference cylinders at the core center. The reactivity change associated with this oscillation was measured with a calibrated fine-autorod. Initially, the relative worth of an evacuated sample cylinder was measured. The cylinder was then pressurized to nominally 150 and 300 psia of helium and the relative worth again measured. The net worth of the helium was, therefore, the worth of the pressurized sample cylinder relative to the voided sample cylinder. A single sample cylinder was used for each of the three measurements. In order to examine the effect of local flux distortions on the sample worth, the set of measurements (0, 150, and 300 psia of helium) were made using both an aluminum and a stainless steel sample cylinder; the dimensions of the two cylinder types were nominally the same.

### C. Experimental Equipment

The oscillator drawer was designed to contain both the sample and the air-filled reference cylinders. Drawer sections, fitted with bearings to facilitate oscillation, were connected between and on each end of the cylinder compartments. The drawer was designed such that when one cylinder was positioned at the core center the other was entirely withdrawn from the assembly. The separation between cylinder centers was 57.42 in. Structural materials were loaded along sections of the oscillator drawer to effect a near axial reactivity balance with the sample and reference cylinders and



thereby allow the servo-controlled fine-autorod to maintain a null reactivity change during drawer oscillations; no fuel material was loaded into this drawer.

The external dimensions of the sample and reference cylinders were nominally 31 cm in length and 5.1 cm in diameter; the vacuum/pressure valve extended an additional 8 cm in the axial direction. Two sets of cylinders were constructed. One was wrought aluminum alloy type 5052 (2.2 - 2.8 w/o Mg, 0.15 - 0.35 w/o Cr) and the other was type-304 stainless steel. The valves were composed principally of type-316 stainless steel and aluminum. Because the cylinder walls were constructed from stock material (1/32 in.-wall tubing) the inner diameter of the aluminum and stainless steel cylinders differ. The internal volume of the aluminum cylinder was  $576.2 \pm 0.8 \text{ cm}^3$  and the stainless steel cylinder was  $583.3 \pm 0.8 \text{ cm}^3$ . The mass of the aluminum cylinder was  $181.8 \pm 0.1 \text{ g}$  and the stainless steel cylinder was  $480.3 \pm 0.1 \text{ g}$ ; the mass of the valve was an additional  $88.8 \pm 0.1 \text{ g}$ .

The helium gas used in the measurement had a quoted purity of 99.9999%. Each of the impurities ( $\text{N}_2$ ,  $\text{O}_2$ , Ar, Ne,  $\text{H}_2$ ,  $\text{CO}_2$ , and  $\text{CH}_4$ ) were present in concentrations less than 0.1 ppm. The dew point was given as  $-110^\circ\text{F}$ , corresponding to 0.63 ppm of water. The procedure for pressurizing the sample cylinders was as follows. The cylinder was first evacuated to a pressure of a few microns and then filled to  $\sim 30$  psia with helium. The cylinder was evacuated a second time and then slowly filled ( $\sim 2$  min) with helium to the desired pressure. Finally, the cylinder was given at least 5 min to reach thermal equilibrium ( $23^\circ\text{C}$ ). The pressure was measured with a calibrated bourdon-tube gauge; the uncertainty in the pressure was less than  $\pm 0.5$  psi. Since the filling system was adequately flushed before each use, no impurities were added to the sample during the pressurizing operation.

The matrix loading configuration for the helium worth experiment is shown in Fig. III-2. The oscillator drawer and fine-autorod, extending through both halves of the assembly, were positioned in matrix locations S/M-23/23 and S/M-23/14, respectively. The core/radial blanket interface was adjusted to achieve criticality with the experimental equipment in place; the measured excess reactivity was  $\sim 80$  lh. In order to obtain low statistical uncertainties, the measurements were made at a power level of  $\sim 54 \text{ W}$ , corresponding to a central fission rate of  $6.9 \times 10^4$  fissions/sec per gram of  $^{239}\text{Pu}$ .

#### D. Results and Analysis

The cross-section set used for the analysis was generated from ENDF/B-IV data. Elemental worths were calculated using first-order perturbation (FOP) theory with 29-group RZ diffusion theory fluxes. The central worths (expressed in lh per  $10^{24}$  atoms) of  $^4\text{He}$ ,  $^3\text{He}$ , and the impurities are listed in Table IV-1. Also given in the table are the concentrations of the impurity atoms per  $10^6$  helium atoms; the ratio of  $^4\text{He}$  to  $^3\text{He}$  is the natural isotopic abundance. None of the impurities were present in sufficient concentration to significantly alter the sample worth.

The atom densities of the pressurized helium samples were computed using van der Waals' equation of state for a real gas; that is,

$$\left(P + \frac{n^2 a}{V^2}\right)(V - nb) = nRT$$

where  $P$  is measured in psia,  $V$  in  $\text{cm}^3$ ,  $T$  in  $^\circ\text{K}$ , and  $n$  in moles. The gas constant  $R = 1.20589 \times 10^3 \text{ (lb/in}^2\text{)(cm}^3\text{)/(mole} \cdot ^\circ\text{K)}$ ; for helium, the constants<sup>9</sup>  $a = 5.015 \times 10^5 \text{ (lb/in}^2\text{)(cm}^3\text{)}^2\text{/(mole)}^2$  and  $b = 2.370 \times 10^1 \text{ (cm}^3\text{/mole)}$ . The resulting number densities are  $\sim 1\%$  less than those predicted by the ideal gas law at 150 psia and  $\sim 2\%$  less at 300 psia (for the volumes and temperatures of this experiment).

The measured net worths of the helium samples are shown in Table IV-2; these worths are also plotted in Fig. IV-1 as a function of the sample mass. Note that the helium worth as measured in the stainless steel cylinder is  $\sim 8\%$  smaller in magnitude than that in the aluminum cylinder. Calculated sample worths and the corresponding C/E's are also given in Table IV-2. These calculated worths were obtained using FOP estimates of the  $^4\text{He}$  worth summed over the axial extent of the sample cylinder. The ratio of this axially-averaged worth to the FOP central worth for  $^4\text{He}$  is 0.955; to adjust the measured sample worth to a central worth, the measured net worth must be divided by this ratio. A one-dimensional, perturbation-integral transport formulation<sup>8</sup> was employed to account for local flux distortions introduced by the removal of the core materials and the addition of the oscillator drawer and sample cylinder. The resulting distortion-corrected worth calculations are  $\sim 10\%$  less than the simple FOP calculations; about the same percentage distortion effect was computed for the stainless steel and aluminum cylinders. The experimental estimate of the central worth is  $-170 \pm 4 \text{ Ih/kg}$  or  $-1.13 \pm 0.02 \text{ Ih}/10^{24} \text{ atoms}$ ; this value is obtained from the average central worth as measured in the aluminum cylinder, adjusted with the calculated axially-averaged to central worth ratio.

The full core worth of helium at 85 atm and  $700^\circ\text{K}$  in the GCFR Phase-II assembly (1300 liter core, 42 v/o void fraction) is calculated to be  $\sim 99 \text{ Ih}$  or  $31\text{c}$ . This calculation was based on the average central worth as measured in the aluminum cylinders. First-order perturbation theory estimates of the worth of  $^4\text{He}$  throughout the core region determined the core-averaged to central worth ratio to be 0.182.

The reactivity worths of other materials measured at the center of the GCFR Phase-II assembly also reflect a bias in the ratio of the calculated to the experimental worths (see Section III). Carbon and  $\text{BeO}$ , which like helium are light materials that are primarily elastic scatterers, have C/E's of 2.06 and 2.03, respectively. Heavier elements which have considerable capture and inelastic scattering in addition to elastic scattering, such as the components of stainless steel, have C/E's on the order of 1.5 or 1.6. Strong absorbers characteristically have C/E's near unity; i.e., 1.00 for  $^{10}\text{B}$ , 1.01 for  $\text{Eu}_2\text{O}_3$ , and 1.15 for  $^6\text{Li}$ . Fissionable materials have C/E's of 1.21 for  $^{239}\text{Pu}$ , 1.30 for  $^{241}\text{Pu}$ , and 1.23 for  $^{235}\text{U}$ . The C/E for the fertile isotope  $^{238}\text{U}$  is 1.12. Thus, the C/E's obtained for the He measurements (1.5-1.6) appear to be consistent with the general class of scattering materials. Since the He cross-section is well known and the gas samples are very close to ideal "small" perturbation samples, these gas sample measurements would seem to indicate that the C/E discrepancy is due, in most part, to the calculated real and adjoint spectra.

An examination of the helium reactivity worth experiment reveals possible sources of the discrepancy between the calculated and the experimental worths.

Natural helium is essentially a pure elastic scatterer ( $\sim 99.9\%$ ); consequently, according to first-order perturbation theory in the diffusion theory approximation, its worth is expressed by

$$\left(\frac{\delta k}{k^2}\right)_{\text{scatterer}} = - \frac{\int_V dV \sum_{g=1}^{N-1} \phi_g \sum_{k=g+1}^N \delta \Sigma_{g \rightarrow k} (\phi_g^* - \phi_k^*)}{\frac{1}{k} \int_V dV \sum_{g=1}^N \phi_g (\nu \Sigma_g) \times \sum_{g=1}^N \chi_g \phi_g^*}$$

A plot of the calculated real and adjoint fluxes for the GCFR Phase-II assembly is presented in Fig. IV-2; also given is the helium elastic scattering cross-section as obtained from the ENDF/B-IV data.

Since the helium scattering cross-section is well known, this factor by itself, is not suspect in contributing to the C/E discrepancy. The gas sample was extremely dilute ( $\sim 5 \times 10^{20}$  atoms/cm<sup>3</sup> at 300 psia) and consequently the cross-section requires no self-shielding or sample-size correction factors. This is in evidence from calculations which showed close agreement ( $\sim 0.2\%$ ) between first-order and exact perturbation worths of helium at 300 psia. This is also shown experimentally by the fact that the measured sample worth is directly proportional to the sample mass (Fig. IV-1).

Additional possible sources of the C/E discrepancy have been identified. The neutron spectrum has been measured at the center of the GCFR Phase-II core in the energy range from 1 to 2000 keV (see Section X). The discrepancies between the calculated and measured fluxes will alter the C/E ratio. The worth of scattering materials is particularly sensitive to the adjoint flux since it depends on the difference in the adjoint of the initial and final energy groups. In elastic scattering with a helium nucleus the majority of neutrons downscatter one energy group; nearly all the remainder suffer in-group or 2-group downscattering. Since the adjoint flux is slowly varying in the energy region where the scattering reaction rate is high, the calculated worth depends on the difference of two nearly equal quantities. The effect of the coarseness of the group structure on the calculated scattering component of the worth is unknown. Accounting for fine-structure (using more energy groups) or using bilinear (real and adjoint spectra) weighting in the energy group cross-section preparation algorithms would perhaps reduce some of the discrepancy between measured and calculated worths. Since the worth of scattering materials are strongly dependent upon the adjoint spectrum shape, it is possible that  $\phi^*$  weighting would be more appropriate for collapsing fine-group scattering cross-sections to broad groups. Presently,  $\phi$  weighting is used for all cross-section types in the MC<sup>2</sup>-2/SDX cross-section generation codes.

#### E. Central Worth of Air

The reactivity worth of the air that fills the simulated voids and gas-coolant channels in a critical assembly has been assumed to be small; a more-precise knowledge of its worth may be of interest in evaluating certain critical experiments. The central worth of an air sample was also measured

using the same equipment and technique developed for the helium worth measurement. The measurement was made using the aluminum sample cylinder filled with compressed breathing air at  $153 \pm 0.5$  psia. The air sample was a blend of  $N_2$  and  $O_2$  gases containing less than 500 ppm  $CO_2$  and 10 ppm CO. The dew point of the mixture was between  $-60$  and  $-66^\circ F$ , corresponding to between 22 and 34 ppm  $H_2O$ .

The measured net worth of the air sample was  $-0.275 \pm 0.006$  Ih; the uncertainty includes both the statistical uncertainty and a conservative estimate of the fine-autorod calibration uncertainty. The sample worth was calculated to be  $-0.407$  Ih by employing FOP theory to find the worth of "air" along the axial extent of the sample cylinder. The air sample was assumed to be composed solely of  $N_2$  and  $O_2$  in the ratio of their natural abundances; the reactivity effects associated with the impurities and the water vapor are negligible. (The FOP estimates of the elemental central worths were given in Table IV-1). The value of this axially-averaged to central worth ratio for the nitrogen-oxygen mixture is 0.950. The measured sample worth can be adjusted to an "experimental" central worth by dividing by this ratio. The constants in the equation of state were computed by abundance weighting the respective values for  $N_2$  and  $O_2$ ; the resulting values were  $a = 2.034 \times 10$  and  $b = 3.759 \times 10^1$ . The resulting C/E for the air sample is 1.48; this value is in excellent agreement with that obtained for the helium worth measurement made in the aluminum cylinder. Since flux distortion effects due to the gas sample are small, the flux-distortion correction factor is the same as for the helium-filled aluminum cylinder. The resulting flux distortion corrected C/E is estimated to be  $\sim 1.3$ .

The measured worth for the  $7.18 \pm 0.02$  g sample yields an experimental central worth for dry air of  $-40.3 \pm 0.9$  Ih/kg or  $-1.93 \pm 0.04$  Ih/ $10^{24}$  molecules of air; this translates into a central worth of  $-4.78 \times 10^{-5}$  Ih/ $cm^3$  at 76 cm Hg and  $25^\circ C$ . Assuming the central worth of hydrogen to be  $+3$  Ih/ $10^{24}$  atoms, the worth of air 100% saturated with water vapor at  $25^\circ C$  is 9.4% less negative than dry air at that temperature. An uncertainty of  $\pm 1$  Ih in the hydrogen worth would result in a  $9.4 \pm 3.4\%$  decrease in magnitude relative to the dry air worth. The full core worth of dry air in the Phase-II assembly is 3.4 Ih or 1.0¢; the calculation of this value includes the measured central worth and a (FOP) calculated core-averaged to central worth ratio of 0.129.

## V. $^{238}U$ DOPPLER EFFECT MEASUREMENT

### A. Introduction

The  $^{238}U$  Doppler effect was measured for a natural uranium-oxide sample located at the center of the GCFR Phase-II unreflected assembly. The sample was nominally 12 in. long, 1 in. in diameter and weighted  $\sim 1.27$  kg. The assembly configuration for the measurement is shown in Fig. V-1. This is a modification of the Phase-II reference configuration in which the Doppler equipment was installed in matrix location 23/23 and a fine-autorod installed in 23/14. The radial blanket/core interface was also adjusted to achieve criticality with the experimental equipment in-place. These adjustments increased the effective core radius from 58.23 to 59.06 cm, the fissile material loading from 622.74 to 634.70 kg, and decreased the radial blanket thickness from 24.53 to 23.70 cm.

The Doppler reactivity worth was measured using the sample-oscillation reactivity-difference technique. In this technique, the temperature controlled Doppler sample is oscillated (axially) in and out of the core and the reactivity worth difference is inferred from the difference in critical-rod-position of the calibrated, servo-controlled, fine-autorod (FAR). As the sample temperature is varied, the change in the reactivity worth difference is a measure of the temperature reactivity effect of the sample including Doppler, expansion and structural material effects.

## B. Experimental Measurements

The Doppler sample used in this measurement was of the freely expanding (FE) type and was encapsulated in an inconel-600 capsule. A Doppler effect measurement of a nominally identical empty inconel-600 capsule was also measured for the purpose of correcting the Doppler sample measurement for capsule reactivity effects. Table V-1 summarizes the physical descriptions of the natural  $\text{UO}_2$  Doppler sample (N-1) and the empty inconel-600 capsule (MT-1).

Table V-2 tabulates the experimental Doppler results. The table shows as a function of sample temperature, the difference ( $\bar{D}$ ) in the FAR critical-rod-position when the sample was in the core minus the position when the sample was out of the core. This difference is expressed as a percentage of the total travel of the FAR from full-out to full-in. In order to establish the precision of the measured difference, the method of Bennett and Long<sup>5</sup> for measuring small reactivity differences was used. This precision is tabulated in the column headed  $\sigma_{\bar{D}}$ . The last two columns ( $\rho$  and  $\sigma_{\rho}$ ) express the Doppler reactivity worth and uncertainty between the initial (cold) sample temperature and each elevated (hot) sample temperature. These reactivity results were obtained by multiplying the FAR position difference results by the reactivity worth of the FAR per percent travel of the FAR. In addition,  $\sigma_{\rho}$  includes a 1% uncertainty in the FAR calibration factor in order to account for any reactivity nonlinearity of the FAR.

Because the Doppler worths of N-1 and MT-1 were measured at different elevated temperatures, there is no common correspondence between the two measurements as a function of sample temperature. In order to put the two measurements on a common basis, the reactivity data of Table V-2 were separately fitted<sup>10</sup> (in a least-squares sense) to the expression

$$\rho(T) = \frac{C_1 T_0}{1-\gamma} [(T/T_0)^{1-\gamma} - 1] + C_2 \quad (\text{V-1})$$

where  $C_1$ ,  $C_2$ , and  $\gamma$  are fitting parameters,  $T_0$  is taken as 300°K, and  $\rho(T)$  is the reactivity as a function of temperature in degrees Kelvin. (Equation V-1 is the integral of the theoretical Doppler coefficient expression

$$d\rho/dT \propto (T_0/T)^{\gamma} \quad (\text{V-2})$$

where  $\gamma \neq 1$ .) Using the fitted parameters for each experimental data set,  $\rho(T)$  was then calculated between 300 and 1100°K in 100°K increments. These fits evaluate the Doppler effect between the reference temperature of each sample and common elevated temperatures over the experimental temperature range of the reactivity measurements. The sample reference temperatures were 298°K for N-1 and 301°K for MT-1 (see Table V-2).

The results of these fits are shown in the second and third columns of Table V-3 for the N-1 and the MT-1 samples, respectively. Since these reactivity worths are relative to each sample's reference temperature an adjustment to a common 300°K reference temperature was made by subtracting the 300°K reactivity worth from the reactivity worth at all temperatures. Then using these adjusted results, the empty capsule Doppler effect (prorated by the ratio of inconel masses of N-1 to MT-1) was subtracted from the N-1 results to obtain the net UO<sub>2</sub> sample Doppler effect at each elevated temperature (column 4, Table V-3). In addition, the net UO<sub>2</sub> Doppler worth per kilogram of <sup>238</sup>U in the N-1 sample (1.10818 kg) was evaluated and listed in the last column. The least-squares fit of the latter worth per kilogram Doppler data results in a temperature exponent  $\gamma$  value of  $0.94 \pm 0.05$  for the theoretical Doppler coefficient. Figures V-2 and -3 graphically present the data of Table V-3.

The experimental <sup>238</sup>U Doppler worth between 300 and 1100°K at the center of the GCFR Phase-II assembly is  $0.623 \pm 0.009$  Ih/kg <sup>238</sup>U. The reactivity effect of UO<sub>2</sub> expansion and the <sup>235</sup>U Doppler effect were not evaluated, however, those reactivity contributions are negligible in comparison to the <sup>238</sup>U Doppler effect. The above <sup>238</sup>U Doppler result does however include the correction for the structural Doppler effect of the inconel capsule which in this case was 5.6% of the total reactivity signal of N-1 at 1100°K. Between 300 and 1100°K the capsule was worth  $-0.0372 \pm 0.0069$  Ih/kg of <sup>238</sup>U in the sample and the total worth of the sample plus capsule was  $-0.6606 \pm 0.0062$  Ih/kg.

### C. Calculational Model

#### 1. Perturbation formulation

The perturbation formulation used to compute the Doppler reactivity effect of the UO<sub>2</sub> sample was similar to the method outlined in Ref. 11. In this method the reactivity is based upon the change in <sup>238</sup>U capture of the hot sample relative to the cold sample.\* The method also includes hot-sample cold-reactor resonance interaction effects<sup>12,13</sup> based upon the change in <sup>238</sup>U capture in the core when the sample is heated.\*\* The reactivity expression is of the form

$$\delta k/k = \frac{k}{D} \int \delta \Sigma_c^{28} \phi_0 \phi_0^* dV \quad (V-3)$$

where D is the perturbation denominator,  $\phi_0$  and  $\phi_0^*$  are the (unperturbed) real and adjoint reactor fluxes at the position of the measurement, and the Doppler difference cross-sections are

$$\delta \Sigma_c^{28} = \delta \Sigma^S (\phi_h^S \phi_c^S / \phi_0 \phi_0^*) + \delta \Sigma^C (\phi_h^C \phi_c^C / \phi_0 \phi_0^*) \frac{A^C}{A^S} \quad (V-4)$$

---

\*Only the change in <sup>238</sup>U capture cross-section is important since the reactivity contribution for minor constituents of the sample are negligible.

\*\*Only the change in <sup>238</sup>U capture cross-section in the zone of the core surrounding the sample is important since the sample/core resonance interaction occurs within a few mean-free neutron paths of the sample with the greatest effect occurring between resonances of the same isotope in both regions.

where the superscripts s and c are for sample and core, respectively, and the subscripts h and c are for hot and cold, respectively. The integral is over the volume of the sample, and  $A^s$  and  $A^c$  are the cross sectional areas of the sample and core regions, respectively.

Since the Eq. V-3 fluxes are unperturbed reactor fluxes, i.e. without the sample in-place, the Eq. V-4 flux ratios account for the reactor flux perturbation with the sample in-place. The second term in Eq. V-4 accounts for the hot-sample cold-reactor resonance interaction effect.

## 2. Cross-section preparation

The cross-sections used to calculate  $\phi_0$ ,  $\phi_0^*$ , and D in Eq. V-3 were from the 29-group diffusion theory calculations (with Benoist anisotropic diffusion coefficients) for the GCFR Phase-II unreflected reference configuration in RZ geometry. The Doppler difference cross-sections for the sample and core in Eq. V-4 were explicitly calculated for the experiment. For the calculations the energy region of importance for the  $^{238}\text{U}$  Doppler effect are groups 13 through 27 of the 29 broad-group energy structure shown in Table II-1. Groups 13-17 (40.87 through 3.35 keV) cover the  $^{238}\text{U}$  unresolved resonance region and groups 18-27 (3.35 keV through 1.86 eV) cover the  $^{238}\text{U}$  resolved resonance region.

Cross-sections for two unit-cell types were generated: one using equivalence theory for the treatment of spatial heterogeneity effects and another using integral-transport theory. Both unit cells are shown in Table V-4. In addition to the sample region shown in Table V-4, a jacket and filter region are also defined. These regions correspond to the environs of the sample which are shown in a cross sectional view of the Doppler oscillator drawer in Fig. V-4. The inconel jacket region includes the inner jacket and heater coil, and the stainless steel filter region includes the outer tube, capsule cover, oscillator drawer and matrix. Surrounding these regions is a core region which is divided into two parts. Ring 01 is the area of an octagon around the oscillator drawer (see Fig. V-1) equivalent in area to seven matrix tubes, and the Core A region extends out to 20 cm for the integral transport unit-cell and out to 59 cm (the core region radius in Fig. V-1) for the equivalence theory unit cell. The homogeneous atom densities of the materials in these regions are shown in Table V-5. (The radial blanket composition also shown in Table V-5 was used later in the reactor modeling when diffusion theory fluxes were generated to collapse fine-group equivalence theory cross-sections into broad groups.)

The sample cross-sections in the equivalence theory model were calculated in the MC<sup>2</sup>-2/SDX cross-section code using a 226 fine-group base library of ENDF/B-IV data. These cross-sections were collapsed to broad groups using a fine-group weighting spectrum characteristic of the GCFR-II core composition. Two SDX models were used to determine if the presence of the sample environs would significantly influence the broad-group cross-sections. The diffusion theory models for generating the core spectrum in the sample region are shown in Table V-6. Homogeneous cross-sections for the (core, inconel, stainless steel, and radial blanket) materials in the various regions of Table V-6 for the two models were calculated in the same SDX run that the equivalence theory sample cross-sections were calculated.

The 2-region model assumed none of structure of the measurement configuration while the 6-region model assumed the exact Doppler measurement configuration, i. e., the same as Fig. V-1. The conclusion from this comparison was that there was negligible difference in the sample cross-sections. Therefore, because the 6-region model also generated cross-sections for the jacket and filter regions, this model was used so that a consistent set of sample, jacket and filter material cross-sections could be used in subsequent calculations when the flux ratios of Eq. V-4 were determined.

Cross-sections in the integral-transport theory model were calculated using ENDF/B-IV data by MC<sup>2</sup>-2 on an ultra-fine-group basis ( $\Delta u = 1/120$ ) over the resolved resonance region of  $^{238}\text{U}$ . These cross-sections were calculated for the regions of the transport unit-cell model (Table V-4) and collapsed to broad groups using an ultra-fine-group transport theory weighting spectrum. The purpose of these calculations was two-fold. First, they were intended to generate more accurate resolved resonance cross-sections for  $^{238}\text{U}$  than are calculated by the narrow resonance approximation assumed in the equivalence theory treatment, and second, to determine the sample/core resonance interaction effect which is represented by  $\delta\sum^{\text{C}}$  in Eq. V-4.

### 3. Doppler difference cross-sections

The Doppler difference sample cross-sections ( $\delta\sigma^{\text{S}}$ ) were obtained by generating the above described cross-sections for an elevated sample temperature of 1100°K and for a base sample temperature of 300°K and taking the difference in each energy group. The Doppler difference core cross-sections ( $\delta\sigma^{\text{C}}$ ) at 300°K were obtained as the difference in core cross-sections when the sample was hot and when the sample was cold.

The  $\delta\sigma^{\text{S}}$  and  $\delta\sigma^{\text{C}}$  cross-sections generated using equivalence theory and integral-transport theory are shown in Table V-7 for the sample and the Ring 01 region of the core. Below 4 keV (which is the top of the  $^{238}\text{U}$  resolved resonance region in ENDF/B-IV) the integral-transport theory Doppler difference cross-sections were used for groups 18-27 and below 46.3 keV (which is the top of the  $^{238}\text{U}$  unresolved resonance region in ENDF/B-IV) the equivalence theory Doppler difference cross-sections were used for groups 13-17. Table V-7 also shows the equivalence theory cross-sections in the resolved region for comparison with the integral-transport cross-sections.

### 4. Flux ratios

The perturbed fluxes of Eq. V-4 were from 29-group integral-transport theory calculations using the PIT code<sup>8</sup> for the (transport) unit cell of Table V-4. The cold fluxes  $\phi_{\text{S}}^{\text{C}}$  and  $\phi_{\text{C}}^{\text{C}}$  were calculated using (cold) SDX composition cross-sections for the sample, jacket, and filter regions and previously developed cell-averaged core cross-sections for the Ring 01 and Core A regions. The hot fluxes  $\phi_{\text{S}}^{\text{H}}$  and  $\phi_{\text{C}}^{\text{H}}$  were calculated with these same base cross-sections modified by the addition of the Doppler difference cross-sections of Table V-7. The  $\delta\sum^{\text{S}}$  cross-sections were added to the sample region and  $\delta\sum^{\text{C}}$  were added to the Ring 01 region.

The flux ratios of the cold and hot fluxes with respect to  $\phi_0$  and  $\phi_0$ , and the product of the real and adjoint flux ratios for the sample and Ring 01 regions are shown in Table V-8.



#### D. Discussion of Results

A summary of the  $^{238}\text{U}$  Doppler effect calculations are shown in Table V-9. The calculated Doppler effect per kilogram of  $^{238}\text{U}$  (item #6) is  $-0.515 \text{ Ih/kg}$  which compares with the experimental value of  $-0.623 \pm 0.009 \text{ Ih/kg}$ . The calculated to experimental worth ratio is 0.827.

Table V-9 also shows several of the components and factors which influence the calculated Doppler effect and which were implicitly or explicitly represented in the calculational model. These include:

- a. the axial flux shape over the 12 in.-long sample (item #2),
- b. the sample flux perturbation (item #3),
- c. the hot-sample cold-reactor resonance interaction (item #5),
- d. the unresolved/resolved resonance region split (item #9),
- e. the Doppler difference cross-section preparation (item #10a), and
- f. the diffusion theory fluxes and perturbation denominator (item #10b).

For these particular GCFR-II calculations these effects are generally small and tend to cancel one another as is indicated below.

1. For a base Doppler effect calculation which excludes the axial flux shape factor, the sample flux perturbation, and the hot-sample cold-reactor resonance interaction, the calculated worth is  $-0.5174 \text{ Ih/kg}$ . The axial flux shape reduces the base Doppler effect by a factor of 0.9761 whereas the flux ratios increases it by a factor of 1.0148 resulting in a calculated sample Doppler effect of  $-0.5125 \text{ Ih/kg}$ .

2. The hot-sample cold-reactor resonance interaction effect is calculated to be only  $-0.0028 \text{ Ih/kg}$  or about 0.5% of the sample Doppler effect.

3. Approximately 42% of the Doppler effect is from the unresolved resonance region (groups 13-17) and 58% from the resolved region (groups 18-27) and mostly from groups 18-23.

4. Using the (SDX) equivalence theory Doppler difference cross-sections (Table V-7) in the resolved resonance region decreases the calculated  $-0.5125 \text{ Ih/kg}$  Doppler effect by 3.7%.

5. The real and adjoint fluxes ( $\phi_0$  and  $\phi_0^*$ ) and the perturbation denominator (D) used in these calculations were from 29-group diffusion theory calculations using anisotropic diffusion coefficients in order to account for neutron streaming effects in GCFR-II. If, however,  $\phi_0$ ,  $\phi_0^*$ , and D from diffusion theory calculations using isotropic diffusion coefficients are used, then the calculated Doppler effect ( $-0.5125 \text{ Ih/kg}$ ) is increased 6.2% to  $-0.5444 \text{ Ih/kg}$ . This calculated worth plus the sample/core resonance interaction effect ( $-0.0030 \text{ Ih/kg}$ ) results in a calculated Doppler effect of  $-0.547 \text{ Ih/kg}$  and a C/E value of 0.878.

Based upon the foregoing discussion it is seen that the net calculated  $^{238}\text{U}$  Doppler effect of  $-0.515$  Ih/kg is approximately the same as the base Doppler effect of  $-0.517$  Ih/kg which neglects several aspects of the calculational model. At least for GCFR-II the axial flux shape, the sample flux perturbation, and the hot-sample cold-reactor resonance interaction are not too significant. The use of integral-transport theory Doppler difference cross-sections improves the calculation relative to the equivalence theory cross-section preparation. However, this too, is not too significant for the generally hard GCFR type spectrum because of the nearly equal split between the unresolved and resolved resonance regions and because of the large contribution from groups 18-23 in the resolved region where the Doppler difference cross-sections (Table V-7) are not too different.

Neglecting neutron streaming using isotropic diffusion coefficients increases the calculated Doppler effect to  $-0.547$  Ih/kg which gives a C/E value of 0.878 relative to the measured  $^{238}\text{U}$  Doppler effect of  $-0.623 \pm 0.009$  Ih/kg. Note that this larger C/E value is consistent with C/E values for the  $^{238}\text{U}$  Doppler effect in sodium-voided LMFBRs which have been calculated in the past and which have neglected neutron streaming.<sup>14</sup> Thus, neutron streaming must be accounted for in the GCFR as well as in the similar situation of sodium-voided LMFBRs.

The capsule Doppler effect arising from the inconel jacket surrounding the  $\text{UO}_2$  sample was not calculated for this experiment because of code limitations in generating cross-sections for light nuclides. In this case, only smooth cross-section data are used for all resonant and nonresonant materials of atomic mass  $<100$  amu and therefore Fe, Ni, and Cr Doppler difference cross-sections were unavailable.

## VI. CENTRAL REACTION RATES AND UNIT-CELL MEASUREMENTS

### A. Introduction

Central reaction rates were measured at the center of the GCFR Phase-II unreflected assembly using Kirn-type counters for the fission rates and off-line gamma-ray analysis of irradiated foils for capture rates. In addition, detailed intra-cell reaction rates were measured at several locations in the core and blankets using foil irradiation techniques. Cell-averaged reaction rates from these irradiated foils are compared to the fission counter measurements and to calculated cell-averaged reaction rates. The core configuration for the measurements is shown in Fig. VI-1.

### B. Central Rate Measurements

#### 1. Experimental technique

Absolute fission rates were measured for  $^{239}\text{Pu}$ ,  $^{240}\text{Pu}$ ,  $^{241}\text{Pu}$ ,  $^{235}\text{U}$ ,  $^{238}\text{U}$ , and  $^{232}\text{Th}$  at the center of the assembly (location S-23/22, a Type-1 drawer, next to the central drawer S-23/23) using a 5.1 cm diameter Kirn-type fission counter. A second counter was positioned in drawer S-23/16 to normalize successive reactor runs. Figure VI-2 shows the position of the detector within the drawers. The front two inches of drawer materials were removed to accommodate the detector, with the fission source positioned 1.91 cm from the front of the drawer.

Scaler data was accumulated along with the fission product spectrum for each sample, the latter being used to calculate the tailing correction factor. Central capture rates in  $^{232}\text{Th}$  and  $^{238}\text{U}$  were measured by placing 0.5 in.-diameter, 5 mil-thick foils of depleted uranium and  $^{232}\text{Th}$  (four of each) in the central fission counter cavity, with the counter removed. A special holder positioned these foils in the same vertical plane at the same location as the fission counter sources. The foils were then counted off-line to determine the capture rates.

## 2. Data reduction and results

Scaler data from the fission counters were corrected for the low-energy tailing and alpha-particle contributions by using a factor calculated from the multichannel analyzer spectra. Table VI-1 lists the fission rates measured at matrix location S-23/22. These numbers are fissions per second per microgram of source material normalized to 500 counts/sec in the monitor  $^{239}\text{Pu}$  counter, corresponding to a reactor power level of  $\sim 120$  W.

Table VI-2 lists the isotopic compositions and masses of the fission counter sources which were used for the isotopic corrections to the measured fission rates listed in Table VI-1. Since the fission rates of  $^{242}\text{Pu}$ ,  $^{234}\text{U}$ , and  $^{236}\text{U}$  were not measured, calculated values were used for these corrections. A correction was also made for the presence of  $^{241}\text{Am}$  in the  $^{241}\text{Pu}$  sample using a calculated value of the  $^{241}\text{Am}/^{239}\text{Pu}$  fission rate ratio.

The foils irradiated for the central capture rate measurement were counted off-line for capture-product gamma-rays using a Ge(Li) detector system. Counting results were corrected for detector efficiency, gamma-ray intensity, irradiation history and decay time. Table VI-3 lists the measured and calculated isotopic reaction rate ratios at the central detector position.

## C. Unit-Cell Measurements

### 1. Experimental technique

Detailed intra-cell reaction rates were measured at several locations in the core and both (radial and axial) blankets of the assembly. These results provide cell-averaged reaction rate ratios and are also used to convert point reaction rate data to cell-averaged results. In addition, the effect of fuel plate cladding on the  $^{238}\text{U}$  capture rate was measured by inserting extra stainless steel next to the fuel, then extrapolating to zero-thickness clad.

Foils were held in 1 mil-thick aluminum folders as shown in Fig. VI-3. Packets containing plutonium foils were placed only next to the fuel plates. In the central 3-drawer unit cell, the normal 0.25 in.-thick fuel plates were replaced by pairs of 0.125 in.-thick plates, and foil packets placed between them. Wherever possible, the uranium-oxide plates were also replaced with half-thickness plates for a more detailed analysis. Table VI-4 describes the foils used for the unit-cell measurements.

The fuel plates are clad in 15 mil-thick stainless steel. The half-width fuel plates introduce 0.030 in. of extra stainless steel into the drawer, and this is expected to affect the  $^{238}\text{U}$  capture rate measured between

the plates. To determine the effect of the stainless steel clad, an auxiliary measurement was made in which extra stainless steel was inserted between the fuel and foils, and the results extrapolated to zero-thickness cladding.

## 2. Data reduction

After irradiation, the gamma activity of the irradiated foils was counted with NaI(Tl) scintillator detectors in an automatic foil counting system.<sup>15</sup> Fission rates were determined by counting fission-product gamma-rays with energies greater than 550 keV. The counting data were then processed using the computer codes NURF and COMBO.<sup>16</sup> With these codes, the data are corrected for decay rates, counting system dead-time and background radiation. From the normalized data, the relative reaction rates per unit mass of foil material were determined for each foil type.

After the fission-product counting of the depleted uranium foils, the same foils were counted for the relative capture rates. Differential counting was used with a window set on the composite  $\gamma$ -ray/x-ray peak at 106 keV in the decay spectrum of  $^{239}\text{Np}$ . Coincidences between two NaI(Tl) crystals were recorded and used to determine the relative capture rate for each foil.<sup>17</sup>

Uncertainties in the data are both statistical and positional. For each reaction rate and for each unit-cell position, the effect of an uncertainty of  $\pm 0.125$  in. in positioning was calculated from either radial or axial traverse curves. This uncertainty was added in quadrature to the statistical uncertainty from counting each foil.

In some locations, the foils could not be placed between every pair of plates because of the limited drawer width. To calculate the drawer average, the data at those positions were calculated based on ratios of foils within specific plate groupings. In those cases, higher uncertainties reflect the combination of uncertainties of more than one data point.

## 3. Normalization

All foil data were normalized to absolute fission counter results given in Table VI-1. During the foil irradiation, a Kirm-type counter (the same type used in the central rate measurements) was placed in matrix location S-25/22 with two foils of each type (plutonium, enriched and depleted uranium) on the face of the counter. The foils are in the same environment as the source on the Kirm-counter, and assuming that the reaction rate ratios are independent of power level, these foils should measure the same absolute rates as the fission counters. Thus, to get a normalization factor for each foil type, the average value of the relative rates of each pair of foils was equated to the appropriate rate given in Table VI-1 (isotopic compositions were accounted for). Using these normalization factors and the COMBO relative foil rates, the absolute rates were calculated so that ratios could be formed.

This normalization technique assumes only that the foils placed on the front of the counter react to the same flux as the counter itself. While the detector cavity does perturb the local flux, no assumption is made that the detector samples a unit-cell-averaged reaction rate or any representative drawer-averaged rate.

#### 4. Stainless steel corrections to capture rates

As noted above, the stainless steel clad of the fuel plates is expected to influence the measured  $^{238}\text{U}$  capture rate. Four locations along row 22 were used to insert extra stainless steel between the foil and the cladding of the normal 0.25 in.-wide plates. Four locations along row 24 were used to insert extra stainless steel on each side of a foil placed between the half-width fuel plates. In the drawers with half-width plates, uranium foils were placed between the plates with 0.015 in. (clad only), 0.025 in., 0.030 in., and 0.035 in. of stainless steel on each side of the foils. In the normal-plate drawers, foils were positioned against one side of the fuel plate with 0.015 in. (clad only), 0.025 in., 0.035 in., and 0.045 in. of stainless steel between the foils and the fuel.

To derive a stainless steel correction factor, the four positions were first normalized to the same radial distance from core-center. This was done by fitting a zero-order Bessel function to a row 23 radial capture rate traverse and using the fitted curve to eliminate gross flux shape effects from each of the data points.

A linear least-squares fit to the four points for each case was extrapolated to zero-thickness clad, and the ratio of the zero-thickness rate to the 15 mil-thickness rate was used to correct all other capture rate data. Table VI-5 lists the data used to derive the correction factors, and also the radially corrected values. Figure VI-4 shows the linear fits leading to the correction factors for foils next to normal fuel plates ( $0.999 \pm 0.008$ ) and for foils between half-width plates ( $0.984 \pm 0.008$ ).

#### 5. Unit-cell reaction rates

Intra-cell reaction rates were measured by placing foils between the plates of selected 3-drawer unit cells in the core and axial blanket, and 1-drawer unit cells in the radial blanket. In addition to the normal circular foils, a small number of rectangular, integrating foils were used. These foils are approximately  $0.375 \times 0.22$  in. and are placed horizontally between special 1 in.-high, 0.25 in.-wide depleted uranium-oxide plates. The rectangular foil in effect integrates the reaction rate across the width of the plate. Plutonium foils were used only in the core region, and only next to the fuel plates.

In order to eliminate the effects of gross flux shapes through the unit-cell regions, results were corrected for positional differences. Multi-parameter polynomial curves were fit to the experimental reaction rate distribution data. These curves were interpolated to give a value of each reaction rate at each foil location within the unit cells. Using the position of one foil as a reference (the foil next to the left-hand fuel plate in the Type-2 core drawer,  $x = 2.375$  in. within the 3-drawer core cells; the foil at  $x = 2.375$  in. within the 3-drawer axial blanket cells; and the foil at  $x = 0.375$  in. within the radial blanket cells), and setting its value equal to 1000, the ratios of the value at the reference position to the values at the other positions were formed. The data at each foil location in the unit cells were multiplied by the appropriate ratio to yield radially corrected data.

Figure VI-5 shows a typical distribution of plutonium reaction rates in a core region unit cell after radial corrections. Figures VI-6 to -8 show representative distributions of the  $^{235}\text{U}$  fission rate in the core, axial blanket, and radial blanket regions, respectively. Figures VI-9 to -11 show distributions of the  $^{238}\text{U}$  fission rate and Figs. VI-12 to -14 show the  $^{238}\text{U}$  capture rate distributions in these same regions. Tables VI-6 to -11 summarize the radially-corrected foil data for each of the unit-cell locations. Stainless steel corrections have not been applied to the capture rate data in these tables.

Drawer-averaged reaction rates were calculated according to

$$\bar{R} = \sum R_j N_j / \sum N_j \quad (\text{VI-1})$$

where  $R_j$  is the average reaction rate in plate  $j$  and  $N_j$  is the atom density of a given isotope in that plate. The summation is over all plates in the drawer, or over all plates in the unit cell.

Two methods were used for determining plate-averaged rates. In all cases except  $^{238}\text{U}$  capture in fuel plates, linear averages were calculated across the plates using the foil data at the plate edges. For the cases where circular foil data overlaps integrating foil data, a comparison is made in Table VI-12 which indicates that the linear interpolation method generally agrees with the depleted uranium integrating foil results. The integrating foil data were not used to calculate cell averages.

Capture rates in fuel plates were determined by fitting a curve between the three foil data points (two surface and one center). This curve was drawn to match the results of a simulated fuel-plate experiment, which were also verified by Monte Carlo calculations. Figure VI-15 shows an example of this curve, which was numerically integrated to give an average capture rate in the fuel plate. Using the four half-width fuel plate results, a ratio of plate average to surface-foil average was used to derive other fuel plate capture rates. Table VI-13 lists the ratios of plate average to surface-foil average rates and plate average to center-foil rates for the half-width plate locations.

A two-step procedure was used for determining absolute cell-averaged reaction rates. First, the relative cell average rate calculated with Eq. VI-1, and the relative "mapping" foil (so-called because their position within the unit cell is the same as that used for distribution mappings) rates were used to find a cell-average to mapping-foil ratio for each mapping foil in the unit cell. Then the mapping foil relative rates were changed to absolute values using the normalization procedure discussed above, and absolute cell average rates were calculated using the cell-average to mapping-foil ratios. Within each 3-drawer core unit cell, there are four mapping foils, and because of the asymmetric nature of the unit cell, a cell correction factor is listed for each one. The cell-average to mapping-foil ratios for each position are tabulated in Table VI-14.

Table VI-15 lists the mapping foil reaction rate values which have been normalized using the absolute counter data of Table VI-1. Note that this data are not corrected for radial position differences. The average reaction rate across the unit cell will therefore reflect the changing flux across the cell.

To facilitate the calculation of reaction rate ratios, an axial position correction has been applied to both the plutonium and enriched uranium foil data, so that all numbers in any unit cell represent foils at the same axial position. Axial correction factors were taken from multiparameter polynomial fits to axial reaction rate distributions. These factors and the absolute normalization factors are listed in Table VI-16.

## 6. Results

Using the normalized mapping foil data in Table VI-15 and the unit-cell factors in Table VI-14, the cell-averaged reaction rates are calculated and given for each location in Table VI-17. The  $^{238}\text{U}$  and  $^{235}\text{U}$  reaction rates were found by solving the simultaneous equations involving the enriched and depleted values, along with the foil composition data of Table VI-4.

Using the cell-averaged reaction rates of Table VI-17, reaction rate ratios were formed to be compared to calculated values. These ratios are on a per atom basis, and represent statistically weighted averages of the ratios calculated from individual points within each unit cell. Table VI-18 lists the average experimental reaction rate ratios.

### D. Calculations

Calculations for the GCFR Phase-II models were made with 29-group, two-dimensional diffusion theory. Benoist diffusion coefficients were used to account for anisotropic neutron streaming. The flux used to calculate the central rates were derived from the XY model of the assembly. Cross-sections were generated from ENDF/B-IV data, accounting for spatial and energy self-shielding for each region of the assembly. To calculate the reaction rates measured with the Kirn-type counters, "detector" cross-sections were also generated. These cross-sections do not include the plate self-shielding and are representative of an infinitely dilute detector material.

The calculated central reaction rate ratios and the corresponding C/E values are given in Table VI-3. The reaction rates calculated with the cross-sections and the XY model flux, while appropriate for the fission sources on the Kirn-counters, do not in any way account for the fact that a 2 in.-cubical void was created in the core, and that extra stainless steel (the counter) was placed around the source. In many cases, e.g., threshold fissioning isotope rates and capture rates, the effects of these perturbations are not negligible. Studies done in the GCFR Phase-I assembly indicate that threshold fission might be reduced by ~10% in the cavity environment, with smaller but substantial effects on the capture rate. Similar discrepancies between foil and counter measurements have been reported in SNEAK 3A-2<sup>18</sup> and in ZPPR-2.<sup>19</sup>

Calculated values of the unit-cell-averaged reaction rates are derived from the shielded cross-sections using the XY flux for all unit cells at the reactor midplane. A flux distribution calculated from the RZ model of the assembly was used to calculate unit-cell reaction rates at axial locations other than the midplane.

The XY model had four mesh regions per drawer and the RZ model had a mesh spacing of  $\sim 2$  cm. This gives twelve reaction rate values in a 3-drawer unit cell. To calculate unit-cell reaction rate ratios, the ratio was formed for each mesh interval and the average value of the ratios was taken to be the cell average ratio.

Table VI-18 lists the calculated cell-averaged reaction rate ratios and the C/E values. These values compare well to the experimental data near the core center except for the  $c^{28}/f^{49}$  ratio C/E value. Values of C/E in the core near the blanket are also good except for the  $f^{28}/f^{49}$  ratio near the axial blanket. The  $^{238}\text{U}$  fission rate decreases in this region and the C/E value is not unexpected.

In the blanket regions, calculated reaction rate values are typically lower than experimental data.\* The C/E values for the ratios are greater than unity because of the combination of the C/E values for  $f^{28}$  and  $f^{25}$  or  $c^{28}$  and  $f^{25}$ . In row 22, some discrepancy may arise from the fact that the radial flux distribution is rapidly decreasing in the radial blanket. Radial distance corrections within the unit cell are therefore quite large and may lead to some uncertainty. Since all radial distances in the row 33 unit cell are approximately the same, the position-correction uncertainty would not be present there.

Comparison of the calculated and experimental reaction rate distribution curves\* shows that the  $^{238}\text{U}$  fission rate is calculated well, even in the blankets. The  $^{235}\text{U}$  fission rate and  $^{238}\text{U}$  capture rate are in general underpredicted in the blanket regions. It is this underprediction of the  $^{235}\text{U}$  fission rate which gives the high C/E values for the  $f^{28}/f^{25}$  ratio, and which causes the C/E values to increase as one goes further into the blanket. Since  $f^{25}$  and  $c^{28}$  are both underpredicted in the blanket, the C/E values for their ratio remain reasonably constant.

While it is difficult to evaluate the meaning of these C/E values based on the unit-cell ratios alone, some conclusions can be drawn if the traverse data\* is also considered. The case where the experimental  $^{238}\text{U}$  fission rate agrees well with calculations has appeared before in the unreflected GCFR Phase-I assembly. Reflection may be taking place from the knees and bed of the reactor. These reflected neutrons have no effect on the threshold fission of  $^{238}\text{U}$ , but increase both  $c^{28}$  and  $f^{25}$  above what calculations predict. The unit-cell measurements were made without a reflector. Reflection from the empty matrix tubes, the knees, and the bed of the reactor may have increased the measured nonthreshold rates above their calculated values. In order to improve C/E values, these structures would have to be included in the reactor model.

## VII. REACTION RATE DISTRIBUTIONS

### A. Introduction

In both the unreflected (Fig. I-9) and reflected (Fig. I-10) Phase-II assemblies, the following radial and axial reaction rate distributions were measured using thin foils: fission rates in  $^{235}\text{U}$  and  $^{238}\text{U}$ , and the capture

---

\*See Section VII.



rate in  $^{238}\text{U}$ . The radial and axial fission rate distribution of  $^{239}\text{Pu}$  was also measured in the unreflected assembly. During one specific loading of the unreflected assembly, a  $^{238}\text{UO}_2$  pin zone composed of a  $7 \times 7$  drawer array was loaded in the central part of the axial blanket region of the movable-half. Neutron-streaming effects in the pin zone (movable-half) were expected to differ from those in the opposite plate-loaded stationary-half axial blanket region. Fission rates of  $^{235}\text{U}$  and  $^{238}\text{U}$ , and the capture rate of  $^{238}\text{U}$  were measured in both the pin and plate zones.

## B. Reaction Rate Distributions

### 1. Radial traverses

Radial distributions of the uranium fission rates and the  $^{238}\text{U}$  capture rate were measured along row 23 in both the unreflected and reflected reference Phase-II assemblies. The radial distribution of the plutonium fission rate was measured in the unreflected reference Phase-II assembly.

Foils were placed in the front portion of the stationary-half drawers for the traverses. Each foil was placed at the mid-height of its drawer. In the core region the foils were placed against the left side of the fuel plate in each drawer. In the radial blanket drawers, the foils were placed between each pair of uranium-oxide plates (see Figs. I-1 and -2). The plutonium foils were positioned 1.25 in., the depleted uranium foils 0.625 in., and the enriched uranium foils 1.875 in. from the midplane.

Plutonium foils, used in the first of two irradiations in the unreflected assembly, were held inside folded lengths of 1 mil-thick aluminum as shown in Fig. VI-3(a). A strip of stainless steel 15 mils thick and 0.125 in. wide was used on each side of the folder to prevent compression of the clad foil. Depleted and enriched uranium foils, used in the second of two irradiations in the unreflected assembly and in the only irradiation in the reflected assembly, were held in folders as shown in Fig. VI-3(b). Table VI-4 describes the foils used in the experiment.

### 2. Axial traverses

Axial distributions of the uranium fission rates and the  $^{238}\text{U}$  capture rate were measured in the central matrix location, 23/23, in both the unreflected and reflected reference Phase-II assemblies. Foils were placed at mid-height of the central matrix location, held inside folded lengths of 1 mil aluminum. The traverse foil holder was positioned against the left side of the right-hand fuel plate in drawer S-23/23 and against the right side of the left-hand fuel plate in drawer M-23/23.

The axial distribution of the plutonium fission rate was also measured in the unreflected reference Phase-II assembly. Plutonium foils, used in the first of two irradiations in the unreflected assembly, extended through the 24 in.-core half-height of the stationary-half. Pieces of stainless steel 0.75 in. square and 15 mils thick were inserted between some of the plutonium foils to prevent compression of the clad foils.

Enriched and depleted uranium foils, used in the second of two irradiations in the unreflected assembly and in the only irradiation in the reflected assembly, were spaced at regular intervals in the same axial traverse. In the unreflected assembly, the traverse extended through the core region of both the movable and stationary halves and through the axial blanket region of the stationary-half. Only the stationary-half was used in the reflected assembly. The 1/8 and 1/4 in.-thick uranium-oxide plate columns in the axial blanket region (Fig. I-5) were interchanged to provide a straight channel for the axial traverse.

### 3. Uranium-oxide pin zone traverse

During one loading of the unreflected Phase-II assembly, a 49-drawer pin zone (Fig. VII-1) was constructed in the central part of the movable-half axial blanket region. Each drawer was loaded with calandria containing a square array of 16 pins. Each pin consisted of two rods containing depleted uranium-oxide pellets approximately 0.338 in. diameter by 0.625 in. long. Each stainless steel clad rod contained 10 pellets.

Within the pin zone, one drawer was selected to hold enriched uranium foils (M-23/22) and one to hold depleted uranium foils (M-23/24). Within two pins of each of the two drawers, as indicated in Fig. VII-1, 0.346 in.-diameter foils were placed between the pellets. Their locations in the axial direction was approximately that shown in Fig. VII-2. With this arrangement of foils in a unit-cell calandria, the cell-averaged reaction rate may be obtained directly.

## C. Foil Data Reduction

### 1. Fission rates

For the fission rate analysis, the gamma activity of the irradiated foils was counted with NaI(Tl) scintillator detectors in an automatic foil counting system.<sup>15</sup> Fission rates were determined by counting fission-product gamma-rays with energies greater than 550 keV. The counting data were then processed using the computer codes NURF and COMBO.<sup>16</sup> With these codes, the data are corrected for decay rates, counting system dead-time and background radiation. From the normalized data, the relative reaction rates per unit mass of foil material were determined for the enriched uranium, depleted uranium, and plutonium foils.

### 2. Capture rates

After the fission-product counting of the depleted uranium foils, the same foils were counted for the relative capture rates. Differential counting was used with a window set on the composite  $\gamma$ -ray/x-ray peak at 106 keV in the decay spectrum of  $^{239}\text{Np}$ . Coincidences between two NaI(Tl) crystals were recorded and used to determine the relative capture rate for each foil.<sup>17</sup>

### 3. Unit cell and stainless steel corrections and normalization

With the foil data from the detailed unit-cell measurements of Section VI, the ratio of the cell-averaged reaction rate to the rate at any other foil position can be calculated. These ratios were then used, for

example, to convert the traverse foil results to cell-averaged rate values. In addition, the effect of the stainless steel cladding on the fuel plate was accounted for. No unit-cell correction factors have been applied in the pin zone, but because of the placement of foils in the calandria and the uniform loading of this zone, the results are unit-cell-averaged values.

The experimental fission rate data from the depleted and enriched uranium traverse foils were isotopically corrected to fission rates in  $^{235}\text{U}$  and  $^{238}\text{U}$  by placing enriched and depleted uranium foils on the face of a fission counter in matrix position S-25/22 and counting these fission counter foils along with the traverse foils. The reaction rates measured with the fission counter foils were equated to the absolute fission counter rates, then solved for the isotopic rates using the simultaneous equation technique. The capture rate of  $^{238}\text{U}$  is taken to be the capture rate observed in the depleted uranium foils.

For each reaction rate in both the radial and axial direction of both the unreflected and reflected assemblies, the cell-averaged, isotopically corrected experimental data were fit using a least-squares code from the core center to  $\sim 40$  cm. The experimental data were then normalized to 1000 at the peak value given by the fit.

#### D. Calculational Procedure

Calculations for the GCFR Phase-II models were made with 29-group, two-dimensional diffusion theory. Benoist diffusion coefficients were used to account for anisotropic neutron streaming. Cross-sections were generated from ENDF/B-IV data, accounting for spatial and energy self-shielding for each region of the assembly.

Calculated values of the cell-averaged reaction rates were derived from the shielded cross-sections using the flux from a half-plane XY model of the assembly for radial traverses. The reaction rates given by the XY model are symmetrical about row 23 and the calculated data for the radial reaction rates were normalized to 1000 at the core center. The inner most mesh region of the RZ model was centered at  $z = 1.021$  cm. For the calculated data in the axial direction, therefore, a least-squares fit was obtained and the data normalized to 1000 at the peak value of the fit.

#### E. Results

Tables VII-1 to -5 and Figs. VII-3 to -16 compare the experimental and calculated  $^{239}\text{Pu}_f$ ,  $^{235}\text{U}_f$ ,  $^{238}\text{U}_f$ , and  $^{238}\text{U}_c$  reaction rate distributions for the unreflected and reflected assemblies in the radial and axial directions. In both the tables and the figures, the locations of the experimental data points are the actual radial or axial distances of the foils from the core center. The locations of the calculated data are presented as obtained from the calculational models, i.e., centers of the mesh intervals.

In the axial direction, calculated results are presented for the stationary-half only since a full-core calculation including the uranium-oxide pin zone was not performed.

Radially, the agreement between calculated and experimental data for the reflected assembly was significantly better than for the unreflected assembly. The presence of the reflector in reducing neutron leakage, in comparison to not accounting for neutron reflection from the reactor bed and knees, can be seen. Axially, no appreciable difference was detected in comparing the agreement between calculated and experimental data for the reflected and unreflected assemblies.

The measured axial distributions in the stationary and movable halves show little difference. There is a slight increase in the reaction rates in the movable-half core, just in front of the pin zone, but distributions in the pin-zone axial blanket and plate-loaded axial blanket are nearly identical. Although streaming in the pin-zone blanket is expected to differ from the plate-loaded blanket, the difference in composition and possible reflection effects in the axial direction seem to cancel any effect that can be attributed solely to streaming changes.

## VIII. MEASUREMENT OF ABSORPTION-TO-FISSION RATIOS AND THE CENTRAL-POINT BREEDING RATIO

### A. Introduction

Spectrum-averaged capture-to-fission ratio or alpha ( $\bar{\alpha}$ ) measurements in fast critical assemblies are of considerable interest because they provide spectral indices which can be compared with calculations based on differential cross-section data. Furthermore, the breeding ratio depends on the value of the absorption (capture plus fission)-to-fission ratio ( $1 + \bar{\alpha}$ ). Because of the low fluxes characteristic of critical assemblies, integral  $\bar{\alpha}$  values cannot be determined by a mass spectrometric measurement of the neutron capture product relative to the parent isotope. Therefore, the reactivity-reaction rate method<sup>20</sup> was used to determine the ( $1 + \bar{\alpha}$ ) values reported here. These ( $1 + \bar{\alpha}$ ) measurements were made in the GCFR Phase-II assembly for the isotopes  $^{239}\text{Pu}$ ,  $^{240}\text{Pu}$ ,  $^{241}\text{Pu}$ ,  $^{233}\text{U}$ ,  $^{235}\text{U}$ ,  $^{238}\text{U}$ , and  $^{232}\text{Th}$ . The results are combined with a measurement of the cell-averaged reaction rate ratio,  $^{28}\text{C}/^{49}\text{F}$ , to obtain the point breeding (or conversion) ratio at the center of the assembly.

### B. Reactivity-Reaction Rate Method

This method depends on a combination of relative reactivity and absolute reaction rate measurements plus calculated values of  $\bar{\nu}$ , the average number of neutrons per fission, and various correction terms. Beginning with the perturbation theory expression for the reactivity of a small sample, it can be shown that the position-dependent, spectrum-weighted, absorption-to-fission ratio is

$$1 + \bar{\alpha}(\underline{r}) = \frac{D(^6\text{Li})}{\phi_a^*(\underline{r})} \left[ \frac{\bar{\nu}(\underline{r})\phi_f^*(\underline{r})}{D(^{252}\text{Cf})} - \frac{\rho(\underline{r}) \text{RCF}(\underline{r})}{R_f(\underline{r})} \right] - \text{FCF}(\underline{r}) \quad (\text{VIII-1})$$

where

$$\begin{aligned}\bar{\phi}_f^*(\underline{r}) &\equiv \sum_{i=1}^{NG} \phi_i^*(\underline{r}) \chi_i \\ \bar{\phi}_a^*(\underline{r}) &\equiv \sum_{i=1}^{NG} \phi_i^*(\underline{r}) \sigma_{ai} \phi_i(\underline{r}) \bigg/ \sum_{i=1}^{NG} \sigma_{ai} \phi_i(\underline{r}) \equiv \sum_{i=1}^{NG} \phi_i^*(\underline{r}) \chi_i(\underline{r}) \\ \bar{v}(\underline{r}) &\equiv \sum_{i=1}^{NG} (v\sigma_f)_i \phi_i(\underline{r}) \bigg/ \sum_{i=1}^{NG} \sigma_{fi} \phi_i(\underline{r}).\end{aligned}$$

In these equations  $\phi_i$  and  $\phi_i^*$  are the flux and adjoint distribution, respectively, while the absorption and fission cross-sections are represented by the symbols  $\sigma_{ai}$  and  $\sigma_{fi}$ . The spectrum of prompt fission neutrons is given by  $\chi_i$ . RCF is a reactivity correction factor which adjusts the measured reactivity  $\rho$  for scattering and leakage effects in the sample. The other correction factor, FCF, accounts for absorbing events other than capture and fission which occur in the sample. Thus,

$$RCF \equiv [1 - (\rho_s + \rho_\ell)/\rho] \text{ and } FCF \equiv (R_p + R_\alpha - R_{n2n})/R_f.$$

Two independent determinations of the perturbation denominator D are available from the  ${}^6\text{Li}$  and  ${}^{252}\text{Cf}$  measurements.

$$D({}^6\text{Li}) = - \frac{\bar{\phi}_a^* (\text{Li}) R_\alpha (\text{Li}) \text{ACF} (\text{Li})}{\rho (\text{Li}) \text{RCF} (\text{Li})} \quad (\text{VIII-2})$$

$$D({}^{252}\text{Cf}) = \bar{\phi}_f^* (\text{Cf}) S (\text{Cf}) / \rho' (\text{Cf}) \quad (\text{VIII-3})$$

Absorption processes in  ${}^6\text{Li}$  other than the  $(n, \alpha)$  reaction are accounted for by the small correction term  $\text{ACF} \equiv 1 + (R_\gamma + R_p)/R_\alpha$ . The emission rate of neutrons from the  ${}^{252}\text{Cf}$  spontaneous fission source<sup>a</sup> is S.

Equation VIII-1 assumes that the reaction rates  $R_f$  and  $R_\alpha$  ( ${}^6\text{Li}$ ) and the apparent worth of the  ${}^{252}\text{Cf}$  source neutrons,  $\rho' (\text{Cf})$ , have been normalized to a common power level. If the value of the perturbation denominator is insensitive to the local perturbation by the sample,  $D({}^6\text{Li}) = D({}^{252}\text{Cf})$  and Eq. VIII-1 becomes

$$1 + \bar{\alpha}(\underline{r}) = \frac{1}{\bar{\phi}_a^*(\underline{r})} \left\{ \bar{v}(\underline{r}) \bar{\phi}_f^*(\underline{r}) - \frac{D \rho(\underline{r}) \text{RCF}(\underline{r})}{R_f(\underline{r})} \right\} - \text{FCF}(\underline{r}). \quad (\text{VIII-4})$$

The measured quantities are the relative reactivities  $\rho(^6\text{Li})$ ,  $\rho'(^{252}\text{Cf})$ , and  $\rho(r)$  for the fissile and fertile samples, the absolute reaction rates  $R_f$  and  $R$  ( $^6\text{Li}$ ) and the neutron emission rate  $S(\text{Cf})$ . The remaining terms in Eqs. VIII-1 to -4 are calculated from fundamental nuclear data. Since the reactivities appear as ratios in Eqs. VIII-1 and -4, the  $(1 + \bar{\alpha})$  results are independent of any absolute reactivity calibration.

Unlike the mass spectrometer method, the reactivity-reaction rate technique does depend on prior knowledge of  $\bar{v}$  and in that sense is an indirect measurement of the absorption-to-fission ratio. However, the technique does lend itself to  $(1 + \bar{\alpha})$  measurements in ZPR critical facilities where flux levels are too low for capture rate determinations by mass spectrometer methods. In fact, no method which does not depend on  $\bar{v}$  is available for measuring  $\bar{\alpha}$  for the fissile nuclei in ZPR facilities.

### C. Measured Quantities

Absolute reaction rate measurements for the  $^6\text{Li}(n,\alpha)$  and the  $^{239}\text{Pu}(n,f)$  processes are shown in Table VIII-1. These samples were irradiated within the traverse tube of the radial sample changer (see Fig. III-1). The measured reaction rates were multiplied by a calculated correction term,  $R/R_0$ , which accounts for flux distortions due to the stainless steel tubes and cladding surrounding the sample and flux perturbations from the sample itself. Flux distortion factors calculated by the perturbation integral-transport code PIT<sup>8</sup> were used to evaluate  $R/R_0$ .  $R_0$  is the zero-thickness reaction rate and  $R$  is the small-sample reaction rate.

Metallic lithium samples (98.5 w/o  $^6\text{Li}$ ), having a diameter of 0.309 in. and clad in 20 mil aluminum, were used for both absorption rate and reactivity measurements. The absorption rate in  $^6\text{Li}$  is strongly dominated by the  $^6\text{Li}(n,\alpha)^3\text{H}$  reaction. In fact, only a few hundredths of one percent of the absorptions result from  $(n,\gamma)$  and  $(n,p)$  processes. Thus, the  $^6\text{Li}$  absorption rates were determined by measuring the tritium activity induced in the irradiated samples. Tritium was removed from these samples by an isotopic dilution method using normal hydrogen as the carrier gas. After converting this hydrogen-tritium mixture to water, liquid scintillation counting methods were used to determine the tritium activity. An NBS tritiated water standard<sup>21,22</sup> was used to calibrate the counting system. This technique for determining  $^6\text{Li}(n,\alpha)$  absolute reaction rates has been described previously.<sup>23</sup> To correct for decay, a tritium half-life of  $12.302 \pm 0.040$  yr<sup>24</sup> was used.

$^{239}\text{Pu}$  fission rates were measured by gamma counting irradiated plutonium foils 0.0005 in. thick using Ge(Li) detectors. Foils irradiated on the face of an absolute Kirn-type fission chamber were used for calibration purposes. The fission rates for the other isotopes ( $^{232}\text{Th}$ ,  $^{233}\text{U}$ ,  $^{235}\text{U}$ ,  $^{238}\text{U}$ ,  $^{240}\text{Pu}$ , and  $^{241}\text{Pu}$ ) were obtained by combining measured fission ratios with the  $^{239}\text{Pu}$  fission rate. Table VI-3 shows the results of fission ratio measurements made at the center of the GCFR assembly.

Small-sample reactivity worth measurements that were made are shown in Table VIII-2. As before, the sample-size correction factor,  $\rho/\rho_0$ , was calculated using the PIT code.<sup>8</sup> The term  $\rho/\rho_0$  converts the measured reactivity to that of the principal isotope (i) in the sample. Thus,  $\rho_0$  is the specific

isotopic reactivity corrected for local flux distortions. Since the reactivities appear as ratios in the expression for  $(1 + \alpha)$ , the errors in Table VIII-2 do not include uncertainties in the calibration of the autorod. Also, no error has been assigned to the calculation of the sample-size correction factor.

Table VIII-3 shows the measured apparent worth of a source of  $^{252}\text{Cf}$  spontaneous fission neutrons of strength  $S$ . In this table the measured apparent worth,  $\rho'(E)$ , was evaluated at a power level corresponding to the absolute reaction rates given in Table VIII-1. At each radial position the  $^{252}\text{Cf}$  measurements were made at two power levels, differing by about an order of magnitude, in order to account for the reactivity effect of the source container. The source was calibrated relative to a weaker  $^{252}\text{Cf}$  source whose strength was determined by the manganese bath technique.<sup>25</sup> For decay corrections, a value of  $2.640 \pm 0.008$  yr was used for the  $^{252}\text{Cf}$  half-life. This value is the weighted mean of four measurements reported in the literature.<sup>26, 27, 28, 29</sup> The source strength shown in Table VIII-3 was evaluated on the date of the  $^{252}\text{Cf}$  worth measurements.

#### D. Calculated Quantities

Appropriate flux and adjoint distributions and multigroup cross-sections are needed to calculate spectrum-averaged values of  $\bar{v}$ , the importance terms  $\phi_f^*$  and  $\phi_a^*$ , and the correction factors RCF, FCF, and ACF which appear in Eqs. VIII-1 to -4. The 29 broad-group cross-sections were generated for GCFR Phase II using ENDF/B-IV data. Shielded cross-sections, which include the effects of plate spatial self-shielding and resonance energy self-shielding, were used in a half-plane XY diffusion theory calculation (one mesh point per drawer) with Benoist anisotropic diffusion coefficients to determine flux and adjoint distributions. These fluxes and adjoints were used with "detector" cross-sections, which do not include plate spatial self-shielding effects, to calculate the required quantities in Eqs. VIII-1 to -4. These quantities are shown in Table VIII-4 (see Table VIII-3 for  $\phi_f^*(\text{Cf})$ ) and refer to a thin-sample spanning the width of the matrix drawer.

#### E. Perturbation Denominator Measurements

The  $^{252}\text{Cf}$  data and the  $^6\text{Li}$  data provide independent measurements of the perturbation denominator, as indicated by Eqs. VIII-2 and -3.  $D(^{252}\text{Cf})$  was evaluated from the data in Table VIII-3 and the results are shown in Table VIII-5. The data point at the matrix positions S-23/32 ( $r = 49.720$  cm) yielded an unusually low value of  $D(^{252}\text{Cf})$  and was omitted in determining the average value of the perturbation denominator. This point was located near the core/radial blanket interface where neutron-leakage effects are relatively large. The evaluation of  $D(^6\text{Li})$  from Eq. VIII-2 has led to inconsistent results. Therefore, the value of the perturbation denominator is presently based only on the  $^{252}\text{Cf}$  data (Eq. VIII-3).

The magnitude of the perturbation denominator depends on the reactor power level and therefore a normalization is required if the measured results are to be compared with calculation. A convenient normalization factor  $(\text{NF})^{30}$  is

$$NF \equiv \frac{S^*(0) S(0)}{Ih/\delta k/k} = \left[ \sum_{i=1}^{NG} \chi_i^{core} \phi_i^*(0) \right] \left[ \sum_{j=1}^{NI} \sum_{i=1}^{NG} (\nu \Sigma_f)_{ij} \phi_i(0) \right] / \frac{Ih}{\delta k/k} \quad (VIII-5)$$

where NG and NI are the number of groups and the number of isotopes, respectively, and where  $S^*(\underline{r})$  and  $S(\underline{r})$  are evaluated at the center of the reactor. The  $Ih/(\delta k/k)$  term is needed because the reactivities in Eqs. VIII-2 and -3 are measured in inhours. The normalized calculated perturbation denominator,  $D_n(C)$ , is

$$D_n(C) = \int_{\text{reactor}} S^*(\underline{r}) S(\underline{r}) dV / S^*(0) S(0). \quad (VIII-6)$$

A RZ model calculation was used to evaluate  $D_n(C)$ . Table VIII-6 compares the measured and calculated perturbation denominators. The 0.85 C/E ratio is larger than the value (0.75) for the Phase-I measurements. However, this is consistent with the fact that the reactivity C/E values for Phase II (Table VIII-5) are consistently lower (8-9%) than the corresponding values for Phase I.

#### F. Absorption-To-Fission Ratios

Using the value of  $\bar{D}(^{252}\text{Cf})$  given in Table VIII-5, isotopic absorption (capture plus fission)-to-fission ratios were evaluated from Eq. VIII-4 and the data shown in Tables VIII-1 to -3 and VI-3. These  $(1 + \alpha)$  values are given in Table VIII-7 and refer to a thin-detector spanning the width of the matrix drawer. The errors ( $1\sigma$ ) shown in this table account for the uncertainties in  $\nu$ , the relative reactivities and the absolute reaction rate measurements. However, no error has been assigned to the calculation of sample-size effects, the importance terms which appear in the reactivity-reaction rate expression for  $(1 + \alpha)$ , nor to the small correction factors, RCF and FCF. Generally, the measured values are in close agreement with the calculated ones. The  $^{241}\text{Pu}$  result is subject to considerable error because the reactivity sample contains less than 0.4 g  $^{241}\text{Pu}$  and so a precise reactivity measurement for this isotope is not possible. These are the first measurements of  $(1 + \alpha)$  that have been made by the reactivity-reaction rate method for the isotopes  $^{232}\text{Th}$  and  $^{233}\text{U}$ .

Errors and error sensitivities are summarized in Tables VIII-8 and -9. For example, a 1.0% increase in the measured reactivity  $\rho$  would decrease the  $(1 + \alpha)$  values by 1.9, 0.86, 1.8, 1.8, and 1.8% for  $^{239}\text{Pu}$ ,  $^{240}\text{Pu}$ ,  $^{241}\text{Pu}$ ,  $^{233}\text{U}$ , and  $^{235}\text{U}$ , respectively, but would increase the values for  $^{238}\text{U}$  and  $^{232}\text{Th}$  by 0.40 and 0.88%. If  $\nu$  is increased by 1.0%, the absorption-to-fission ratios for  $^{239}\text{Pu}$ ,  $^{240}\text{Pu}$ ,  $^{241}\text{Pu}$ ,  $^{233}\text{U}$ ,  $^{235}\text{U}$ ,  $^{238}\text{U}$ , and  $^{232}\text{Th}$  would increase by 2.9, 1.9, 2.8, 2.8, 2.3, 0.59, and 0.11%, respectively. For the fissile materials, the values of  $\nu_{th}/\nu$  for  $^{239}\text{Pu}$ ,  $^{241}\text{Pu}$ ,  $^{233}\text{U}$ , and  $^{235}\text{U}$  are 0.971, 0.978, 0.992, and 0.982, respectively. Thus, for these isotopes nearly all the error in  $\nu$  is associated with the thermal value,  $\nu_{th}$ . In a recent evaluation of the 2200 m/sec constants, Lemmel<sup>31</sup> assigns errors to  $\nu_{th}$  of 0.28%, 0.34%, 0.24%, and 0.21% for  $^{239}\text{Pu}$ ,  $^{241}\text{Pu}$ ,  $^{233}\text{U}$ , and  $^{235}\text{U}$ , respectively. Assuming  $\nu$  may be written in the form  $\nu = \nu_{th} + f(E)$  and that  $f(E)$  is uncertain by  $\pm 25\%$ , errors



of 0.6%, 0.6%, 0.7%, and 0.5% have been attributed to the calculation of  $\bar{\nu}$  for  $^{239}\text{Pu}$ ,  $^{241}\text{Pu}$ ,  $^{233}\text{U}$ , and  $^{235}\text{U}$ . Guided by the evaluation of  $\nu(E)$  by Manero and Konshin<sup>32</sup>, uncertainties of 2.5%, 1.0%, and 2.0% have been assigned to  $\bar{\nu}$  for  $^{232}\text{Th}$ ,  $^{238}\text{U}$ , and  $^{240}\text{Pu}$ . Note that nearly all the error in  $(1 + {}^{240}\bar{\alpha})$  is due to the uncertainty in  $\bar{\nu}$ , as Table VIII-8 shows.

### G. Central-Point Breeding Ratio

The instantaneous breeding ratio (BR) may be defined as the rate of production of fissile material divided by the rate of loss. In a similar way, the point breeding ratio ( $\text{BR}_p$ ) may be defined in terms of cell-averaged reaction rates evaluated at a particular location. Thus,

$$\text{RR}_p = \frac{{}^{28}\text{N}^{28}\text{c} + {}^{40}\text{N}^{40}\bar{\alpha}^{40}\text{f}}{{}^{49}\text{N}^{49}\text{f} (1 + {}^{49}\bar{\alpha}) + {}^{41}\text{N}^{41}\text{f}(1 + {}^{41}\bar{\alpha}) + {}^{25}\text{N}^{25}\text{f}(1 + {}^{25}\bar{\alpha})} \quad (\text{VIII-7})$$

where  ${}^i\text{N}$  is the atom density of isotope  $i$  and where  ${}^i\text{c}$  and  ${}^i\text{f}$  are the per atom capture and fission rates. The experimental value of  $\text{BR}_p$  at the center of the assembly (see Table VIII-10) was found to be  $0.471 \pm 0.014$  as compared with a calculated value of 0.5169. Cell-averaged  $(1 + \bar{\alpha})$  values were obtained by dividing the calculated cell-averaged absorption-to-fission ratios by the corresponding thin-sample C/E ratios. The measurement of the cell-averaged reaction rate ratio  ${}^{28}\text{c}/{}^{49}\text{f}$  has been reported in Section VI. An examination of Table VIII-10 shows that the most important reason why the point breeding ratio is overcalculated by nearly 10% is the overprediction of  ${}^{28}\text{c}/{}^{49}\text{f}$ .

### H. Summary

Absorption-to-fission ratios  $(1 + \bar{\alpha})$  have been measured in the core region of the GCFR Phase-II assembly by the reactivity-reaction rate technique for  $^{232}\text{Th}$ ,  $^{233}\text{U}$ ,  $^{235}\text{U}$ ,  $^{238}\text{U}$ ,  $^{239}\text{Pu}$ ,  $^{240}\text{Pu}$ , and  $^{241}\text{Pu}$ . Generally, the results are in very favorable agreement with calculations based on ENDF/B-IV data. Because of the small mass of  $^{241}\text{Pu}$  in the reactivity sample, the  $(1 + {}^{41}\bar{\alpha})$  measurement is subject to large uncertainties ( $\sim 10\%$ ). All the  $(1 + \bar{\alpha})$  values are based on a measurement of the perturbation denominator using a calibrated  $^{252}\text{Cf}$  source.

The point breeding ratio was evaluated at the center of the GCFR Phase-II assembly by combining the absorption-to-fission ratio measurements with a determination of the cell-averaged  ${}^{28}\text{c}/{}^{49}\text{f}$  reaction rate ratio. Because of the overprediction of  ${}^{28}\text{c}/{}^{49}\text{f}$ , the point breeding ratio is overcalculated by nearly 10%.

## IX. GCFR CONTROL ROD WORTHS

Worth measurements of simulated GCFR control rods were made at the center (S/M-23/23) of the GCFR-II unreflected configuration shown in Fig. I-9. The worth of three control rod compositions were measured as a function of  $\text{B}_4\text{C}$  mass and  $^{10}\text{B}$  enrichment in the  $\text{B}_4\text{C}$ . Figure IX-1 shows the drawer compositions of the three  $\text{B}_4\text{C}$  control rod compositions, the control rod worth reference composition (no  $\text{B}_4\text{C}$  present), and for comparison, the Type-2 GCFR core composition normally present in the measurement location.

As indicated by Fig. IX-1, only one-half of the Type-2 core composition was modified to accommodate each of the control rod compositions. This sub-region of the Type-2 core composition corresponds to the third platelet unit cell of the four subunit cells of the GCFR core composition shown in Fig. I-1. The control rod worths were, therefore, measured relative to the replacement of one subunit of average core composition with each type of control rod composition. All measurements were made over the full core height of 48 in.; no modification to the axial blanket composition was made.

The  $B_4C(N)$  and  $B_4C(E)$  designations in Fig. IX-1 stand for natural (18.32 w/o or 19.78 a/o  $^{10}B/B$ ) and enriched (89.89 w/o or 90.72 a/o  $^{10}B/B$ )  $B_4C$  platelets used to form the compositions. The amount of  $^{10}B$  per inch over the the 48 in.-core height was 4.6272 g/in. for composition No. 1, 9.2544 g/in. for composition No. 2, and 16.1796 g/in. for composition No. 3. Composition No. 1 simulates a lightly loaded natural  $B_4C$  control rod (19.78 a/o  $^{10}B/B$ ), No. 2 a heavily loaded rod (twice No. 1), and composition No. 3 is an enriched  $B_4C$  rod (38.54 a/o  $^{10}B/B$ ). The atom densities of the five compositions of Fig. IX-1 are shown in Table IX-1.

Table IX-2 shows the measured and calculated reactivity of each measurement configuration and the reactivity difference (exchange worth) between configurations. The measured reactivity of each configuration was determined using the rod-drop inverse-kinetics technique. The calculated reactivities were made using a two-dimensional RZ diffusion theory model of the GCFR reference configuration in which the rectangularly shaped S/M-23/23 matrix location at the center (2.175 in. square by 48 in.) was represented with an equivalent cylindrically shaped region of equal volume with a radius of 3.12 cm. Each composition of Table IX-1 was then substituted into this test region and the eigenvalue was calculated for each measurement configuration.

Cross-sections used for the control rod compositions were the cell-averaged cross-sections generated explicitly for the Type-2 unit-cell structure; infinitely dilute cross-sections were taken for the boron isotopes. In all cases, account of neutron-streaming effects using bidirectional diffusion coefficients for the core and blanket regions were included in the calculations. (The core material diffusion-coefficient multipliers (Table II-3) were used for each control rod composition substituted into the test region.)

As seen from Table IX-2 the use of infinitely dilute boron cross-sections in the GCFR control rod worth calculations tend to overpredict the measured rod worths. This overprediction also tends to become larger as the mass of the  $B_4C$  rod increases. The smallest mass rod was overpredicted approximately 6%, the intermediate mass rod by 9%, and the heaviest rod by 18%. It would be expected that the use of self-shielded boron cross-sections would reduce the C/E values. For comparison, the central worth of a small-sample of enriched boron (0.433 g  $^{10}B$ ) was measured to be worth -3428 lh/kg and the calculated worth, using the same boron cross-sections as used above, gives a C/E value of 0.998.

## X. CENTRAL SPECTRUM MEASUREMENT

The central neutron spectrum was measured during the approach-to-critical of the GCFR Phase-II unreflected assembly using in-core proton-recoil pro-

portional counters. A similar measurement had been performed in the GCFR Phase-I critical assembly. The same counters and same data-reduction techniques were used.

A counter was placed in a special drawer containing a preamplifier and that part of the drawer not containing the detector, preamplifier, and lead-in cables was filled with nominal Type-2 drawer composition. The plate-material pattern is indicated in Fig. X-1. The measurement was made with all DP rods removed and eight of the boron blades inserted. The reactor was  $\sim 0.75\% \Delta k/k$  subcritical.

The measured central spectrum is shown in Fig. X-2. The measurement extends from 1 keV to 2 MeV. The error bars on the measured points reflect only the statistical uncertainty. The corrections for systematic sources of error generally introduce less than 5% changes. The experimental resolution is 8% over most of the energy range. At low energies the statistics in the ionization process broaden the resolution so that at 1 keV the resolution is about 20%. Numerical results are contained in Table X-1. At each energy the flux, statistical error, and resolution are listed. The normalization of the flux is arbitrary.

The calculated spectrum, represented by a histogram, is also shown in Fig. X-2. The histogram is the result of an SDX calculation using a 226-group structure and ENDF/B-IV data. In this and the subsequent plots the two curves are normalized to produce equal areas (equal flux) over the energy range of the measurement. The calculation was smoothed with a Gaussian response function, whose width as a function of energy, was determined by the experimental resolution. In general, the agreement between measurement and calculation is only fair. The calculation overpredicts the flux near 600 keV, and the calculated and measured spectra have different shapes in the 100 to 300 keV range. The measured low-energy flux is consistently higher than the prediction.

Figure X-3 shows the measured and calculated spectra for Phase I. In general, the agreement between calculated and measured spectra is similar for Phases I and II. However, in Phase II better agreement between calculation and experiment was obtained in the 40 to 100 keV and the 700 to 1300 keV ranges than was obtained in Phase I. Figures X-4 and -5 show a comparison of the calculated and measured spectra for the two phases on a broad-group basis. The differences between the two phases are small. Figures X-6 and -7 show a comparison of the calculated and measured spectra for the two assemblies on a broad-group basis. It is readily seen that there is a consistent trend in the nature of disagreement between the calculated and measured spectra for the two phases -- i.e., the calculated spectrum is generally too hard in the 100 to 1000 keV range.

## XI. KINETIC PARAMETER VERIFICATION

Measurements by noise methods of the ratio of effective beta-squared to the Diven factor were made for Phase II (both with and without reflector regions) using the same method as for Phase I. These measurements consist of a determination of a mean-square fractional dispersion in detector output at known subcriticality (as measured by rod-drop) for cores in which the absolute fission rate has been established. The expression

$$F(\tau\sigma^2) = \frac{3}{2} \frac{D}{\beta^2(1 + \beta)^2} \quad (\text{XI-1})$$

relates fission rate (F) and joint detector dispersion ( $\sigma^2$ ) over intervals  $\tau$ , to the Diven factor (D) and effective beta and subcriticality.

The Phase-I measurement was done only once at a subcriticality of about 0.8\$ and the first Phase-II measurement (before the axial and radial reflector was added) was made at about 0.7\$. It is of interest to examine whether or not the simple expression of Eq. XI-1 holds as subcriticality increases since the changing spatial distribution of real and adjoint flux can be expected to ultimately invalidate the simple kinetics model.

Measurements and calculations of the subcriticality-dependence of point-model noise have been reported previously. Carpenter<sup>33</sup> concludes that below 4.5\$ the effects of detector displacement at near-constant efficiency are small for ZPPR-3. Carpenter also observed that substantial effects from detector-efficiency changes were seen at 7\$. ORNL numerical work<sup>34</sup> using a one-dimensional code, developed specifically for kinetics, was used to analyze the noise dependence upon subcriticality for some FTR-3 cores used in the ORNL-RSP program on ZPR-9. The conclusions were that detector-efficiency-corrected "amplitude" noise results were within about 10% of the true lambda subcriticality at 30\$; the error decreased rapidly with subcriticality and was negligible below 7\$. "Amplitude" noise from that part of the spectrum below roll-off and above delayed-neutron decay times is used by the polarity-coherence and variance-sampling techniques. Interesting, static-multiplication methods, after detector-efficiency corrections were made, were found to be no better than "amplitude" noise measurements in the ORNL study. At 28\$ subcritical, both techniques provided subcriticality estimates that were biased about 10% high regardless of detector type or location.

To test the dependence of results upon subcriticality we note that F in Eq. XI-1 may be replaced by

$$F = \frac{S}{\beta\beta} \quad (\text{XI-2})$$

where S is an "effective" neutron-source strength. Eqs. XI-1 and -2 may be combined to give

$$\frac{\beta D}{S} = \frac{2}{3} \tau\sigma^2 / [\beta / (1 + \beta)^2]. \quad (\text{XI-3})$$

For changes in subcriticality which do not appreciably alter  $\beta$ , D, or S, the measured quantity on the right of Eq. XI-3 should not change. If no change occurs, it will indicate that the basic kinetics model retains validity and is not compromised by phenomena such as higher-harmonic contamination complicated by detector type and placement. The expression in Eq. XI-3 does not contain detector efficiency and one would expect that any observed variation would test the kinetics model validity without the complication of the detectors themselves.

The results of a variance analysis of noise from the GCFR Phase-II unreflected assembly at 0.398, 1.03, and 3.99\$ subcritical are shown in Fig. XI-1. Within the limits of statistical error, there is no significant

variation in the measured ratio of  $\tau\sigma^2/[\beta/(1+\beta)^2]$  up to 4 $\beta$ ; limitations on detectors and electrometers prevent meaningful results at larger subcriticalities. The level of error shown in Fig. XI-1 is much in excess of that which is attainable with the technique. Response-speed limitations of the detectors forces low-rate sampling which limits precision. Use of long sampling intervals requires that a correction be made for delayed-neutron effects. Also, and less accurately predictable, is a correction for the actual shape of electrometer response roll-off. The data at 0.4 and 1 $\beta$  subcritical have been corrected by less than 5% for these effects. The residual systematic error from delayed neutrons and electrometer roll-off should be much less than statistics at these subcriticalities. The result at 4 $\beta$  subcritical contains corrections of about 10% for delayed neutrons and 20% for roll-off; however, and it is quite likely, that a systematic-error residue exists which is comparable or larger than statistics. Nevertheless, these results are consistent with other results on large fast spectrum cores indicating that amplitude-type noise measurements are not subject to significant error close to critical.

By use of measured results for  $F$ ,  $\tau\sigma^2$ , and  $\beta$  in Eq. XI-1, values for the  $\beta^2/D$  ratio have been established as

$$\frac{\beta^2}{D} = 1.40 \times 10^{-5} \text{ } (\pm 5\%) \text{ Phase I}$$

$$\frac{\beta^2}{D} = 1.34 \times 10^{-5} \text{ } (\pm 5\%) \text{ Unreflected Phase II}$$

$$\frac{\beta^2}{D} = 1.23 \times 10^{-5} \text{ } (\pm 5\%) \text{ Reflected Phase II}$$

Some preliminary results for Phase I indicate that  $D$  may be 14% or so in excess of its point-model value of  $\sim 0.80$ . If the preliminary  $D$  value is correct, it would imply that the beta inferred from the noise measurement is almost 10% higher than calculated; this discrepancy would lie outside of estimates for measurement error or for basic data error.

It is also of interest to compare values for  $\beta D/S$  for the different configurations since this quantity is independent of errors in the absolute fission rate determination (Eq. XI-3). For Phase I

$$\frac{\beta D}{S} = 0.559 \times 10^{-5} \text{ } (\pm 2.5\%).$$

For the unreflected Phase-II core

$$\frac{\beta D}{S} = 0.969 \times 10^{-5} \text{ } (\pm 3.5\%)$$

and for the reflected Phase-II core

$$\frac{\beta D}{S} = 1.03 \times 10^{-5} \text{ } (\pm 2.5\%).$$

The measured values of  $\beta D/S$  are essentially within statistics for the unreflected and reflected Phase-II assemblies. The change in  $\beta D/S$  from Phase I to Phase II, by a factor of 1.78, is mostly in consequence of the change in fissile content by a factor of 1.92. To first approximation the  $^{240}\text{Pu}$  source,  $S$ , is proportional to the fissile loading.

## XII. REFERENCES

1. S. K. Bhattacharyya, *"An Experimental Study of the Neutronics of the First Gas Cooled Fast Reactor Benchmark Assembly (GCFR Phase-I Assembly)"*, Argonne National Laboratory Report ANL-76-36 (Dec 1976).
2. W. M. Stacey et al., *"A New Space-Dependent Fast Neutron Multigroup Cross-Section Preparation Capability"*, Trans. Am. Nucl. Soc., 15, 292 (1972).
3. H. Henryson, B. J. Toppel and C. G. Stenberg, *"ETOE-2/MC<sup>2</sup>-2/SDX Multigroup Neutron Cross-Section Processing"*, Seminar on Nuclear Data Processing Codes, Ispra, Italy, December 5-7, 1973, EACRP-U-52.
4. H. Henryson, B. J. Toppel and C. G. Stenberg, *"MC<sup>2</sup>-2: A Code to Calculate Fast Neutron Spectra and Multigroup Cross-Section"*, Argonne National Laboratory Report ANL-8144 (June 1976).
5. E. F. Bennett and R. L. Long, *"Precision Limitations in the Measurement of Small Reactivity Changes"*, Nucl. Sci. Eng., 17, 425 (1963).
6. C. E. Cohn, R. A. Karam, J. E. Marshall and J. M. vanDoorninch, *"Computer-Axial Calibration of a Fine Autorod"*, Nucl. Appl. Technol., 7, 342 (1969).
7. E. M. Bohn, *"The Central Worth Discrepancy in Three Fast Reactor Benchmark Critical Assemblies"*, Argonne National Laboratory Report ANL-75-14 (June 1975).
8. P. H. Kier and M. Salvatores, *"A Perturbation Integral-Transport Formulation for Computing Central Doppler and Sample Worths"*, Applied Physics Division Annual Report, July 1971 to June 1972, Argonne National Laboratory Report ANL-8010, pp. 312-315.
9. R. C. Weast, Ed., *"Handbook of Chemistry and Physics, 48th Edition"*, The Chemical Rubber Co., Cleveland, Ohio (1967).
10. R. B. Pond, *"Extracting the Temperature-Exponent Uncertainty from Doppler Reactivity Data"*, Applied Physics Division Annual Report, July 1971 to June 1972, Argonne National Laboratory Report ANL-8010, pp. 247-252.
11. P. H. Kier and C. E. Till, *"Analysis of UO<sub>2</sub> Small-Sample Doppler Measurements in FTR-3, ZPR-9 Assembly 26"*, Applied Physics Division Annual Report, July 1970 to June 1971, Argonne National Laboratory Report ANL-7910, pp. 73-79.
12. R. A. Lewis and C. E. Till, *"Analysis of Small-Sample Doppler Effect Measurements"*, Reactor Physics Division Annual Report, July 1966 to June 1967, Argonne National Laboratory Report ANL-7310, pp. 139-143.
13. R. A. Lewis and T. W. Johnson, *"Sensitivity of Small-Sample Doppler Effect Measurements to Environment"*, Reactor Physics Division Annual Report, July 1967 to June 1968, Argonne National Laboratory Report ANL-7410, pp. 96-103.

14. R. B. Pond and S. K. Bhattacharyya, *"Measurement of  $^{238}\text{U}$  Doppler Effect in GCFR Critical Assemblies,"* Trans. Am. Nucl. Soc., 24, 478 (1976).
15. K. E. Plumlee and M. T. Wiggins, *"Automatic Foil Activity Counting Facility and Data-Reduction Program,"* Argonne National Laboratory Report ANL-6628 (1962).
16. G. S. Stanford, *"The Codes NURF, COMBO and TWOSORCE for Processing Foil Counting Data,"* Argonne National Laboratory Report ANL-7356 (August 1967).
17. R. Sher, *"Gamma-Gamma Coincidence Method for Measuring Resonance Escape Probability in  $^{238}\text{U}$  Lattices,"* Nucl. Sci. Eng., 7, 479 (1960).
18. R. Böhme and H. Senfert, *"Uranium Reaction Rate Measurements in the Steam-Cooled Fast Reactor SNEAK, Assembly 3A-2,"* KFK-811, EUR3970e, Kernforschungszentrum Karlsruhe, Germany (1968).
19. D. W. Maddison and J. M. Gasidlo, *"Foil Activation Analysis in Critical Facilities Assemblies,"* Trans. Am. Nucl. Soc., 15, 930 (1972).
20. M. M. Bretscher and W. C. Redman, *"Low-Flux Measurements of  $^{239}\text{Pu}$  and  $^{235}\text{U}$  Capture-to-Fission Ratios in a Fast Reactor Spectrum,"* Nucl. Sci. Eng., 39, 368 (1970).
21. A. Spornol and B. Denecke, Intern. J. Appl. Rad. Isotopes, 15, 241 (1964).
22. W. B. Mann and A. Spornol, Intern. J. Appl. Rad. Isotopes, 15, 628 (1964).
23. M. M. Bretscher, *" $^6\text{Li}$  as a Reference Absorber for Capture-to-Fission Ratio Measurements in Zero Power Fast Critical Assemblies,"* Reactor Physics Division Annual Report, July 1967 to June 1968, Argonne National Laboratory Report ANL-7410, pp. 178-182.
24. R. Sher, *"Half Lives of  $^3\text{H}$  and  $^{238}\text{Pu}$ ,"* BNL-50 233 (1970).
25. A. DeVolpi, K. G. Porges and R. J. Armani, *"Absolute Calibration of Fission Neutron Source Strength Relying Upon an Improved Manganese Bath Technique and Absolute Beta-Gamma Coincidence Counting,"* Symposium on Standardization of Radionuclides, pp. 717-727, IAEA, Vienna (1967).
26. D. Metta et al., J. Inorg. Nucl. Chem., 27, 33 (1965).
27. A. DeVolpi and K. G. Porges, Inorg. Nucl. Chem. Letters, 5, 699 (1969).
28. B. J. Mijneer and E. Van den Hauten-Zuidema, Intl. J. Appl. Radiat. Isotop., 24, 185 (1973).
29. V. Spiegel, Nucl. Sci. Eng., 53, 326 (1974).
30. W. C. Redman and M. M. Bretscher, *"Experimental Determination of the Perturbation Denominator in Fast Critical Assemblies,"* Nucl. Sci. Eng., 44, 450 (1971).



31. H. D. Lemmel, "*The Third IAEA Evaluation of 2200 m/sec and 20°C Maxwellian Neutron Data for  $^{233}\text{U}$ ,  $^{235}\text{U}$ ,  $^{239}\text{Pu}$ , and  $^{241}\text{Pu}$* ," Conference on Neutron Cross-Sections and Technology, Washington, D. C., March 3-7, 1975.
32. F. Maero and V. A. Konshin, Atomic Energy Review, 10, 637 (1972).
33. S. G. Carpenter, Argonne National Laboratory, private communication (October 1973).
34. A. R. Buhl, J. C. Robinson and N. J. Ackermann, "*An Intercomparison of Techniques for Inferring Subcriticality in Fast Reactors*," Trans. Am. Nucl. Soc., 15, 493 (June 1972).

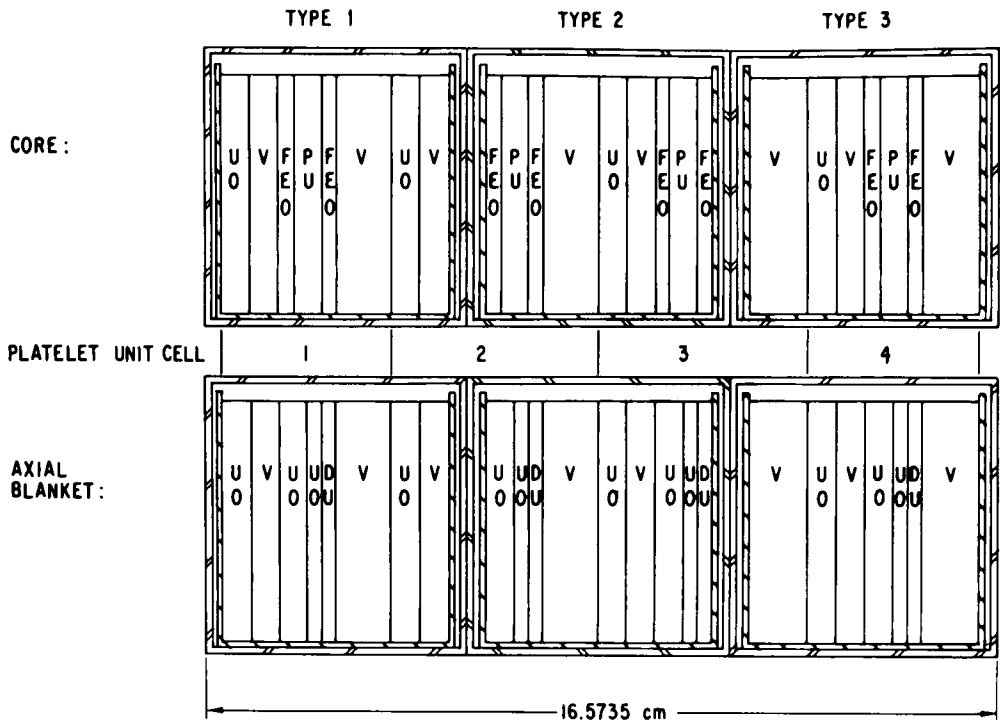


Figure I-1. Unit-Cell Structure of the Core and Axial Blanket.  
ANL Neg. No. 116-77-73

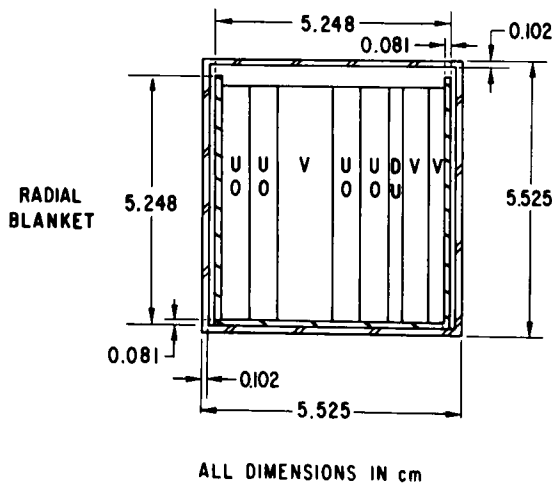


Figure I-2. Unit-Cell Structure of the Radial Blanket.  
ANL-Neg. No. 116-77-74

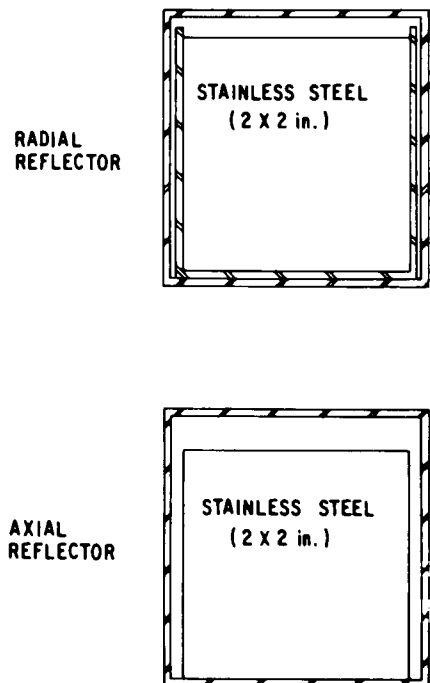


Figure I-3. Unit-Cell Structure of the Axial and Radial Reflectors. ANL Neg. No. 116-77-75



DRAWER MASTER NO. 2903-F S - 1  
GCFR PHASE-II TYPE 3

DATE 11-13-75

APPROVED \_\_\_\_\_

1	VDCG						VDCG						VDCG					
2	U008	U008	U008	U008	U008	U008	U008	U008	U008	U008	U008	U008	U008	U008	U008	U008	U008	U008
3	VDCG						VDCG						VDCG					
4	FE0H	FE0H	FE0H	FE0H	FE0H	FE0H	FE0H	FE0H	FE0H	FE0H	FE0H	FE0H	U008	U008	U008	U008	U008	U008
5	PUMN (8)				PUMN (7)				PUMN (5)				U008	U008	U008	U008	U008	U008
6	FE0H	FE0H	FE0H	FE0H	FE0H	FE0H	FE0H	FE0H	FE0H	FE0H	FE0H	FE0H	U008	U008	U008	U008	U008	U008
7	VDCG						VDCG						VDCG					
8	VDCG						VDCG						VDCG					
9	VDCG						VDCG						VDCG					
10	VDCG						VDCG						VDCG					
11	VDCG						VDCG						VDCG					
12	VDCG						VDCG						VDCG					
13	VDCG						VDCG						VDCG					
14	VDCG						VDCG						VDCG					
15	VDCG						VDCG						VDCG					
16	VDCG						VDCG						VDCG					

TOTAL U-235 IN CORE .006599 KG.

TOTAL PU-239 IN PU FUEL .653833 KG.  
TOTAL PU-241 IN PU FUEL .009671 KG.

Figure I-6. Stationary-Half Type-3 Drawer Loading Master for the Core and Axial Blanket. ANL Neg. No. 116-77-118

DRAWER MASTER NO. 2910-F S - 1  
RADIAL BLANKET - FIRST 24 INCHES

DATE 11-13-75

APPROVED \_\_\_\_\_

1	U008	U008	U008	U008	U008	U008	U008	U008	U008	U008	U008	U008
2	U008	U008	U008	U008	U008	U008	U008	U008	U008	U008	U008	U008
3	U008	U008	U008	U008	U008	U008	U008	U008	U008	U008	U008	U008
4	U008	U008	U008	U008	U008	U008	U008	U008	U008	U008	U008	U008
5	VDCG						VDCG					
6	VDCG						VDCG					
7	VDCG						VDCG					
8	VDCG						VDCG					
9	U008	U008	U008	U008	U008	U008	U008	U008	U008	U008	U008	U008
10	U008	U008	U008	U008	U008	U008	U008	U008	U008	U008	U008	U008
11	U008	U008	U008	U008	U008	U008	U008	U008	U008	U008	U008	U008
12	U008	U008	U008	U008	U008	U008	U008	U008	U008	U008	U008	U008
13	UD	UD	UD	UD	UD	UD	UD	UD	UD	UD	UD	UD
14	VDCG						VDCG					
15	VDCG						VDCG					
16	VDCG						VDCG					

TOTAL U-235 IN CORE .000000 KG.

TOTAL PU-239 IN PU FUEL .000000 KG.  
TOTAL PU-241 IN PU FUEL .000000 KG.

Figure I-7. Stationary-Half 24 in.-Section Drawer Loading Master for the Radial Blanket. ANL Neg. No. 116-77-115

DRAWER MASTER NO. 2910-B S - 1  
RADIAL BLANKET -LAST 12 INCHES

DATE 11-13-75

APPROVED \_\_\_\_\_

1						
2	UO08	UO08	UO08	UO08	UO08	UO08
3						
4	UO08	UO08	UO08	UO08	UO08	UO08
5	VDCG			VDCG		
6						
7						
8						
9	UO08	UO08	UO08	UO08	UO08	UO08
10						
11	UO08	UO08	UO08	UO08	UO08	UO08
12						
13	UD	UD	UD	UD	UD	UD
14	VDCG			VDCG		
15						
16	VDCG			VDCG		
	2	4	6	8	10	12

TOTAL U-235 IN CORE .000000 KG.

TOTAL PU-239 IN PU FUEL .000000 KG.  
TOTAL PU-241 IN PU FUEL .000000 KG.

Figure I-8. Stationary-Half 12 in.-Section Drawer Loading  
Master for the Radial Blanket. ANL Neg.  
No. 116-77-100.

☒ D.P. CONTROL ROD      { ☐ MOVABLE HALF  
   { ☐ STATIONARY HALF  
☐ INSERTION SAFETY ROD  
 T THERMOCOUPLE DRAWER

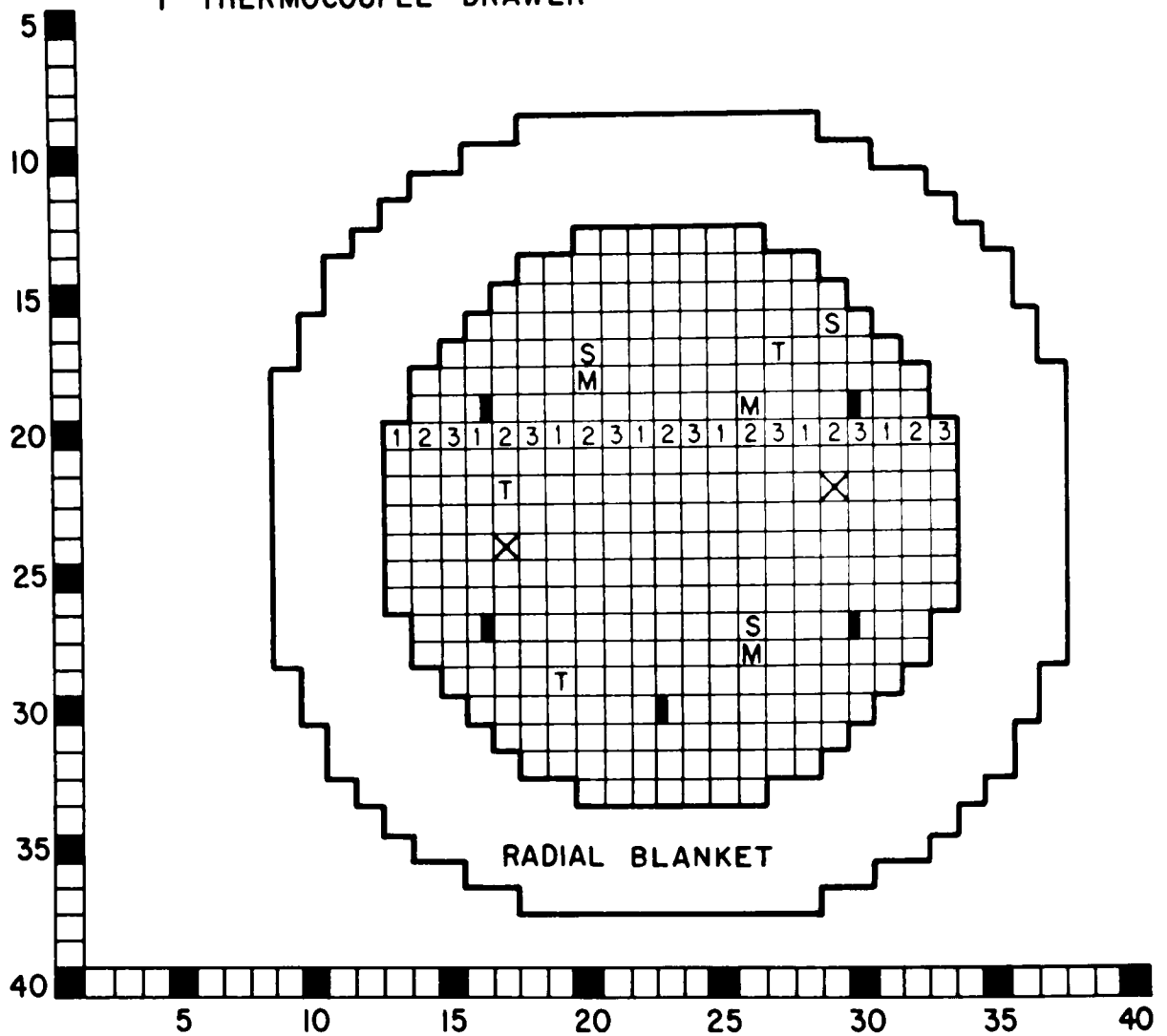


Figure I-9. Unreflected Reference Configuration. ANL Neg. No. 116-77-114

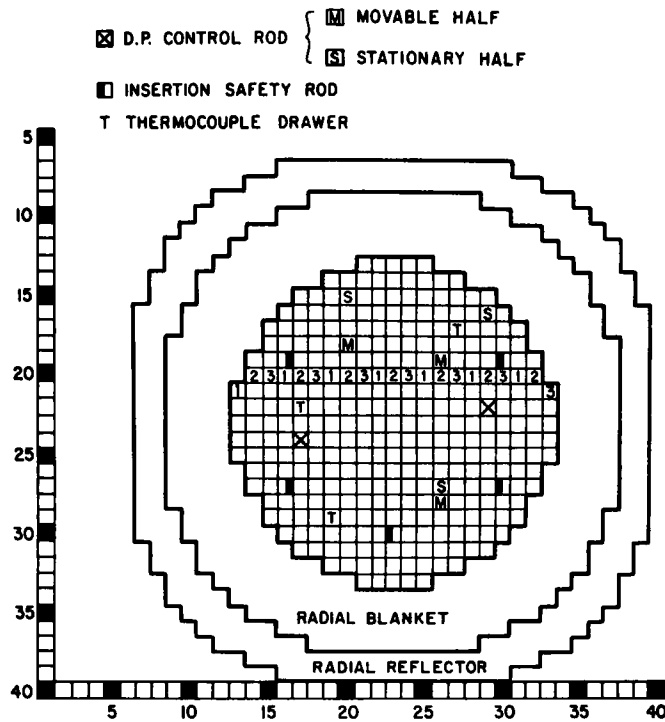


Figure I-10. Reflected Reference Configuration. ANL Neg. No. 116-77-121

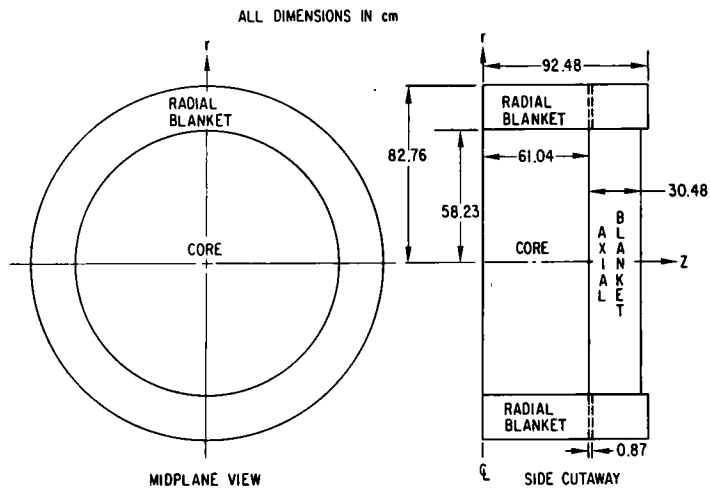


Figure I-11. Sketch of the Unreflected Critical Reference Assembly. ANL Neg. No. 116-77-123

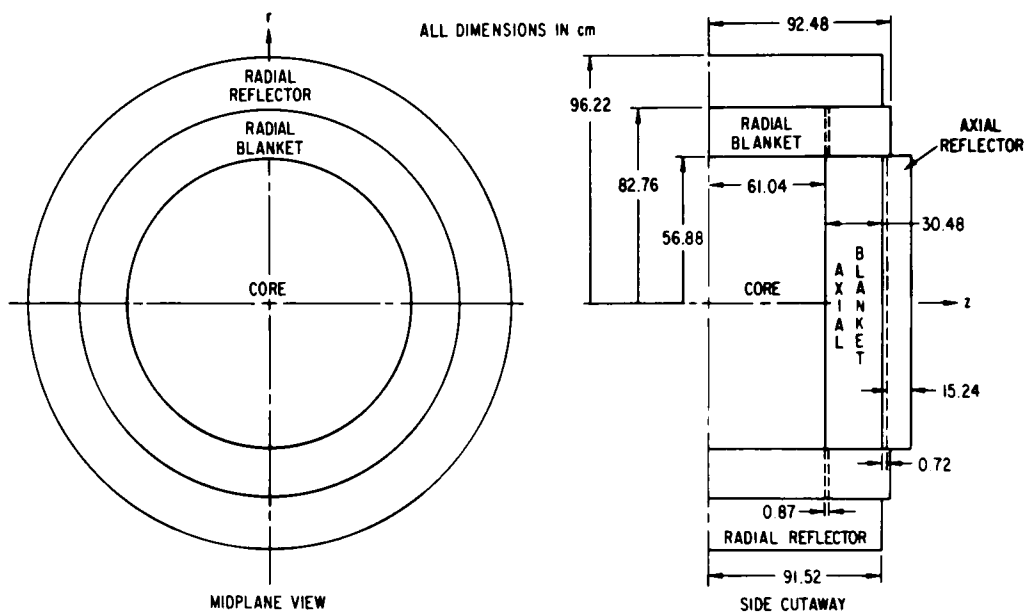


Figure I-12. Sketch of the Reflected Critical Reference Assembly. ANL Neg. No. 116-77-83.



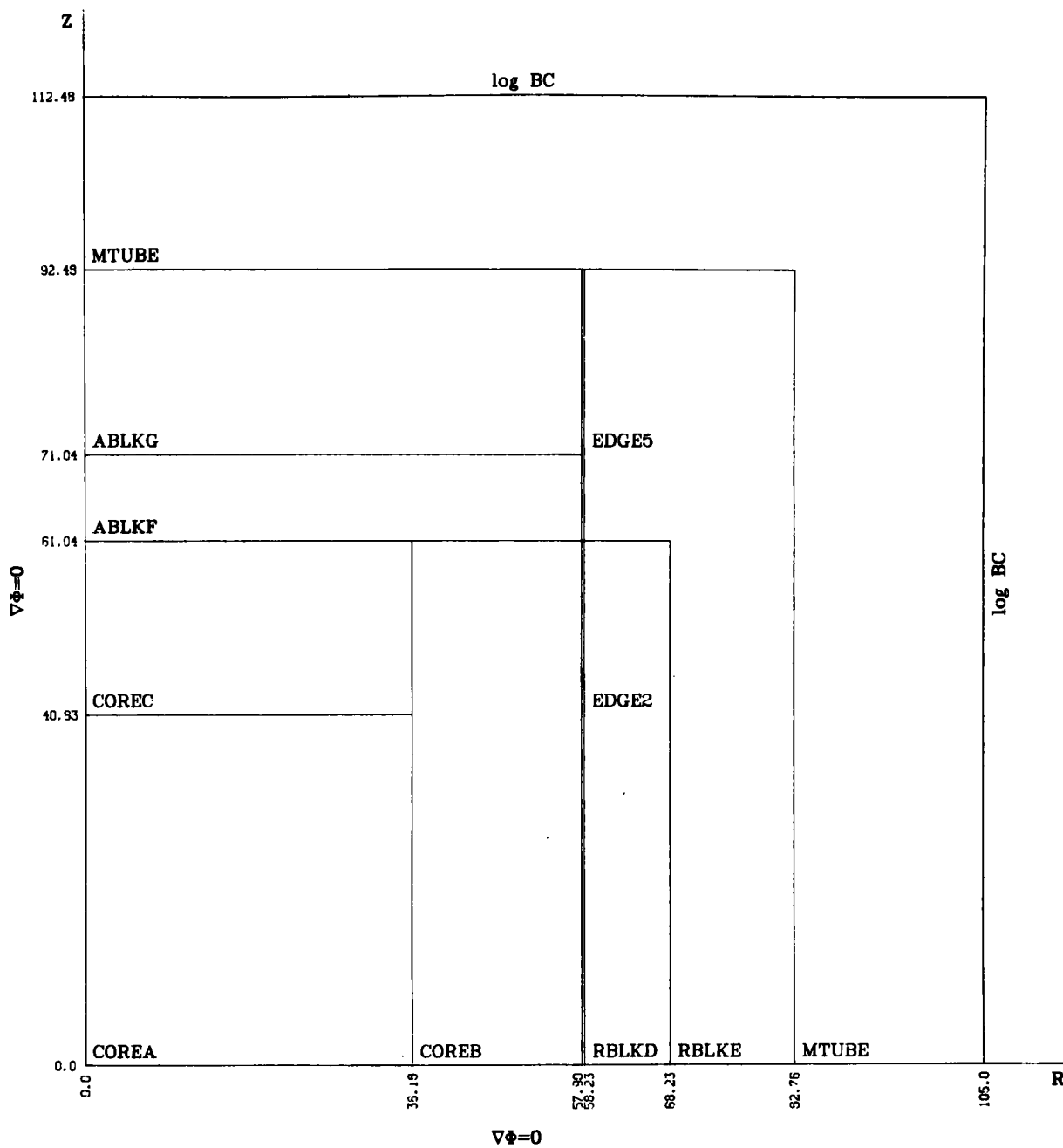


Figure II-1. RZ Unreflected Calculational Model. ANL Neg. No. 116-77-105

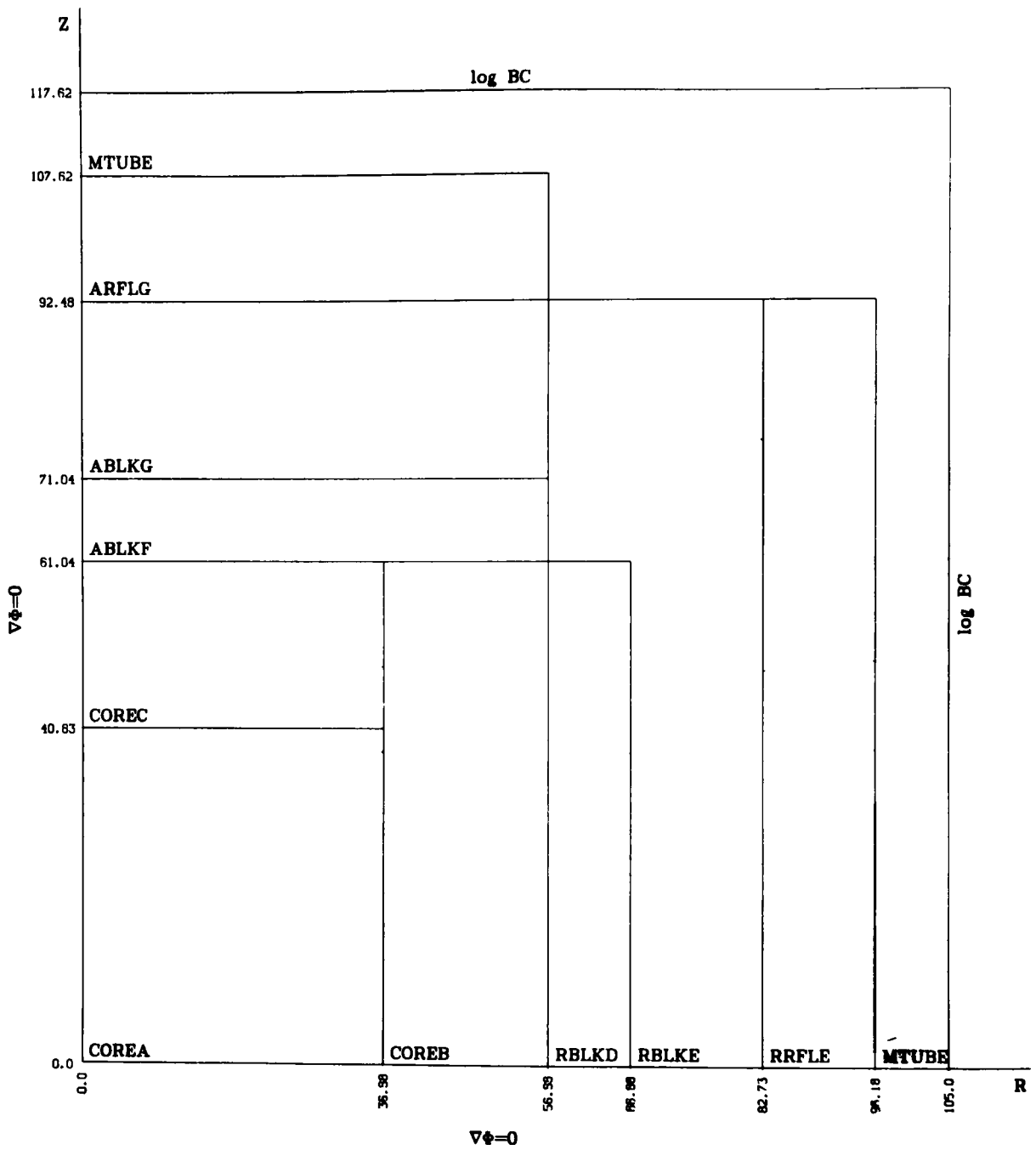


Figure II-2. RZ Reflected Calculational Model. ANL Neg. No. 116-77-106

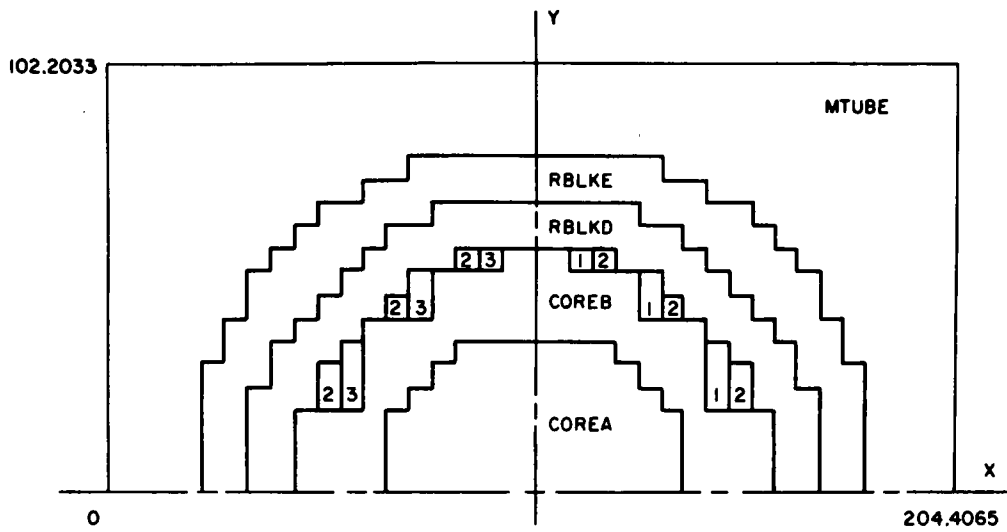


Figure II-3. XY Unreflected Calculational Model.  
ANL Neg. No. 116-77-98.

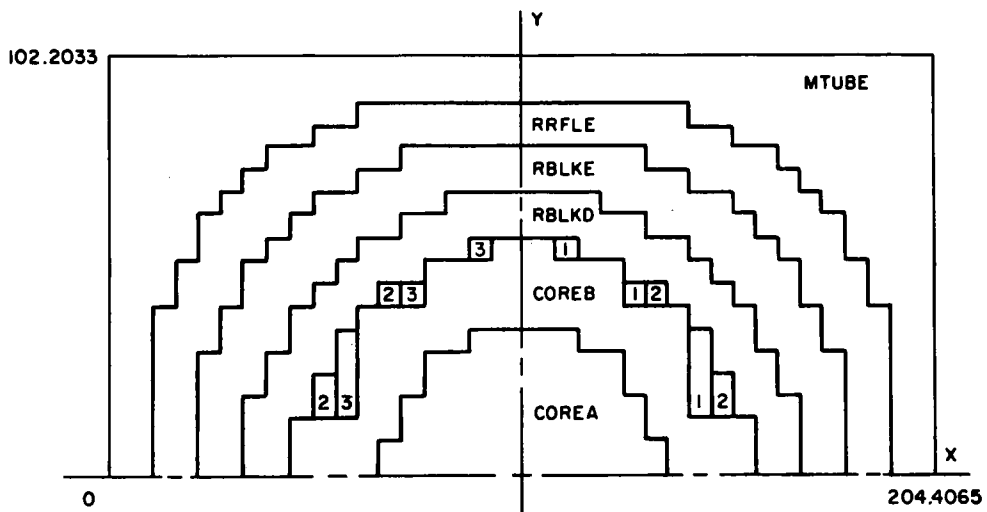


Figure II-4. XY Reflected Calculational Model.  
ANL Neg. No. 116-77-110.

Figure III-1

Unreflected Reactor Configuration  
for the Small-Sample Central and  
Radial Reactivity Worth Measure-  
ments. ANL Neg. No. 116-77-86.

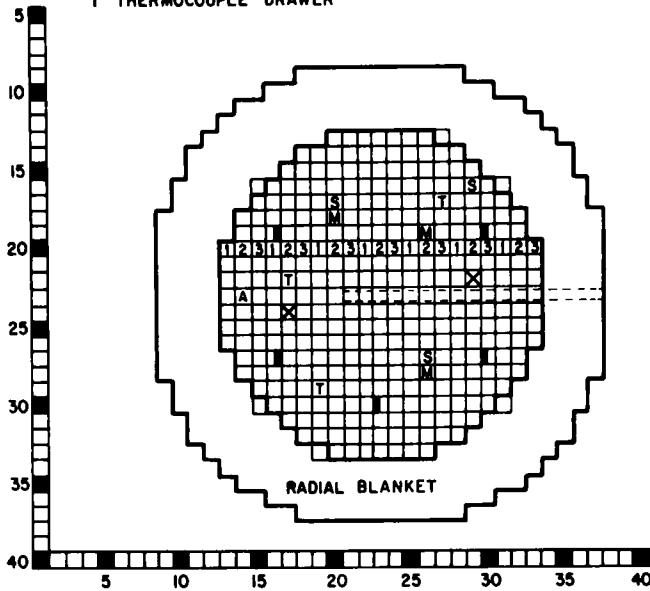
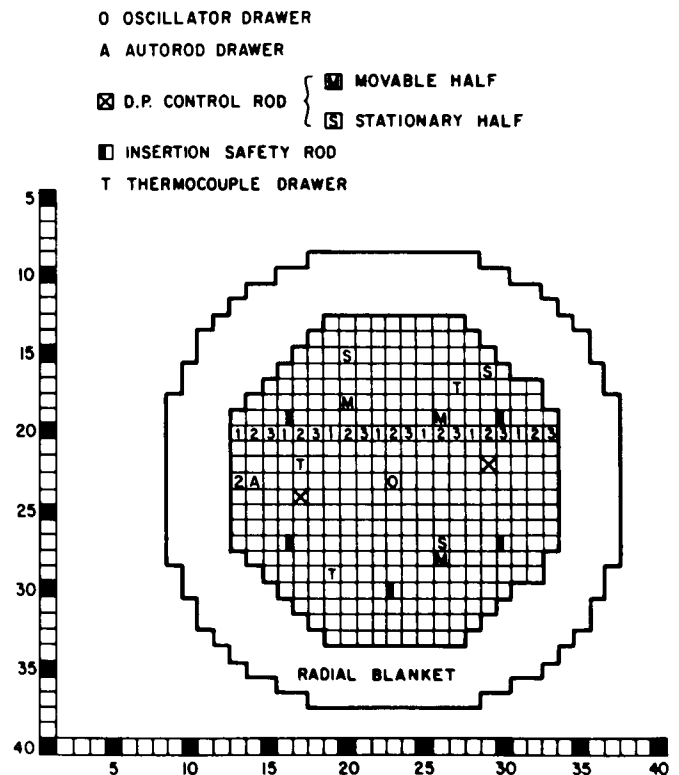


Figure III-2

Unreflected Reactor Configuration  
for the Small-Sample Axial Reac-  
tivity Worth Measurements.  
ANL Neg. No. 116-77-130.





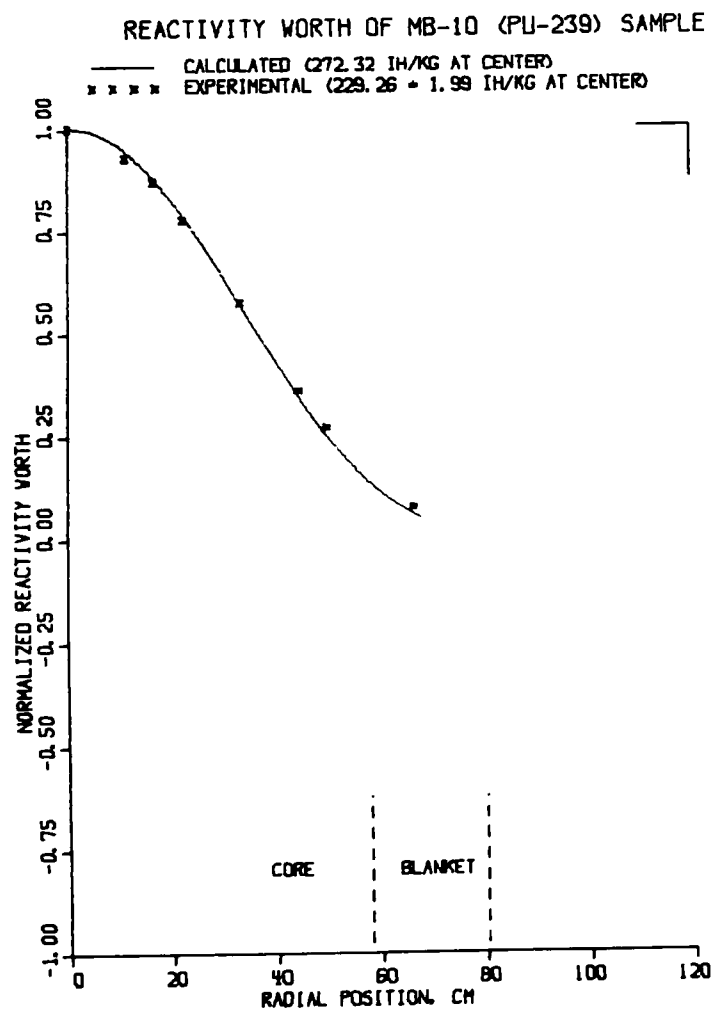


Figure III-4. Radial Traverse of MB-10 ( $^{239}\text{Pu}$ ).  
 ANL Neg. No. 116-77-80

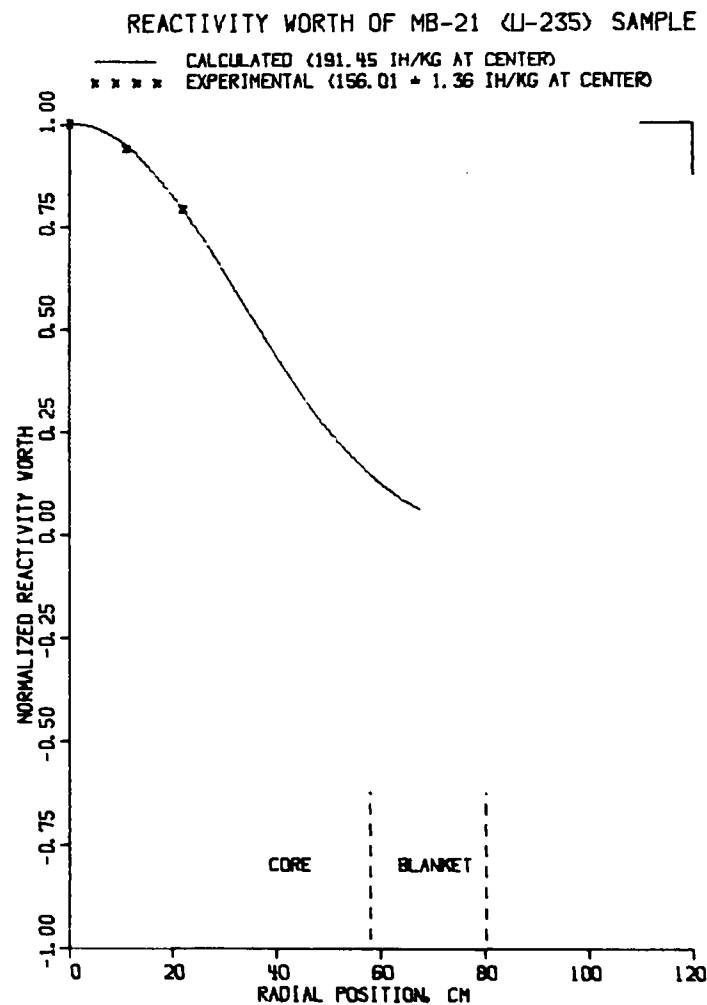


Figure III-5. Radial Traverse of MB-21 ( $^{235}\text{U}$ ).  
 ANL Neg. No. 116-77-88

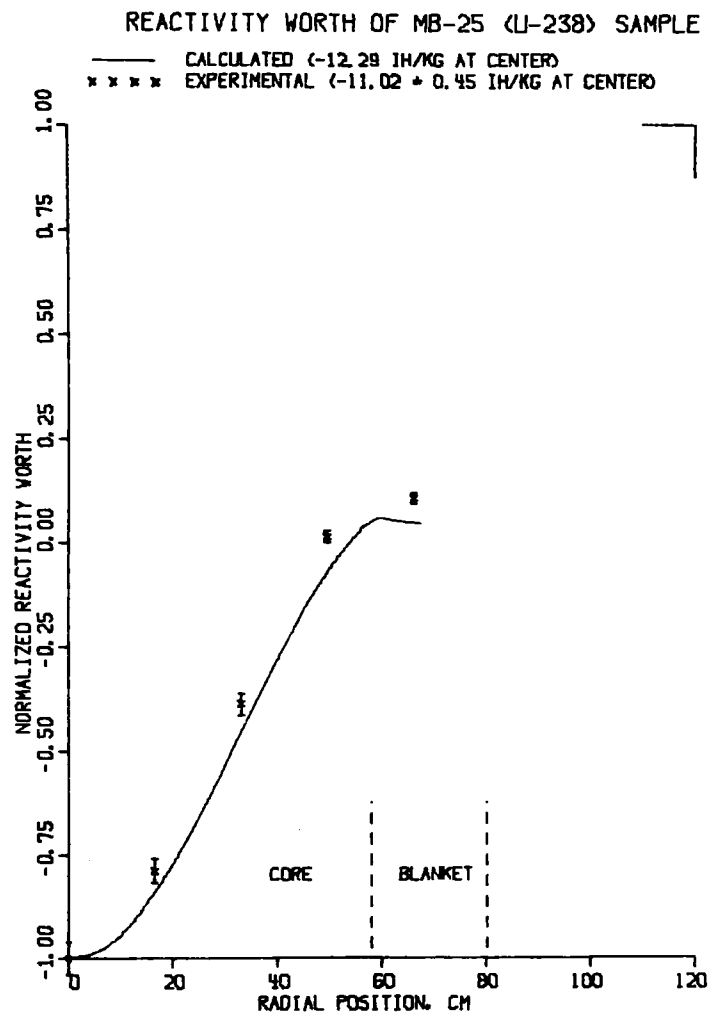


Figure III-6. Radial Traverse of MB-25 ( $^{238}\text{U}$ ).  
 ANL Neg. No. 116-77-131

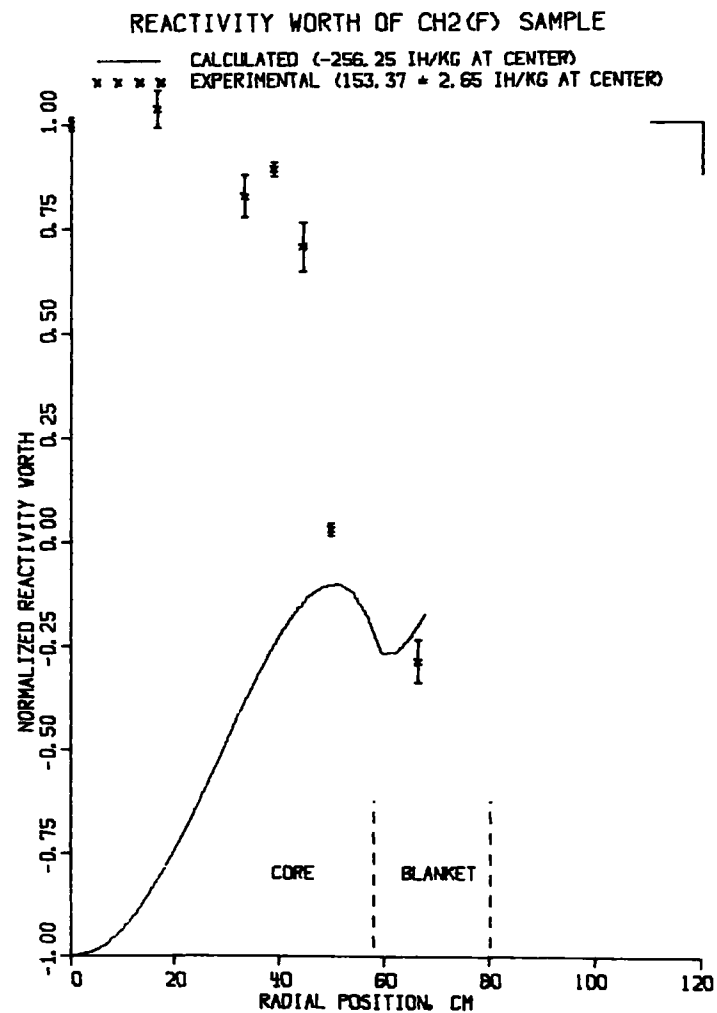


Figure III-7. Radial Traverse of  $\text{CH}_2(\text{F})$ -4  
 (Polyethylene Foam)  
 ANL Neg. No. 116-77-133

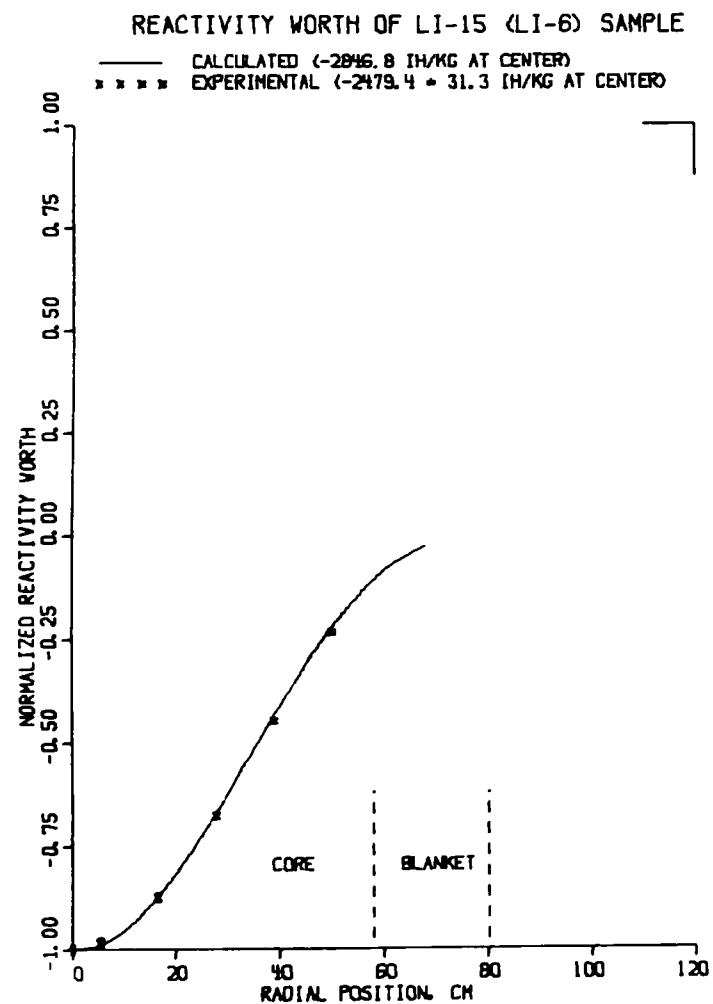


Figure III-8. Radial Traverse of Li-15 ( $^6\text{Li}$ ).  
ANL Neg. No. 116-77-144

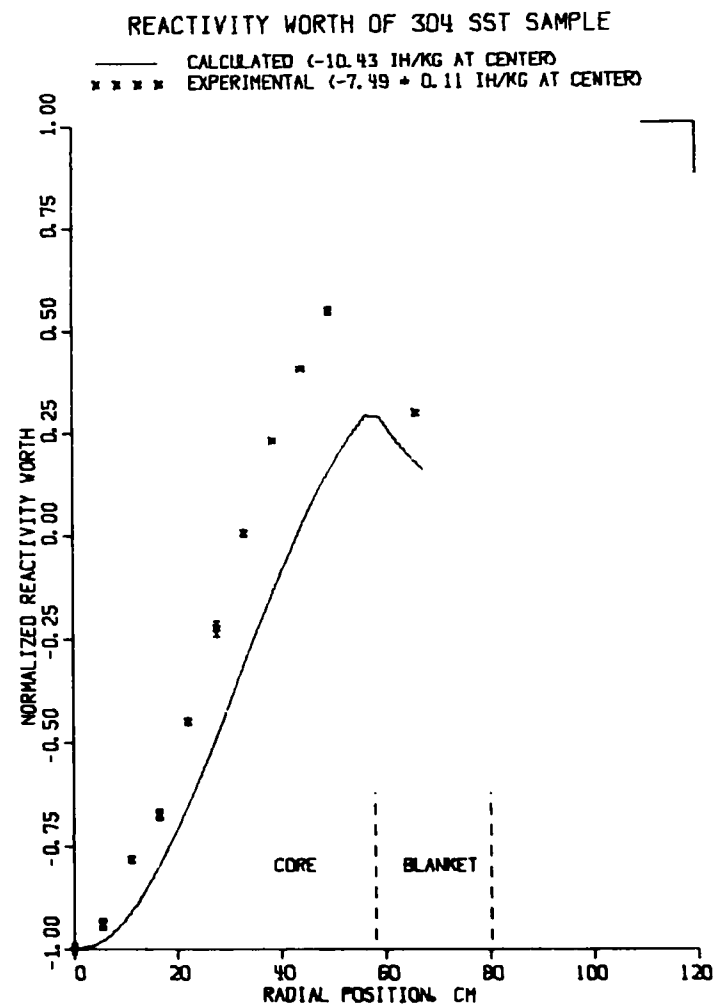


Figure III-9. Radial Traverse of 304 SST.  
ANL Neg. No. 116-77-81



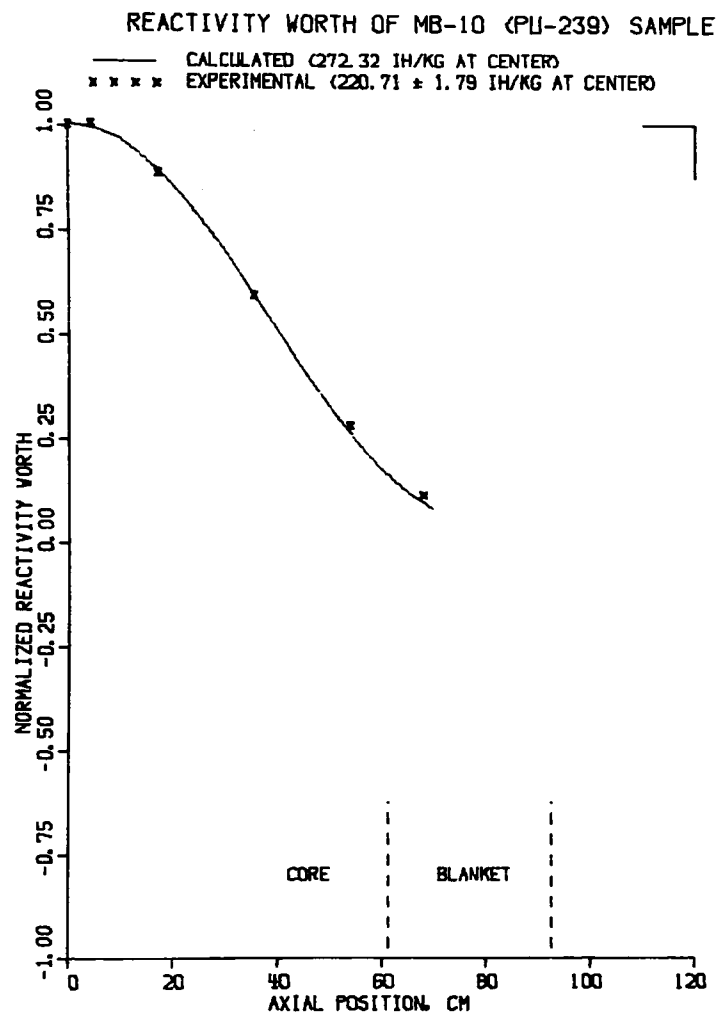


Figure III-10. Axial Traverse of MB-10 ( $^{239}\text{Pu}$ ).  
 ANL Neg. No. 116-77-129

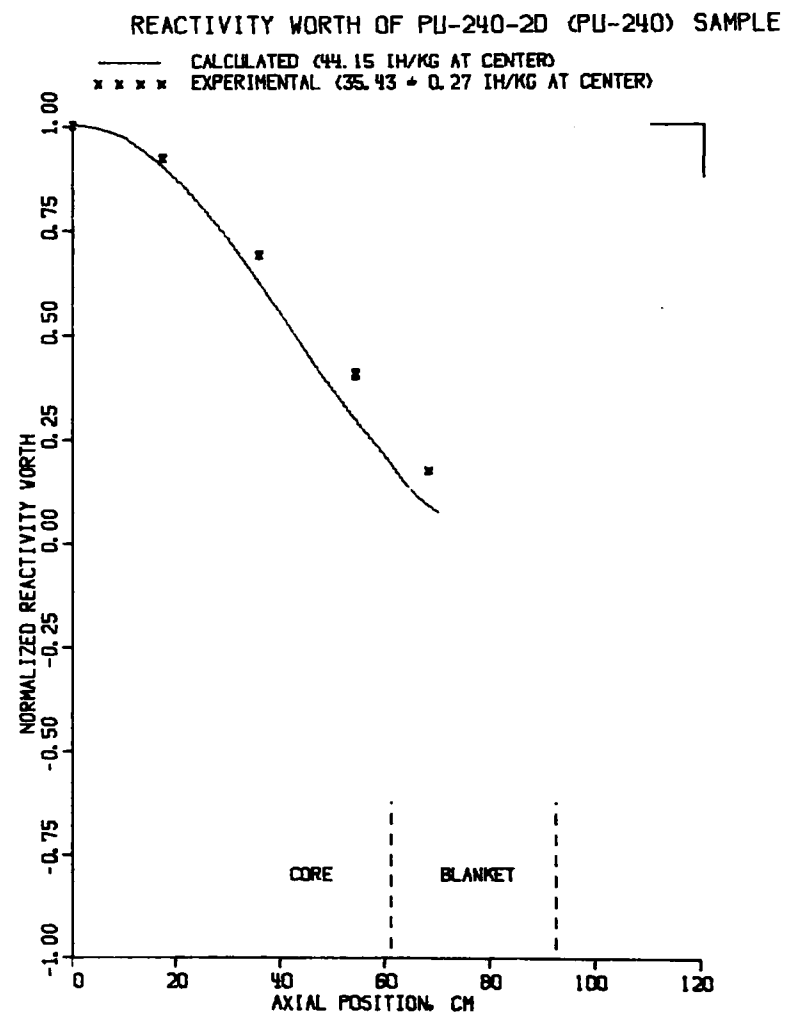


Figure III-11. Axial Traverse of Pu-240-2D ( $^{240}\text{UO}_2$ )  
 ANL Neg. No. 116-77-84

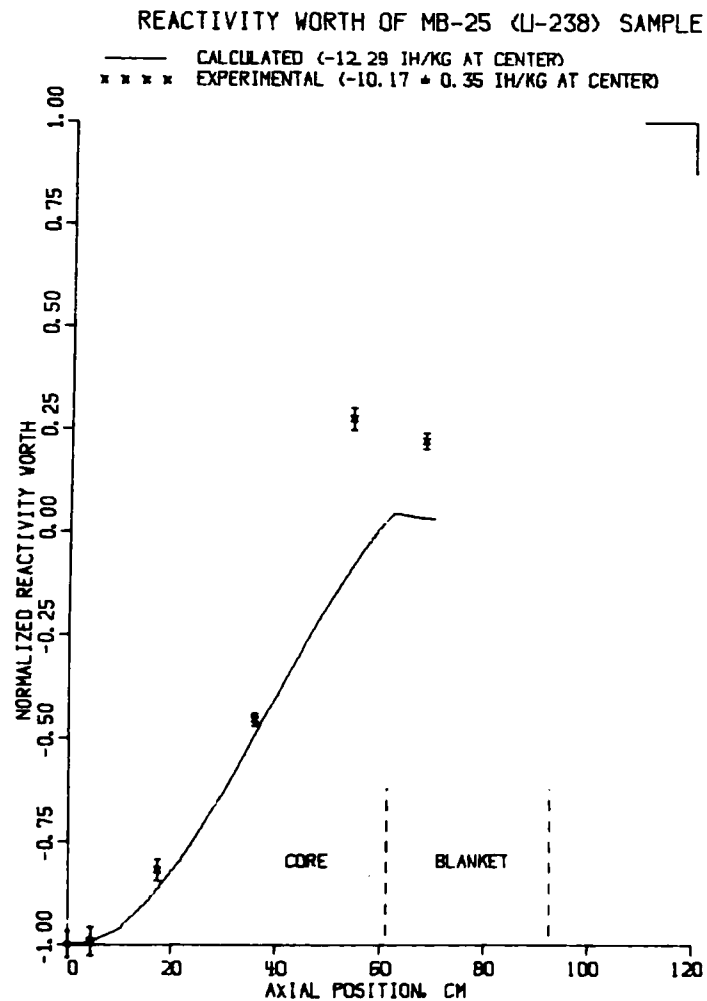


Figure III-12. Axial Traverse of MB-25 ( $^{238}\text{U}$ ).  
 ANL Neg. No. 116-77-89

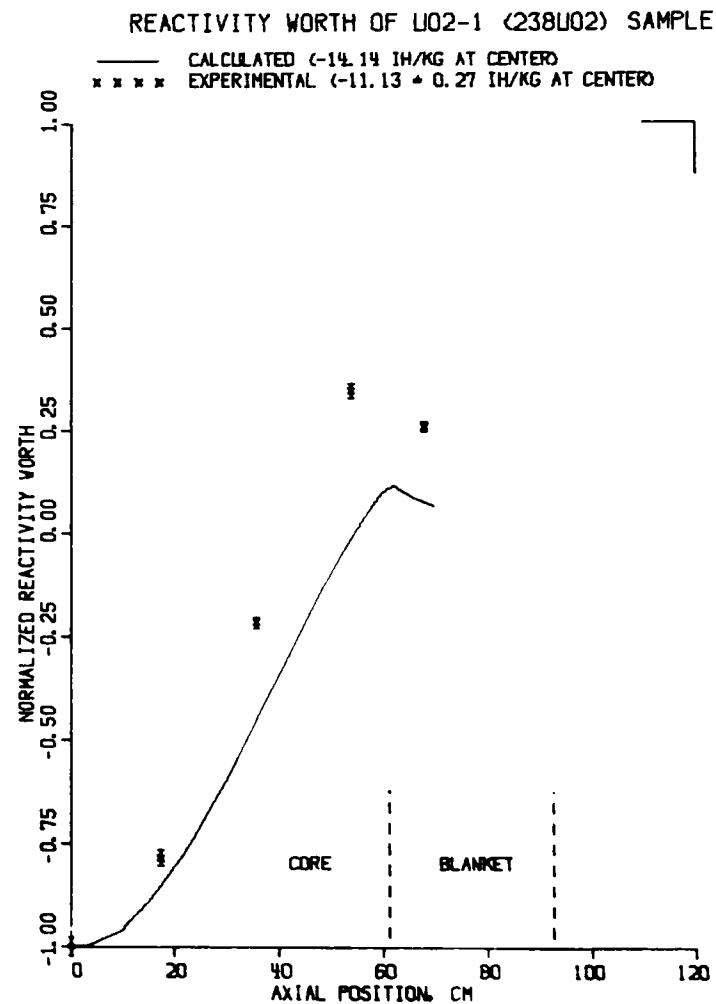


Figure III-13. Axial Traverse of UO<sub>2</sub>-1 ( $^{238}\text{UO}_2$ ).  
 ANL Neg. No. 116-77-85

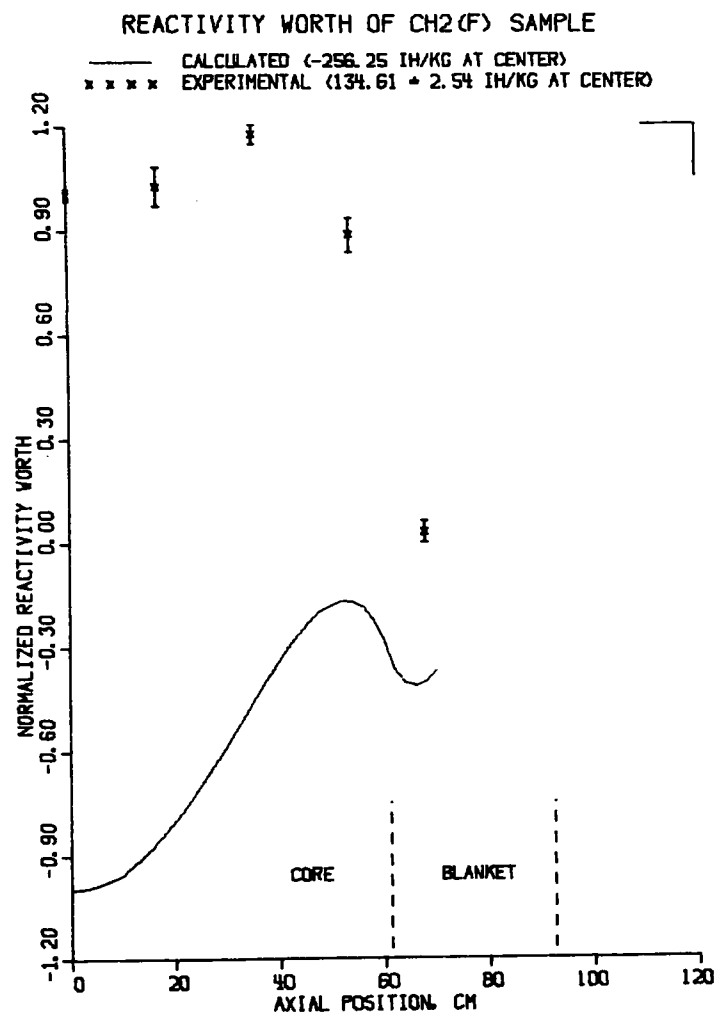


Figure III-14. Axial Traverse of CH<sub>2</sub>(F)-4  
 (Polyethylene Foam)  
 ANL Neg. No. 116-77-79

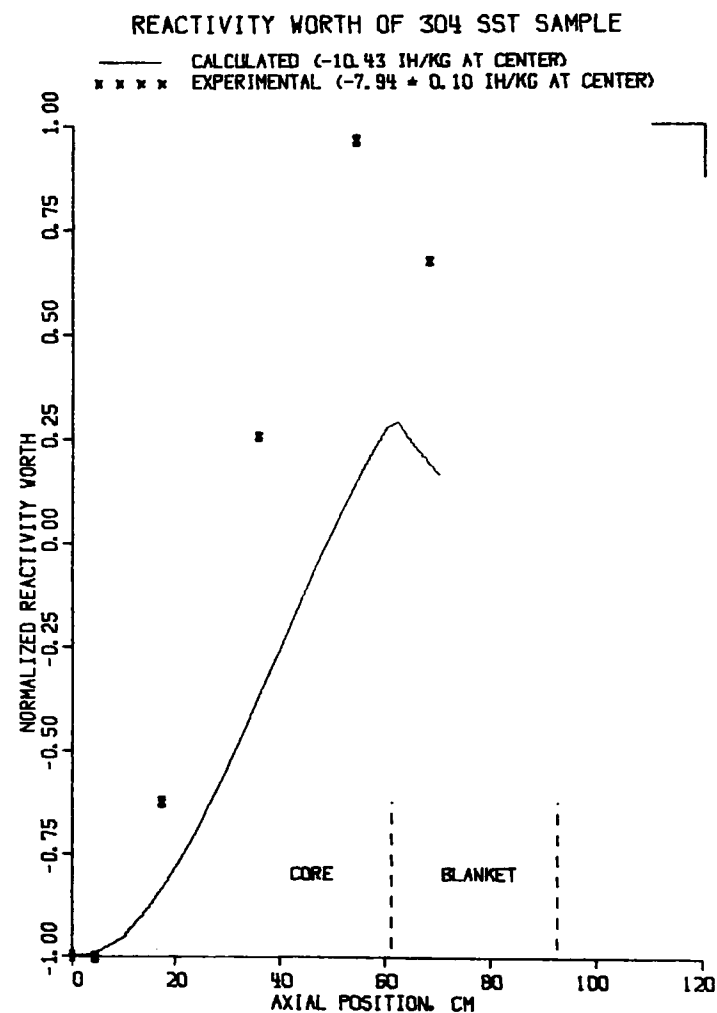


Figure III-15. Axial Traverse of 304 SST.  
 ANL Neg. No. 116-77-76

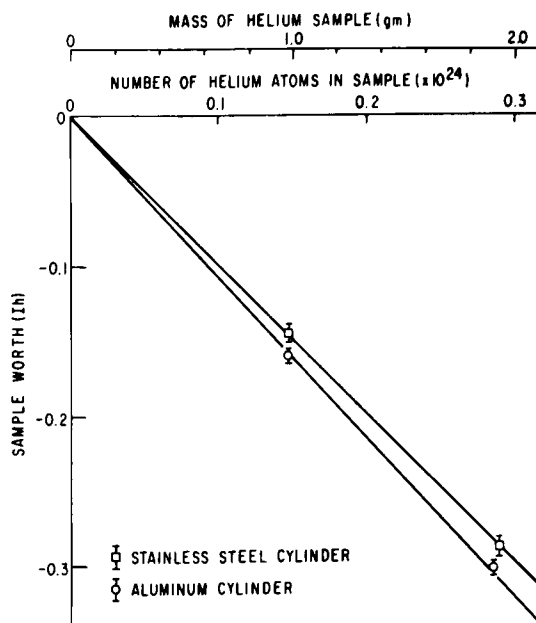


Figure IV-1. Measured Net Worth of the Helium Samples. ANL Neg. No. 116-77-117.

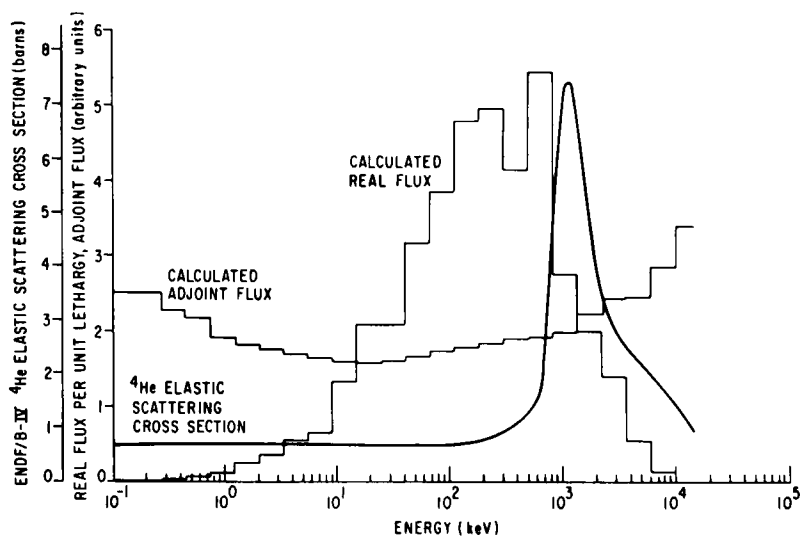


Figure IV-2. Graph of the Calculated Real and Adjoint Fluxes and the ENDF/B-IV He Elastic Scattering Cross-Section. ANL Neg. No. 116-77-122.

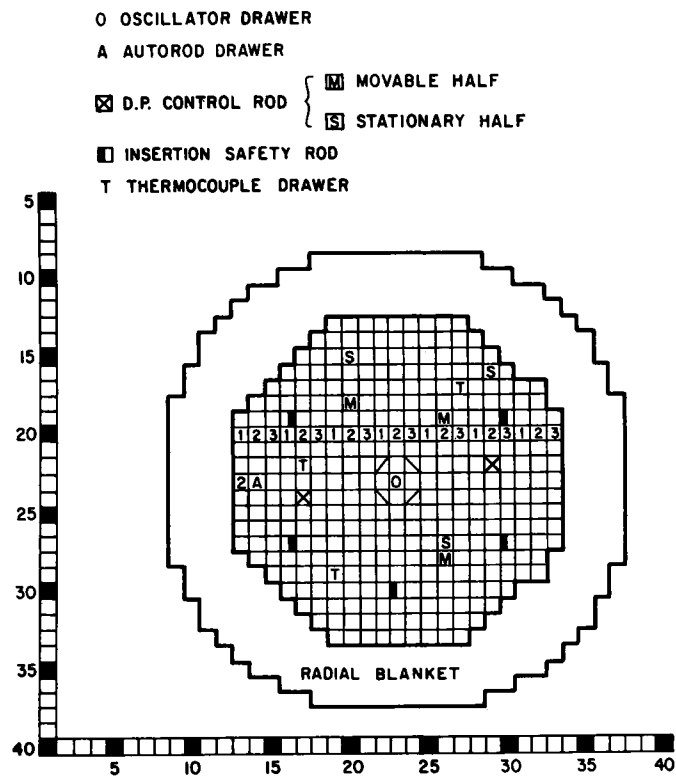


Figure V-1.  $^{238}\text{U}$  Doppler Effect Measurement Configuration. ANL Neg. No. 116-77-108

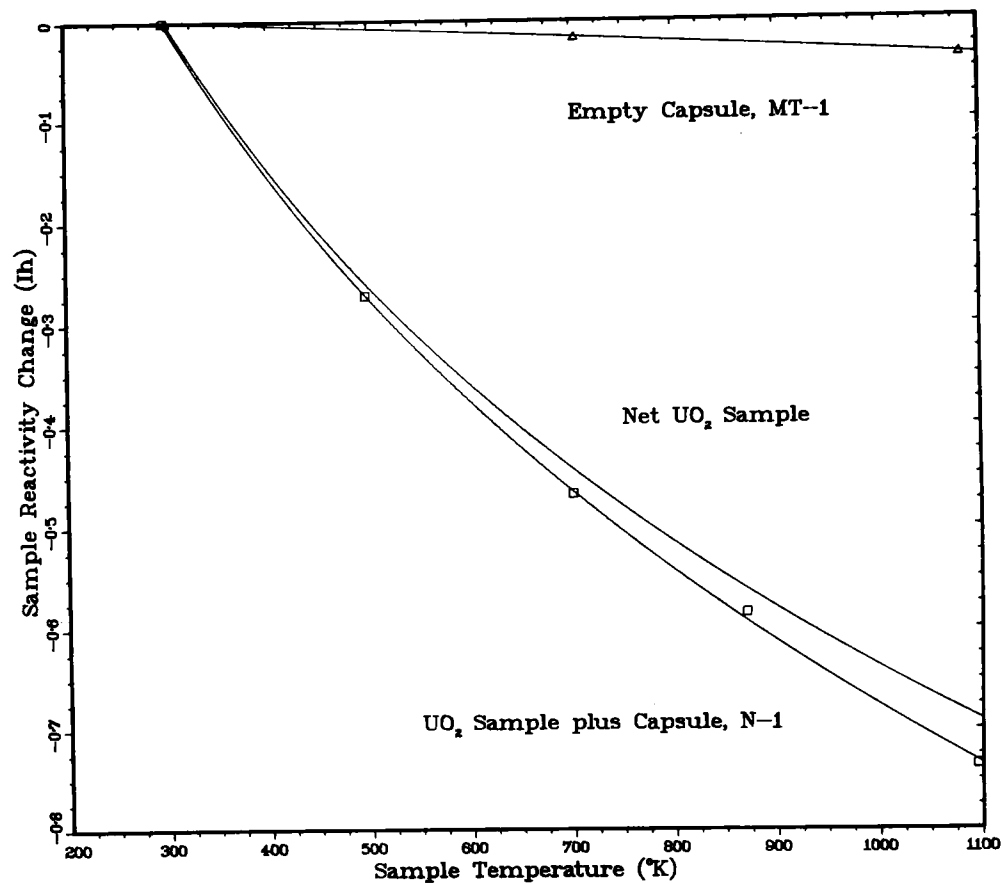


Figure V-2. Doppler Effect for Samples N-1, MT-1, and  $\text{UO}_2$ . ANL Neg. No. 116-77-104

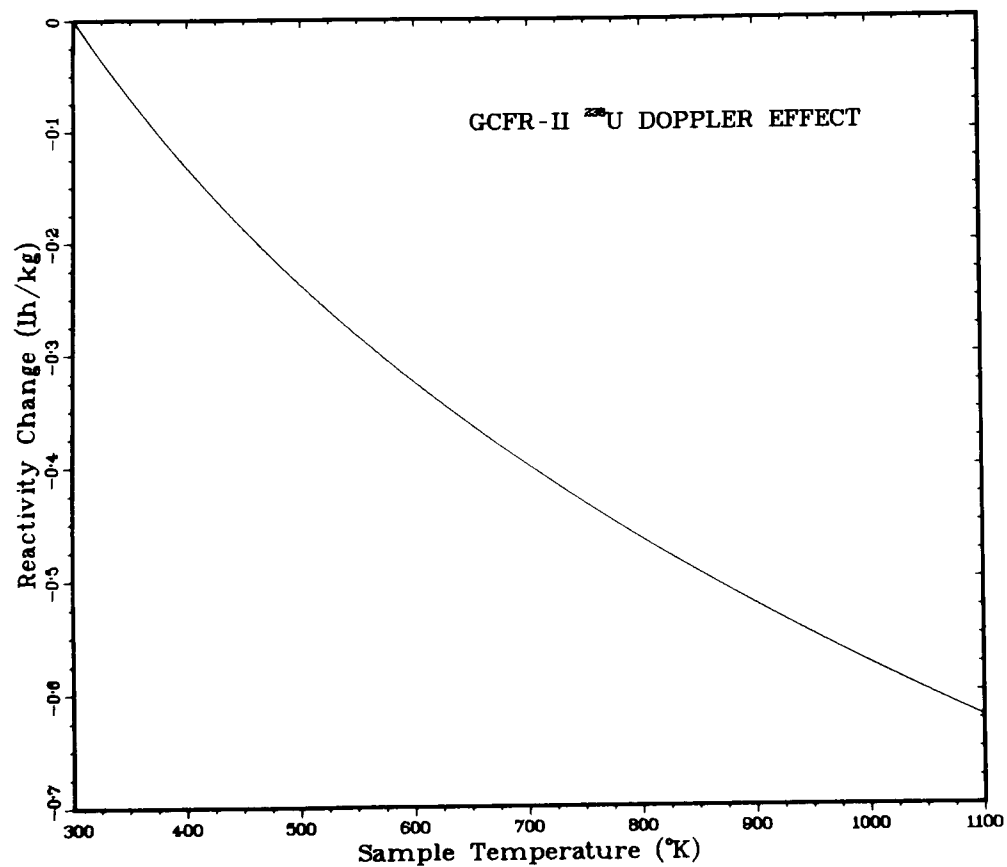


Figure V-3. Doppler Effect per Kilogram of <sup>238</sup>U.  
ANL Neg. No. 116-77-141.

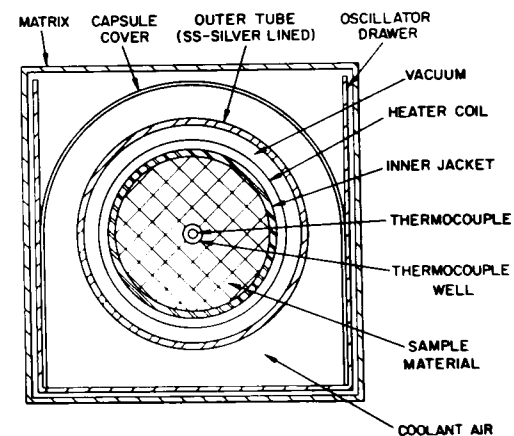


Figure V-4. Cross Sectional  
View of the Oscil-  
lator Drawer and  
Doppler Capsule.  
ANL Neg. No.  
116-417.

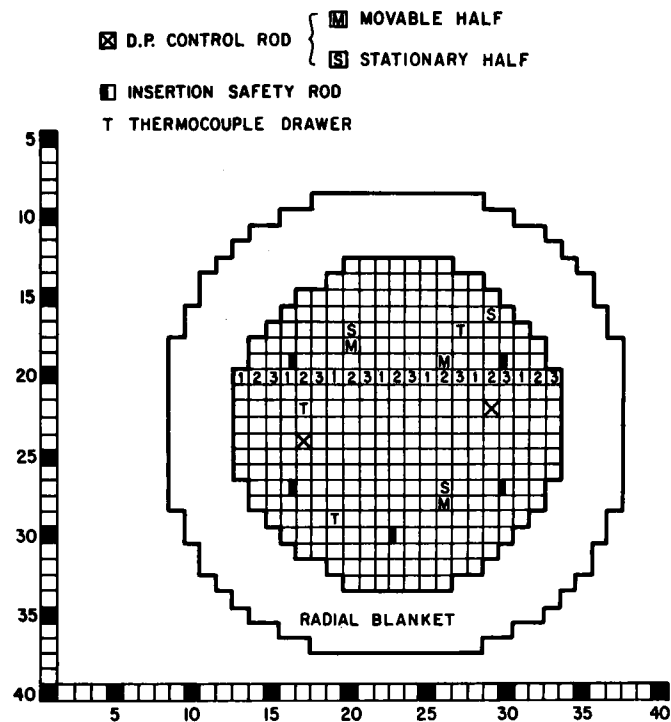


Figure VI-1. Core Configuration for Reaction Rate Measurements. ANL Neg. No. 116-77-109

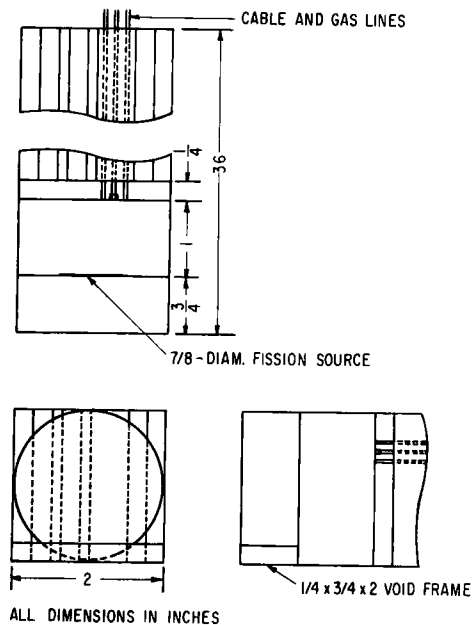


Figure VI-2. Fission Chamber Position Within Stationary-Half Type-1 Core Drawer. ANL Neg. No. 116-77-119

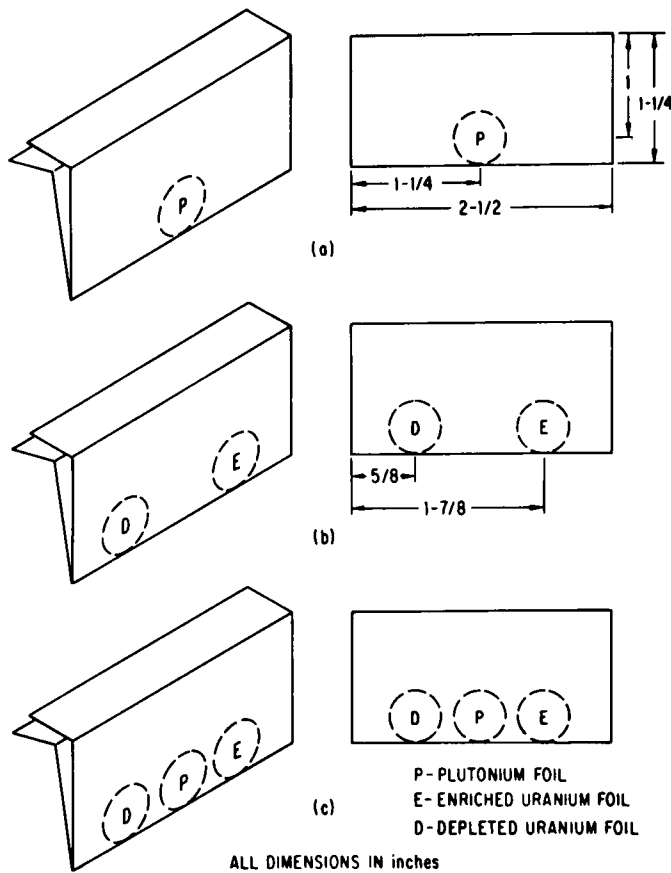


Figure VI-3  
Aluminum Foil Holders.  
ANL Neg. No. 116-77-78.

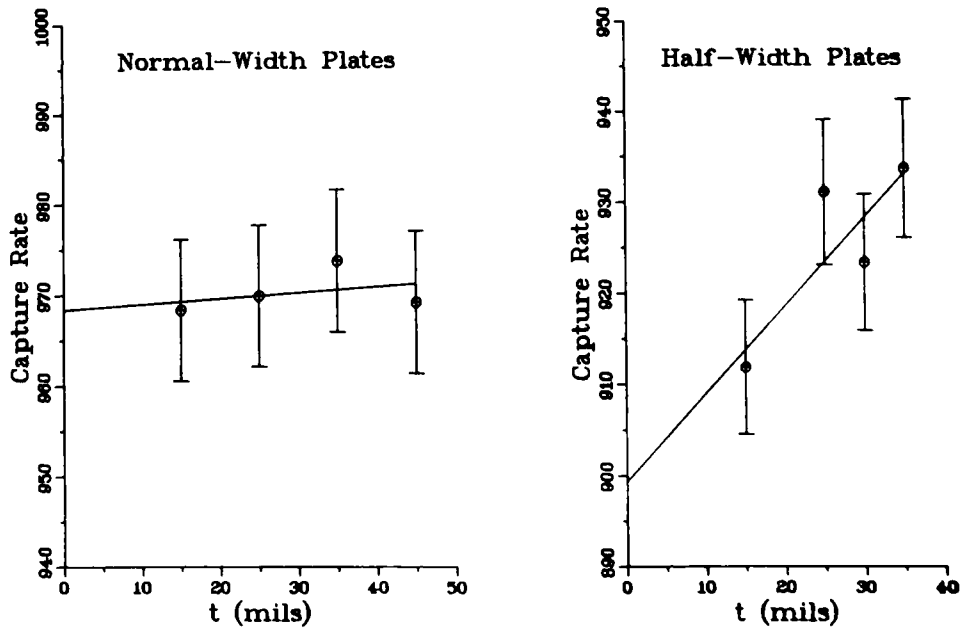


Figure VI-4. Linear Least-Squares Fits Used to Derive Stainless Steel Correction Factors for Capture Rates. ANL Neg. No. 116-77-124



Pu Fission, Row 22 Core Unit Cell, 0-2 in.

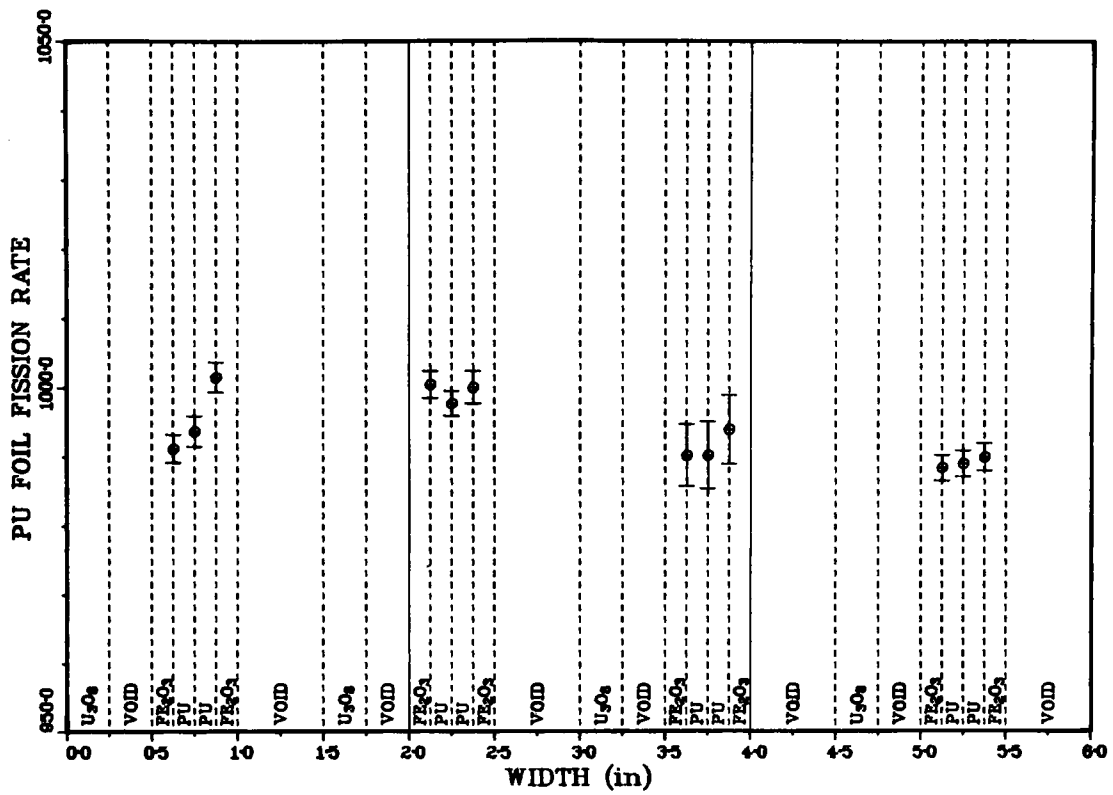


Figure VI-5. Intra-Cell Plutonium Fission Rates in the Core Region.  
ANL Neg. No. 116-77-140

## Enriched U Fission, Row 22 Core, 0-2 in.

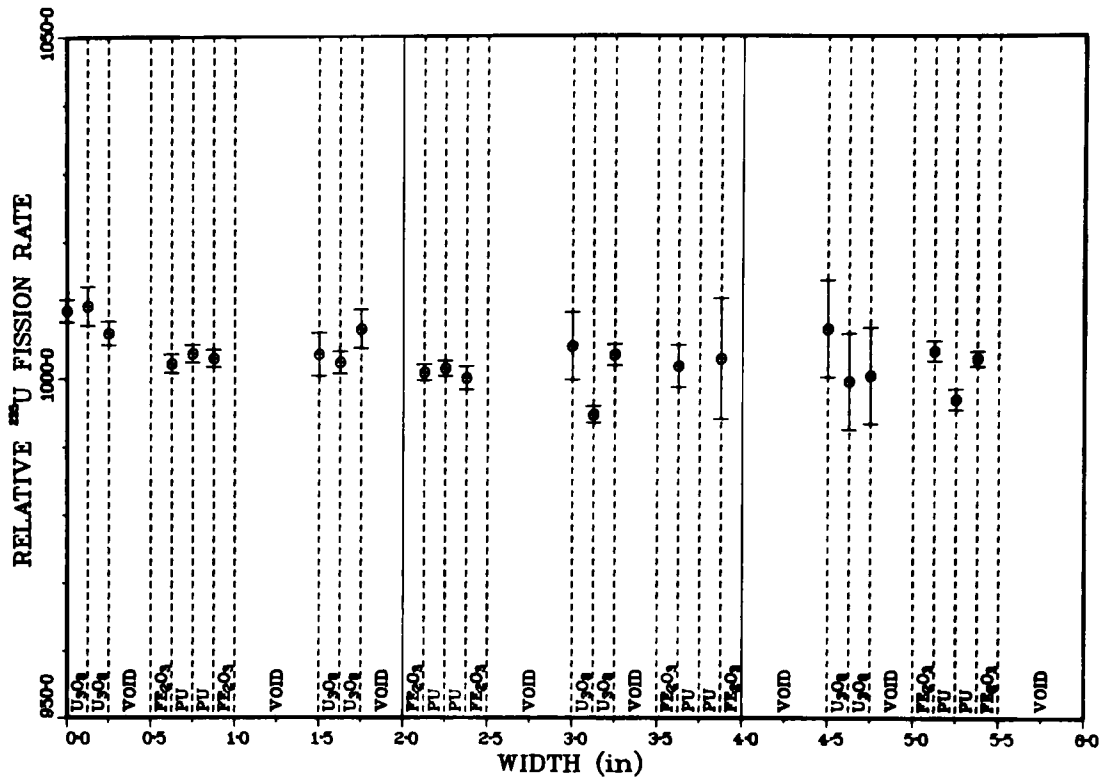


Figure VI-6. Intra-Cell Enriched Uranium Fission Rates in the Core Region.  
ANL Neg. No. 116-77-91

Enriched U Fission, Row 22 Axial Blanket, 24-26 in.

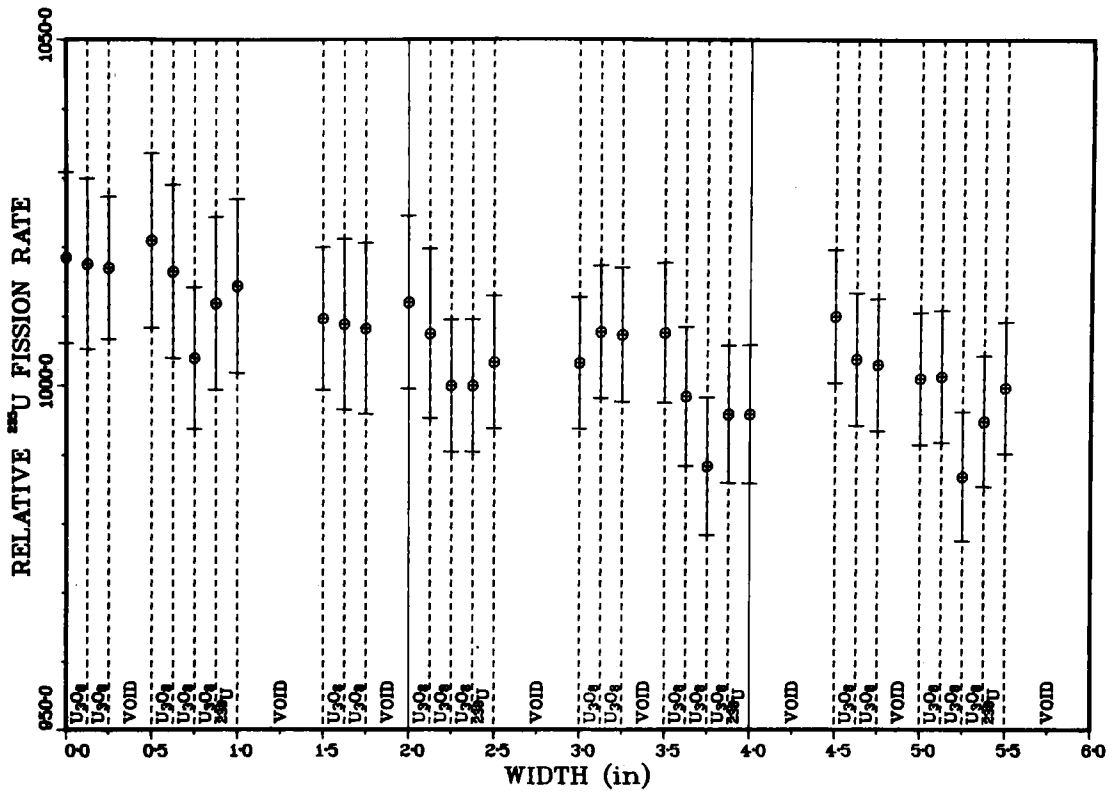


Figure VI-7. Intra-Cell Enriched Uranium Fission Rates in the Axial Blanket Region. ANL Neg. No. 116-77-75

Enriched U Fission, Row 34 Radial Blanket

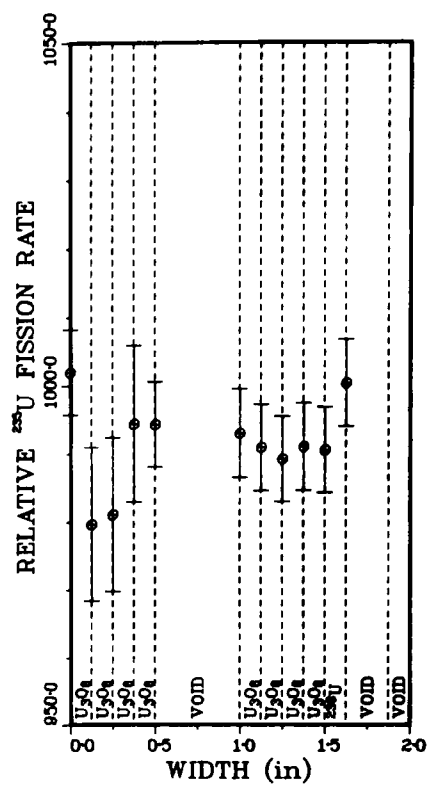


Figure VI-8. Intra-Cell Enriched Uranium Fission Rates in the Radial Blanket Region.  
ANL Neg. No. 116-77-138

## Depleted U Fission, Row 22 Core Unit Cell, 0-2 in.

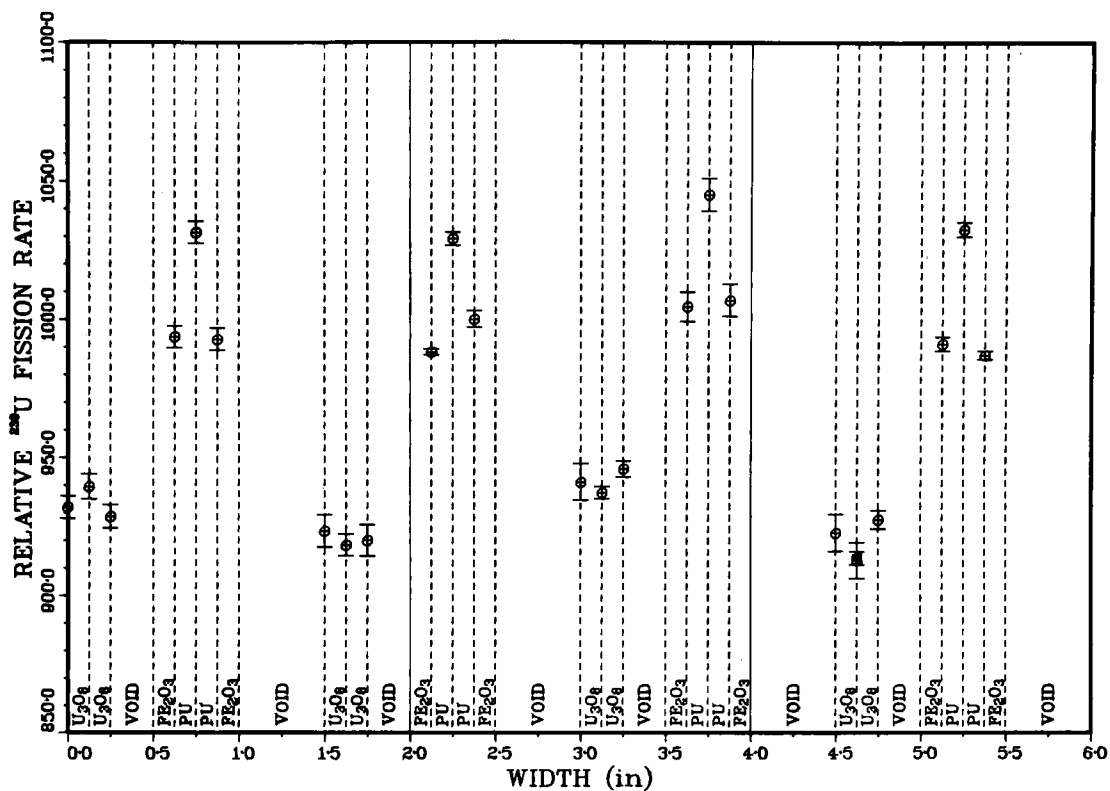


Figure VI-9. Intra-Cell Depleted Uranium Fission Rates in the Core Region.  
ANL Neg. No. 116-77-146

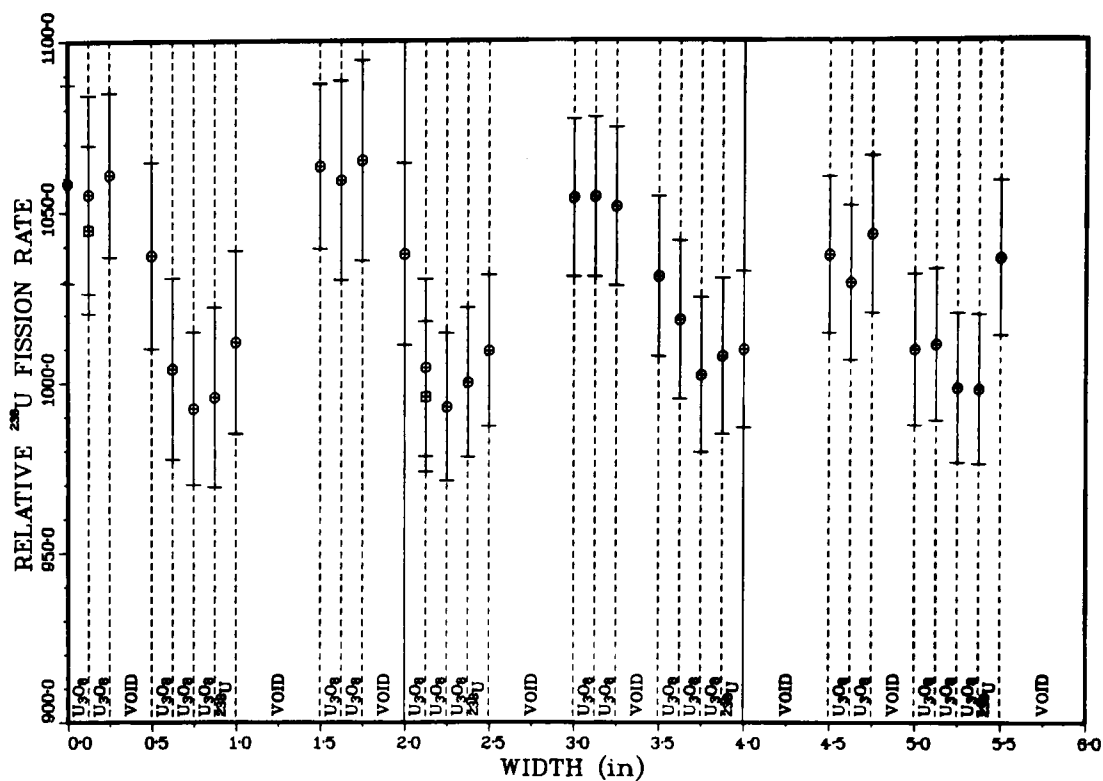


Figure VI-10. Intra-Cell Depleted Uranium Fission Rates in the Axial Blanket Region. ANL Neg. No. 116-77-132

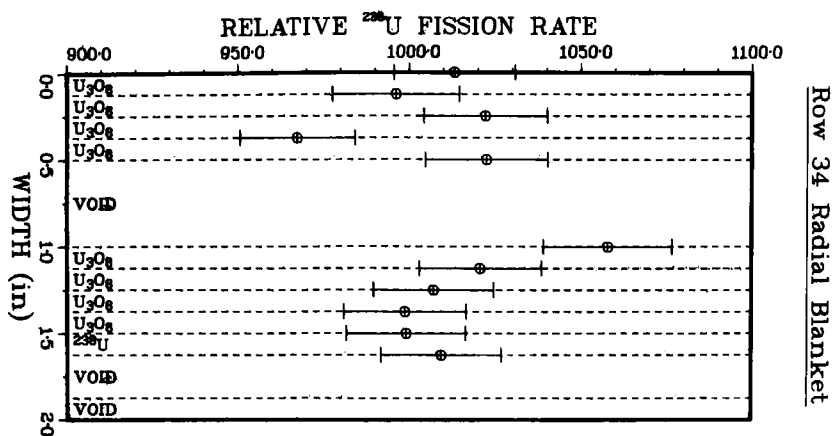


Figure VI-11. Intra-Cell Depleted Uranium Fission Rates in the Radial Blanket Region.  
ANL Neg. No. 116-77-94.

Depleted U Capture, Row 22 Core, 0-2 in.

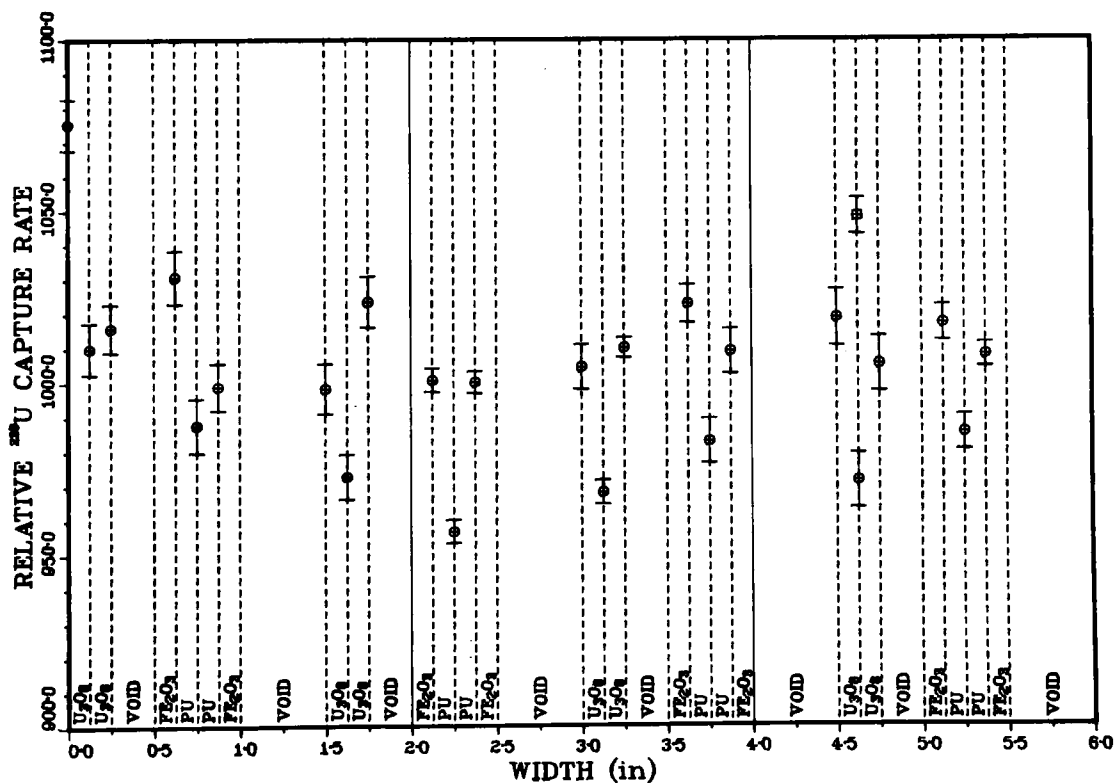


Figure VI-12. Intra-Cell Depleted Uranium Capture Rates in the Core Region.  
ANL Neg. No. 116-77-139

Depleted U Capture, Row 22 Ax. Blanket, 24-26 in.

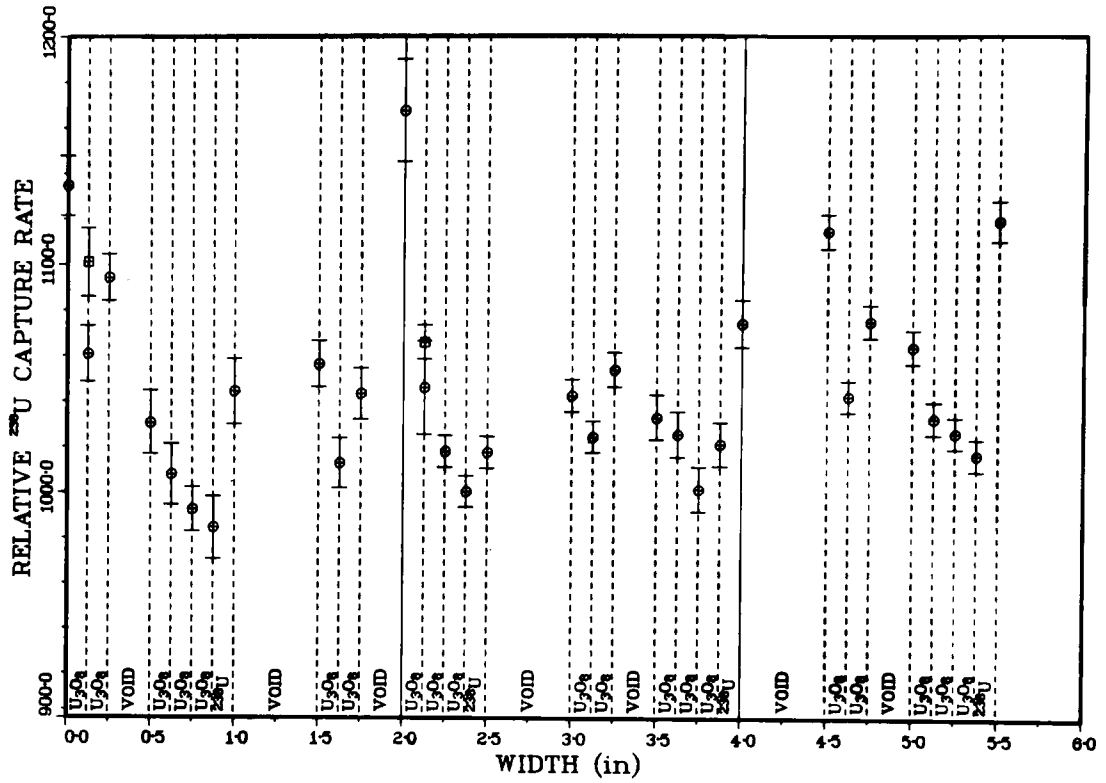


Figure VI-13. Intra-Cell Depleted Uranium Capture Rates in the Axial Blanket region. ANL Neg. No. 116-77-72



Depleted U Capture, Row 34 Radial Blanket

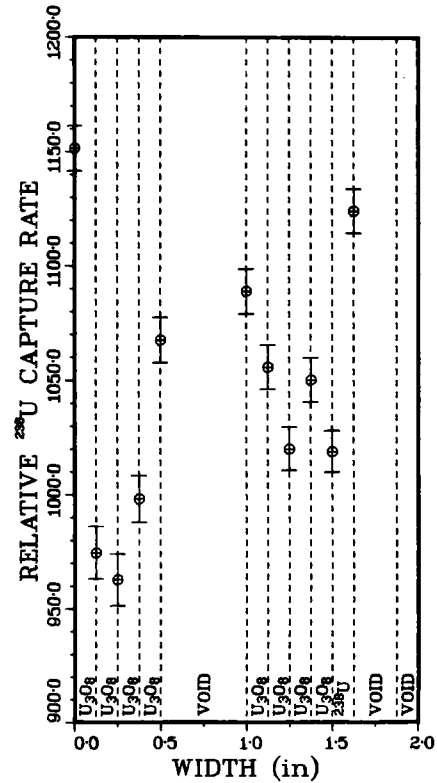


Figure VI-14. Intra-Cell Depleted Uranium Capture Rates in the Radial Blanket Region. ANL Neg. No. 116-77-137

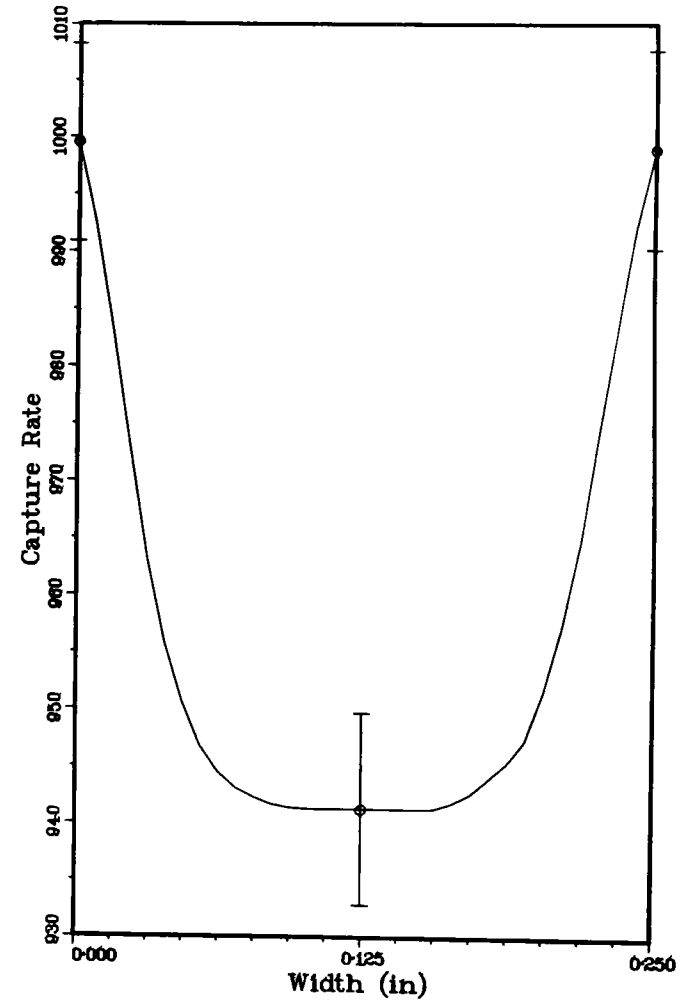


Figure VI-15. Example of Interpolated Curve Used to Determine the  $^{238}\text{U}$  Capture Rate in a Fuel Plate. ANL Neg. No. 116-77-93

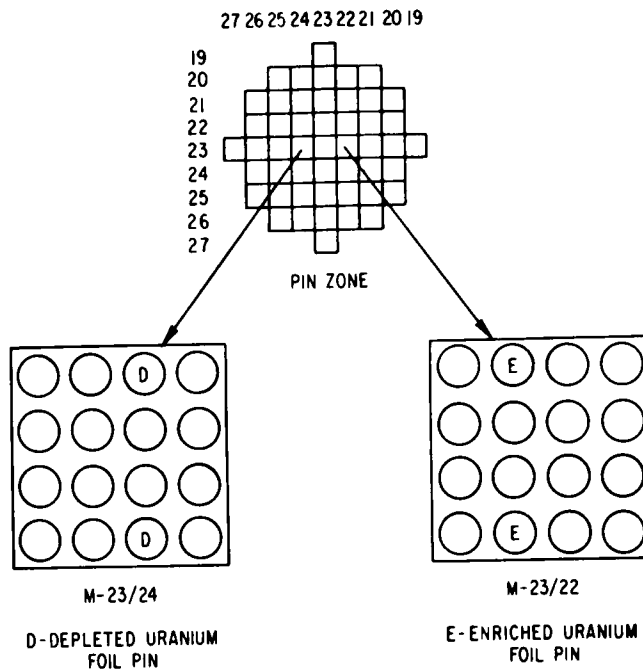


Figure VII-1. Movable-Half Axial Blanket Pin Zone.  
ANL Neg. No. 116-77-112

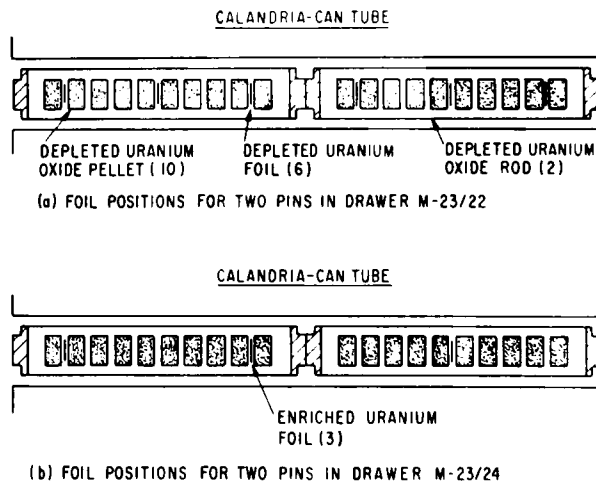


Figure VII-2. Location of Enriched and Depleted Uranium Foils Within Selected Rods of the Pin Zone. ANL Neg. No. 116-77-120

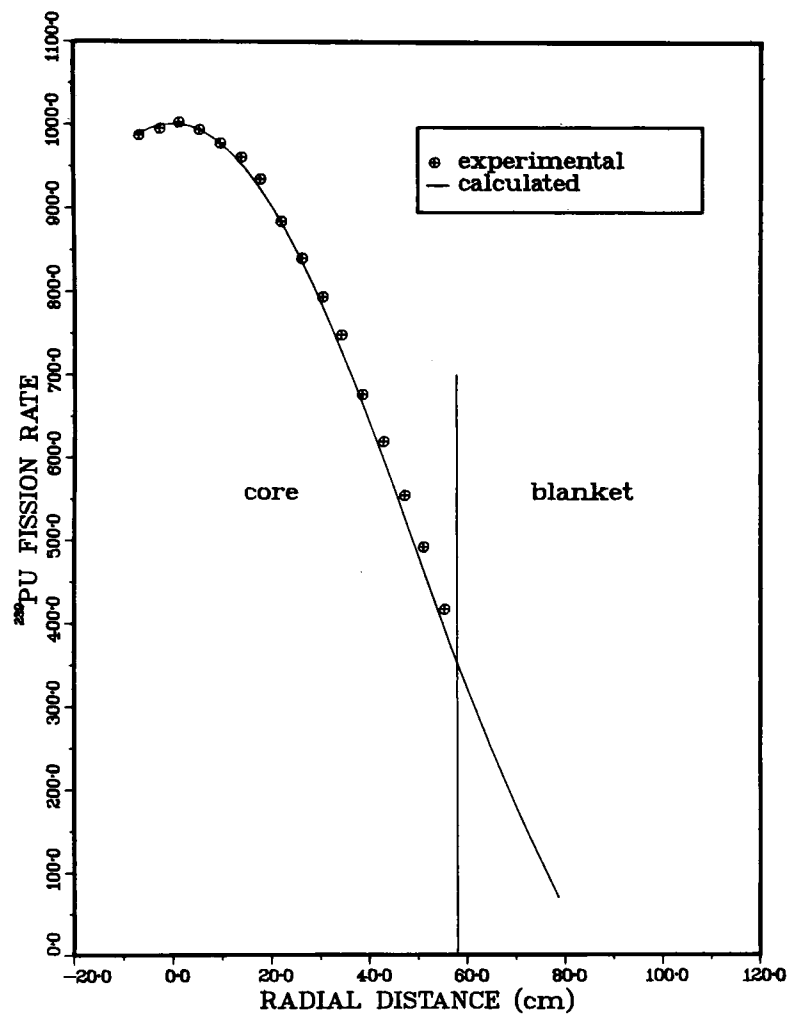


Figure VII-3.  $^{239}\text{Pu}$  Radial Fission Rate Distribution, Unreflected Assembly. ANL Neg. No. 116-77-113

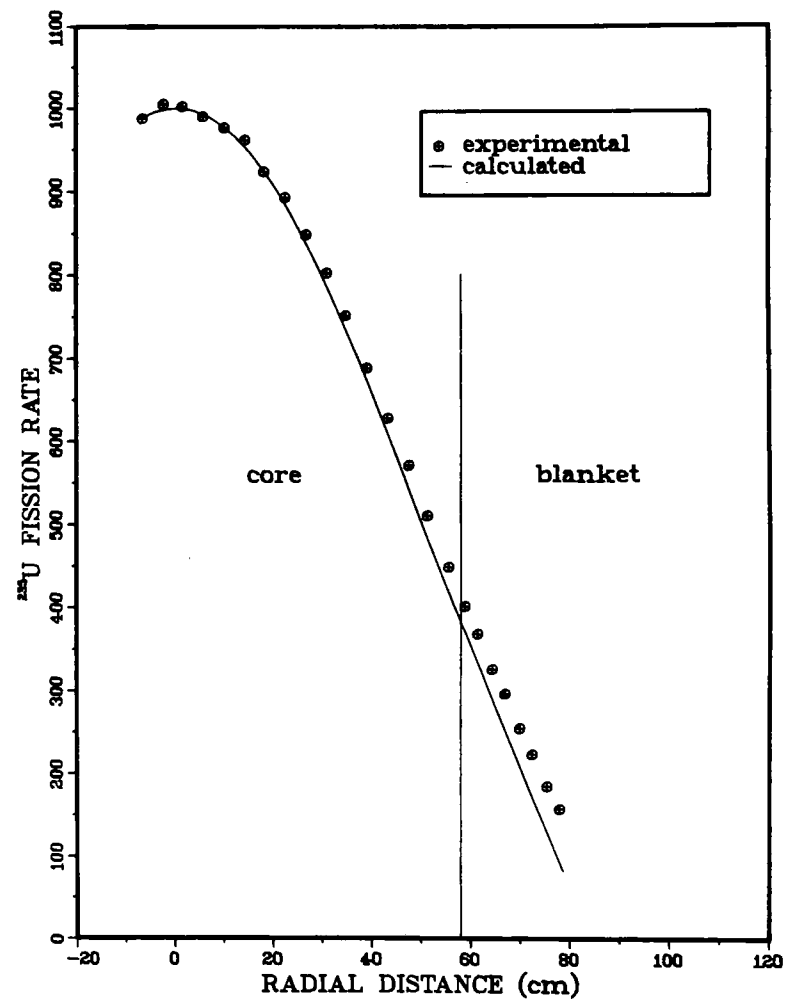


Figure VII-4.  $^{235}\text{U}$  Radial Fission Rate Distribution, Unreflected Assembly. ANL Neg. No. 116-77-111

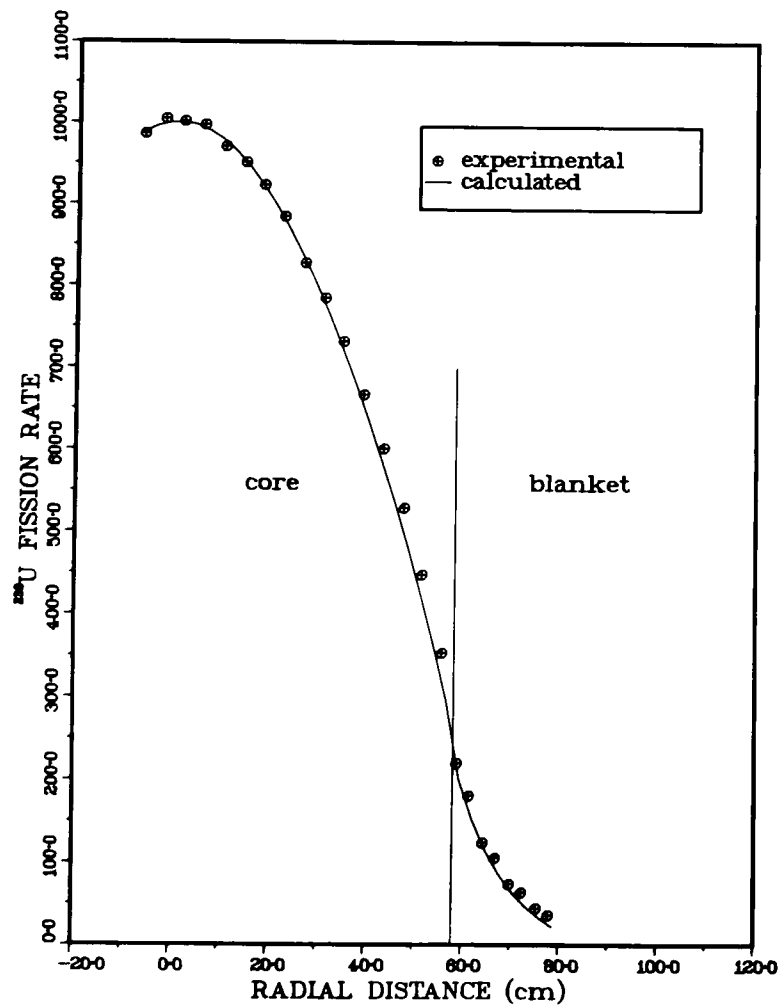


Figure VII-5.  $^{238}\text{U}$  Radial Fission Rate Distribution, Unreflected Assembly.  
ANL Neg. No. 116-77-125

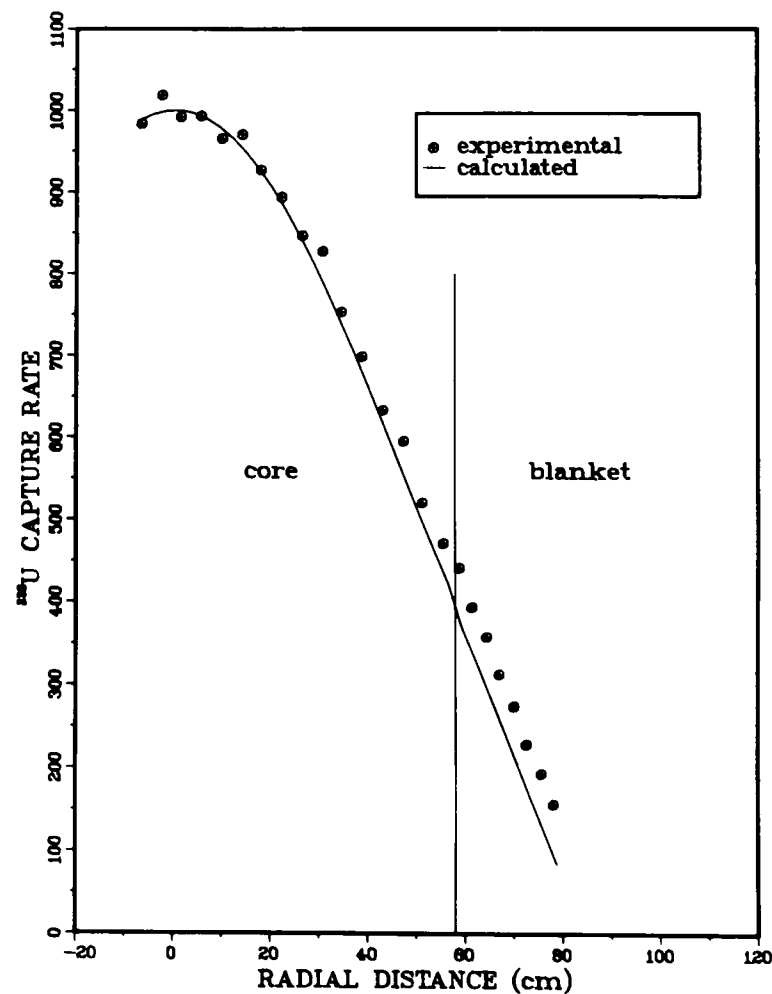


Figure VII-6.  $^{238}\text{U}$  Radial Capture Rate Distribution, Unreflected Assembly.  
ANL Neg. No. 116-77-134

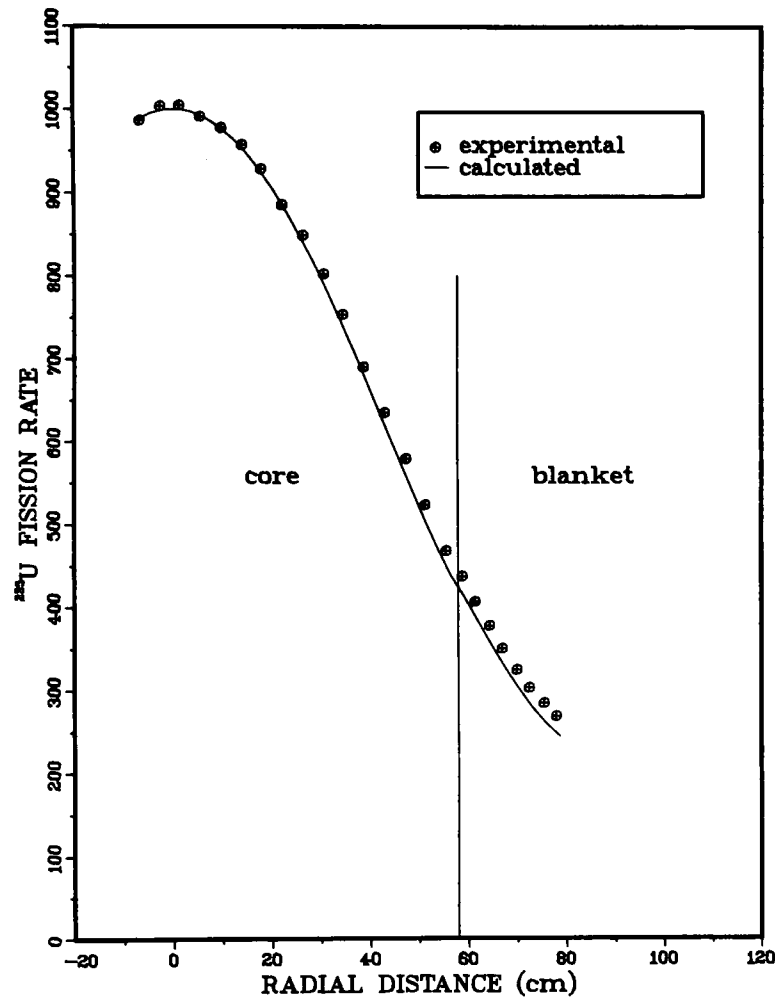


Figure VII-7.  $^{235}\text{U}$  Radial Fission Rate Distribution, Reflected Assembly.  
ANL Neg. No. 116-77-92

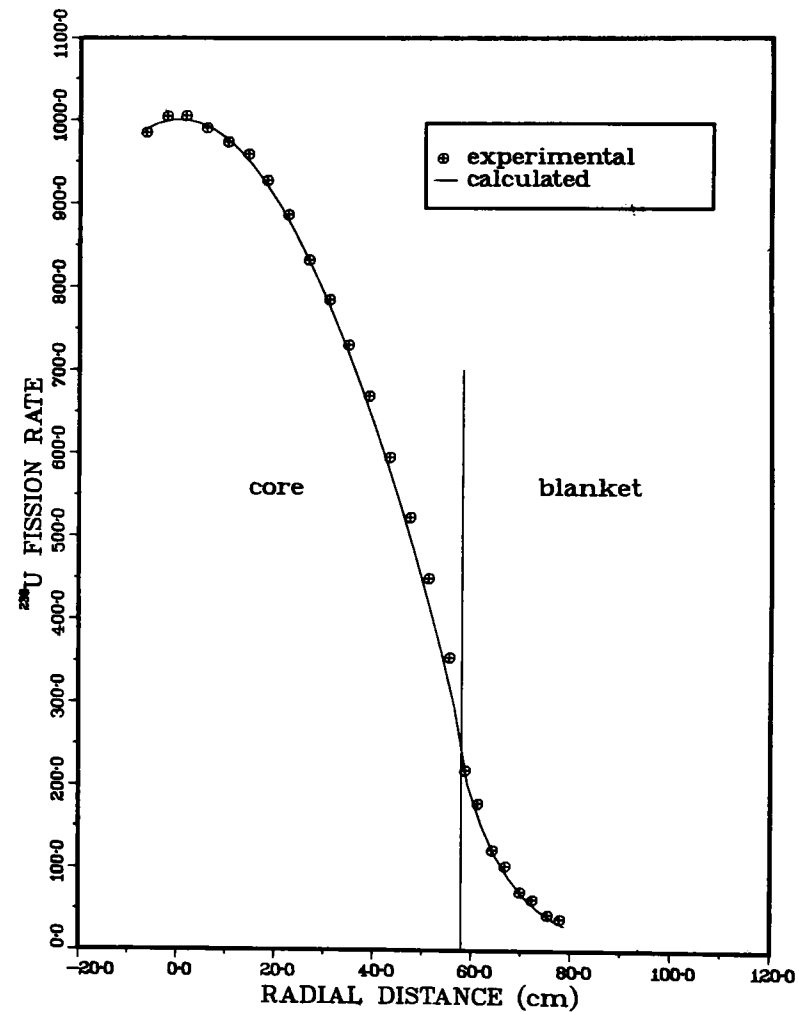


Figure VII-8.  $^{238}\text{U}$  Radial Fission Rate Distribution, Reflected Assembly.  
ANL Neg. No. 116-77-77

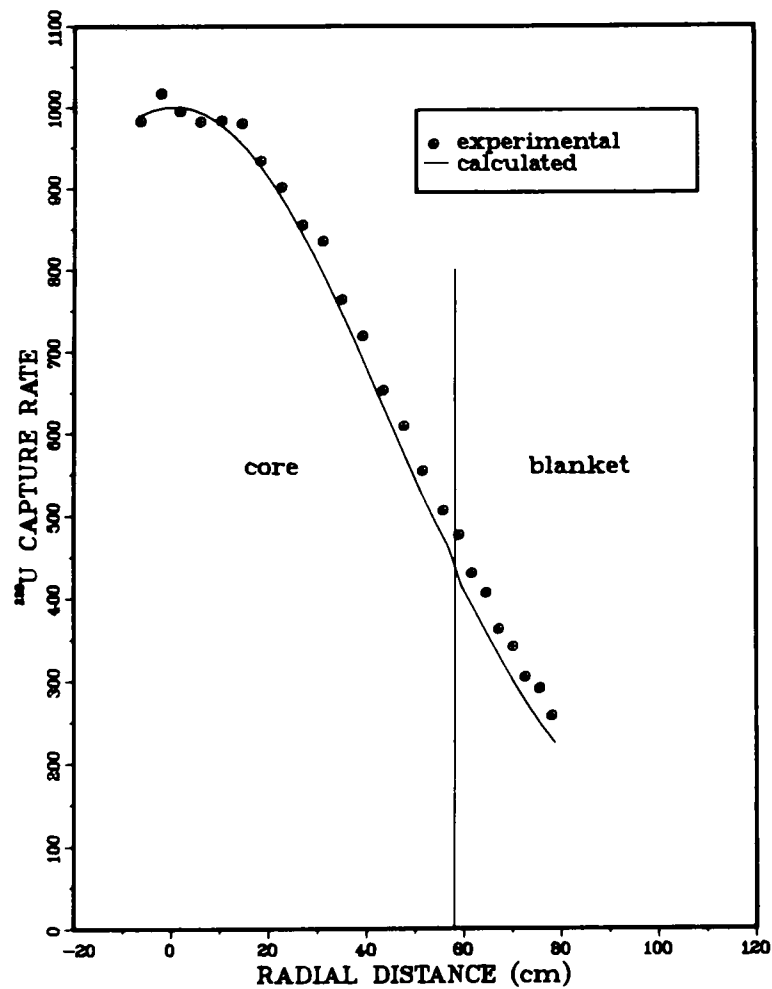


Figure VII-9.  $^{238}\text{U}$  Radial Capture Rate Distribution, Reflected Assembly.  
ANL Neg. No. 116-77-82

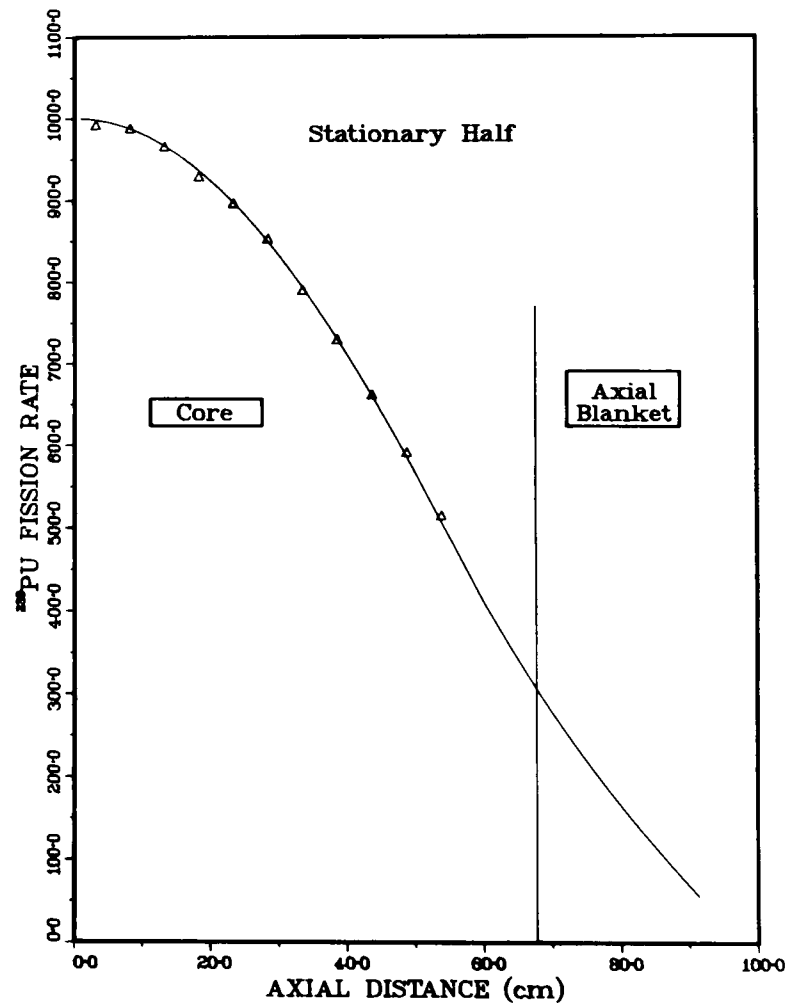


Figure VII-10.  $^{239}\text{Pu}$  Axial Fission Rate Distribution, Unreflected Assembly.  
ANL Neg. No. 116-77-136

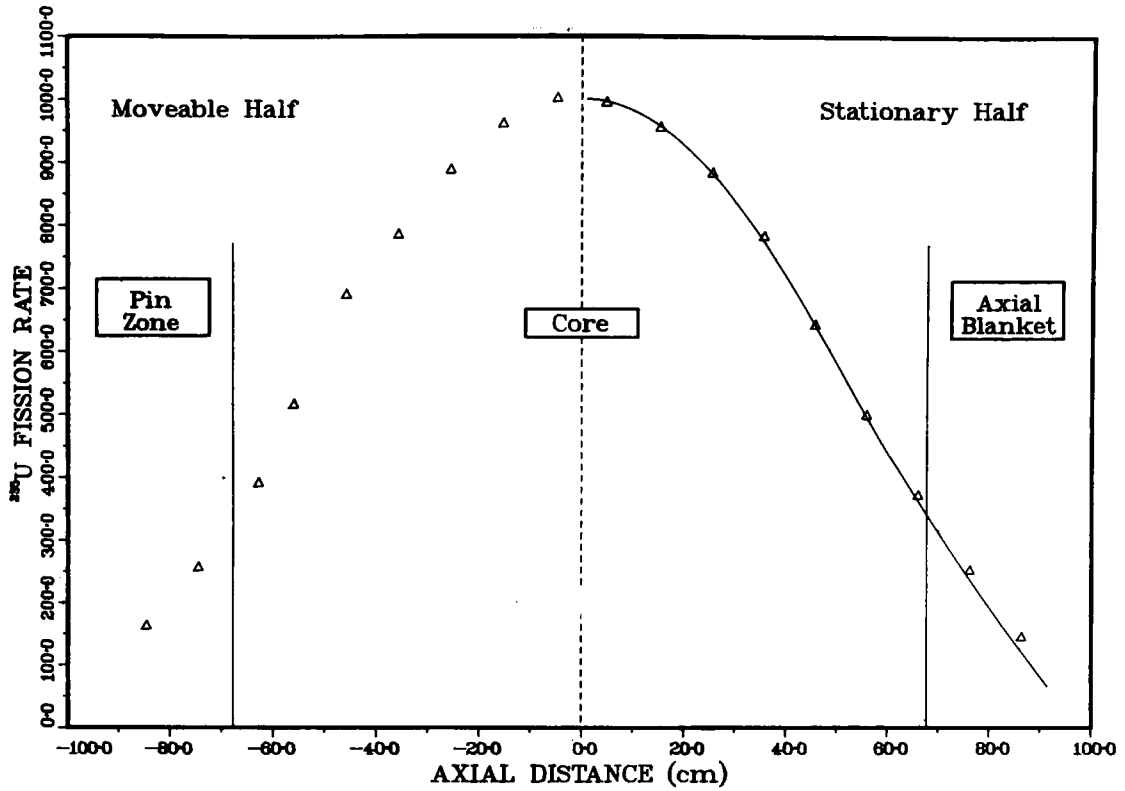


Figure VII-11.  $^{235}\text{U}$  Axial Fission Rate Distribution, Unreflected Assembly.  
ANL Neg. No. 116-77-71

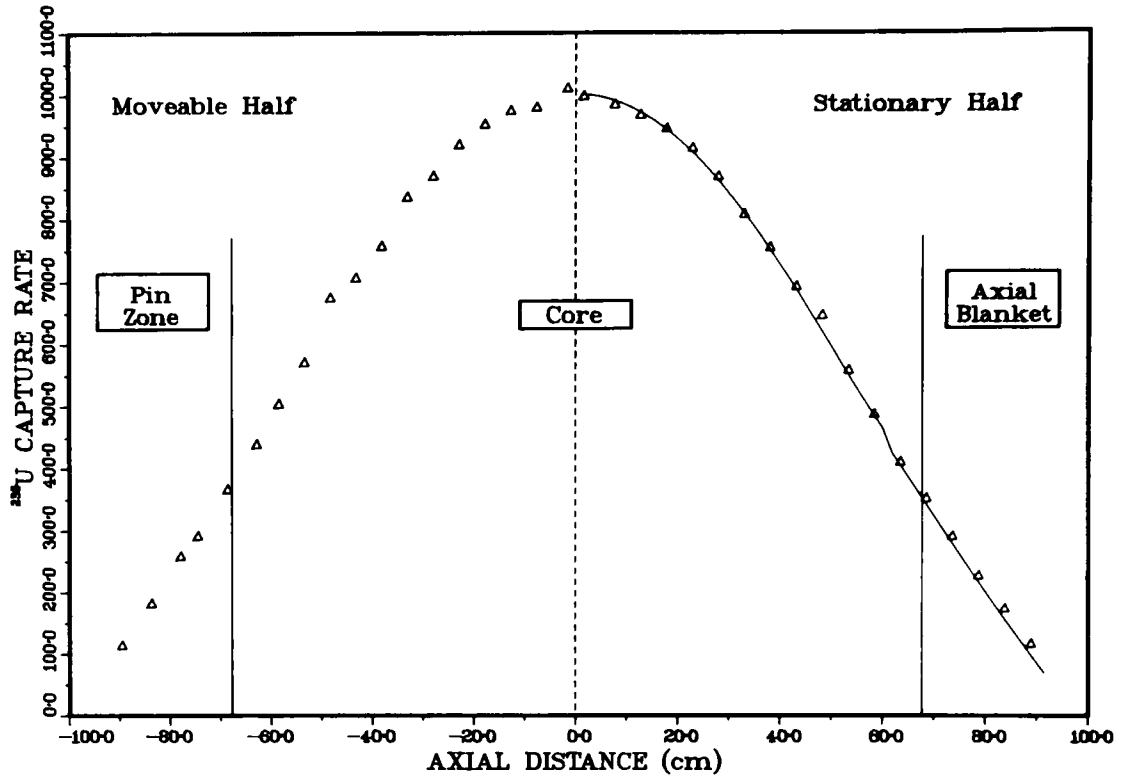


Figure VII-12.  $^{238}\text{U}$  Axial Fission Rate Distribution, Unreflected Assembly.  
ANL Neg. No. 116-77-90



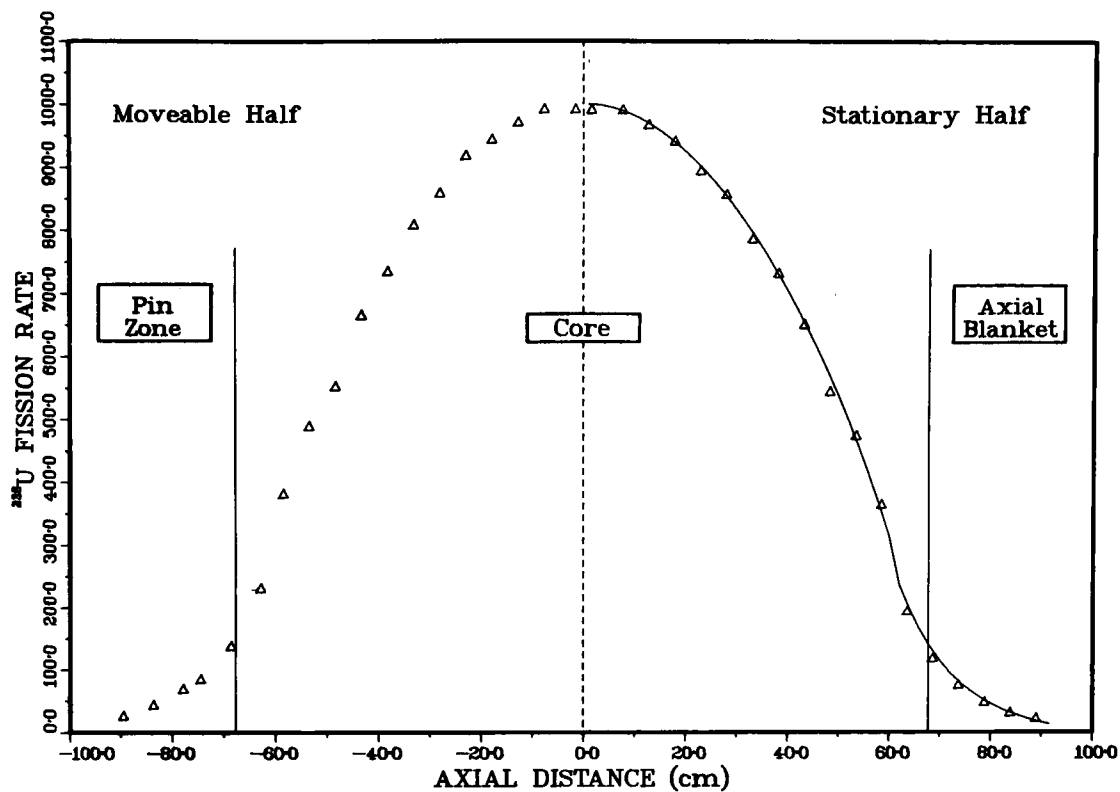


Figure VII-13.  $^{238}\text{U}$  Axial Capture Rate Distribution, Unreflected Assembly.  
ANL Neg. No. 116-77-128

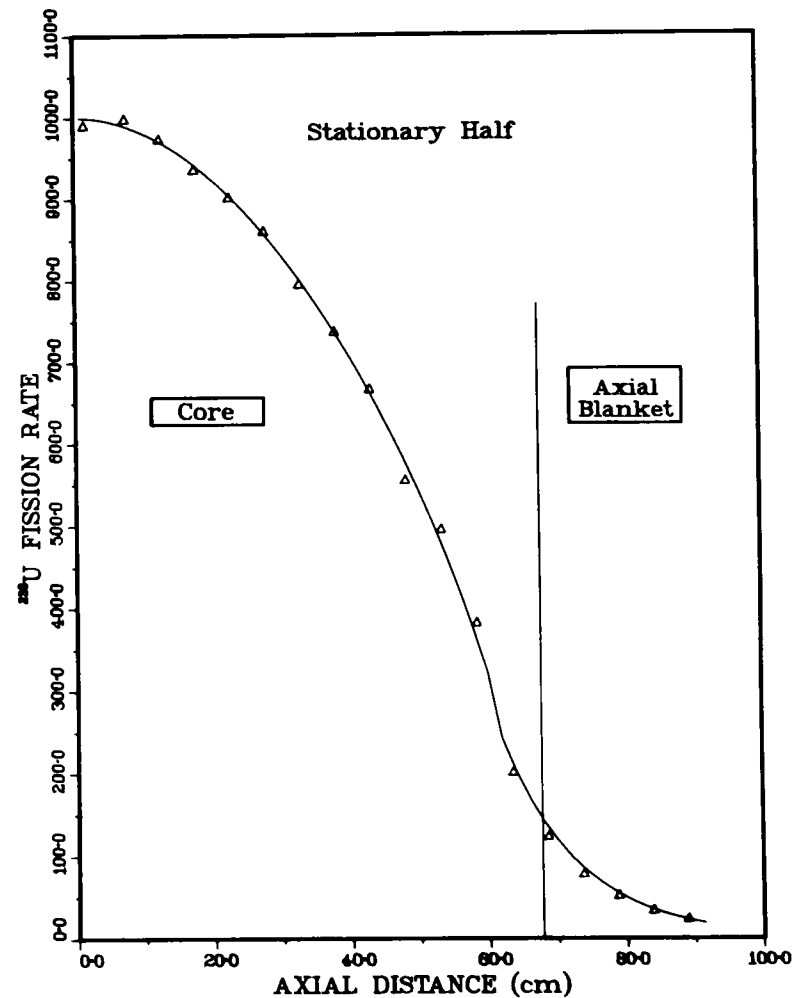
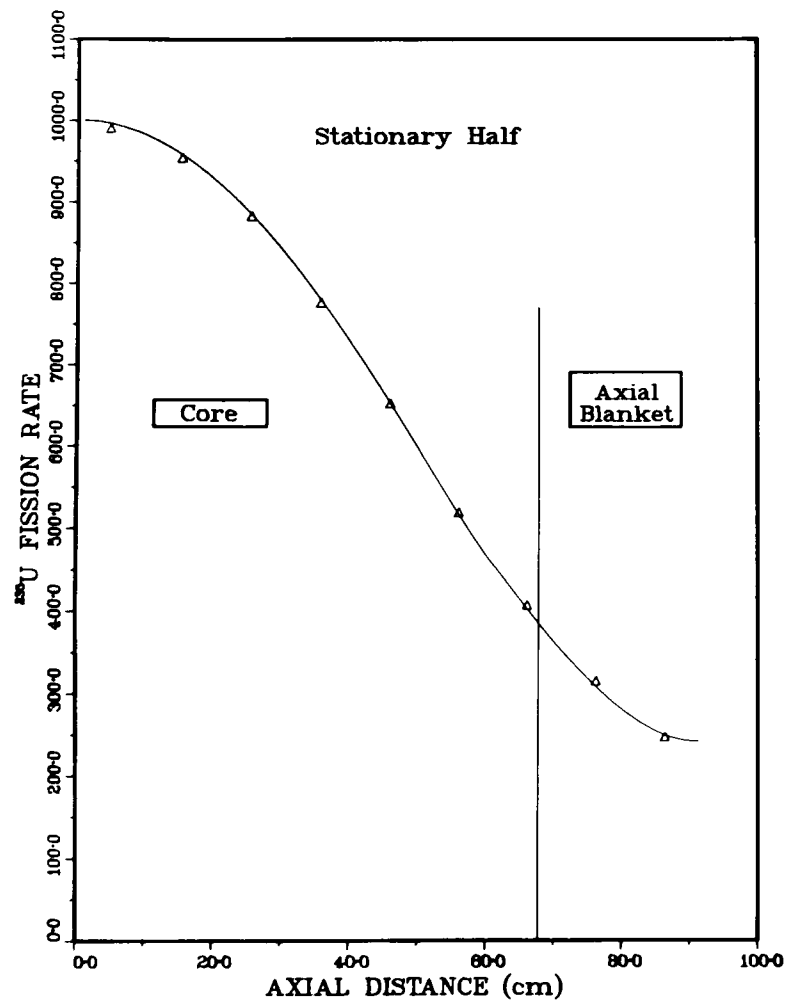


Figure VII-14.  $^{235}\text{U}$  Axial Fission Rate Distribution, Reflected Assembly.  
ANL Neg. No. 116-77-127

Figure VII-15.  $^{238}\text{U}$  Axial Fission Rate Distribution, Reflected Assembly.  
ANL Neg. No. 116-77-142

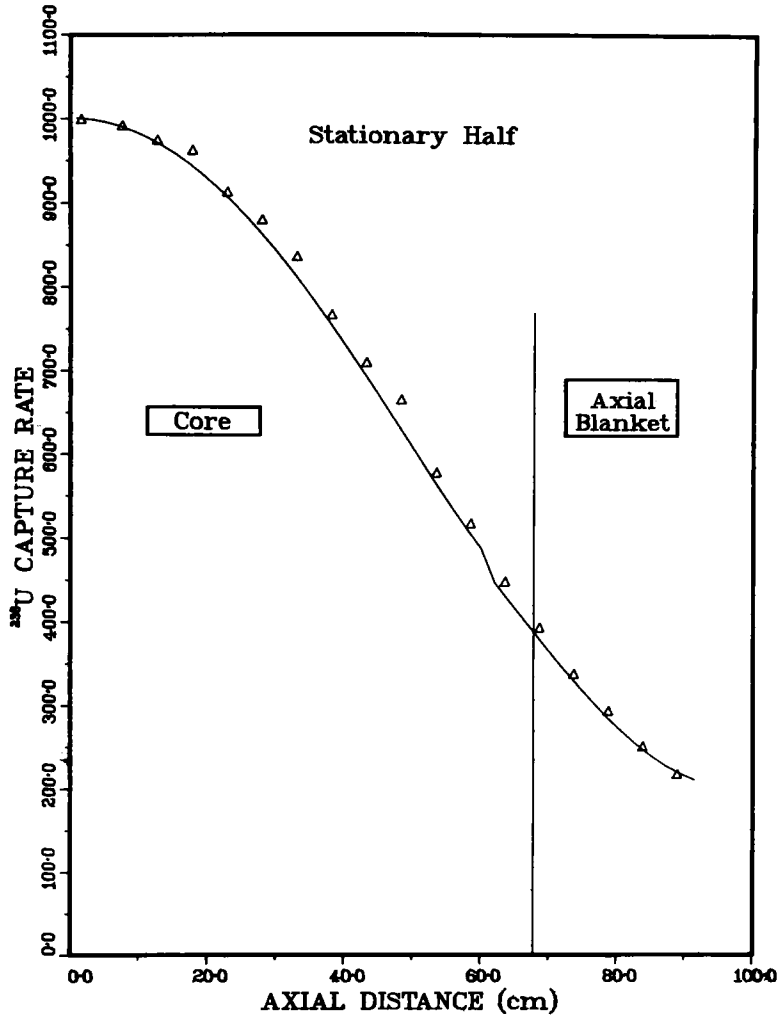


Figure VII-16.  $^{238}\text{U}$  Axial Capture Rate Distribution, Reflected Assembly.  
ANL Neg. No. 116-77-143

CONTROL ROD COMPOSITION #3	CONTROL ROD COMPOSITION #2	CONTROL ROD COMPOSITION #1	CONTROL ROD COMPOSITION #0 (REFERENCE)	TYPE 2 CORE COMPOSITION																																			
<table><tr><td>Fe 20.3 (h)</td></tr><tr><td>Pu/DU/Mo (ZPPR)</td></tr><tr><td>Fe 20.3 (h)</td></tr><tr><td>V61D</td></tr><tr><td>B4C (N)</td></tr><tr><td>B4C (E)</td></tr><tr><td>B4C (N)</td></tr></table>	Fe 20.3 (h)	Pu/DU/Mo (ZPPR)	Fe 20.3 (h)	V61D	B4C (N)	B4C (E)	B4C (N)	<table><tr><td>Fe 20.3 (h)</td></tr><tr><td>Pu/DU/Mo (ZPPR)</td></tr><tr><td>Fe 20.3 (h)</td></tr><tr><td>V61D</td></tr><tr><td>B4C (N)</td></tr><tr><td>B4C (N)</td></tr></table>	Fe 20.3 (h)	Pu/DU/Mo (ZPPR)	Fe 20.3 (h)	V61D	B4C (N)	B4C (N)	<table><tr><td>Fe 20.3 (h)</td></tr><tr><td>Pu/DU/Mo (ZPPR)</td></tr><tr><td>Fe 20.3 (h)</td></tr><tr><td>V61D</td></tr><tr><td>V61D</td></tr><tr><td>B4C (N)</td></tr></table>	Fe 20.3 (h)	Pu/DU/Mo (ZPPR)	Fe 20.3 (h)	V61D	V61D	B4C (N)	<table><tr><td>Fe 20.3 (h)</td></tr><tr><td>Pu/DU/Mo (ZPPR)</td></tr><tr><td>Fe 20.3 (h)</td></tr><tr><td>V61D</td></tr><tr><td>V61D</td></tr><tr><td>V61D</td></tr><tr><td>V61D</td></tr></table>	Fe 20.3 (h)	Pu/DU/Mo (ZPPR)	Fe 20.3 (h)	V61D	V61D	V61D	V61D	<table><tr><td>Fe 20.3 (h)</td></tr><tr><td>Pu/DU/Mo (ZPPR)</td></tr><tr><td>Fe 20.3 (h)</td></tr><tr><td>V61D</td></tr><tr><td>U308</td></tr><tr><td>V61D</td></tr><tr><td>Fe 20.3 (h)</td></tr><tr><td>Pu/DU/Mo (ZPPR)</td></tr><tr><td>Fe 20.3 (h)</td></tr></table>	Fe 20.3 (h)	Pu/DU/Mo (ZPPR)	Fe 20.3 (h)	V61D	U308	V61D	Fe 20.3 (h)	Pu/DU/Mo (ZPPR)	Fe 20.3 (h)
Fe 20.3 (h)																																							
Pu/DU/Mo (ZPPR)																																							
Fe 20.3 (h)																																							
V61D																																							
B4C (N)																																							
B4C (E)																																							
B4C (N)																																							
Fe 20.3 (h)																																							
Pu/DU/Mo (ZPPR)																																							
Fe 20.3 (h)																																							
V61D																																							
B4C (N)																																							
B4C (N)																																							
Fe 20.3 (h)																																							
Pu/DU/Mo (ZPPR)																																							
Fe 20.3 (h)																																							
V61D																																							
V61D																																							
B4C (N)																																							
Fe 20.3 (h)																																							
Pu/DU/Mo (ZPPR)																																							
Fe 20.3 (h)																																							
V61D																																							
V61D																																							
V61D																																							
V61D																																							
Fe 20.3 (h)																																							
Pu/DU/Mo (ZPPR)																																							
Fe 20.3 (h)																																							
V61D																																							
U308																																							
V61D																																							
Fe 20.3 (h)																																							
Pu/DU/Mo (ZPPR)																																							
Fe 20.3 (h)																																							

Figure IX-1. Drawer Loading for the Type-2 Core Composition and the GCFR Control Rod Compositions. ANL Neg. No. 116-77-102

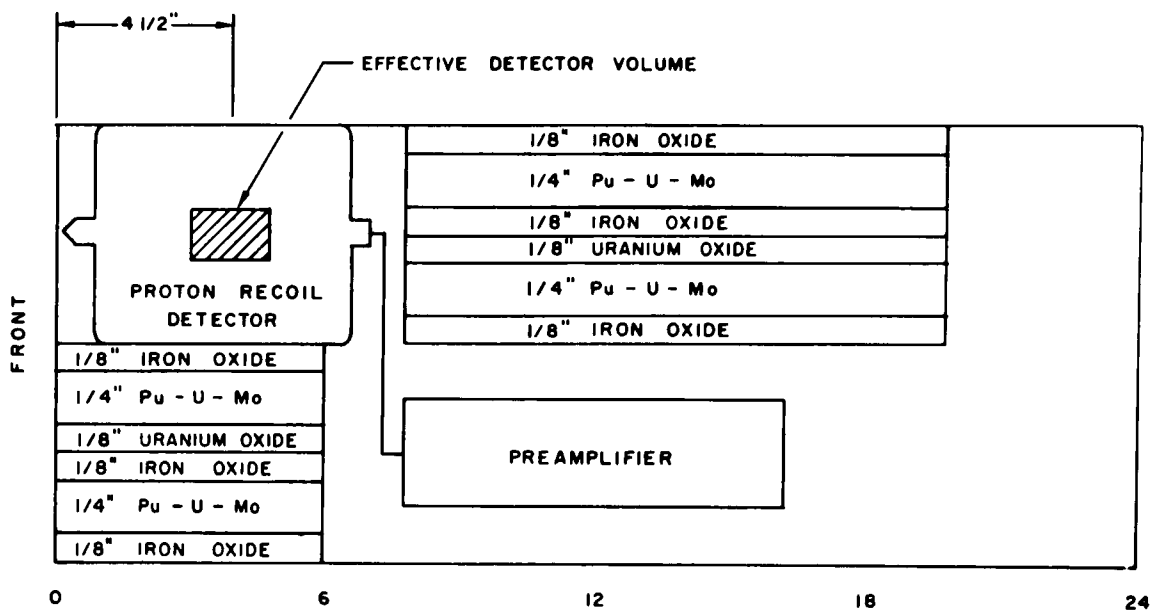


Figure X-1. Spectrum Measurement Central-Drawer Loading.  
ANL Neg. No. 116-77-145

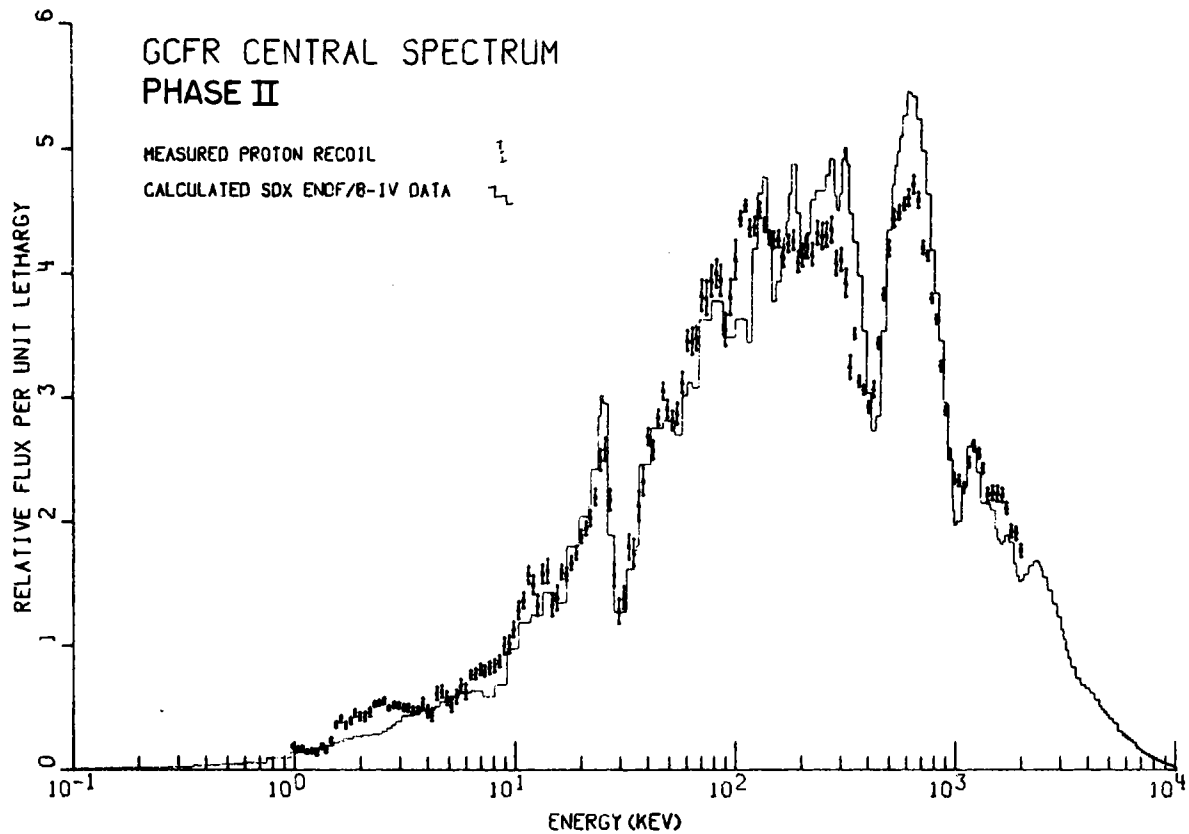


Figure X-2. Measured and Calculated Spectra at the Center of the GCFR Phase-II Core. ANL Neg. No. 116-77-107

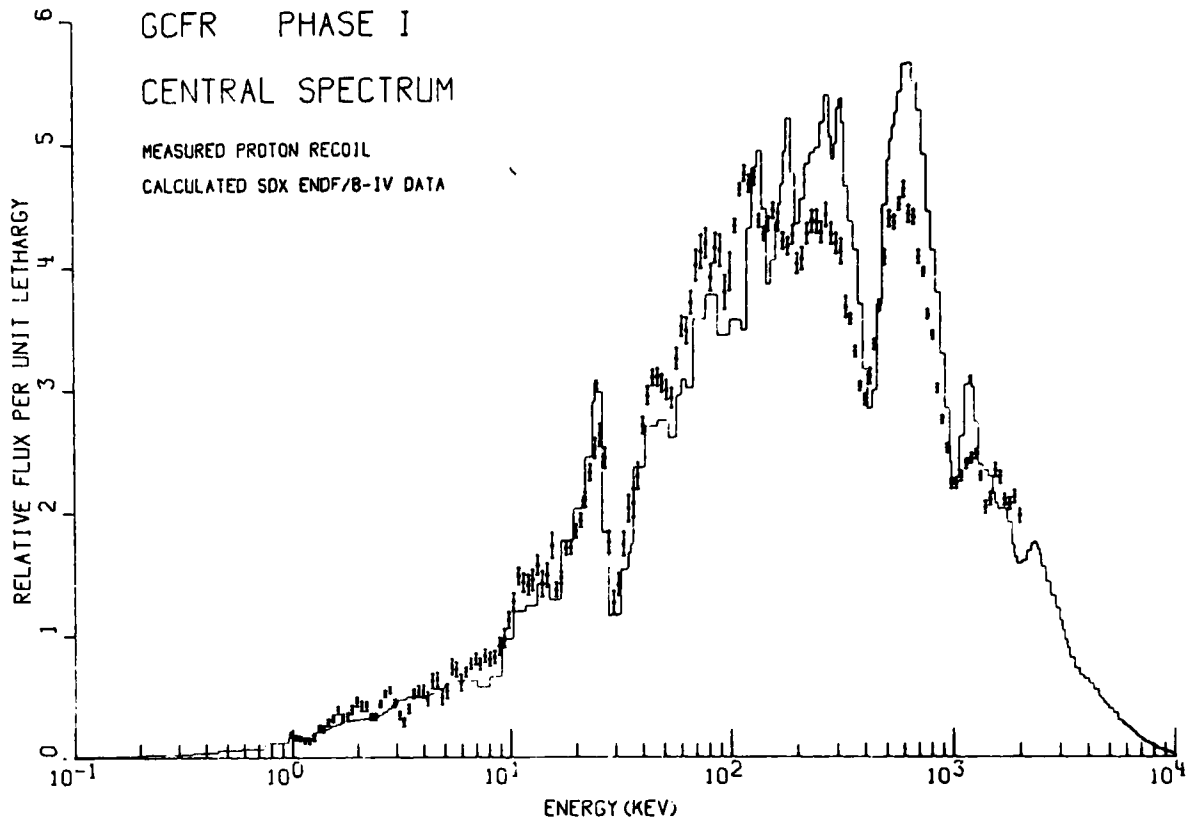


Figure X-3. Measured and Calculated Spectra at the Center of the GCFR Phase-I Core. ANL Neg. No. 116-77-103

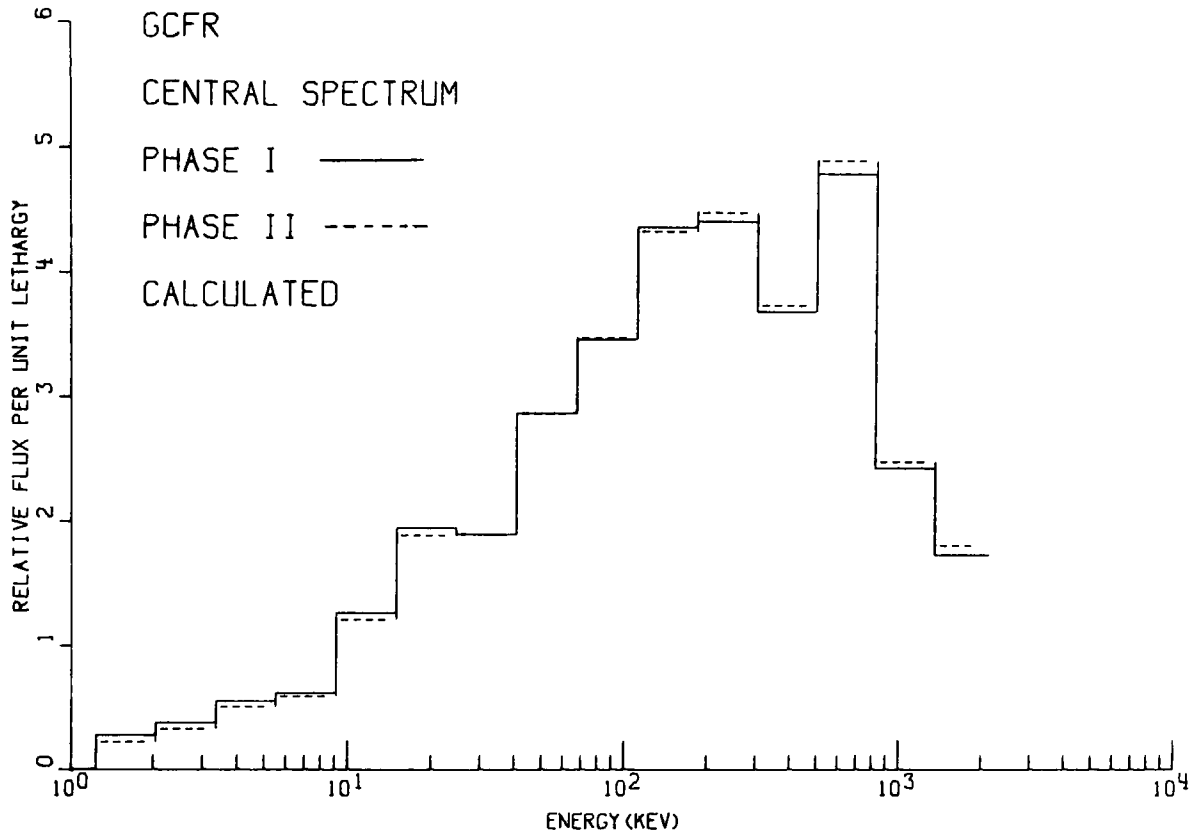


Figure X-4. Broad-Group Calculated Spectra for GCFR Phase-I and -II Cores.  
ANL Neg. No. 116-77-99

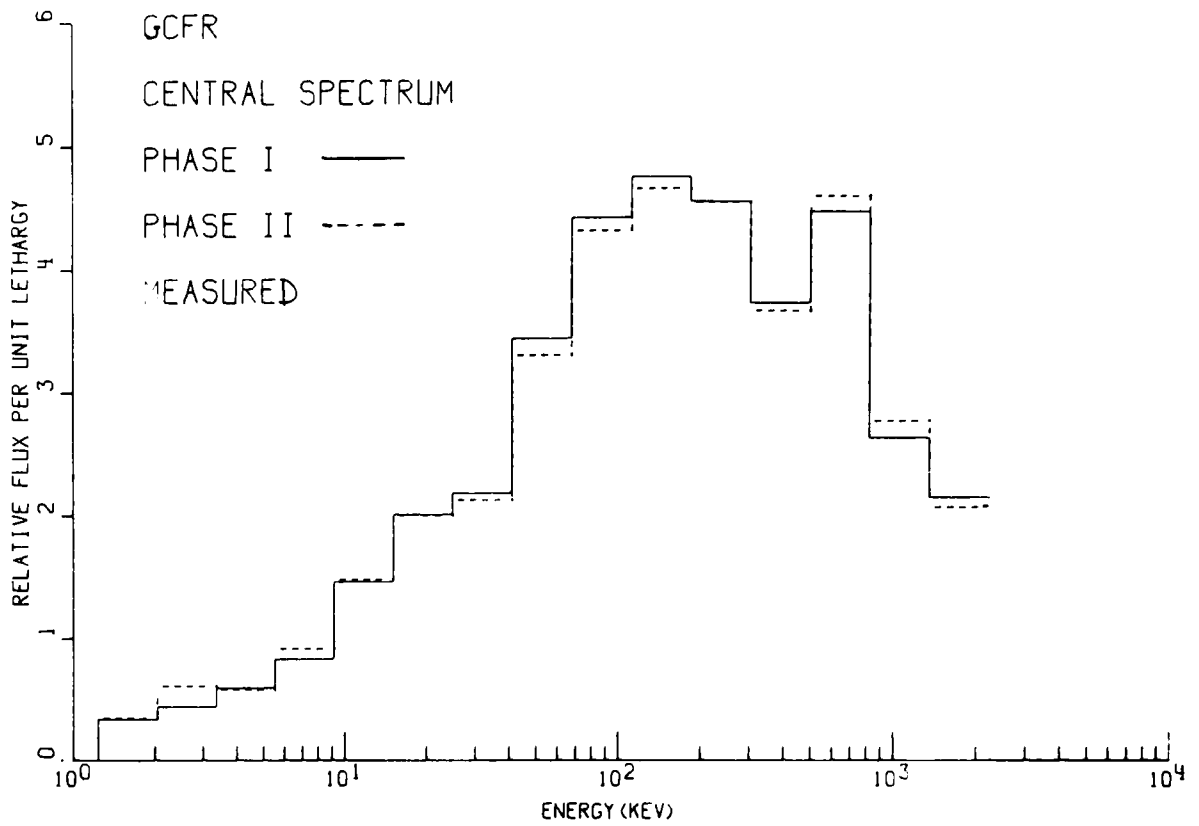


Figure X-5. Broad-Group Measured Spectra for GCFR Phase-I and -II Cores.  
ANL Neg. No. 116-77-95



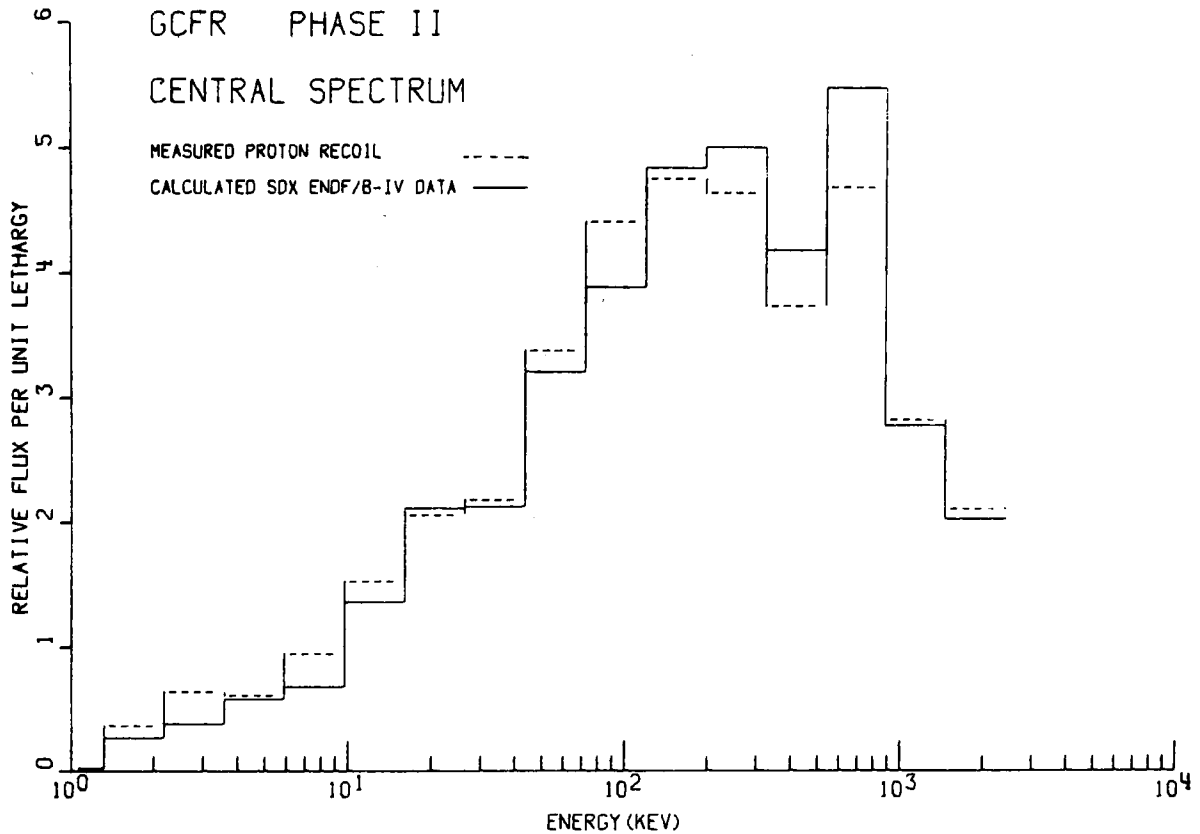


Figure X-6. Broad-Group Measured and Calculated Spectra at the Center of the GCFR Phase-II Core. ANL Neg. No. 116-77-116

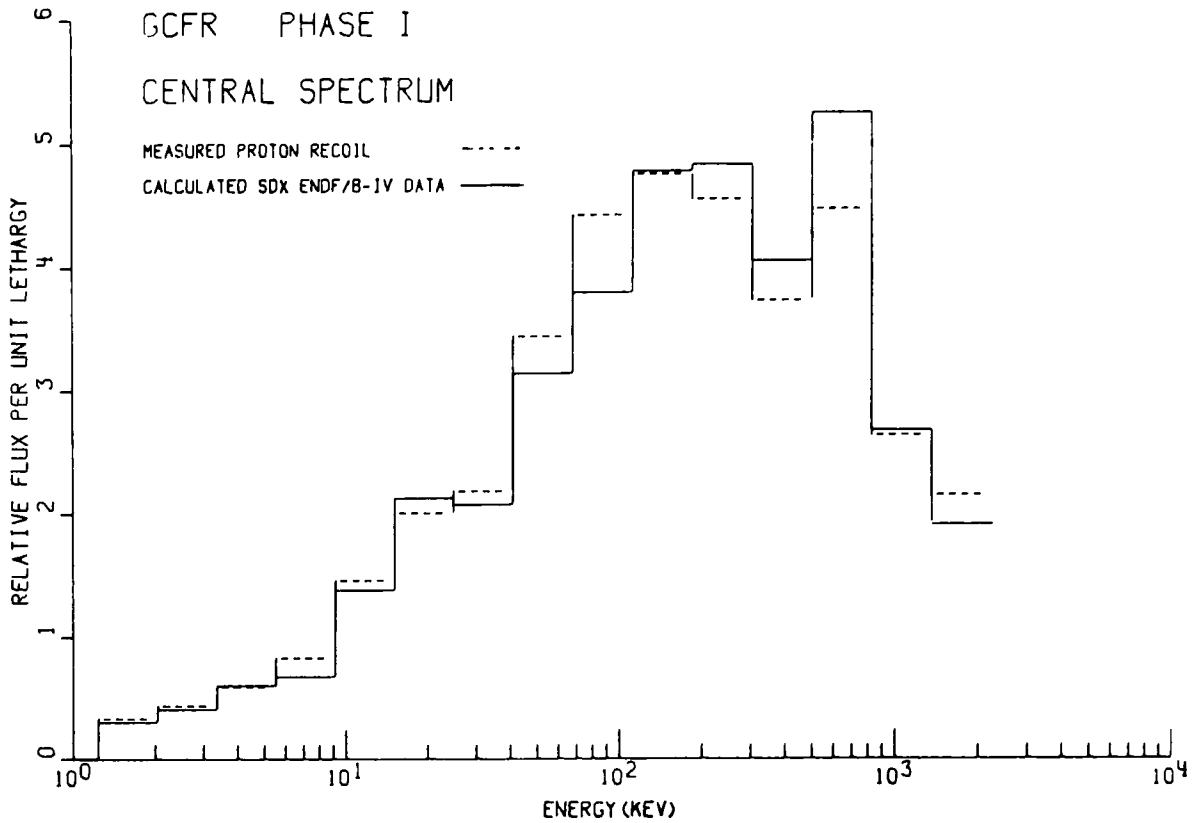


Figure X-7. Broad-Group Measured and Calculated Spectra at the Center of the GCFR Phase-I Core. ANL Neg. No. 116-77-97

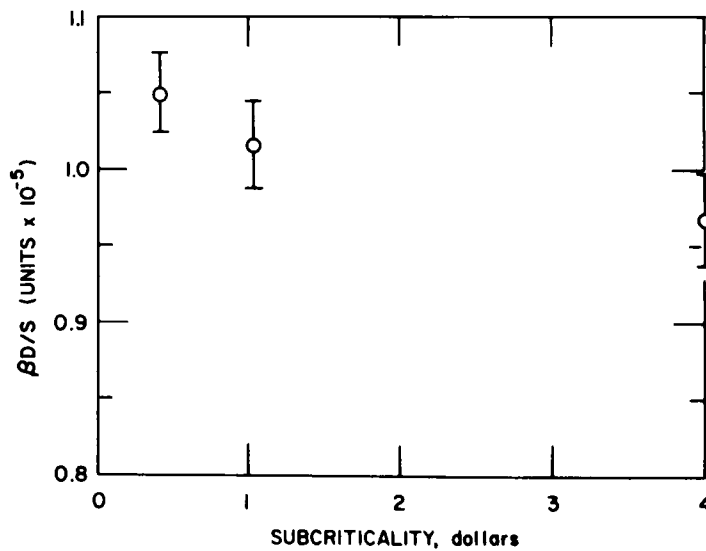


Figure XI-1.  $\beta D/S$  vs Subcriticality.  
ANL Neg. No. 116-77-126

TABLE I-1. Composition Void Volume Fractions

Composition	Void Fraction, v/o
Core and axial blanket	42.3
Type 1	41.9
Type 2	32.7
Type 3	52.3
Axial reflector	8.06
Radial blanket	37.3
Radial reflector	3.90

TABLE I-2. Composition Average Atom Densities,<sup>a</sup> 10<sup>21</sup> atoms/cm<sup>3</sup>

Composition	Fe	Ni	Cr	Mn	Mo	C	Si	Cu	S	P	Co
<b>Core:</b>											
Type 1	13.9313	1.3171	2.8592	0.2232	0.2355	0.0300	0.1784	0.0195	0.0019	0.0052	0.0090
Type 2	18.0097	1.3367	2.9038	0.2296	0.4651	0.0306	0.1788	0.0193	0.0020	0.0052	0.0093
Type 3	14.0220	1.3305	2.8853	0.2252	0.2355	0.0302	0.1800	0.0197	0.0019	0.0052	0.0091
Unit Cell	15.3210	1.3281	2.8828	0.2260	0.3121	0.0303	0.1791	0.0195	0.0019	0.0052	0.0092
<b>Axial Blanket:</b>											
Type 1	9.0453	1.1784	2.5822	0.1996	0.0097	0.0282	0.1635	0.0185	0.0016	0.0048	0.0084
Type 2	8.2253	1.0575	2.3460	0.1820	0.0097	0.0269	0.1487	0.0173	0.0014	0.0045	0.0081
Type 3	9.1362	1.1919	2.6083	0.2015	0.0097	0.0284	0.1651	0.0187	0.0016	0.0048	0.0085
Unit Cell	8.8023	1.1426	2.5122	0.1944	0.0097	0.0278	0.1591	0.0182	0.0016	0.0047	0.0083
<b>Axial Reflector:</b>											
Radial Blanket:	52.8807	6.6746	15.0985	1.4434	0.0055	0.2370	1.0056	0.0146	0.0371	0.0454	0.0073
Radial Reflector:	8.7909	1.1371	2.5087	0.1944	0.0099	0.0281	0.1591	0.0179	0.0016	0.0047	0.0082
Matrix Tube:	55.5448	6.7956	15.7448	1.3279	0.0730	0.2164	0.9052	0.0548	0.0377	0.0405	0.0473
Composition	Al	O	<sup>235</sup> U	<sup>238</sup> U	<sup>238</sup> Pu	<sup>239</sup> Pu	<sup>240</sup> Pu	<sup>241</sup> Pu <sup>b</sup>	<sup>242</sup> Pu	<sup>241</sup> Am <sup>b</sup>	
<b>Core:</b>											
Type 1	0.0061	14.4846	0.0126	5.8106	0.0006	0.8842	0.1171	0.0130	0.0019	0.0051	
Type 2	0.0073	15.7637	0.0147	6.6559	0.0008	1.7812	0.2364	0.0228	0.0032	0.0177	
Type 3	0.0062	10.0817	0.0091	4.1606	0.0006	0.8842	0.1171	0.0130	0.0019	0.0051	
Unit Cell	0.0065	13.4423	0.0122	5.5421	0.0007	1.1832	0.1569	0.0163	0.0023	0.0093	
<b>Axial Blanket:</b>											
Type 1	0.0037	15.3421	0.0175	8.1759	---	---	---	---	---	---	
Type 2	0.0025	17.4673	0.0244	11.3987	---	---	---	---	---	---	
Type 3	0.0038	10.9365	0.0140	6.5249	---	---	---	---	---	---	
Unit Cell	0.0033	14.5819	0.0186	8.6998	---	---	---	---	---	---	
<b>Radial Blanket:</b>											
	0.0031	17.7994	0.0194	9.0911	---	---	---	---	---	---	

<sup>a</sup> Estimated uncertainty of ±10% for densities < 0.1 × 10<sup>21</sup> atoms/cm<sup>3</sup> and ±1% for densities ≥ 0.1 × 10<sup>21</sup> atoms/cm<sup>3</sup>.<sup>b</sup> Decay of <sup>241</sup>Pu → <sup>241</sup>Am adjusted to June 30, 1975.

TABLE I-3. Reference Configuration Dimensions

Region	Unreflected Configuration		Reflected Configuration	
	Number of Tubes	Radius, <sup>a</sup> cm	Number of Tubes	Radius, <sup>a</sup> cm
Core <sup>b</sup>	349	58.23	333	56.88
Type 1	115		111	
Type 2	119		111	
Type 3	115		111	
Blanket	356	82.76	372	82.76
Reflector	-	-	248	96.22

<sup>a</sup>The cumulative sum of the area of the (2.175 in.) square matrix tubes translated into an equivalent radius.

<sup>b</sup><sup>239</sup>+<sup>241</sup>Pu mass: 1.327008 kg, Types 1 and 3; 2.668338 kg, Type 2. (The number of significant figures are for fuel (type) inventory purposes only and do not represent or imply knowledge of the accuracy of the fissile material mass. The fissile material mass has an estimated uncertainty of ±1%.)

TABLE I-4. Summary of Operational Measurements and Parameters

	Unreflected Configuration	Reflected Configuration
1. Core/radial blanket interface exchange worth, <sup>a</sup> $\text{Ih/kg } ^{239+241}\text{Pu}$	$31.24 \pm 0.16$	$33.36 \pm 0.22$
2. Reactivity, $\text{Ih}$ measured calculated	$+112.6 \pm 0.7$ $-323.7$	$+66.4 \pm 0.8$ $-55.2$
3. RZ model calculated effective multiplication, <sup>b</sup> $k_{\text{eff}}$	0.996690	0.999432 <sup>c</sup>
4. Inhours per percent reactivity	974.779	971.972
5. Critical mass, $\text{kg } ^{239+241}\text{Pu}$ as-built, adjusted <sup>d</sup>	$622.74 \pm 6.23$ $619.14 \pm 6.23$	$590.78 \pm 5.91$ $588.79 \pm 5.91$
6. Temperature coefficient, $\text{Ih}/^\circ\text{C}$	$-2.19 \pm 0.03$	-
7. Configuration reproducibility uncertainty, $\text{Ih}$	$\pm 0.57$	-
8. Control rod position uncertainty, $\text{Ih}$	$\pm 0.25$	-
9. $^{241}\text{Pu}$ reactivity decay coefficient, $\text{Ih/day}$	$-0.02 \pm 0.01^e$	-
10. Table gap worth, $\text{Ih/mil}$	1.25	-
11. $^{10}\text{B}$ blade and fuel rod worths	see Table I-5	
12. Central tube/void exchange worth, $\text{Ih/kg } ^{239+241}\text{Pu}$	$152.72 \pm 1.07$	-
13. Kinetics parameters	see Table I-6	see Table I-6
14. Beta effective, $\beta_{\text{eff}}$	$3.30039^{-3}$	$3.30648^{-3}$
15. Prompt neutron lifetime, $\lambda$ (sec)	$3.20634^{-7}$	$3.45497^{-7}$
16. Inhours per dollar reactivity	321.715	321.381
17. Normalized perturbation denominator	$1.93451^{+5}$	$1.94842^{+5}$

<sup>a</sup> Average of Types 1, 2 and 3 core composition (including axial blanket and reflector) vs radial blanket composition.

<sup>b</sup> Convergence criteria  $\Delta k < 10^{-6}$ .

<sup>c</sup> Eigenvalue for the same configuration but without the reflector is 0.987916.

<sup>d</sup> As-built critical mass adjusted to  $k_{\text{eff}} = 1.0$  using the core/radial blanket interface worth to remove the measured excess reactivity.

<sup>e</sup> Based upon limited data. Because of the uncertainty, the experimental  $^{241}\text{Pu}$  reactivity decay coefficient is assumed to be zero for GCFR-II.

<sup>f</sup>  $\int \frac{SS^* dV}{(SS^*)_{\text{center}}}$  where  $S = \sum_{\text{groups}} v \Sigma_f \phi$  and  $S^* = \sum_{\text{groups}} \chi \phi^*$ .

TABLE I-5. Location and Worth of ZPR-9 Fuel and  $^{10}\text{B}$  Rods

Rod Type and Number	Stationary or Movable Half	Matrix Location		Radius, cm	Measured Worth, 1h
		Row	Column		
Fuel Rods: <sup>a</sup>					
1	M	19	26	27.6	135.8
2	M	22	29	33.6	119.3
3	M	28	26	32.2	122.3
4	M	24	17	33.6	118.0
5	M	18	20	32.2	121.9
6	S	16	29	50.9	69.3
7	S	22	29	33.6	118.6
8	S	27	26	27.6	137.5
9	S	24	17	33.6	117.7
10 <sup>a</sup>	S	17	20	37.1	109.9
10 <sup>b</sup>	S	15	20	47.2	78.8
<sup>10</sup> B Rods: <sup>c</sup>					
1	M	30	23	38.7	166.8
2	M	19	30	42.8	132.4
3	M	27	30	42.8	132.1
5	M	27	16	42.8	132.4
6	M	19	16	42.8	132.7
7	S	30	23	38.7	166.1
8	S	19	30	42.8	134.6
9	S	27	30	42.8	132.8
11	S	27	16	42.8	132.4
12	S	19	16	42.8	130.5

<sup>a</sup> The calculated worth of Types 1 and 3, and Type 2 core drawers are taken respectively to be 3/4 and 3/2 times the average worth of core composition in the same matrix location. All fuel rod locations listed here are Type 2 core drawers which contain two fuel columns.

<sup>b</sup> Moved to this new location in loading 46.

<sup>c</sup> The measured worths are ~65% of the calculated worths.

TABLE I-6. Delayed Neutron Fractions and Effective Decay Constants for the Reference Configurations

Unreflected Configuration								
Isotope (i)	Family (j)						Total <sup>a</sup>	Effective Decay Constant, <sup>c</sup> sec <sup>-1</sup>
	1	2	3	4	5	6		
<sup>235</sup> U	1.73653 <sup>-6</sup>	1.05563 <sup>-5</sup>	8.73228 <sup>-6</sup>	1.90349 <sup>-5</sup>	5.98640 <sup>-6</sup>	1.21599 <sup>-6</sup>	4.72623 <sup>-5</sup>	7.74564 <sup>-2</sup>
<sup>238</sup> U	2.06914 <sup>-5</sup>	2.34926 <sup>-4</sup>	2.61068 <sup>-4</sup>	6.28487 <sup>-4</sup>	3.62485 <sup>-4</sup>	1.20828 <sup>-4</sup>	1.62849 <sup>-3</sup>	1.27286 <sup>-1</sup>
<sup>238</sup> Pu+ <sup>239</sup> Pu	5.50671 <sup>-5</sup>	4.32813 <sup>-4</sup>	3.14075 <sup>-4</sup>	4.81034 <sup>-4</sup>	1.51056 <sup>-4</sup>	5.13299 <sup>-5</sup>	1.48538 <sup>-3</sup>	6.71684 <sup>-2</sup>
<sup>240</sup> Pu	2.01406 <sup>-6</sup>	2.09363 <sup>-5</sup>	1.38573 <sup>-5</sup>	2.54762 <sup>-5</sup>	9.31702 <sup>-6</sup>	2.11089 <sup>-6</sup>	7.37118 <sup>-5</sup>	7.29205 <sup>-2</sup>
<sup>241</sup> Pu+ <sup>242</sup> Pu	6.40836 <sup>-7</sup>	1.56563 <sup>-5</sup>	1.11241 <sup>-5</sup>	2.52941 <sup>-5</sup>	1.18039 <sup>-5</sup>	1.03770 <sup>-6</sup>	6.55569 <sup>-5</sup>	8.82462 <sup>-2</sup>
Total <sup>b</sup>	8.01500 <sup>-5</sup>	7.14888 <sup>-4</sup>	6.08856 <sup>-4</sup>	1.17933 <sup>-3</sup>	5.40649 <sup>-4</sup>	1.76523 <sup>-4</sup>	3.30039 <sup>-3e</sup>	---
Effective Decay Constant, <sup>d</sup> sec <sup>-1</sup>	1.29798 <sup>-2</sup>	3.14158 <sup>-2</sup>	1.35613 <sup>-1</sup>	3.45932 <sup>-1</sup>	1.36726 <sup>+0</sup>	3.74704 <sup>+0</sup>	---	8.85488 <sup>-2f</sup>
Reflected Configuration								
Isotope (i)	Family (j)						Total <sup>a</sup>	Effective Decay Constant, <sup>c</sup> sec <sup>-1</sup>
	1	2	3	4	5	6		
<sup>235</sup> U	1.89828 <sup>-6</sup>	1.17282 <sup>-5</sup>	9.57837 <sup>-6</sup>	2.09030 <sup>-5</sup>	6.57392 <sup>-6</sup>	1.33533 <sup>-6</sup>	5.20171 <sup>-5</sup>	7.72260 <sup>-2</sup>
<sup>238</sup> U	2.07013 <sup>-5</sup>	2.36505 <sup>-4</sup>	2.61515 <sup>-4</sup>	6.29625 <sup>-4</sup>	3.63018 <sup>-4</sup>	1.21006 <sup>-4</sup>	1.63237 <sup>-3</sup>	1.27027 <sup>-1</sup>
<sup>238</sup> Pu+ <sup>239</sup> Pu	5.49248 <sup>-5</sup>	4.33252 <sup>-4</sup>	3.13293 <sup>-4</sup>	4.79991 <sup>-4</sup>	1.50729 <sup>-4</sup>	5.12186 <sup>-5</sup>	1.48341 <sup>-3</sup>	6.70982 <sup>-2</sup>
<sup>240</sup> Pu	1.98882 <sup>-6</sup>	2.07430 <sup>-5</sup>	1.36849 <sup>-5</sup>	2.51664 <sup>-5</sup>	9.20370 <sup>-6</sup>	2.08521 <sup>-6</sup>	7.28720 <sup>-5</sup>	7.28407 <sup>-2</sup>
<sup>241</sup> Pu+ <sup>242</sup> Pu	6.42570 <sup>-7</sup>	1.57570 <sup>-5</sup>	1.11553 <sup>-5</sup>	2.53736 <sup>-5</sup>	1.18410 <sup>-5</sup>	1.04097 <sup>-6</sup>	6.58105 <sup>-5</sup>	8.81124 <sup>-2</sup>
Total <sup>b</sup>	8.01558 <sup>-5</sup>	7.17985 <sup>-4</sup>	6.09227 <sup>-4</sup>	1.18106 <sup>-3</sup>	5.41366 <sup>-4</sup>	1.76686 <sup>-4</sup>	3.30648 <sup>-3e</sup>	-
Effective Decay Constant, <sup>d</sup> sec <sup>-1</sup>	1.29794 <sup>-2</sup>	3.14174 <sup>-2</sup>	1.35585 <sup>-1</sup>	3.45899 <sup>-1</sup>	1.36742 <sup>-0</sup>	3.74774 <sup>-0</sup>	-	8.84570 <sup>-2f</sup>

$$^a \beta_i = \sum_j \beta_{ij}$$

$$^b \beta_j = \sum_i \beta_{ij}$$

$$^c \lambda_i = \beta_i / \sum_j (\beta_{ij} / \lambda_{ij}); \text{ see Table I-7 for decay constants.}$$

$$^d \lambda_j = \beta_j / \sum_i (\beta_{ij} / \lambda_{ij}); \text{ see Table I-7 for decay constants.}$$

$$^e \beta = \sum_i \beta_i = \sum_j \beta_j$$

$$^f \lambda = \beta / \sum_i (\beta_i / \lambda_i) = \beta / \sum_j (\beta_j / \lambda_j)$$

TABLE I-7. Decay Constants ( $\lambda_{ij}$ ),  $\text{sec}^{-1}$ 

Isotope (i)	Family (j)					
	1	2	3	4	5	6
$^{235}\text{U}$	0.01272	0.03174	0.116	0.311	1.40	3.87
$^{238}\text{U}$	0.01323	0.03212	0.139	0.359	1.41	4.03
$^{239}\text{Pu}^a$	0.01290	0.03110	0.134	0.332	1.26	3.21
$^{240}\text{Pu}$	0.01294	0.03131	0.135	0.333	1.36	4.03
$^{241}\text{Pu}^b$	0.01280	0.02990	0.124	0.352	1.61	3.47

<sup>a</sup> $^{239}\text{Pu}$  data used for  $^{238}\text{Pu}$ .<sup>b</sup> $^{241}\text{Pu}$  data used for  $^{242}\text{Pu}$ .

TABLE I-8. Reactivity Worths of Steps Toward the Establishment of the Axial and Radial Stainless Steel Reflector

Loading No.	Measurement	Reactivity, <sup>a</sup> Ih	Worth of Fuel, <sup>b</sup> at Core Edge, Ih/kg	Worth of Stainless Steel Reflector, <sup>b</sup> Ih
54	Reference, Unreflected Assembly (Fig. I-9)	112.6 $\pm$ 0.2	-	-
55	Removal of 6.65 kg fuel at core edge <sup>c</sup>	-68.9 $\pm$ 0.2	27.30 $\pm$ 0.13	-
56	Addition of SST radial and axial reflector to one octant of assembly	16.8 $\pm$ 0.2	-	85.7 $\pm$ 0.9
65	Addition of SST radial and axial reflector to remaining seven octants of assembly and removal of 26.64 kg fuel at core edge	22.0 $\pm$ 0.2	-	-
66	Addition of 1.33 kg fuel at core edge- Reference, Reflected Assembly (Fig. I-10)	66.4 $\pm$ 0.5	33.46 $\pm$ 0.75	-
72	Removal of 42.58 kg fuel at core edge <sup>d</sup>	-1354.0 $\pm$ 9.4	33.36 $\pm$ 0.22	-

<sup>a</sup>Temperature coefficient of  $-2.19 \pm 0.03$  Ih/ $^{\circ}\text{C}$  used to correct reactivity data to 25 $^{\circ}\text{C}$ .<sup>b</sup>Decay of  $^{241}\text{Pu}$  assumed to be negligible in correcting measurements to reference loading. Configuration reproducibility uncertainty of 0.57 Ih and control rod position uncertainty of 0.25 Ih (critical configurations) added in quadrature to measurement uncertainties.<sup>c</sup>Nonsymmetric fuel unloading.<sup>d</sup>Type-1, -2 and -3 core drawers evenly distributed.



TABLE II-1. Energy Structure of the 29-Group Cross-Section Set

Group No.	Upper Energy, eV	Lethargy
1	$1.4191 \times 10^7$	0.00
2	$1.0000 \times 10^7$	0.35
3	$6.0653 \times 10^6$	0.85
4	$3.6788 \times 10^6$	1.35
5	$2.2313 \times 10^6$	1.85
6	$1.3534 \times 10^6$	2.35
7	$8.2085 \times 10^5$	2.85
8	$4.9787 \times 10^5$	3.35
9	$3.0197 \times 10^5$	3.85
10	$1.8316 \times 10^5$	4.35
11	$1.1109 \times 10^5$	4.85
12	$6.7379 \times 10^4$	5.35
13	$4.0868 \times 10^4$	5.85
14	$2.4788 \times 10^4$	6.35
15	$1.5034 \times 10^4$	6.85
16	$9.1188 \times 10^3$	7.35
17	$5.5308 \times 10^3$	7.85
18	$3.3546 \times 10^3$	8.35
19	$2.0347 \times 10^3$	8.85
20	$1.2341 \times 10^3$	9.35
21	$7.4852 \times 10^2$	9.85
22	$4.5400 \times 10^2$	10.35
23	$2.7536 \times 10^2$	10.85
24	$1.0130 \times 10^2$	11.85
25	$3.7267 \times 10^1$	12.85
26	$1.3740 \times 10^1$	13.85
27	$5.0435 \times 10^0$	14.85
28	$1.8554 \times 10^0$	15.85
29	$4.1399 \times 10^{-1}$	17.35

TABLE II-2. Cross-Sections Generated

Composition	Core			Radial Blanket		Axial Blanket	
Spectrum Region	A	B	C	D	E	F	G
Cross-Section Type <sup>a</sup>	SDPT	SDPT	SDPT	SDPT	SDPT	SDPT	SDPT
Cell Type:							
Unit cell	SDPT	SD-T	SD-T	SD-T	SDPT	SD-T	SDPT
Type 1	S---	----	----			----	S---
Type 2	S---	----	----			----	S---
Type 3	S---	----	----			----	S---

<sup>a</sup>S-Shielded cross-sections include both energy and spatial self-shielding for the composition isotopes in the cell type. These are the homogeneous cross-sections which are equivalent to the heterogeneous plate cross-sections (P) in that the cell average reaction rates are preserved.

D-Detector cross-sections include only energy self-shielding for the composition isotopes in the cell type. The cell type is treated as a homogeneous mixture of the composition isotopes.

P-Plate cross-sections for the heterogeneous cell type composition. These cross-sections are used to generate the shielded cross-sections (S).

T-Trace cross-sections for isotopes which are not included or are not part of the cell type composition. These isotopes are included at infinitely dilute concentrations in the homogeneous mixture of the cell type when generating the detector cross-sections (D).

TABLE II-3. Benoist Anisotropic Diffusion-Coefficient Multipliers

Group	Core Region		Radial Blanket		Axial Blanket	
	$M_{  }$	$M_{\perp}$	$M_{  }$	$M_{\perp}$	$M_{  }$	$M_{\perp}$
1	1.0445	1.0014	1.0262	1.0008	1.0280	1.0007
2	1.0465	1.0017	1.0262	1.0009	1.0281	1.0008
3	1.0531	1.0021	1.0294	1.0011	1.0312	1.0010
4	1.0562	1.0025	1.0300	1.0012	1.0318	1.0011
5	1.0659	1.0029	1.0415	1.0017	1.0076	1.0010
6	1.0880	1.0035	1.0756	1.0035	1.0728	1.0031
7	1.0810	1.0036	1.0608	1.0027	1.0612	1.0026
8	1.1260	1.0067	1.1144	1.0075	1.1095	1.0065
9	1.1174	1.0071	1.0929	1.0061	1.0932	1.0057
10	1.1265	1.0082	1.1009	1.0070	1.1022	1.0066
11	1.1354	1.0110	1.0955	1.0078	1.0995	1.0074
12	1.1440	1.0130	1.0975	1.0085	1.1021	1.0082
13	1.1535	1.0174	1.0811	1.0095	1.0881	1.0089
14	1.1411	1.0110	1.1079	1.0092	1.1136	1.0088
15	1.1430	1.0157	1.0892	1.0096	1.0958	1.0092
16	1.1758	1.0338	1.0892	1.0198	1.0911	1.0160
17	1.1561	1.0253	1.0850	1.0150	1.0899	1.0130
18	1.1638	1.0270	1.0846	1.0148	1.0892	1.0128
19	1.1757	1.0259	1.0853	1.0116	1.0918	1.0107
20	1.1854	1.0293	1.0848	1.0122	1.0911	1.0112
21	1.1914	1.0311	1.0803	1.0177	1.0859	1.0106
22	1.1894	1.0385	1.0883	1.0206	1.0881	1.0164
23	1.2253	1.0418	1.0852	1.0134	1.0911	1.0120
24	1.2885	1.0614	1.0798	1.0125	1.0848	1.0110
25	1.2686	1.0501	1.1242	1.0197	1.1350	1.0185
26	1.3744	1.0906	1.0864	1.0134	1.0931	1.0121
27	1.2003	1.0351	1.0807	1.0128	1.0860	1.0114
28	1.5473	1.1618	1.0760	1.0125	1.0799	1.0109
29	3.7989	2.4907	1.0842	1.0174	1.0865	1.0143

TABLE II-4. With-Streaming Neutron Balance from RZ Calculations

Quantity	Unreflected Configuration		Reflected Configuration		
	Core	Core + Blankets	Core	Core + Blankets	Core + Blankets + Reflectors
H/2, cm	61.04	92.48	61.04	92.48	107.72
R, cm	58.23	82.76	56.88	82.76	96.22
D/H	0.954	0.895	0.932	0.895	0.893
k no streaming	1.01347	-	1.01481	-	-
k with streaming	0.99669	-	0.99943	-	-
$\Delta k$ streaming	-0.01678	-	-0.01538	-	-
$k_{\infty}$ <sup>a</sup>	1.5939	1.2774	1.5809	1.1620	1.1252
L = Leakage probability <sup>b</sup> , %	37.47	21.98	36.78	13.99	11.18
Axial leakage fraction <sup>c</sup> , %	29.08	23.08	28.97	28.71	28.63
Radial leakage fraction <sup>c</sup> , %	70.92	76.92	71.03	71.29	71.37
$B^2$ geometric, cm <sup>-2</sup>	23.68 <sup>-4</sup>	11.33 <sup>-4</sup>	24.50 <sup>-4</sup>	11.33 <sup>-4</sup>	8.373 <sup>-4</sup>
$B^2/B^2_z$ , %	27.97	25.47	27.03	25.47	25.40
$B^2/B^2_R$ , %	72.03	74.53	72.97	74.53	74.60

<sup>a</sup> $k_{\infty}$  defined as  $(\int_{\text{region}} \text{Fission Production}) / (\int_{\text{region}} \text{Absorption})$ .

<sup>b</sup>L defined such that  $k = k_{\infty}(1 - L)$ .

<sup>c</sup>Axial and radial leakage fractions are computed by the RZ code based on surface integrals of net current.

TABLE III-1. Sample Description

Sample Identification	Major Sample Constituent	State	Geometry	Dimensions, In.			Sample Mass, g	Sample Composition <sup>a</sup>	Capsule Mass, g	Capsule Composition
				O.D.	Length	Wall Thickness				
MB-06	<sup>239</sup> Pu	Solid	Annulus	0.835	1.250	0.005	3.524	C-1	13.218	304 SST <sup>b</sup>
MB-10	"	"	"	"	1.156	0.015	9.956	"	13.458	"
MB-11	"	"	"	"	1.250	0.030	21.409	"	13.577	"
Pu-25	"	"	Cylinder	0.100	2.173	-	4.480	C-12	10.758	"
Pu-27	"	"	"	0.200	"	-	17.062	"	11.207	"
Pu-240-1D	<sup>240</sup> PuO <sub>2</sub>	Powder	Annulus	0.526	1.800	0.166	30.735	C-2	24.045	Inconel 600 <sup>c</sup>
Pu-240-2D	"	"	"	0.604	"	0.205	45.135	"	28.821	"
Pu-50	<sup>241</sup> PuO <sub>2</sub>	"	Cylinder	0.210	0.157	-	0.5817	C-3 & C-13	17.722	304 SST
Pu-242-4-1	<sup>242</sup> Pu	Solid	"	0.366	0.813	-	27.295	C-4	20.885	304 L SST & Al
U-233-1	<sup>233</sup> U	"	Rectangular	0.415 <sup>d</sup>	1.805	0.005	1.0351	C-5	16.136	304 SST
U-233-2	"	"	"	0.830 <sup>d</sup>	"	"	2.0457	"	15.651	"
U-233-3	"	"	"	"	"	0.010	4.1576	"	16.513	"
MB-20	<sup>235</sup> U	"	Annulus	0.835	1.688	0.005	5.231	C-6	13.907	"
MB-21	"	"	"	"	"	0.015	15.778	"	13.729	"
MB-22	"	"	"	"	"	0.030	30.838	"	13.580	"
MB-23	<sup>238</sup> U	"	"	"	"	0.006	6.315	C-7	13.867	"
MB-24	"	"	"	"	"	0.018	19.074	"	13.859	"
MB-25	"	"	"	"	"	0.036	38.163	"	13.691	"
UO <sub>2</sub> -1	<sup>238</sup> UO <sub>2</sub>	"	"	0.500	1.994	0.188	61.256	C-14	15.743	304 L SST
Li-15	<sup>6</sup> Li	"	Cylinder	0.309	1.782	-	0.9910	C-15	1.8624	1100 Al
Ta-3	Ta	"	"	0.100	2.173	-	4.681	99.9% Pure	10.614	304 SST
Th-2	Th	"	Annulus	0.835	1.773	0.024	19.8022	C-8	12.811	"
Th-3	Th	"	"	"	1.750	0.047	37.9768	"	13.8975	"
Th-4	Th	"	"	"	1.805	0.094	71.9103	"	13.216	"
B-7	<sup>10</sup> B	Powder	"	0.400	2.173	0.0094	0.4968	C-9	20.776	"
B(L)	<sup>11</sup> B	"	Cylinder	0.125	1.969	-	0.5553	C-10	8.489	"
EuO <sub>3</sub> -3	EuO <sub>3</sub>	Solid	"	0.402	2.163	-	9.963	99.9% Pure	10.578	"
BeO-1	BeO	Powder	"	0.390	2.173	-	12.342	99% Pure	10.348	"
H <sub>2</sub> O-1A	H <sub>2</sub> O	Liquid	"	0.440	1.710	-	4.177	<0.1 PPM Impurities	6.648	"
H <sub>2</sub> O-2A	"	"	"	0.620	"	-	8.274	"	9.299	"
H <sub>2</sub> O-3A	"	"	"	0.835	"	-	15.047	"	13.623	"
Poly-3	Polyethylene	Solid	"	0.12	2.172	-	0.269	[CH <sub>2</sub> -CH <sub>2</sub> ] <sub>n</sub>	10.959	"
Poly-2	"	"	"	0.201	"	-	1.062	"	11.303	"
Poly-1	"	"	"	0.390	2.173	-	4.024	C-11	-	-
CH <sub>2</sub> (F)-1	"	Foam	"	0.875	2.656	-	0.843	"	-	-
CH <sub>2</sub> (F)-2A	"	"	"	0.975	2.00	-	0.910	"	-	-
CH <sub>2</sub> (F)-3A	"	Foam	"	"	"	-	0.448	"	-	-
CH <sub>2</sub> (F)-4	"	Foam	"	"	"	-	0.9063	"	-	-
CH <sub>2</sub> (F)-6	"	"	"	"	"	-	0.8976	"	-	-
C(S)	C	Solid	"	0.829	1.806	-	27.336	99.9% Pure	13.421	304 SST
Fe-1	Fe	"	"	0.389	2.172	-	33.277	99.99% Pure	10.611	"
Ni-1	Ni	"	"	0.390	2.173	-	37.916	99.995% Pure	10.691	"
Cr-3	Cr	"	"	0.375	"	-	26.999	99.996% Pure	10.644	"
Mn-1	Mn	Powder	"	0.399	"	-	18.010	99.99% Pure	10.343	"
Mo-2	Mo	Solid	"	0.200	"	-	11.392	99.95% Pure	10.740	"
Fe <sub>2</sub> O <sub>3</sub> -2	Fe <sub>2</sub> O <sub>3</sub>	Powder	"	0.401	2.169	-	5.265	99.999% Pure	10.624	"
304 SST	304 SST	Solid	"	0.870	2.00	-	154.205	b	-	-
Li-15-DUM	Dummy	-	-	0.352	1.990	0.020	-	-	2.0545	1100 Al
D-1	"	-	-	0.420	2.625	0.010	-	-	10.667	304 SST
MB-19	"	-	-	0.065	2.00	0.015	-	-	13.807	"
DUM-2D	"	-	-	0.670	"	0.033	-	-	24.473	Inconel 600
D-242-4-1	"	-	-	0.580	2.19	0.031	-	-	15.743	304 L SST
				0.468	1.66	"	-	-	5.030	Al

<sup>a</sup>See Table III-2.<sup>b</sup>Typical analysis: Fe-70.39 w/o, Cr-18.45 w/o, Ni-9.71 w/o, Mn-1.46 w/o.<sup>c</sup>Typical analysis: Ni-75.8 w/o, Cr-15.74 w/o, Fe-7.72 w/o, Si-0.22 w/o, Mn-0.20 w/o, Cu-0.11 w/o.<sup>d</sup>Dimension is of sample width.<sup>e</sup>Foam has been perforated with resultant density one-half that of normal foam.

TABLE III-2. Sample Composition

Sample Identification	Composition Identification	Material	Material Mass, g	Material Composition, w/o	Isotopic Composition, w/o
MB-06	C-1	Pu-A1	3.524	Pu - 97.9850	$^{239}\text{Pu}$ - 98.9315
MB-10			9.956	A1 - 1.2075	$^{240}\text{Pu}$ - 1.0123
MB-11			21.409		$^{241}\text{Pu}$ - 0.0528 $^{242}\text{Pu}$ - 0.0034
Pu-240-1D	C-2	PuO <sub>2</sub>	30.735	Pu - 86.10	$^{239}\text{Pu}$ - 1.05
Pu-240-2D			45.135	O - 11.97	$^{240}\text{Pu}$ - 93.73
				H - 0.035	$^{241}\text{Pu}$ - 0.57
				N - 0.02	$^{242}\text{Pu}$ - 4.65
Pu-50	C-3 (Phase I)	PuO <sub>2</sub>	0.5817	Pu - 66.64 <sup>a</sup>	$^{239}\text{Pu}$ - 1.508
				Am - 20.21 <sup>a</sup>	$^{240}\text{Pu}$ - 4.034
				O - 12.05	$^{241}\text{Pu}$ - 92.436
				N - < 0.1	$^{242}\text{Pu}$ - 2.023
				H - < 0.1	
				O - < 0.1	
Pu-242-4-1	C-4	Pu	27.295	Pu - 99.8	$^{239}\text{Pu}$ - 1.4800
					$^{240}\text{Pu}$ - 0.0927
					$^{241}\text{Pu}$ - 0.0069
					$^{242}\text{Pu}$ - 98.4204
U-233-1	C-5	U	1.0351	U - 99.8	$^{233}\text{U}$ - 99.47
U-233-2			2.0457		$^{234}\text{U}$ - 0.183
U-233-3			4.1576		$^{235}\text{U}$ - 0.071
					$^{236}\text{U}$ - 0.014 $^{238}\text{U}$ - 0.266
MB-20	C-6	U	5.231	U -100.0	$^{234}\text{U}$ - 0.6651
MB-21			15.778		$^{235}\text{U}$ - 93.2438
MB-22			30.838		$^{236}\text{U}$ - 0.3162
					$^{238}\text{U}$ - 5.7750
MB-23	C-7	U	6.315	U -100.0	$^{235}\text{U}$ - 0.2328
MB-24			19.074		$^{238}\text{U}$ - 99.7672
MB-25			38.163		
Th-2	C-8	Th	19.8022	Th - 99.9	$^{232}\text{Th}$ -100.0
Th-3			37.9768		
Th-4			71.9103		
B-7	C-9	Boron	0.4968	B - 94.50	$^{10}\text{B}$ - 92.19
				O - 1.43	$^{11}\text{B}$ - 7.81
				C - 0.96	
				Si - 0.26	
				H - 0.09	
				Al - 0.05	
B(L)	C-10	Boron	0.5553	B -100.0	$^{10}\text{B}$ - 19.88
					$^{11}\text{B}$ - 80.12
CH <sub>2</sub> (F)-1	C-11	Poly Foam	0.843	[CH <sub>2</sub> .CH <sub>2</sub> ] <sub>n</sub> -99.8	C - 85.50 <sup>b</sup>
CH <sub>2</sub> (F)-2A			0.910		H - 15.50 <sup>b</sup>
CH <sub>2</sub> (F)-3A			0.448		
CH <sub>2</sub> (F)-4			0.9063		
CH <sub>2</sub> (F)-6			0.8976		
Pu-25	C-12	Pu-A1	4.480	Pu - 98.26	$^{239}\text{Pu}$ - 98.926
Pu-27			17.062	A1 - 0.95	$^{240}\text{Pu}$ - 1.023 $^{241}\text{Pu}$ - 0.049 $^{242}\text{Pu}$ - 0.002
Pu-50	C-13 (Phase II)	PuO <sub>2</sub>	0.5817	Pu - 65.31 <sup>c</sup>	$^{239}\text{Pu}$ - 1.539
				Am - 21.54 <sup>c</sup>	$^{240}\text{Pu}$ - 4.116
				O - 12.05	$^{241}\text{Pu}$ - 92.281
				N - < 0.1	$^{242}\text{Pu}$ - 2.064
				H - < 0.1	
				C - < 0.1	
UO <sub>2</sub> -1	C-14	UO <sub>2</sub>	61.256	U - 88.14	$^{235}\text{U}$ - 99.78
				O - 11.86	$^{238}\text{U}$ - 0.22
Li-15	C-15	Li	0.9910	Li - 99.846	$^6\text{Li}$ - 98.51
				C - 0.085	$^7\text{Li}$ - 1.49

<sup>a</sup> Corrected to 5/2/75 from original analysis date of 5/1/72. A 3.003 yr decay correction was made assuming a 14.5 yr half-life for  $^{241}\text{Pu} \rightarrow ^{241}\text{Am}$  decay.

<sup>b</sup> Determined from C and H analysis of polyethylene foam.

<sup>c</sup> Corrected to 10/16/75 from original analysis date of 5/1/72. A 3.460 yr decay correction was made assuming a 14.5 yr half-life for  $^{241}\text{Pu} \rightarrow ^{241}\text{Am}$  decay.

TABLE III-3. Results of FAR Calibrations

Measurement	Total Worth, <sup>a</sup> Ih
Central and Radial Unreflected	4.5965 ± 0.0460
Axial Unreflected	5.5625 ± 0.0556
Central Reflected	5.5732 ± 0.0557

<sup>a</sup>The uncertainty is conservatively estimated to be 1% of the total worth of the FAR.

TABLE III-4. Experimental Small-Sample Central Reactivity Worths in the Unreflected Assembly

Sample I.D.	Principal Material or Isotope	Sample, Sample Capsule and SST <sup>a</sup> Worth, Ih	Sample Capsule SST <sup>a</sup> Mass, g	Dummy Capsule I.D.	Dummy Capsule and SST <sup>a</sup> Worth, Ih	Dummy Capsule and SST <sup>a</sup> Mass, g	Ratio of Sample Capsule Plus SST <sup>a</sup> Mass to Dummy Capsule Plus SST <sup>a</sup> Mass	Adjusted Worth of Dummy, Ih	Net Sample Worth, Ih	Sample Mass, g	Specific Sample Worth, Th/kg
MB-06	<sup>239</sup> Pu	0.261 ± 0.004	70.856	MB-19	-0.535 ± 0.008	71.386	0.99258	-0.531 ± 0.008	0.792 ± 0.009	3.524	224.75 ± 2.51
MB-10	<sup>239</sup> Pu	1.751 ± 0.018	70.923	MB-19	"	"	0.99351	-0.532 ± 0.008	2.283 ± 0.020	9.956	229.26 ± 1.99
Pu-25	<sup>239</sup> Pu	0.520 ± 0.006	70.463	D-1	-0.509 ± 0.007	70.484	0.99970	-0.509 ± 0.007	1.029 ± 0.009	4.480	229.65 ± 1.91
Pu-27	<sup>239</sup> Pu	3.493 ± 0.035	71.166	D-1	"	"	1.00968	-0.514 ± 0.007	4.007 ± 0.036	17.062	234.84 ± 2.11
Pu-240-2D	<sup>240</sup> PuO <sub>2</sub>	0.828 ± 0.009	96.170	DUM-2D	-0.771 ± 0.007	95.858	1.00325	-0.774 ± 0.007	1.602 ± 0.012	45.135	35.48 ± 0.26
Pu-50	<sup>241</sup> PuO <sub>2</sub>	-0.456 ± 0.005	77.485	D-1	-0.509 ± 0.007	70.484	1.09933	-0.560 ± 0.007	0.104 ± 0.009	0.5817	178.03 ± 14.99
Pu-242-4-1	<sup>242</sup> Pu	0.274 ± 0.005	84.028	D-242-4-1	-0.649 ± 0.009	83.917	1.00132	-0.650 ± 0.009	0.924 ± 0.010	27.295	33.85 ± 0.37
U-233-3	<sup>233</sup> U	0.665 ± 0.008	74.057	MB-19	-0.535 ± 0.008	71.386	1.03742	-0.555 ± 0.008	1.220 ± 0.011	4.158	293.41 ± 2.74
MB-21	<sup>235</sup> U	1.928 ± 0.020	71.302	MB-19	"	"	0.99882	-0.534 ± 0.008	2.462 ± 0.021	15.778	156.06 ± 1.36
MB-25	<sup>238</sup> U	-0.954 ± 0.015	71.156	MB-19	"	"	0.99678	-0.533 ± 0.008	-0.421 ± 0.017	38.163	-11.02 ± 0.45
Th-3	<sup>232</sup> Th	-1.347 ± 0.014	71.442	MB-19	"	"	1.00078	-0.535 ± 0.008	-0.812 ± 0.017	37.977	-21.37 ± 0.43
B-7	<sup>10</sup> B	-2.065 ± 0.021	80.554	D-1	-0.509 ± 0.007	70.484	1.14287	-0.582 ± 0.007	-1.483 ± 0.022	0.4968	-2985.7 ± 44.3
B(L)	<sup>11</sup> B	-0.849 ± 0.009	66.062	D-1	"	"	0.93726	-0.477 ± 0.006	-0.372 ± 0.011	0.5553	-669.79 ± 19.57
Eu <sub>2</sub> O <sub>3</sub> -3	Eu <sub>2</sub> O <sub>3</sub>	-2.516 ± 0.026	70.411	D-1	"	"	0.99896	-0.508 ± 0.007	-2.008 ± 0.027	9.963	-201.50 ± 2.68
BeO-1	BeO	-0.766 ± 0.008	70.404	D-1	"	"	0.99886	-0.508 ± 0.007	-0.258 ± 0.011	12.342	-20.87 ± 0.85
Li-15	<sup>6</sup> Li	-2.959 ± 0.030	65.333	Li-DUM	-0.501 ± 0.007	65.248	1.00130	-0.502 ± 0.007	-2.457 ± 0.031	0.9910	-2479.66 ± 31.33
H <sub>2</sub> O-1A	H <sub>2</sub> O	0.714 ± 0.008	71.228	MB-19	-0.535 ± 0.008	71.386	0.99779	-0.534 ± 0.008	1.248 ± 0.011	4.177	298.73 ± 2.74
CH <sub>2</sub> (F)-4	CH <sub>2</sub> (Foam)	0.139 ± 0.002	-	MB-19	-	-	-	-	0.139 ± 0.002	0.9063	153.37 ± 2.65
C(S)	C	-1.113 ± 0.018	71.058	-	-0.535 ± 0.008	71.386	0.99541	-0.533 ± 0.008	-0.580 ± 0.020	27.336	-21.23 ± 0.72
Ta-3	Ta	-0.750 ± 0.014	70.355	D-1	-0.509 ± 0.007	70.484	0.99817	-0.508 ± 0.007	-0.242 ± 0.016	4.681	-51.68 ± 3.34
Fe <sub>2</sub> O <sub>3</sub> -2	Fe <sub>2</sub> O <sub>3</sub>	-0.559 ± 0.006	70.545	D-1	"	"	1.00087	-0.509 ± 0.007	-0.0496 ± 0.009	5.265	-9.41 ± 1.67
Fe-1	Fe	-0.721 ± 0.008	70.452	D-1	"	"	0.99955	-0.509 ± 0.007	-0.212 ± 0.010	33.277	-6.38 ± 0.31
Ni-1	Ni	-0.873 ± 0.011	70.604	D-1	"	"	1.00170	-0.510 ± 0.007	-0.363 ± 0.013	37.916	-9.58 ± 0.34
Cr-3	Cr	-0.700 ± 0.008	70.648	D-1	"	"	1.00233	-0.510 ± 0.007	-0.190 ± 0.010	26.999	-7.03 ± 0.39
Mn-1	Mn	-0.695 ± 0.008	70.234	D-1	"	"	0.99645	-0.507 ± 0.007	-0.188 ± 0.010	18.010	-10.43 ± 0.57
Mo-2	Mo	-0.748 ± 0.008	70.549	D-1	"	"	1.00092	-0.509 ± 0.007	-0.239 ± 0.010	11.392	-20.94 ± 0.87
D-1	Dummy (SST)	-0.509 ± 0.007	-	-	-	-	-	-	-0.509 ± 0.007	70.484	-7.22 ± 0.09
DUM-2D	Dummy (SST + Inconel)	-0.771 ± 0.007	-	-	-	-	-	-	-0.771 ± 0.007	95.858	-8.04 ± 0.08
D-242-4-1	Dummy (SST + Al)	-0.649 ± 0.009	-	-	-	-	-	-	-0.649 ± 0.009	83.917	-7.73 ± 0.11
Li-15-DUM	Al	-0.501 ± 0.007	63.194	MB-19	-0.535 ± 0.008	71.386	0.88524	-0.474 ± 0.007	-0.0274 ± 0.010	2.055	-13.33 ± 4.92
Li-15-DUM	Dummy (SST + Al)	-0.501 ± 0.007	-	-	-	-	-	-	-0.501 ± 0.007	65.249	-7.68 ± 0.11
MB-19	Dummy (SST)	-0.535 ± 0.008	-	-	-	-	-	-	-0.535 ± 0.008	71.386	-7.49 ± 0.11

<sup>a</sup>SST refers to stainless steel capsule holders and stainless steel shims or spacers if used.

TABLE III-5. Calculated Small-Sample Central Reactivity Worths in the Unreflected Assembly With Comparison to Experimental Worths

Sample	Principal Material or Isotope	Sample Worth, <sup>a</sup> 1h/kg		C/E <sup>a</sup>	Sample-Size Correction Factor, <sup>b</sup> $\rho_o/\rho$
		Calculated	Experimental		
MB-06	<sup>239</sup> Pu	272.32	224.75 ± 2.51	1.21	1.00944
MB-10	<sup>239</sup> Pu	272.32	229.26 ± 1.99	1.19	1.00678
Pu-25	<sup>239</sup> Pu	272.92	229.65 ± 1.91	1.19	1.00144
Pu-27	<sup>239</sup> Pu	272.92	234.84 ± 2.11	1.16	0.98255
Pu-240-2D	<sup>240</sup> PuO <sub>2</sub>	44.16	35.48 ± 0.26	1.24	1.02166
Pu-50	<sup>241</sup> PuO <sub>2</sub>	230.95	178.03 ± 14.99	1.30	1.01288
Pu-242-4-1	<sup>242</sup> Pu	44.83	33.85 ± 0.37	1.32	0.95828
U-233-3	<sup>233</sup> U	342.69	293.41 ± 2.74	1.17	1.00544
MB-21	<sup>235</sup> U	191.45	156.06 ± 1.36	1.23	1.01923
MB-25	<sup>238</sup> U	-12.29	-11.02 ± 0.45	1.12	1.00834
Th-232-3	<sup>232</sup> Th	-25.70	-21.37 ± 0.43	1.20	1.02903
B-7	<sup>10</sup> B	-2985.6	-2985.7 ± 44.3 <sup>c</sup>	1.00	-
B(L)	<sup>11</sup> B	-720.16	-669.79 ± 19.57	1.08	-
Eu <sub>2</sub> O <sub>3</sub> -3	Eu <sub>2</sub> O <sub>3</sub>	-202.91	-201.50 ± 2.68	1.01	-
BeO-1	BeO	-44.12	-20.87 ± 0.85	2.11	-
Li-15	<sup>6</sup> Li	-2846.8	-2479.7 ± 31.3	1.15	1.06374
H <sub>2</sub> O-1A	H <sub>2</sub> O	-193.86 <sup>d</sup>	298.73 ± 2.74	-0.65	-
CH <sub>2</sub> (F)-4	CH <sub>2</sub> (Foam)	-256.24 <sup>d</sup>	153.37 ± 2.65	-1.67	-
Fe <sub>2</sub> O <sub>3</sub> -3	Fe <sub>2</sub> O <sub>3</sub>	-14.83	-9.41 ± 1.67	1.58	-
D-1	304 SST	-10.43	-7.22 ± 0.09 <sup>e</sup>	1.45	-
MB-19	304 SST	-10.43	-7.49 ± 0.11 <sup>f</sup>	1.39	-
C(S)	C	-43.78	-21.23 ± 0.72	2.06	-
Ta-3	Ta	-59.55	-51.68 ± 3.34	1.15	-
Fe-1	Fe	-9.32	-6.38 ± 0.31	1.46	-
Ni-1	Ni	-15.69	-9.58 ± 0.34	1.64	-
Cr-3	Cr	-11.23	-7.03 ± 0.39	1.60	-
Mn-1	Mn	-18.89	-10.43 ± 0.57	1.81	-
Mo-2	Mo	-26.73	-20.94 ± 0.87	1.27	-
Al	Al	-15.15	-13.33 ± 4.92	1.14	-

<sup>a</sup> Experimental samples were measured at  $z = 4.45$  cm from the reactor midplane. RZ model calculated results were obtained at  $z = 1.02$  cm from the reactor midplane. The ratio of calculated results at 1.02 cm to calculated results at 4.45 cm is  $\sim 1.01$ . No corrections for these different  $Z$  values have been made in the reported data. Similarly, no sample-size effect corrections were made.

<sup>b</sup> Sample-size correction factors were calculated with the PIT code. These factors have not been applied to any of the calculated or experimental data, but are listed to demonstrate that sample size effects are generally small for these samples.

<sup>c</sup> Expected magnitude of the sample-size correction for <sup>10</sup>B sample is about 3% from previous evaluation for ZPR-6 Assembly 7 (See Ref. 7).

<sup>d</sup> It should be noted that the calculations mispredicted the sign of the central worth for these materials. This was consistent with GCFR Phase-I results.

<sup>e</sup> The sample for this measurement was the D-1 dummy capsule and capsule holder No. 10.

<sup>f</sup> The sample for this measurement was the MB-19 dummy capsule and capsule holder No. 6.

TABLE III-6. Calculated and Experimental Isotopic or Elemental Central Reactivity Worths in the Unreflected Assembly

Isotope or Element	Central Worth, <sup>a</sup> 1h/kg		C/E
	Calculated	Experimental	
<sup>239</sup> Pu	280.20	231.43 ± 2.59 <sup>b</sup>	1.21
<sup>240</sup> Pu	51.35	42.19 ± 0.38 <sup>b</sup>	1.22
<sup>241</sup> Pu	374.39	288.04 ± 2.48 <sup>b</sup>	1.30
<sup>242</sup> Pu	41.35	30.92 ± 0.38 <sup>b</sup>	1.34
<sup>233</sup> U	345.00	295.38 ± 2.76	1.17
<sup>234</sup> U	16.07	-	-
<sup>235</sup> U	206.07	168.08 ± 1.46 <sup>b</sup>	1.23
<sup>236</sup> U	-19.49	-	-
<sup>238</sup> U	-12.80	-11.44 ± 0.45 <sup>b</sup>	1.12
<sup>232</sup> Th	-25.72	-21.37 ± 0.43	1.20
<sup>10</sup> B	-3421.8	-3428.3 ± 52.0 <sup>b</sup>	1.00
<sup>11</sup> B	-49.81	-	-
<sup>151</sup> Eu	-283.47	-	-
<sup>153</sup> Eu	-182.12	-	-
<sup>9</sup> Be	-73.38	-	-
<sup>6</sup> Li	-2893.3	-2520.1 ± 31.8 <sup>c</sup>	1.15
<sup>7</sup> Li	-66.91	-	-
H	-1513.3	-	-
C	-43.78	-21.23 ± 0.72	2.06
O	-27.64	-16.46 ± 5.60 <sup>d</sup>	1.68
Ta	-59.55	-51.68 ± 3.34	1.15
Fe	-9.32	-6.38 ± 0.31	1.46
Ni	-15.69	-9.58 ± 0.34	1.64
Cr	-11.23	-7.03 ± 0.39	1.60
Mn	-18.89	-10.43 ± 0.57	1.81
Mo	-26.73	-20.94 ± 0.87	1.28
Al	-15.15	-13.33 ± 4.92	1.14

<sup>a</sup> Experimental samples were measured at  $z = 4.45$  cm from the reactor midplane. RZ model calculated results were obtained at  $z = 1.02$  cm from the reactor midplane. The ratio of calculated results at 1.02 cm to calculated results at 4.45 cm is  $\sim 1.01$ . No corrections for these different  $Z$  values have been made in the reported data. Similarly, no sample-size effect corrections were made.

<sup>b</sup> The isotopic worths of <sup>235</sup>U and <sup>238</sup>U, <sup>10</sup>B, and the Pu isotopes were determined from the experimental worths of enriched and depleted U, enriched and natural B, and Pu sample respectively by solving simultaneous equations relating isotopic worths to sample worths. The sample worths of samples of smallest mass were used for cases where more than one sample size was measured.

<sup>c</sup> The isotopic worth of <sup>6</sup>Li was determined from the worth of the Li-15 sample (98.36% <sup>6</sup>Li) and the calculated worth of <sup>7</sup>Li.

<sup>d</sup> The isotopic worth of <sup>16</sup>O was determined from the worth of the Fe<sub>2</sub>O<sub>3</sub>-2 sample (30.06% <sup>16</sup>O) and the experimental worth of Fe measured in the Fe-1 sample.

TABLE III-7. Experimental Small-Sample Central Reactivity Worths in the Reflected Assembly

Sample I.D.	Principal Material or Isotope	Sample, Sample Capsule and SST <sup>a</sup> Worth, Ih	Sample Capsule and SST <sup>a</sup> Mass, g	Dummy Capsule I.D.	Dummy Capsule and SST <sup>a</sup> Worth, Ih	Dummy Capsule and SST <sup>a</sup> Mass, g	Ratio of Sample Capsule Plus SST <sup>a</sup> Mass to Dummy Capsule Plus SST <sup>a</sup> Mass	Adjusted Worth of Dummy, Ih	Net Sample Worth, Ih	Sample Mass, g	Specific Sample Worth, Ih/kg
MB-10	<sup>239</sup> Pu	1.761 ± 0.018	70.923	MB-19	-0.546 ± 0.006	71.477	0.99225	-0.542 ± 0.006	2.303 ± 0.019	9.956	231.30 ± 1.91
MB-11	<sup>235</sup> U	1.953 ± 0.020	71.273	MB-19	-0.546 ± 0.006	71.477	0.99715	-0.544 ± 0.006	2.497 ± 0.021	15.778	158.29 ± 1.30
MB-25	<sup>238</sup> U	-0.958 ± 0.010	71.264	MB-19	-0.546 ± 0.006	71.477	0.99702	-0.544 ± 0.006	-0.414 ± 0.012	38.163	-10.84 ± 0.31
B-7	<sup>10</sup> B	-2.085 ± 0.021	80.698	D-1	-0.529 ± 0.006	70.408	1.14615	-0.606 ± 0.007	-1.479 ± 0.022	0.4968	-2976.4 ± 44.4
Poly-2	CH <sub>2</sub> (Solid)	-0.202 ± 0.005	71.145	D-1	-0.529 ± 0.006	70.408	1.01047	-0.535 ± 0.006	0.333 ± 0.008	1.062	313.12 ± 7.19
CH <sub>2</sub> (F)-6	CH <sub>2</sub> (Foam)	0.143 ± 0.006	-	-	-	-	-	-	0.143 ± 0.006	0.8976	159.31 ± 6.91
MB-19	Dummy (304 SST)	-0.546 ± 0.006	71.477	-	-	-	-	-	-0.546 ± 0.006	71.477	-7.64 ± 0.08
D-1	Dummy (304 SST)	-0.529 ± 0.006	70.408	-	-	-	-	-	-0.529 ± 0.006	70.408	-7.51 ± 0.09

<sup>a</sup>SST refers to stainless steel capsule holders and stainless steel shims or spacers if used.



TABLE III-8. Calculated and Experimental Small-Sample Central Reactivity Worths in the Reflected Assembly with Comparison to Unreflected Results

Sample	Principal Material or Isotope	Sample Worth, <sup>a</sup> Ih/kg		C/E	Ratio of Reflected to Unreflected Results	
		Calculated	Experimental		Calculated	Experimental
MB-10	<sup>239</sup> Pu	268.53	231.30 ± 1.91	1.16	0.99	1.01
MB-21	<sup>235</sup> U	189.05	158.29 ± 1.30	1.19	0.99	1.01
MB-25	<sup>238</sup> U	-12.26	-10.84 ± 0.31	1.13	1.00	0.98
B-7	<sup>10</sup> B	-2965.3	-2976.4 ± 44.4	1.00	0.99	1.00
Poly-2	CH <sub>2</sub> (Solid)	-273.65 <sup>b</sup>	313.12 ± 7.19	-0.87	1.07	-
CH <sub>2</sub> (F)-6	CH <sub>2</sub> (Foam)	-273.65 <sup>b</sup>	159.31 ± 6.91	-1.72	1.07	1.04
MB-19	Dummy (304 SST)	-10.35	-7.64 ± 0.08 <sup>c</sup>	1.35	0.99	1.02
D-1	Dummy (304 SST)	-10.35	-7.51 ± 0.09 <sup>d</sup>	1.38	0.99	1.04

<sup>a</sup> Experimental samples were measured at  $z = 4.45$  cm from the reactor midplane. RZ model calculated results were obtained at  $z = 1.02$  cm from the reactor midplane. The ratio of calculated results at 1.02 cm to calculated results at 4.45 cm is  $\sim 1.01$ . No corrections for these different  $Z$  values have been made in the reported data. Similarly, no sample-size effect corrections were made.

<sup>b</sup> It should be noted that the calculations mispredicted the sign of the central worth for these materials. This was consistent with GCFR Phase-I results.

<sup>c</sup> The sample for this measurement was the D-1 dummy capsule and capsule holder No. 10.

<sup>d</sup> The sample for this measurement was the MB-19 dummy capsule and capsule holder No. 4.

TABLE III-9. Isotopic Central Reactivity Worths in the Reflected Assembly with Comparison to Unreflected Results

Isotope	Central Worth, <sup>a</sup> Ih/kg		C/E	Ratio of Reflected to Unreflected Results	
	Calculated	Experimental		Calculated	Experimental
<sup>239</sup> Pu	276.48	238.08 ± 1.97 <sup>b</sup>	1.16	0.99	1.03
<sup>235</sup> U	203.49	170.45 ± 1.40 <sup>c</sup>	1.19	0.99	1.01
<sup>238</sup> U	-12.77	-11.26 ± 0.31 <sup>c</sup>	1.13	1.00	0.98
<sup>10</sup> B	-3398.5	-3412.3 ± 50.9 <sup>b</sup>	1.00	0.99	1.00

<sup>a</sup> Experimental samples were measured at  $z = 4.45$  cm from the reactor midplane. RZ model calculated results were obtained at  $z = 1.02$  cm from the reactor midplane. The ratio of calculated results at 1.02 cm to calculated results at 4.45 cm is  $\sim 1.01$ . No corrections for these different  $Z$  values have been made in the reported data. Similarly, no sample-size effect corrections were made.

<sup>b</sup> The results reported for <sup>239</sup>Pu and <sup>10</sup>B have been evaluated from the measured worths of the MB-10 and B-7 samples, respectively, and the calculated worths of the lesser isotopes in each sample.

<sup>c</sup> The results reported for <sup>235</sup>U and <sup>238</sup>U have been determined from the experimental results of the MB-21 and MB-25 samples by solving simultaneous equations relating isotopic worths to sample worths.

TABLE III-10. Experimental Small-Sample Radial Reactivity Worth Traverses in the Unreflected Assembly

Sample I.D.	Principal Material or Isotope	Radial Position, cm	Sample, Sample Capsule and SST <sup>a</sup> Worth, Th	Sample Capsule and SST <sup>a</sup> Mass, g	Dummy Capsule I.D.	Dummy Capsule and SST <sup>a</sup> Worth, Th	Dummy Capsule and SST <sup>a</sup> Mass, g	Ratio of Sample Capsule Plus SST <sup>a</sup> Mass to Dummy Capsule Plus SST <sup>a</sup> Mass	Adjusted Worth of Dummy, Th	Net Sample Worth, Th	Sample Mass, g	Specific Sample Worth, Th/kg
MB-10	<sup>239</sup> Pu	0.00	1.751 ± 0.018	70.923	MB-19	-0.535 ± 0.008	71.386	0.99351	-0.532 ± 0.008	2.283 ± 0.012	9.956	229.26 ± 1.99
		11.05	1.701 ± 0.017			-0.419 ± 0.004			-0.416 ± 0.004	2.117 ± 0.018		212.66 ± 1.79
		16.57	1.626 ± 0.018			-0.361 ± 0.006			-0.359 ± 0.006	1.985 ± 0.019		199.34 ± 1.92
		22.10	1.534 ± 0.016			-0.241 ± 0.004			-0.239 ± 0.004	1.773 ± 0.016		178.13 ± 1.61
		33.15	1.313 ± 0.014			0.002 ± 0.004			0.002 ± 0.004	1.311 ± 0.015		131.68 ± 1.46
		44.20	1.036 ± 0.010			0.216 ± 0.002			0.215 ± 0.002	0.821 ± 0.011		82.50 ± 1.07
		49.72	0.900 ± 0.009			0.291 ± 0.005			0.289 ± 0.005	0.611 ± 0.010		61.36 ± 1.05
		66.29	0.328 ± 0.003			0.158 ± 0.003			0.157 ± 0.003	0.171 ± 0.004		17.18 ± 0.42
MB-21	<sup>235</sup> U	0.00	1.928 ± 0.020	71.302	MB-19	-0.535 ± 0.008	71.386	0.99882	-0.534 ± 0.008	2.462 ± 0.021	15.778	156.06 ± 1.36
		11.05	1.893 ± 0.019			-0.419 ± 0.004			-0.419 ± 0.004	2.312 ± 0.020		146.50 ± 1.23
		22.10	1.708 ± 0.017			-0.241 ± 0.004			-0.241 ± 0.004	1.949 ± 0.018		123.51 ± 1.11
MB-25	<sup>238</sup> U	0.00	0.954 ± 0.015	71.156	MB-19	-0.535 ± 0.008	71.386	0.99686	-0.533 ± 0.008	-0.421 ± 0.017	38.163	-11.02 ± 0.45
		16.57	0.691 ± 0.007			-0.361 ± 0.006			-0.360 ± 0.006	-0.331 ± 0.012		-8.68 ± 0.31
		33.15	0.161 ± 0.010			0.002 ± 0.004			0.002 ± 0.004	-0.163 ± 0.011		-4.27 ± 0.28
		49.72	0.296 ± 0.003			0.291 ± 0.005			0.290 ± 0.005	0.006 ± 0.006		0.155 ± 0.152
		66.29	0.202 ± 0.005			0.158 ± 0.003			0.158 ± 0.003	0.044 ± 0.005		1.17 ± 0.13
CH <sub>2</sub> (F)-4	CH <sub>2</sub> (Foam)	0.00	0.139 ± 0.002	-	-	-	-	-	-	0.139 ± 0.002	0.9063	153.37 ± 2.65
		16.57	0.144 ± 0.006							0.144 ± 0.006		158.89 ± 6.84
		33.15	0.115 ± 0.007							0.115 ± 0.007		126.89 ± 7.83
		38.67	0.124 ± 0.002							0.124 ± 0.002		136.82 ± 2.65
		44.20	0.098 ± 0.008							0.098 ± 0.008		108.13 ± 8.94
		49.72	0.004 ± 0.002							0.004 ± 0.002		4.41 ± 2.21
		66.29	-0.040 ± 0.007							-0.040 ± 0.007		-44.14 ± 7.72
Li-15	<sup>6</sup> Li	0.00	-2.959 ± 0.030	65.333	Li-DUM	-0.501 ± 0.007	65.248	1.00130	-0.502 ± 0.007	-2.457 ± 0.031	0.9910	-2479.36 ± 31.33
		5.52	-2.869 ± 0.032			-0.451 ± 0.006			-0.452 ± 0.006	-2.417 ± 0.033		-2439.37 ± 32.76
		16.57	-2.469 ± 0.025			-0.322 ± 0.008			-0.322 ± 0.008	-2.147 ± 0.026		-2166.00 ± 26.30
		27.62	-1.760 ± 0.018			-0.095 ± 0.003			-0.095 ± 0.003	-1.665 ± 0.019		-1680.08 ± 18.73
		38.67	-0.983 ± 0.010			0.128 ± 0.005			0.128 ± 0.005	-1.111 ± 0.012		-1121.26 ± 11.65
		49.72	-0.309 ± 0.006			0.279 ± 0.005			0.279 ± 0.005	-0.588 ± 0.008		-593.71 ± 7.74
Li-DUM	SST-A1	0.00	-0.501 ± 0.007	65.248	-	-	-	-	-	-	-	-
		5.52	-0.451 ± 0.006									
		16.57	-0.322 ± 0.008									
		27.62	-0.095 ± 0.003									
		38.67	0.128 ± 0.005									
		49.72	0.279 ± 0.005									
MB-19 Cap. Hold. No. 6	<sup>304</sup> SST	0.00	-0.535 ± 0.008	71.386	-	-	-	-	-	-0.535 ± 0.008	71.386	-7.49 ± 0.11
		5.52	-0.502 ± 0.006							-0.502 ± 0.006		-7.03 ± 0.09
		11.05	-0.419 ± 0.004							-0.419 ± 0.004		-5.87 ± 0.06
		16.57	-0.361 ± 0.006							-0.361 ± 0.006		-5.06 ± 0.09
		22.10	-0.241 ± 0.004							-0.241 ± 0.004		-3.38 ± 0.05
		27.62	-0.121 ± 0.010							-0.121 ± 0.010		-1.70 ± 0.14
		33.15	0.002 ± 0.004							0.002 ± 0.004		0.028 ± 0.056
		38.67	0.122 ± 0.002							0.122 ± 0.002		1.71 ± 0.03
		44.20	0.216 ± 0.002							0.216 ± 0.002		3.03 ± 0.03
		49.72	0.291 ± 0.005							0.291 ± 0.005		4.08 ± 0.07
		66.29	0.158 ± 0.003							0.158 ± 0.003		2.21 ± 0.04

<sup>a</sup> SST refers to stainless steel capsule holders and stainless steel shims or spacers if used.<sup>b</sup> No sample-size effect corrections have been made.

TABLE III-11. Experimental Small-Sample Axial Reactivity Worth Traverses in the Unreflected Assembly

Sample I.D.	Principal Material or Isotope	Axial Position, cm	Sample, Sample Capsule and SST <sup>a</sup> Worth, lh	Sample Capsule and SST <sup>a</sup> Mass, g	Dummy Capsule I.D.	Dummy Capsule and SST <sup>a</sup> Worth, lh	Dummy Capsule and SST <sup>a</sup> Mass, g	Ratio of Sample Capsule Plus SST <sup>a</sup> Mass to Dummy Capsule Plus SST <sup>a</sup> Mass	Adjusted Worth of Dummy, lh	Net Sample Worth, lh	Sample Mass, g	Specific Sample Worth, lh/kg
MB-10	<sup>239</sup> Pu	0.00	1.634 ± 0.016	70.923	MB-19	-0.567 ± 0.007	71.380	0.99360	-0.563 ± 0.007	2.197 ± 0.018	9.956	220.71 ± 1.79
		4.45	1.640 ± 0.017			-0.568 ± 0.008			-0.564 ± 0.008	2.204 ± 0.019		221.41 ± 1.88
		17.35	1.597 ± 0.017			-0.355 ± 0.006			-0.353 ± 0.006	1.950 ± 0.018		195.83 ± 1.77
		35.73	1.450 ± 0.015			0.145 ± 0.005			0.144 ± 0.005	1.306 ± 0.015		131.17 ± 1.55
		54.04	1.161 ± 0.014			0.546 ± 0.007			0.543 ± 0.007	0.618 ± 0.016		62.12 ± 1.55
Pu-240-2D	<sup>240</sup> Pu	0.00	0.767 ± 0.009	96.290	DUM-2D	-0.828 ± 0.009	95.820	1.00491	-0.832 ± 0.009	1.599 ± 0.012	45.135	35.43 ± 0.27
		17.35	0.954 ± 0.010			-0.518 ± 0.008			-0.521 ± 0.008	1.475 ± 0.013		32.67 ± 0.28
		35.73	1.279 ± 0.013			0.175 ± 0.002			0.176 ± 0.002	1.103 ± 0.013		24.44 ± 0.29
		54.04	1.438 ± 0.017			0.785 ± 0.008			0.789 ± 0.008	0.649 ± 0.018		14.38 ± 0.41
		68.04	0.813 ± 0.009			0.534 ± 0.006			0.537 ± 0.006	0.276 ± 0.010		6.12 ± 0.23
MB-25	<sup>238</sup> U	0.00	-0.954 ± 0.011	71.235	MB-19	-0.567 ± 0.007	71.380	0.99797	-0.566 ± 0.007	-0.388 ± 0.013	38.163	-10.17 ± 0.35
		4.45	-0.952 ± 0.012			-0.568 ± 0.008			-0.567 ± 0.008	-0.385 ± 0.014		-10.19 ± 0.37
		17.35	-0.672 ± 0.007			-0.355 ± 0.006			-0.354 ± 0.006	-0.318 ± 0.010		-8.33 ± 0.25
		35.73	-0.032 ± 0.002			0.145 ± 0.005			0.145 ± 0.005	-0.177 ± 0.006		-4.63 ± 0.15
		54.04	0.651 ± 0.008			0.546 ± 0.007			0.545 ± 0.007	0.106 ± 0.011		2.78 ± 0.28
UO <sub>2</sub> -1	<sup>238</sup> UO <sub>2</sub>	0.00	-1.309 ± 0.014	78.979	MB-19	-0.567 ± 0.007	71.380	1.10646	-0.627 ± 0.008	-0.682 ± 0.016	61.256	-11.13 ± 0.27
		17.35	-0.928 ± 0.010			-0.355 ± 0.006			-0.393 ± 0.007	-0.535 ± 0.012		-8.74 ± 0.20
		35.73	0.012 ± 0.008			0.145 ± 0.005			0.160 ± 0.006	-0.148 ± 0.010		-2.42 ± 0.16
		54.04	0.840 ± 0.009			0.546 ± 0.007			0.604 ± 0.008	0.236 ± 0.012		3.85 ± 0.20
		68.04	0.599 ± 0.007			0.382 ± 0.006			0.423 ± 0.006	0.176 ± 0.009		2.88 ± 0.15
CH <sub>2</sub> (F)-4	CH <sub>2</sub> (Foam)	0.00	0.122 ± 0.002	-	-	-	-	-	-	0.122 ± 0.002	0.9063	134.61 ± 2.54
		17.35	0.125 ± 0.007							0.125 ± 0.007		137.92 ± 7.83
		35.17	0.144 ± 0.003							0.144 ± 0.003		158.89 ± 3.64
		54.04	0.108 ± 0.006							0.108 ± 0.006		119.17 ± 6.73
		68.04	0.004 ± 0.004							0.004 ± 0.004		4.41 ± 4.41
CH <sub>2</sub> (F)-6	CH <sub>2</sub> (Foam)	0.00	0.120 ± 0.005	-	-	-	-	-	-	0.120 ± 0.005	0.8976	133.69 ± 5.68
304 SST	304 SST	0.00	-1.586 ± 0.018	57.580	MB-19	-0.567 ± 0.007	71.380	0.80667	-0.457 ± 0.006	-1.129 ± 0.019	154.205	-7.32 ± 0.12
		17.35	-1.101 ± 0.013			-0.355 ± 0.006			-0.286 ± 0.005	-0.815 ± 0.013		-5.28 ± 0.09
		35.73	0.097 ± 0.004			0.145 ± 0.005			0.117 ± 0.004	-0.020 ± 0.006		-0.129 ± 0.038
		54.04	1.207 ± 0.012			0.546 ± 0.007			0.440 ± 0.006	0.767 ± 0.014		4.97 ± 0.09
		68.04	0.889 ± 0.009			0.382 ± 0.006			0.308 ± 0.004	0.581 ± 0.010		3.77 ± 0.07
MB-19 and Cap. Hold. No. 3	304 SST	0.00	-0.567 ± 0.007	71.380	-	-	-	-	-	-0.567 ± 0.007	71.380	-7.94 ± 0.10
		4.45	-0.568 ± 0.008							-0.568 ± 0.008		-7.96 ± 0.11
		17.35	-0.355 ± 0.006							-0.355 ± 0.006		-4.97 ± 0.09
		35.73	0.145 ± 0.005							0.145 ± 0.005		2.03 ± 0.07
		54.04	0.546 ± 0.007							0.546 ± 0.007		7.65 ± 0.1
DUM-2D	Inconel and 304 SST	0.00	-0.828 ± 0.009	95.820	-	-	-	-	-	0.382 ± 0.006		5.35 ± 0.08
		17.35	-0.518 ± 0.008							-		-
		35.73	0.175 ± 0.002							-		-
		54.04	0.785 ± 0.008							-		-
		68.04	0.534 ± 0.006							-		-

<sup>a</sup> SST refers to stainless steel capsule holders and stainless steel shims or spacers if used.<sup>b</sup> No sample-size effect corrections have been made.

TABLE III-12. Comparison of the C/E Values for Isotopic Central Worths in the GCFR Phase-I Assembly and the GCFR Phase-II Unreflected Assembly

Isotope	C/E adjusted by the C/E of the:					
	C/E from FOP Calculation		Perturbation Denominator <sup>a</sup>		<sup>239</sup> Pu Worth	
	Phase I	Phase II	Phase I	Phase II	Phase I	Phase II
<sup>239</sup> Pu	1.28	1.21	0.96	1.03	1.00	1.00
<sup>240</sup> Pu	1.33	1.22	1.00	1.04	1.04	1.01
<sup>241</sup> Pu	1.21	1.30	0.91	1.11	0.95	1.07
<sup>242</sup> Pu	1.43	1.34	1.07	1.14	1.12	1.11
<sup>233</sup> U	1.22	1.17	0.92	0.99	0.95	0.97
<sup>235</sup> U	1.31	1.23	0.98	1.05	1.02	1.02
<sup>238</sup> U	1.23	1.12	0.92	0.95	0.96	0.93
<sup>232</sup> Th	1.27	1.20	0.95	1.02	0.99	0.99
<sup>10</sup> B	1.12	1.00	0.84	0.85	0.88	0.83
<sup>6</sup> Li	----	1.15	----	0.98	----	0.95
C	1.84	2.06	1.38	1.75	1.44	1.70
O	----	1.68	----	1.43	----	1.39
Ta	----	1.15	----	0.98	----	0.95
Fe	1.44	1.46	1.08	1.24	1.33	1.21
Ni	----	1.64	----	1.39	----	1.36
Cr	----	1.60	----	1.36	----	1.32
Mn	----	1.81	----	1.54	----	1.50
Mo	----	1.28	----	1.09	----	1.06
Al	----	1.14	----	0.97	----	0.94

<sup>a</sup>The C/E for the perturbation denominator was determined to be 0.75 for Phase I and 0.85 for Phase II.

TABLE IV-1. Concentrations and Central Worths of the Helium and Sample Impurities

	Concentrations, atoms/10 <sup>6</sup> He atoms	FOP Central Worth, 1h/10 <sup>24</sup> atoms
<sup>4</sup> He	10 <sup>6</sup>	-1.677
<sup>3</sup> He	1.3	-71.85
H	~2	-2.53
O	~1	-0.73
C	~0.2	-0.87
N	~0.2	-1.62
Ne	~0.1	-
Ar	~0.1	-

TABLE IV-2. Experimental and Calculated Worths of the Helium Samples

	Experimental, <sup>a</sup> 1h	FOP Calculated, 1h	C/E	Flux Distortion Corrected C/E
<u>Stainless Steel Cylinder</u>				
Helium @ 150.9 ± 0.5 psia	-0.145 ± 0.006	-0.235	1.62	1.44
Helium @ 300.1 ± 0.5 psia	-0.288 ± 0.007	-0.464	1.61	1.43
<u>Aluminum Cylinder</u>				
Helium @ 152.4 ± 0.5 psia	-0.161 ± 0.004	-0.235	1.46	1.31
Helium @ 299.4 ± 0.5 psia	-0.302 ± 0.005	-0.457	1.51	1.36

<sup>a</sup>Quoted uncertainties include both the statistical uncertainty and a conservative estimate of the fine-aurorod calibration uncertainty.

TABLE V-1. Description of Doppler Samples

Doppler Sample	Type	Capsule		Sample					
		Material <sup>a</sup>	Mass, g	Material	Dimensions, in.	Mass, g			
						UO <sub>2</sub>	<sup>238</sup> U	<sup>235</sup> U	O
N-1	FE	Inconel-600	421.3	UO <sub>2</sub> pellets (12)	1.0 × 12.0	1266.29 <sup>b</sup>	1108.18	7.99	150.06
MT-1	FE	Inconel-600	388.5	-	-	-	-	-	-

<sup>a</sup>Composition: 7 w/o Fe, 77 w/o Ni, 15 w/o Cr, 0.25 w/o Mn, 0.25 w/o Si.

<sup>b</sup>Composition: 88.15 w/o U, 11.85 w/o O and 0.0057 w/o <sup>234</sup>U, 0.7158 w/o <sup>235</sup>U, 99.2785 w/o <sup>238</sup>U.

TABLE V-2. Doppler Effect Worth Measurements

Sample	Average Temperature, °K	FAR Position Difference, % Travel		Doppler Reactivity Worth, <sup>a</sup> Ih	
		$\bar{D}$	$\sigma_{\bar{D}}$	$\frac{-b}{\rho}$	$\sigma_{\rho}^c$
N-1	298	-0.4538	0.0824	0.000	0.005
	496	-5.3529	0.0628	-0.272	0.005
	700	-8.8788	0.0585	-0.468	0.006
	870	-10.9877	0.1177	-0.585	0.009
	1095	-13.7019	0.0504	-0.736	0.008
MT-1	301	6.4325	0.0796	0.000	0.006
	705	6.1150	0.0575	-0.017	0.005
	1083	5.7588	0.0583	-0.037	0.005

<sup>a</sup>FAR position difference times a FAR calibration factor. For N-1 the calibration factor is +0.0555732 Ih/% travel and for MT-1 the calibration factor is +0.0551134 Ih/% travel. Estimated uncertainty in a calibration factor is ±1% of the factor value.

<sup>b</sup>Average reactivity relative to 298°K for N-1 and 301°K for MT-1.

<sup>c</sup>Average reactivity uncertainty includes 1% uncertainty in FAR calibration factor, i. e.  $\sigma_{\rho} = D [(0.01)^2 + (\sigma_{\bar{D}}/\bar{D})^2]^{1/2}$  times the appropriate FAR calibration factor.

TABLE V-3. Summary of Experimental Doppler Results

Temperature °K	Doppler Reactivity Worth, Ih			
	UO <sub>2</sub> Sample + Capsule, N-1	Empty Capsule, MT-1	UO <sub>2</sub> Sample, <sup>a</sup> (N-1)-(MT-1)	Sample, <sup>b</sup> Worth, Ih/kg of <sup>238</sup> U
300	-0.004 ± 0.004	+0.000 ± 0.005	0.000 ± 0.007	0.000 ± 0.006
400	-0.155 ± 0.003	-0.004 ± 0.005	-0.147 ± 0.006	-0.133 ± 0.005
500	-0.276 ± 0.003	-0.008 ± 0.004	-0.264 ± 0.005	-0.238 ± 0.005
600	-0.378 ± 0.003	-0.012 ± 0.003	-0.361 ± 0.005	-0.326 ± 0.004
700	-0.466 ± 0.003	-0.017 ± 0.003	-0.444 ± 0.005	-0.401 ± 0.004
800	-0.544 ± 0.004	-0.022 ± 0.003	-0.517 ± 0.005	-0.466 ± 0.004
900	-0.614 ± 0.004	-0.027 ± 0.003	-0.581 ± 0.006	-0.524 ± 0.005
1000	-0.678 ± 0.005	-0.032 ± 0.004	-0.639 ± 0.006	-0.576 ± 0.006
1100	-0.736 ± 0.005	-0.038 ± 0.005	-0.691 ± 0.007	-0.623 ± 0.007

<sup>a</sup>The N-1 capsule signal was obtained by prorating the signal of MT-1 by the ratio of the N-1 capsule mass to the MT-1 capsule mass. The ratios (421.3g/388.5g). Results are relative to a temperature of 300°K.

<sup>b</sup>UO<sub>2</sub> sample worth divided by the mass of <sup>238</sup>U in the sample. The <sup>238</sup>U mass is 1.10818 kg.

TABLE V-4. Unit-Cell Specifications for the Doppler Calculations

Region	Material <sup>c</sup>	Resolved Resonance Region <sup>a</sup> Integral Transport Theory		Unresolved Resonance Region <sup>b</sup> Equivalence Theory	
		Outer Radius, cm	Mesh Points	Outer Radius, cm	Mesh Points
Sample	UO <sub>2</sub>	1.270	2	1.270	2
Jacket	Inconel	1.524	1	1.524	1
Filter	Stainless Steel	3.117	2	3.117	2
Ring 01	Core	8.246	5	8.246	5
Core A	Core	20.000	6	59.056	20

<sup>a</sup> ENDF/B-IV data  $\leq 4.000$  keV for <sup>238</sup>U. Calculated for groups 18-27 (3.355 keV to 1.855 eV).

<sup>b</sup> ENDF/B-IV data  $\leq 46.309$  keV for <sup>238</sup>U. Calculated for groups 13-17 (40.868 to 3.355 keV).

<sup>c</sup> The ARC system code structure allows in the integral transport calculation that each material may assume independent temperatures while in the equivalence theory calculation each isotope may assume independent temperatures. Hence, in the resolved region UO<sub>2</sub> was calculated both hot (1100°K) and cold (300°K) with the core held cold; in the unresolved region <sup>234</sup>U, <sup>235</sup>U, and <sup>238</sup>U were either hot or cold in both the UO<sub>2</sub> and the core compositions.

TABLE V-5. Composition Atom Densities used in the Doppler Calculations, 10<sup>21</sup> atoms/cm<sup>3</sup>

Nuclide	UO <sub>2</sub>	Inconel	Stainless Steel	Core	Radial Blanket
Fe	-	3.9991	18.2234	15.3210	8.7909
Ni	-	41.8445	2.2287	1.3281	1.1373
Cr	-	9.2041	5.1729	2.8828	2.5087
Mn	-	0.1452	0.3970	0.2260	0.1944
Mo	-	-	-	0.3121	0.0099
C	-	-	-	0.0303	0.0281
Si	-	0.2840	0.2588	0.1791	0.1591
O	37.1533	-	-	13.4423	17.7994
<sup>234</sup> U	0.0011	-	-	-	-
<sup>235</sup> U	0.1347	-	-	0.0122	0.0194
<sup>238</sup> U	18.4412	-	-	5.5421	9.0911
<sup>238</sup> Pu	-	-	-	0.0007	-
<sup>239</sup> Pu	-	-	-	1.1832	-
<sup>240</sup> Pu	-	-	-	0.1569	-
<sup>241</sup> Pu	-	-	-	0.0163	-
<sup>242</sup> Pu	-	-	-	0.0023	-
<sup>241</sup> Am	-	-	-	0.0093	-

TABLE V-6. One-Dimensional Diffusion Theory Models for Generating Regional Fluxes<sup>a</sup>

Region	Material <sup>d</sup>	2-Region Model <sup>b</sup>		6-Region Model <sup>c</sup>	
		Outer Radius, cm	Mesh Points	Outer Radius, cm	Mesh Points
Sample <sup>e</sup>	Core	0.01	1	1.270	2
Jacket	Inconel	-	-	1.524	1
Filter	Stainless Steel	-	-	3.117	2
Ring 01	Core	-	-	8.247	5
Core A	Core	82.76	40	59.057	20
Blanket	Radial Blanket	-	-	82.759	8

<sup>a</sup>A 226 fine-group calculation with an iteration on the transverse (Z) buckling to critical ( $k = 1.0000 \pm 0.0001$ ). The buckling was assumed to be region and energy independent.

<sup>b</sup> $B^2 = 5.08 \times 10^{-4} \text{ cm}^{-2}$ .

<sup>c</sup> $B^2 = 3.21 \times 10^{-4} \text{ cm}^{-2}$ .

<sup>d</sup>Material cross-sections were collapsed, using the regional fluxes, into the 29 broad-group structure of Table II-1.

<sup>e</sup>Sample region fluxes also used to collapse  $\text{UO}_2$  (equivalence theory) material cross-sections of Table V-4.

TABLE V-7. Doppler Difference <sup>238</sup>U Group Capture Cross-Sections,<sup>b</sup>

Group	Equivalence Theory	Integral Transport Theory	
	Sample <sup>a</sup>	Sample <sup>a</sup>	Ring 01 <sup>b</sup>
13	0.005926	-	-
14	0.011482	-	-
15	0.023666	-	-
16	0.044719	-	-
17	0.080751	-	-
18	0.12449	0.13223	0.00043
19	0.16616	0.1731	0.00017
20	0.25631	0.2790	0.0001
21	0.34992	0.3593	-0.0002
22	0.30588	0.3591	0.0000
23	0.36023	0.4357	-0.0019
24	0.47679	0.3443	-0.0018
25	0.32831	0.4429	-0.0096
26	0.47392	0.02267	-0.0014
27	0.012313	-0.00221	-0.00073

<sup>a</sup> $\text{UO}_2$  sample temperature raised from 300 to 1100°K.

<sup>b</sup>Core temperature 300°K.

TABLE V-8. Integral-Transport Theory Real and Adjoint Flux Ratios

Group	Real Ratio		Adjoint Ratio		Real * Adjoint Ratio	
	Sample	Ring 01	Sample	Ring 01	Sample	Ring 01
13	0.97220	-	0.94890	-	0.92252	-
14	0.96878	-	0.94534	-	0.91583	-
15	1.11697	-	0.93953	-	1.04943	-
16	1.03175	-	0.93876	-	0.96857	-
17	1.04388	-	0.93472	-	0.97574	-
18	1.11221	1.03899	0.93107	0.97685	1.03555	1.01494
19	1.10152	1.05092	0.92819	0.97512	1.02242	1.02477
20	1.12064	1.05404	0.92021	0.97322	1.03122	1.02581
21	1.14640	1.06678	0.92316	0.97596	1.05831	1.04113
22	1.16877	1.07319	0.92142	0.97399	1.07693	1.04528
23	1.27737	1.11424	0.91360	0.97513	1.16701	1.08653
24	1.39094	1.14388	0.87560	0.97176	1.21791	1.11158
25	1.05515	1.09986	0.80277	0.96257	0.84704	1.05869
26	1.10868	1.07175	0.74461	0.95914	0.82553	1.02796
27	1.19603	1.07550	0.88997	0.96239	1.06443	1.03505

TABLE V-9. Summary of  $^{238}\text{U}$  Doppler Effect Calculations<sup>a</sup>

1. Base Doppler effect (Excludes: a. axial flux shape factor b. flux ratio factor c. hot sample-cold reactor effect)	-0.5174 Ih/kg
2. Axial flux shape factor	0.9761
3. Flux ratio factor	1.0148
4. First term of Eq. V-4	-0.5125 Ih/kg
5. Hot sample-cold reactor effect (Second term of Eq. V-4)	-0.0028 Ih/kg
6. Net calculated $^{238}\text{U}$ Doppler effect	-0.515 Ih/kg
7. Net experimental $^{238}\text{U}$ Doppler effect	-0.623 $\pm$ 0.009 Ih/kg
8. C/E Ratio	0.827
9. Resonance region components:	
a. Unresolved, groups 13-17	41.7%
b. Resolved, groups 18-23	58.1%
c. Resolved, groups 24-27	0.2%
10. Calculated $^{238}\text{U}$ Doppler effect using:	
a. Equivalence theory (SDX) $\delta_f^S$	- 3.7%
b. Isotropic diffusion coefficient fluxes	+ 6.2%

<sup>a</sup> Reactivity worths are per kilogram of  $^{238}\text{U}$  in the sample and for a temperature change from 300 to 1100°K.  $1\% \Delta k/k = 974.779 \text{ Ih}$ .



TABLE VI-1. Measured Reaction Rates at Matrix Location S-23/22

Reaction	Measured Rate <sup>a</sup>
f <sup>23</sup>	13.21 ± 0.21
f <sup>25</sup>	8.90 ± 0.10
f <sup>28</sup>	0.2734 ± 0.0022
c <sup>28</sup>	1.1512 ± 0.0064
f <sup>49</sup>	8.823 ± 0.045
f <sup>40</sup>	2.220 ± 0.014
f <sup>41</sup>	10.92 ± 0.14
f <sup>02</sup>	0.0666 ± 0.0040
c <sup>02</sup>	1.6762 ± 0.0093

<sup>a</sup> Reactions/sec/μg of sample; no isotopic corrections have been made; power level ~120 W.

TABLE VI-2. Mass and Composition of Fission Counter Sources

Principal Isotope	Mass, μg	w/o				
		<sup>233</sup> U	<sup>234</sup> U	<sup>235</sup> U	<sup>236</sup> U	<sup>238</sup> U
<sup>233</sup> U	44.555 ± 0.667	99.538	0.184	0.062	0.013	0.20
<sup>235</sup> U	78.167 ± 0.633	-	1.024	98.39	0.446	0.13
<sup>238</sup> U	416.87 ± 3.33	-	-	0.014	-	99.98
		<sup>239</sup> Pu	<sup>240</sup> Pu	<sup>241</sup> Pu	<sup>242</sup> Pu	<sup>241</sup> Am
<sup>239</sup> Pu <sup>a</sup>	81.47 ± 0.41	98.940	1.012	0.049	-	-
<sup>239</sup> Pu	27.064 ± 0.135	98.940	1.012	0.049	-	-
<sup>240</sup> Pu	76.583 ± 0.475	0.770	98.578	0.541	0.111	-
<sup>241</sup> Pu	19.51 ± 0.24	0.732	0.191	80.369	-	18.71
		<sup>232</sup> Th				
<sup>232</sup> Th	535. ± 32.	100.				

<sup>a</sup> Used for monitor counter in S-23/16.

TABLE VI-3. Measured and Calculated Central Reaction Rate Ratios

Ratio	Measured <sup>a</sup>	Calculated	C/E
$f^{23}/f^{49}$	1.460 ± 0.024	1.456	0.997
$f^{25}/f^{49}$	0.992 ± 0.012	0.9876	0.996
$f^{28}/f^{49}$	0.03086 ± 0.00029	0.02993	0.970
$c^{28}/f^{49}$	0.12994 ± 0.00098	0.13430 <sup>b</sup>	1.034
$f^{40}/f^{49}$	0.2527 ± 0.0020	0.2582	1.022
$f^{41}/f^{49}$	1.248 ± 0.018	1.2859	1.030
$f^{02}/f^{49}$	0.00732 ± 0.00044	0.00679	0.928
$c^{02}/f^{49}$	0.1844 ± 0.0014	0.1825 <sup>b</sup>	0.990

<sup>a</sup>Ratios computed on a per-atom basis.

<sup>b</sup>This calculation does not account for the stainless steel of the detector, which has been shown to affect the experimental value.

TABLE VI-4. Description of Activation Foils

Target Isotope	Material and Form	Diameter, in.	Nominal Thickness, mil	Approximate Weight of Target Element, g
U	Enriched Uranium <sup>a</sup>	0.500	4.4	0.25
U	Depleted Uranium <sup>b</sup>	0.500	5.5	0.31
Pu	Pu-Al alloy <sup>c</sup> (clad <sup>d</sup> in 5 mil aluminum)	0.425	0.4	0.02

<sup>a</sup>Isotopic composition of enriched uranium foils:

$^{234}\text{U}$ :	1.03 w/o
$^{235}\text{U}$ :	93.07
$^{236}\text{U}$ :	0.27
$^{238}\text{U}$ :	5.63

<sup>b</sup>Isotopic composition of depleted uranium foils:

$^{235}\text{U}$ :	0.215 w/o
$^{236}\text{U}$ :	0.005
$^{238}\text{U}$ :	99.78

<sup>c</sup>Isotopic composition of the plutonium foil alloy which is 98.0 w/o Pu and 1.3 w/o Al:

$^{239}\text{Pu}$ :	94.98 w/o
$^{240}\text{Pu}$ :	4.7
$^{241}\text{Pu}$ :	0.303
$^{242}\text{Pu}$ :	0.019

<sup>d</sup>Aluminum cladding is 0.5 in. diameter and 5 mils thick.

TABLE VI-5. Relative Depleted Uranium Capture Rates Used to Derive Stainless Steel Correction Factors

Location	Type <sup>a</sup>	Thickness mil <sup>b</sup>	Relative Capture Rate	Radially Corrected Rate
S22/22	N	15	960.0 ± 4.8	968.3 ± 7.8
S22/25	N	25	949.7 ± 4.8	969.9 ± 7.9
S22/28	N	35	837.3 ± 4.2	973.7 ± 7.9
S22/31	N	45	634.3 ± 3.2	969.1 ± 7.9
S24/22	S	15	904.2 ± 4.6	911.9 ± 7.4
S24/25	S	25	910.7 ± 5.3	931.1 ± 8.0
S24/28	S	30	791.1 ± 4.0	923.4 ± 7.5
S24/31	S	35	605.3 ± 3.1	933.6 ± 7.6

<sup>a</sup> N = normal-width fuel plates; S = half-width fuel plate.

<sup>b</sup> Thickness = amount of stainless steel between foil and core of fuel cans.

TABLE VI-6. Relative Unit-Cell Reaction Rates, Core Region, Row 22, 0-2 Inches

Drawer	Position, in.	Interface <sup>c</sup>	Plutonium Fission Rate	Enriched U Fission Rate	Depleted U Fission Rate	Depleted U Capture Rate
S22/22	0.0	DR-UO	-	1009.9 ± 1.7	931.8 ± 4.1	1075.1 ± 7.5
	0.125	UO-UO	-	1010.6 ± 2.9	939.2 ± 4.7	1009.8 ± 7.5
	0.250	UO-V	-	1006.6 ± 1.8	928.2 ± 4.2	1015.8 ± 7.1
	0.625 <sup>a</sup>	FE-PU	991.1 ± 2.1	1002.1 ± 1.4	993.3 ± 4.0	1030.7 ± 7.9
	0.750	PU-PU	993.6 ± 2.2	1003.6 ± 1.3	1031.1 ± 4.1	987.5 ± 7.9
	0.875	PU-FE	1001.4 ± 2.2	1002.9 ± 1.3	992.4 ± 4.0	998.8 ± 7.0
	1.500	V-UO	-	1003.5 ± 3.2	923.1 ± 5.8	998.2 ± 7.4
	1.625	UO-UO	-	1002.3 ± 1.6	918.0 ± 4.0	972.5 ± 6.5
	1.750	UO-V	-	1007.2 ± 2.9	919.7 ± 5.9	1023.4 ± 7.5
S22/23	2.125 <sup>a</sup>	FE-PU	1000.4 ± 2.0	1000.8 ± 1.2	988.2 ± 1.2	1000.5 ± 3.5
	2.250	PU-PU	997.6 ± 1.8	1001.4 ± 1.2	1029.1 ± 2.4	956.5 ± 3.4
	2.357	PU-FE	1000.0 ± 2.4	1000.0 ± 1.7	1000.0 ± 3.0	1000.0 ± 3.3
	3.000	V-UO	-	1004.6 ± 5.0	941.1 ± 6.7	1004.3 ± 6.6
	3.125	UO-UO	-	994.5 ± 1.2	937.3 ± 2.3	967.9 ± 3.5
	3.250	UO-V	-	1003.3 ± 1.6	946.0 ± 3.0	1009.9 ± 3.0
	3.625 <sup>a</sup>	FE-PU	990.1 ± 4.5	1001.6 ± 3.1	1004.6 ± 5.5	1022.6 ± 5.6
	3.750	PU-PU	990.2 ± 4.9	-	1045.2 ± 6.0	982.6 ± 6.5
	3.875	PU-FE	933.9 ± 5.0	1002.7 ± 8.9	1006.9 ± 5.8	1008.8 ± 6.6
S22/24	4.500	V-UO	-	1007.0 ± 6.2	922.7 ± 6.8	1018.4 ± 8.3
	4.625	UO-UO	-	999.3 ± 7.1	912.5 ± 6.6	971.0 ± 8.0
	4.625 <sup>b</sup>	UO-UO	-	-	913.3 ± 2.3	1048.0 ± 5.4
	4.750	UO-V	-	1000.1 ± 7.1	927.5 ± 3.5	1005.1 ± 8.1
	5.125 <sup>a</sup>	FE-PU	988.3 ± 1.9	1003.7 ± 1.5	991.3 ± 2.5	1016.9 ± 5.3
	5.250	PU-PU	988.9 ± 1.9	996.6 ± 1.5	1032.6 ± 2.6	985.0 ± 5.1
	5.375	PU-FE	989.9 ± 2.0	1002.6 ± 1.2	987.1 ± 1.5	1007.6 ± 3.6

<sup>a</sup> Mapping foil locations.

<sup>b</sup> Rectangular integrating foil.

<sup>c</sup> UO = depleted uranium oxide; FE = iron oxide; V = void can; PU = plutonium fuel; DU = depleted uranium; DR = drawer side.

TABLE VI-7. Relative Unit-Cell Reaction Rates, Core Region, Row 22, 22-24 Inches

Drawer	Position, in.	Interface <sup>c</sup>	Plutonium Fission Rate	Enriched U Fission Rate	Depleted U Fission Rate	Depleted U Capture Rate
S22/22	0.0	DR-UO	-	1016.1 ± 8.4	905.9 ± 13.6	1059.4 ± 7.1
	0.125	UO-UO	-	1015.3 ± 8.9	905.5 ± 14.9	1006.1 ± 7.2
	0.250	UO-V	-	1015.2 ± 8.6	920.3 ± 14.0	1023.2 ± 7.2
	0.625 <sup>a</sup>	FE-PU	998.7 ± 8.4	1008.2 ± 8.3	993.2 ± 14.9	992.1 ± 8.2
	0.875	PU-FE	1006.7 ± 8.5	1007.6 ± 8.3	990.5 ± 14.9	997.3 ± 7.0
	1.500	V-UO	-	1005.0 ± 10.2	900.6 ± 16.7	994.1 ± 10.4
	1.625 <sup>b</sup>	UO-UO	-	1004.1 ± 8.3	896.1 ± 13.5	969.6 ± 7.7
	1.625 <sup>b</sup>	UO-UO	-	-	867.3 ± 14.3	1022.1 ± 11.6
	1.750	UO-V	-	1005.1 ± 10.1	905.3 ± 15.7	1031.4 ± 10.7
S22/23	2.125 <sup>a</sup>	FE-PU	990.4 ± 9.2	996.6 ± 9.0	983.1 ± 15.5	1007.8 ± 9.1
	2.375	PU-FE	1000.0 ± 9.3	1000.0 ± 8.7	1000.0 ± 15.9	1000.0 ± 9.0
	3.000	V-UO	-	1004.5 ± 10.6	917.5 ± 15.6	975.9 ± 13.9
	3.125 <sup>b</sup>	UO-UO	-	1004.3 ± 10.2	907.6 ± 15.4	945.8 ± 11.9
	3.125 <sup>b</sup>	UO-UO	-	-	888.7 ± 13.5	1010.8 ± 7.2
	3.250	UO-V	-	1004.8 ± 10.6	914.4 ± 15.3	997.2 ± 14.1
	3.625 <sup>a</sup>	FE-PU	999.5 ± 8.4	1000.6 ± 8.3	993.0 ± 14.9	982.9 ± 6.8
	3.875	PU-FE	1020.6 ± 8.6	1001.1 ± 8.3	991.9 ± 14.9	1017.7 ± 8.0
S22/24	4.500	V-UO	-	1002.1 ± 8.3	914.4 ± 13.8	999.5 ± 7.9
	4.625 <sup>a</sup>	UO-UO	-	1002.6 ± 8.3	892.8 ± 13.4	962.5 ± 6.7
	4.750	UO-V	-	1002.6 ± 8.3	930.0 ± 14.0	1005.8 ± 7.1
	5.125	FE-PU	1011.3 ± 8.6	1005.2 ± 8.3	979.4 ± 14.8	993.2 ± 7.1
	5.375	PU-FE	991.1 ± 8.3	997.7 ± 8.3	973.7 ± 14.7	1019.7 ± 7.0

<sup>a</sup>Mapping foil locations.<sup>b</sup>Rectangular integrating foil.<sup>c</sup>UO = depleted uranium oxide, FE = iron oxide, V = void can; PU = plutonium fuel; DU = depleted uranium; DR = drawer side.

TABLE VI-8. Relative Unit-Cell Reaction Rates, Core Region, Row 33, 0-2 Inches

Drawer	Position, in.	Interface <sup>c</sup>	Plutonium Fission Rate	Enriched U Fission Rate	Depleted U Fission Rate	Depleted U Capture Rate
S33/22	0.0	DR-UO	-	1014.2 ± 12.0	907.8 ± 15.4	1085.3 ± 10.4
	0.125 <sup>b</sup>	UO-UO	-	1014.1 ± 11.6	897.9 ± 15.2	1025.0 ± 7.0
	0.125 <sup>b</sup>	UO-UO	-	-	899.9 ± 14.0	1012.9 ± 14.8
	0.250	UO-V	-	1012.1 ± 12.1	912.6 ± 14.4	1036.8 ± 10.0
	0.625 <sup>a</sup>	FE-PU	996.3 ± 10.7	997.4 ± 11.0	991.0 ± 13.8	1018.8 ± 12.2
	0.875	PU-FE	1008.4 ± 10.9	1006.4 ± 11.1	995.6 ± 13.8	1024.5 ± 11.6
	1.500	V-UO	-	1008.5 ± 11.3	901.8 ± 12.6	997.9 ± 11.5
	1.625	UO-UO	-	1008.0 ± 11.1	892.3 ± 12.3	974.3 ± 10.9
	1.750	UO-V	-	1005.1 ± 11.1	897.6 ± 12.6	1047.5 ± 11.7
S33/23	2.125 <sup>a</sup>	FE-PU	995.5 ± 15.2	998.7 ± 12.1	1003.2 ± 16.5	1004.1 ± 12.6
	2.375	PU-FE	1000.0 ± 10.8	1000.0 ± 11.2	1000.0 ± 14.0	1000.0 ± 11.6
	3.000	V-UO	-	1008.4 ± 14.9	917.5 ± 15.6	1004.6 ± 14.1
	3.125 <sup>b</sup>	UO-UO	-	1000.2 ± 14.8	907.4 ± 15.4	970.9 ± 9.5
	3.125 <sup>b</sup>	UO-UO	-	-	905.2 ± 12.8	1005.3 ± 12.1
	3.250	UO-V	-	999.5 ± 14.8	922.2 ± 14.5	1018.4 ± 14.0
	3.625 <sup>a</sup>	FE-PU	1001.3 ± 10.9	998.1 ± 11.1	1001.5 ± 14.0	1017.3 ± 11.9
	3.875	PU-FE	1005.9 ± 15.4	999.2 ± 13.9	998.3 ± 16.4	1028.4 ± 13.1
S33/24	4.500	V-UO	-	1015.8 ± 11.3	901.0 ± 12.7	1048.9 ± 11.6
	4.625 <sup>a</sup>	UO-UO	-	999.7 ± 11.1	897.1 ± 12.6	994.3 ± 11.1
	4.750	UO-V	-	1001.3 ± 11.1	912.2 ± 12.8	1015.3 ± 11.5
	5.125	FE-PU	1010.1 ± 10.8	1006.0 ± 11.1	999.6 ± 13.9	1016.2 ± 12.2
	5.375	PU-FE	1007.1 ± 10.8	1004.7 ± 11.1	1003.9 ± 13.9	1043.2 ± 12.4

<sup>a</sup>Mapping foil locations.<sup>b</sup>Rectangular integrating foil.<sup>c</sup>UO = depleted uranium oxide; FE = iron oxide; V = void can; PU = plutonium fuel; DU = depleted uranium; DR = drawer side.

TABLE VI-9. Relative Unit-Cell Reaction Rates, Axial Blanket Region, Row 22, 24-26 Inches

Drawer	Position, in.	Interface <sup>c</sup>	Enriched U Fission Rate	Depleted U Fission Rate	Depleted U Capture Rate
S22/22	0.0	DR-UO	1018.4 ± 12.4	1058.2 ± 29.1	1134.4 ± 13.3
	0.125 <sub>b</sub>	UO-UO	1017.5 ± 12.4	1055.0 ± 29.1	1060.5 ± 12.3
	0.125 <sub>b</sub>	UO-UO	-	1044.8 ± 24.6	1100.8 ± 15.2
	0.250	UO-V	1016.9 ± 10.3	1060.8 ± 24.1	1094.1 ± 10.4
	0.500	V-UO	1020.9 ± 12.7	1037.2 ± 27.3	1030.4 ± 14.0
	0.625	UO-UO	1016.4 ± 12.6	1004.0 ± 26.7	1007.7 ± 13.5
	0.750	UO-UO	1003.9 ± 10.3	992.4 ± 22.5	992.4 ± 9.9
	0.875	UO-DU	1011.8 ± 12.5	995.7 ± 26.5	984.3 ± 13.9
	1.000	DU-V	1014.3 ± 12.6	1011.9 ± 26.9	1044.1 ± 14.5
	1.500	V-UO	1009.6 ± 10.3	1063.2 ± 24.1	1056.2 ± 10.2
	1.625	UO-UO	1008.8 ± 12.3	1059.1 ± 29.2	1012.6 ± 10.9
	1.750	UO-V	1008.2 ± 12.4	1065.0 ± 29.3	1043.1 ± 11.3
S22/23	2.000	DR-UO	1012.0 ± 12.5	1037.5 ± 26.7	1167.4 ± 22.6
	2.125 <sub>b</sub>	UO-UO	1007.5 ± 12.3	1004.3 ± 26.1	1045.6 ± 20.5
	2.125 <sub>b</sub>	UO-UO	-	995.7 ± 22.1	1065.5 ± 7.5
	2.250	UO-UO	1000.0 ± 9.6	992.7 ± 21.8	1017.6 ± 7.0
	2.375	UO-DU	1000.0 ± 9.6	1000.0 ± 22.0	1000.0 ± 6.9
	2.500	DU-V	1003.4 ± 9.6	1009.3 ± 22.3	1017.2 ± 7.1
	3.000	V-UO	1003.3 ± 9.6	1053.8 ± 23.1	1042.2 ± 7.2
	3.125	UO-UO	1007.8 ± 9.6	1054.1 ± 23.4	1024.1 ± 7.0
	3.250	UO-V	1007.4 ± 9.7	1051.2 ± 23.1	1053.5 ± 7.7
	3.500	V-UO	1007.7 ± 10.2	1030.8 ± 23.4	1032.5 ± 9.8
	3.625	UO-UO	998.5 ± 10.1	1018.1 ± 23.2	1025.1 ± 10.1
	3.750 <sup>a</sup>	UO-UO	988.4 ± 10.0	1002.0 ± 22.8	1001.0 ± 9.9
	3.875	UO-DU	995.9 ± 10.0	1007.5 ± 22.9	1020.7 ± 9.8
	4.000	DU-V	995.9 ± 10.1	1009.4 ± 23.0	1073.6 ± 10.5
S22/24	4.500	V-UO	1010.1 ± 9.7	1036.9 ± 22.9	1114.0 ± 7.6
	4.625	UO-UO	1003.9 ± 9.6	1028.7 ± 22.7	1041.4 ± 6.9
	4.750	UO-V	1003.1 ± 9.6	1042.9 ± 23.1	1074.4 ± 7.3
	5.000	V-UO	1001.1 ± 9.6	1009.1 ± 22.3	1063.2 ± 7.4
	5.125	UO-UO	1001.4 ± 9.6	1010.6 ± 22.4	1031.8 ± 7.2
	5.250	UO-UO	986.9 ± 9.4	997.9 ± 22.0	1025.5 ± 6.9
	5.375	UO-DU	994.9 ± 9.5	997.5 ± 22.1	1015.8 ± 7.0
	5.500	DU-V	999.8 ± 9.6	1035.9 ± 22.7	1118.6 ± 9.0

<sup>a</sup> Mapping foil locations.<sup>b</sup> Rectangular integrating foils.<sup>c</sup> UO = depleted uranium oxide; DU = depleted uranium; V = void can; DR = drawer side.

TABLE VI-10. Relative Unit-Cell Reaction Rates, Axial Blanket Region, Row 22, 34-36 Inches

Drawer	Position, in.	Interface <sup>c</sup>	Enriched U Fission Rate	Depleted U Fission Rate	Depleted U Capture Rate
S22/22	2.0	DR-UO	1015.1 ± 22.9	991.6 ± 29.2	1155.9 ± 30.6
	2.125	UO-UO	1015.8 ± 22.9	983.6 ± 29.1	1035.3 ± 27.8
	2.250	UO-UO	1013.1 ± 22.8	1047.1 ± 30.3	997.8 ± 27.0
	2.375	UO-DU	1000.0 ± 22.5	1000.0 ± 31.6	1000.0 ± 28.5
	2.500	DU-V	999.5 ± 22.5	1053.2 ± 32.6	1063.7 ± 28.6
	3.000	V-UO	1006.3 ± 24.5	1018.3 ± 31.2	1057.9 ± 27.2
	3.125	UO-UO	1010.8 ± 24.6	1007.1 ± 30.9	1039.6 ± 26.7
	3.125 <sub>b</sub>	UO-UO	-	961.8 ± 27.5	1085.0 ± 26.7
	3.250	UO-V	1010.4 ± 24.6	1023.6 ± 30.8	1069.4 ± 27.7
	3.500	V-UO	1016.4 ± 22.7	1059.0 ± 28.7	1048.1 ± 26.0
	3.625	UO-UO	1006.0 ± 22.4	972.6 ± 26.4	1017.8 ± 24.6
	3.750 <sup>a</sup>	UO-UO	996.6 ± 22.2	966.6 ± 26.4	1001.5 ± 24.3
	3.875	UO-DU	987.3 ± 22.0	971.4 ± 26.3	979.9 ± 23.9
	4.000	DU-V	1008.2 ± 22.4	979.5 ± 26.5	1171.6 ± 28.5

<sup>a</sup> Mapping foil locations.<sup>b</sup> Rectangular integrating foil.<sup>c</sup> UO = depleted uranium oxide; DU = depleted uranium; V = void can; DR = drawer side.

TABLE VI-11. Relative Unit-Cell Reaction Rates, Radial Blanket Region, 0-2 Inches

Drawer	Position, in.	Interface <sup>c</sup>	Enriched U Fission Rate	Depleted U Fission Rate	Depleted U Capture Rate
S22/34	0.0	DR-UO	1038.1 ± 12.2	993.6 ± 20.7	1179.4 ± 14.2
	0.125 <sup>b</sup>	UO-UO	1019.2 ± 11.9	995.5 ± 21.3	995.5 ± 12.5
	0.125 <sup>b</sup>	UO-UO	-	1019.7 ± 16.6	1048.6 ± 12.2
	0.250 <sup>a</sup>	UO-UO	1020.8 ± 6.7	1016.7 ± 15.7	1000.1 ± 9.2
	0.375	UO-UO	1000.0 ± 6.7	1000.0 ± 15.4	1000.0 ± 10.1
	0.500	UO-V	993.7 ± 6.5	1073.9 ± 17.1	1064.9 ± 10.0
	1.000	V-UO	1027.9 ± 6.8	964.7 ± 15.0	993.2 ± 9.3
	1.125	UO-UO	1042.9 ± 13.0	939.6 ± 15.4	962.4 ± 10.3
	1.250 <sup>a</sup>	UO-UO	1026.8 ± 12.9	936.7 ± 15.4	932.5 ± 10.1
	1.375	UO-UO	1022.6 ± 12.8	931.5 ± 16.0	944.2 ± 10.3
	1.500	UO-DU	1004.0 ± 12.6	943.6 ± 15.6	911.7 ± 9.9
	1.625	DU-V	1008.5 ± 6.7	968.2 ± 15.1	1057.3 ± 9.9
S22/37	0.0	DR-UO	1043.3 ± 11.1	909.3 ± 15.5	1181.1 ± 17.1
	0.125	UO-UO	1028.2 ± 10.8	901.0 ± 16.9	1006.9 ± 15.5
	0.250 <sup>a</sup>	UO-UO	1011.5 ± 10.7	906.2 ± 15.5	989.5 ± 15.4
	0.375 <sup>b</sup>	UO-UO	990.9 ± 12.4	879.8 ± 19.2	1006.5 ± 17.9
	0.375 <sup>b</sup>	UO-UO	-	868.1 ± 20.7	983.3 ± 19.7
	0.500	UO-V	984.6 ± 12.2	947.2 ± 21.1	1073.3 ± 19.0
	1.000	V-UO	1065.1 ± 11.3	989.4 ± 17.4	1090.2 ± 17.2
	1.125	UO-UO	1051.5 ± 11.1	936.7 ± 16.9	1040.6 ± 16.6
	1.250 <sup>a</sup>	UO-UO	1035.3 ± 11.0	943.7 ± 17.2	1009.9 ± 16.2
	1.375	UO-UO	1031.1 ± 10.9	941.0 ± 19.3	1017.3 ± 16.7
	1.500	UO-DU	1012.3 ± 10.8	965.2 ± 17.5	986.1 ± 16.5
	1.625	DU-V	990.2 ± 11.1	968.3 ± 18.3	1335.7 ± 20.3
S34/23	0.0	DR-UO	1001.9 ± 6.3	1013.1 ± 17.7	1151.3 ± 9.9
	0.125	UO-UO	979.6 ± 11.3	996.0 ± 18.5	974.3 ± 11.6
	0.250 <sup>a</sup>	UO-UO	981.0 ± 11.4	1022.1 ± 18.1	962.6 ± 11.5
	0.375	UO-UO	994.4 ± 11.5	967.2 ± 16.8	998.1 ± 10.4
	0.500	UO-V	994.2 ± 6.3	1022.4 ± 17.9	1067.6 ± 10.1
	1.000	V-UO	992.9 ± 6.5	1057.7 ± 18.9	1088.9 ± 9.9
	1.125	UO-UO	990.8 ± 6.4	1020.5 ± 17.8	1055.7 ± 9.6
	1.250 <sup>a</sup>	UO-UO	989.1 ± 6.3	1006.9 ± 17.6	1020.0 ± 9.4
	1.375	UO-UO	990.9 ± 6.4	998.6 ± 17.9	1050.2 ± 9.7
	1.500	UO-DU	990.4 ± 6.3	998.9 ± 17.5	1018.8 ± 9.1
	1.625	DU-V	1000.2 ± 6.4	1009.1 ± 17.6	1124.1 ± 9.7
S37/23	0.0	DR-UO	1003.3 ± 9.8	992.6 ± 22.4	1165.1 ± 15.8
	0.125	UO-UO	985.1 ± 9.5	1005.9 ± 24.2	973.3 ± 14.1
	0.250 <sup>a</sup>	UO-UO	986.6 ± 9.6	1043.6 ± 23.3	966.7 ± 14.2
	0.375	UO-UO	1000.0 ± 9.7	1000.0 ± 22.4	1000.0 ± 14.2
	0.500	UO-V	1004.1 ± 9.7	1079.4 ± 25.8	1067.9 ± 14.9
	1.000	V-UO	1007.6 ± 9.8	1062.6 ± 25.4	1064.8 ± 15.3
	1.125	UO-UO	998.2 ± 11.6	1007.0 ± 20.6	1035.5 ± 13.0
	1.250 <sup>a</sup>	UO-UO	996.5 ± 11.6	1003.9 ± 20.6	1003.4 ± 12.7
	1.375	UO-UO	998.3 ± 11.6	998.3 ± 21.0	1016.0 ± 12.9
	1.500	UO-DU	997.8 ± 11.6	1011.3 ± 20.8	981.0 ± 12.4
	1.625	DU-V	1000.3 ± 9.7	1009.0 ± 22.8	1149.2 ± 15.7

<sup>a</sup> Mapping foil locations.<sup>b</sup> Rectangular integrating foil.<sup>c</sup> UO = depleted uranium oxide; DU = depleted uranium; V = void can; DR = drawer side.

TABLE VI-12. Comparison of Integrating Foil Results  
with Linear Integration of Circular Foil  
Results for Selected  $U_3O_8$  Plates

Location	$^{238}U$ Capture Rate		$^{238}U$ Fission Rate	
	Integrating Foil	Circular Foils <sup>a</sup>	Integrating Foil	Circular Foils <sup>a</sup>
S22/22	1022.1 $\pm$ 11.6	991.2 $\pm$ 9.1	867.3 $\pm$ 14.3	899.5 $\pm$ 14.8
S22/23	1010.8 $\pm$ 7.2	966.2 $\pm$ 13.0	888.7 $\pm$ 13.5	911.8 $\pm$ 15.4
S22/24	1048.0 $\pm$ 5.4	991.4 $\pm$ 8.1	913.3 $\pm$ 2.3	918.8 $\pm$ 5.9
S33/22	1012.9 $\pm$ 14.8	1043.0 $\pm$ 8.6	899.9 $\pm$ 14.0	904.0 $\pm$ 15.0
S33/23	1005.3 $\pm$ 12.1	991.2 $\pm$ 11.8	905.2 $\pm$ 12.8	913.6 $\pm$ 15.2
S22/22	1100.8 $\pm$ 15.2	1087.4 $\pm$ 12.1	1044.8 $\pm$ 24.6	1057.2 $\pm$ 27.8
S22/23	1065.6 $\pm$ 7.5	1069.0 $\pm$ 17.6	995.7 $\pm$ 22.1	1009.7 $\pm$ 25.2
S22/34	1048.6 $\pm$ 12.2	1042.6 $\pm$ 12.1	1019.7 $\pm$ 16.6	1000.3 $\pm$ 19.8
S22/37	983.3 $\pm$ 19.7	1018.9 $\pm$ 17.6	868.1 $\pm$ 20.7	903.2 $\pm$ 18.8

<sup>a</sup>Linear integration of straight line joining edge-center-edge foils.

TABLE VI-13.  $^{238}U$  Capture Rate Ratios of Plate-Averaged to Surface-Foil-Averaged and to Center-Foil-Averaged

Location	Plate Average	Plate Average
	Surface-Foil Average <sup>a</sup>	Center-Foil <sup>b</sup>
S22/22	0.9658 $\pm$ 0.0109	1.0086 $\pm$ 0.0114
S22/23	0.9547 $\pm$ 0.0086	1.0146 $\pm$ 0.0091
S22/23	0.9626 $\pm$ 0.0093	1.0112 $\pm$ 0.0097
S22/24	0.9672 $\pm$ 0.0092	1.0102 $\pm$ 0.0096
Average	0.9620 $\pm$ 0.0047	-

<sup>a</sup>No stainless steel corrections have been made to the foil values.

<sup>b</sup>Stainless steel correction factor of 0.984  $\pm$  0.008 applied to center-foil value.

TABLE VI-14. Cell-Average to Mapping-Foil Ratios

Unit-Cell Location	Region	Mapping Foil Location <sup>e</sup>	Cell Average/Mapping Foil			
			Plutonium Fission	Enriched U Fission	Depleted U Fission	Depleted <sub>2</sub> U Capture
Row 22, 0-2 <sup>a</sup>	Core	C-I	1.0024 ± 0.0035	1.0001 ± 0.0032	0.9872 ± 0.0057	0.9542 ± 0.0109
		C-II-L	0.9931 ± 0.0034	1.0014 ± 0.0031	0.9923 ± 0.0043	0.9830 ± 0.0091
		C-II-R	1.0034 ± 0.0053	1.0006 ± 0.0042	0.9761 ± 0.0067	0.9618 ± 0.0098
		C-III	1.0052 ± 0.0053	0.9986 ± 0.0032	0.9892 ± 0.0048	0.9672 ± 0.0097
Row 22, 22-24 <sup>b</sup>	Core	C-I	1.0036 ± 0.0121	0.9957 ± 0.0119	0.9743 ± 0.0192	0.9820 ± 0.0121
		C-II-L	1.0120 ± 0.0128	1.0073 ± 0.0126	0.9843 ± 0.0200	0.9667 ± 0.0124
		C-II-R	1.0028 ± 0.0121	1.0033 ± 0.0120	0.9745 ± 0.0193	0.9912 ± 0.0114
		C-III	0.9911 ± 0.0120	0.9987 ± 0.0120	0.9880 ± 0.0196	0.9809 ± 0.0114
Row 33, 0-2 <sup>c</sup>	Core	C-I	1.0068 ± 0.0161	1.0060 ± 0.0162	0.9821 ± 0.0182	0.9744 ± 0.0165
		C-II-R	1.0018 ± 0.0162	1.0053 ± 0.0163	0.9718 ± 0.0181	0.9758 ± 0.0163
		C-III	0.9930 ± 0.0159	0.9974 ± 0.0161	0.9736 ± 0.0180	0.9769 ± 0.0166
Row 22, 24-26 <sup>d</sup>	Ax. Blanket	A-II-R	-	1.0055 ± 0.0147	1.0006 ± 0.0329	1.0110 ± 0.0140
S34/23	Rad. Blanket	R-I-R	-	1.0019 ± 0.0101	0.9994 ± 0.0248	1.0190 ± 0.0136
S37/23	Rad. Blanket	R-I-L	-	1.0104 ± 0.0145	0.9724 ± 0.0304	1.0648 ± 0.0212
S22/34	Rad. Blanket	R-I-L	-	0.9961 ± 0.0119	0.9548 ± 0.0218	0.9875 ± 0.0138
S22/37	Rad. Blanket	R-I-L	-	1.0073 ± 0.0153	1.0342 ± 0.0263	1.0751 ± 0.0241
		R-I-R	-	0.9841 ± 0.0150	0.9931 ± 0.0260	1.0534 ± 0.0239

<sup>a</sup>Drawers S22/22, S22/23, S22/24, 0-2 in. from axial midplane.<sup>b</sup>Drawers S22/22, S22/23, S22/24, 22-24 in. from axial midplane.<sup>c</sup>Drawers S33/22, S33/23, S33/24, 0-2 in. from axial midplane.<sup>d</sup>Drawers S22/22, S22/23, S22/24, 24-26 in. from axial midplane.<sup>e</sup>First letter denotes region (C = core, A = axial blanket, R = radial blanket), Roman numeral indicates drawer type, second letter denotes either left or right mapping foil location.<sup>f</sup>No stainless steel corrections applied to mapping foil data.

TABLE VI-15. Unit-Cell Mapping Foil Reaction Rates, Normalized to Absolute Fission Counter Result

Unit-Cell Location	Region	Mapping Foil Location <sup>e</sup>	Mapping Foil Reaction Rates, Reactions/sec/g			
			Plutonium Fission (× 10 <sup>7</sup> )	Enriched U Fission (× 10 <sup>7</sup> )	Depleted U Fission (× 10 <sup>6</sup> )	Depleted U Capture (× 10 <sup>6</sup> )
Row 22, 0-2 <sup>a</sup>	Core	C-I	5.0998 ± 0.568%	5.8023 ± 1.151%	1.8246 ± 0.842%	6.4111 ± 0.736%
		C-II-L	5.2057 ± 0.575%	4.8523 ± 1.151%	1.8477 ± 0.818%	6.3785 ± 0.677%
		C-II-R	5.1709 ± 0.703%	4.8676 ± 1.186%	1.8750 ± 0.977%	6.4874 ± 0.800%
		C-III	5.1386 ± 0.570%	4.8383 ± 1.151%	1.8303 ± 0.843%	6.3527 ± 0.774%
Row 22, 22-24 <sup>b</sup>	Core	C-I	2.4723 ± 0.577%	2.4387 ± 1.152%	0.8063 ± 0.835%	3.2646 ± 0.811%
		C-II-L	2.4792 ± 0.702%	2.4390 ± 1.208%	0.8124 ± 0.966%	3.3989 ± 0.889%
		C-II-R	2.5111 ± 0.579%	2.4546 ± 1.150%	0.8192 ± 0.837%	3.2989 ± 0.669%
		C-III	2.5295 ± 0.580%	2.4460 ± 1.151%	0.7993 ± 0.843%	3.2823 ± 0.699%
Row 33, 0-2 <sup>c</sup>	Core	C-I	2.2353 ± 0.580%	2.2470 ± 1.151%	0.6782 ± 0.844%	3.1475 ± 0.775%
		C-II-R	2.2805 ± 0.596%	2.2737 ± 1.161%	0.7047 ± 0.864%	3.1804 ± 0.722%
		C-III	2.2733 ± 0.564%	2.2715 ± 1.151%	0.6880 ± 0.844%	3.1471 ± 0.775%
Row 22, 24-26 <sup>d</sup>	Ax. Blanket	A-II-R	-	2.0394 ± 1.199%	0.4247 ± 1.052%	2.6610 ± 0.960%
S34/23	Rad. Blanket	R-I-R	-	1.9307 ± 1.199%	0.3598 ± 0.975%	2.4417 ± 0.957%
S37/23	Rad. Blanket	R-I-L	-	0.9324 ± 1.210%	0.08814 ± 1.312%	1.1397 ± 1.246%
S22/34	Rad. Blanket	R-I-L	-	1.9730 ± 1.204%	0.4290 ± 0.965%	2.5606 ± 0.920%
S22/37	Rad. Blanket	R-I-L	-	0.8769 ± 1.216%	0.09669 ± 1.261%	1.0960 ± 1.261%
		R-I-R	-	0.7567 ± 1.217%	0.07779 ± 1.410%	0.9221 ± 1.311%

<sup>a</sup>Drawers S22/22, S22/23, S22/24, 0-2 in. from axial midplane.<sup>b</sup>Drawers S22/22, S22/23, S22/24, 22-24 in. from axial midplane.<sup>c</sup>Drawers S33/22, S33/23, S33/24, 0-2 in. from axial midplane.<sup>d</sup>Drawers S22/22, S22/23, S22/24, 24-26 in. from axial midplane.<sup>e</sup>First letter denotes region (C = core, A = axial blanket, R = radial blanket), Roman numeral indicates drawer type, second letter denotes either left or right mapping foil location.<sup>f</sup>No stainless steel corrections applied to mapping foil data.



TABLE VI-16. Normalization Factors and Axial Correction Factors  
for Unit-Cell Data

Reaction	Normalization Factor	Axial Correction Factors		
		0-2 in.	22-24 in.	24-26 in.
$^{239}\text{Pu}$ Fission	$5.2500 \times 10^4 \pm 0.544\%$	0.9916	1.0597	-
Enriched U Fission	$4.8790 \times 10^4 \pm 1.146\%$	0.9956	1.0935	1.1053
Depleted U Fission	$1.9249 \times 10^3 \pm 0.811\%$	-	-	-
$^{238}\text{U}$ Capture	$6.5247 \times 10^2 \pm 0.589\%$	-	-	-

TABLE VI-17. Cell-Averaged Reaction Rates at Unit-Cell Locations

Unit-Cell Location	Region	Mapping Foil Location <sup>e</sup>	Cell Average Reaction Rates, Reactions/sec/g					
			$^{239}\text{Pu}$ Fission ( $\times 10^7$ )	$^{238}\text{U}$ Capture ( $\times 10^6$ )	Enriched U Fission ( $\times 10^7$ )	Depleted U Fission ( $\times 10^5$ )	$^{235}\text{U}$ Fission ( $\times 10^7$ )	$^{238}\text{U}$ Fission ( $\times 10^5$ )
Row 22, 0-2 <sup>a</sup>	Core	C-I	4.9348 $\pm$ 0.631%	6.1053 $\pm$ 1.129%	4.8028 $\pm$ 1.186%	18.012 $\pm$ 0.937%	5.1347 $\pm$ 1.186%	16.944 $\pm$ 0.937%
		C-II-L	4.9906 $\pm$ 0.637%	6.2579 $\pm$ 1.091%	4.8591 $\pm$ 1.186%	18.335 $\pm$ 0.916%	5.1947 $\pm$ 1.186%	17.254 $\pm$ 0.916%
		C-II-R	5.0087 $\pm$ 0.755%	6.2273 $\pm$ 1.171%	4.8705 $\pm$ 1.220%	18.302 $\pm$ 1.060%	5.2070 $\pm$ 1.220%	17.219 $\pm$ 1.060%
		C-III	4.9863 $\pm$ 0.633%	6.1323 $\pm$ 1.154%	4.8315 $\pm$ 1.186%	18.105 $\pm$ 0.938%	5.1654 $\pm$ 1.186%	17.030 $\pm$ 0.938%
Row 22, 22-24 <sup>b</sup>	Core	C-I	2.3952 $\pm$ 1.039%	3.1996 $\pm$ 1.227%	2.4282 $\pm$ 1.442%	7.8558 $\pm$ 1.533%	2.5979 $\pm$ 1.442%	7.3126 $\pm$ 1.533%
		C-II-L	2.4220 $\pm$ 1.113%	3.2793 $\pm$ 1.280%	2.4568 $\pm$ 1.487%	7.9965 $\pm$ 1.608%	2.6284 $\pm$ 1.487%	7.4470 $\pm$ 1.608%
		C-II-R	2.4309 $\pm$ 1.040%	3.2636 $\pm$ 1.138%	2.4627 $\pm$ 1.441%	7.9890 $\pm$ 1.534%	2.6348 $\pm$ 1.441%	7.4381 $\pm$ 1.534%
		C-III	2.4202 $\pm$ 1.041%	3.2134 $\pm$ 1.156%	2.4428 $\pm$ 1.441%	7.8971 $\pm$ 1.463%	2.6135 $\pm$ 1.441%	7.3506 $\pm$ 1.463%
Row 33, 0-2 <sup>c</sup>	Core	C-I	2.1725 $\pm$ 1.324%	3.0669 $\pm$ 1.427%	2.2605 $\pm$ 1.647%	6.6606 $\pm$ 1.487%	2.4195 $\pm$ 1.647%	6.1533 $\pm$ 1.487%
		C-II-R	2.2055 $\pm$ 1.331%	3.1034 $\pm$ 1.399%	2.2858 $\pm$ 1.654%	6.8483 $\pm$ 1.499%	2.4464 $\pm$ 1.654%	6.3356 $\pm$ 1.499%
		C-III	2.1791 $\pm$ 1.317%	3.0744 $\pm$ 1.427%	2.2656 $\pm$ 1.647%	6.6984 $\pm$ 1.487%	2.4249 $\pm$ 1.647%	6.1900 $\pm$ 1.487%
Row 22, 24-26 <sup>d</sup>	Ax. Blanket	A-II-R	-	2.6903 $\pm$ 1.369%	2.0506 $\pm$ 1.595%	4.2495 $\pm$ 2.591%	2.1975 $\pm$ 1.595%	3.7850 $\pm$ 2.591%
S34/23	Rad. Blanket	R-I-R	-	2.4881 $\pm$ 1.442%	1.9344 $\pm$ 1.432%	3.5958 $\pm$ 2.016%	2.0736 $\pm$ 1.432%	3.1566 $\pm$ 2.016%
S37/23	Rad. Blanket	R-I-L	-	1.2136 $\pm$ 1.897%	0.9421 $\pm$ 1.608%	0.8571 $\pm$ 2.556%	1.0113 $\pm$ 1.608%	0.6410 $\pm$ 2.556%
S22/34	Rad. Blanket	R-I-L	-	2.5286 $\pm$ 1.410%	1.9653 $\pm$ 1.566%	4.0961 $\pm$ 1.939%	2.1061 $\pm$ 1.566%	3.6510 $\pm$ 1.939%
S22/37	Rad. Blanket	R-I-L	-	1.1783 $\pm$ 2.051%	0.8833 $\pm$ 1.635%	1.0000 $\pm$ 2.268%	0.9479 $\pm$ 1.635%	0.7979 $\pm$ 2.268%
		R-I-R	-	0.9713 $\pm$ 2.082%	0.7447 $\pm$ 1.636%	0.7725 $\pm$ 2.354%	0.7992 $\pm$ 1.636%	0.6019 $\pm$ 2.354%

<sup>a</sup>Drawers S22/22, S22/23, S22/24, 0-2 in. from axial midplane.

<sup>b</sup>Drawers S22/22, S22/23, S22/24, 22-24 in. from axial midplane.

<sup>c</sup>Drawers S33/22, S33/23, S33/24, 0-2 in. from axial midplane.

<sup>d</sup>Drawers S22/22, S22/23, S22/24, 24-26 in. from axial midplane.

<sup>e</sup>First letter denotes region (C = core, A = axial blanket, R = radial blanket), Roman numeral indicates drawer type, second letter denotes either left or right mapping foil location.

TABLE VI-18. Measured and Calculated Cell-Averaged Reaction Rate Ratios

Location	Region	$f^{28}/f^{49}$			$c^{28}/f^{49}$			$f^{25}/f^{49}$		
		Measured	Calculated	C/E	Measured	Calculated	C/E	Measured	Calculated	C/E
S22/23	Core, 0-2 <sup>a</sup>	0.03303 ± 0.00019	0.03265	0.988	0.1196 ± 0.0008	0.1301	1.088	0.9864 ± 0.0067	0.9707	0.984
S22/23	Core, 22-24 <sup>b</sup>	0.02937 ± 0.00027	0.02692	0.917	0.1290 ± 0.0010	0.1430	1.109	1.0283 ± 0.0092	1.0245	0.996
S33/23	Core, 0-2 <sup>c</sup>	0.02738 ± 0.00032	0.02638	0.963	0.1355 ± 0.0015	0.1446	1.067	1.0554 ± 0.0129	1.0319	0.978
		$f^{28}/f^{25}$			$c^{28}/f^{25}$					
		Measured	Calculated	C/E	Measured	Calculated	C/E			
S22/23	Ax. Bl., 24-26 <sup>d</sup>	0.01744 ± 0.00053	0.01908	1.094	0.1240 ± 0.0026	0.1356	1.094			
S34/23	Rad. Bl., 0-2 <sup>e</sup>	0.01542 ± 0.00038	0.01706	1.107	0.1215 ± 0.0025	0.1364	1.123			
S37/23	Rad. Bl., 0-2 <sup>e</sup>	0.00642 ± 0.00019	0.00886	1.380	0.1215 ± 0.0030	0.1378	1.134			
S22/34	Rad. Bl., 0-2 <sup>e</sup>	0.01756 ± 0.00044	0.01703	0.970	0.1216 ± 0.0026	0.1363	1.121			
S22/37	Rad. Bl., 0-2 <sup>e</sup>	0.00804 ± 0.00016	0.00893	1.111	0.1245 ± 0.0023	0.1376	1.104			

<sup>a</sup> Drawers S22/22, S22/23 and S22/24, 0-2 in. from axial midplane.<sup>b</sup> Drawers S22/22, S22/23 and S22/24, 22-24 in. from axial midplane.<sup>c</sup> Drawers S33/22, S33/23 and S33/24, 0-2 in. from axial midplane.<sup>d</sup> Drawers S22/22, S22/23 and S22/24, 24-26 in. from axial midplane.<sup>e</sup> Radial blanket drawer, 0-2 in. from axial midplane.

TABLE VII-1. Normalized Experimental Radial Reaction Rate Data

Row/Col	Radius of Measurement, cm	Unreflected Assembly				Reflected Assembly		
		$^{239}\text{Pu}_f$	$^{235}\text{U}_f$	$^{238}\text{U}_f$	$^{238}\text{U}_c$	$^{235}\text{U}_f$	$^{238}\text{U}_f$	$^{238}\text{U}_c$
S23/22	- 6.48	987.0	987.8	986.4	983.6	986.7	984.7	982.7
S23/23	- 2.22	994.9	1004.9	1004.6	1018.7	1004.0	1004.1	1016.8
S23/23	1.59	1002.0	1002.3	1001.5	991.8	1004.9	1004.8	994.6
S23/24	5.84	993.3	989.9	997.2	992.9	991.1	990.1	982.0
S23/25	10.10	977.1	976.2	970.6	964.9	977.7	973.2	983.1
S23/26	14.35	960.1	961.2	951.3	970.1	957.2	958.6	979.7
S23/26	18.16	934.1	922.9	923.3	926.5	928.1	927.3	933.4
S23/27	22.42	883.7	892.3	884.7	893.3	884.8	886.0	900.9
S23/28	26.67	839.4	847.8	827.7	846.1	848.5	831.5	854.6
S23/29	30.92	793.5	801.6	785.3	827.2	802.2	784.2	834.8
S23/29	34.73	747.8	750.4	731.9	753.2	753.2	729.8	763.3
S23/30	38.99	676.4	687.3	666.7	699.0	690.3	668.2	718.4
S23/31	43.24	619.7	626.9	600.5	632.8	635.5	594.4	651.9
S23/32	47.50	554.5	570.1	528.1	595.1	579.8	522.1	608.1
S23/32	51.31	492.8	509.7	447.1	520.1	523.9	448.9	553.4
S23/33	55.56	417.8	448.1	352.6	471.1	468.5	354.0	505.3
S23/34	58.86		400.9	219.5	441.1	438.1	217.9	475.5
S23/34	61.40		367.8	180.1	393.7	407.5	178.0	429.4
S23/35	64.39		325.8	123.6	357.9	378.4	121.9	405.7
S23/35	66.93		296.2	105.1	312.8	351.1	102.4	361.6
S23/36	69.91		254.5	73.48	274.4	325.3	71.32	340.7
S23/36	72.45		223.1	63.16	228.8	303.7	61.97	304.0
S23/37	75.44		184.3	44.06	193.3	285.1	43.88	290.3
S23/37	77.98		157.3	35.90	156.5	269.2	38.55	256.8

TABLE VII-2. Normalized Calculated Radial Reaction Rate Data

Radius, cm	Unreflected Assembly				Reflected Assembly			
	$^{239}\text{Pu}_f$	$^{235}\text{U}_f$	$^{238}\text{U}_f$	$^{238}\text{U}_c$	$^{239}\text{Pu}_f$	$^{235}\text{U}_f$	$^{238}\text{U}_f$	$^{238}\text{U}_c$
-6.91	987.9	987.8	987.8	988.0	988.2	988.5	988.3	988.6
-4.14	995.7	995.7	995.9	995.7	995.9	996.0	995.9	996.1
-1.38	999.8	999.8	1000.0	999.8	999.9	999.9	1000.0	999.9
1.38	1000.2	1000.2	1000.0	1000.2	1000.1	1000.1	1000.0	1000.1
4.14	996.7	996.7	996.9	996.7	996.4	996.7	996.4	996.7
6.91	989.5	989.6	989.3	989.7	989.2	989.5	989.3	989.7
9.67	978.6	978.8	978.6	979.1	978.2	978.6	978.1	979.0
12.43	963.9	964.4	963.9	964.9	963.7	964.5	963.4	965.1
15.19	945.6	946.6	945.0	947.1	945.5	946.7	944.6	947.7
17.95	924.0	925.1	923.1	926.2	924.1	925.8	922.7	927.1
20.72	899.1	900.6	897.6	902.2	899.4	901.8	897.7	903.6
23.48	871.0	873.2	869.1	875.1	871.6	874.7	868.8	877.2
26.24	840.1	842.7	837.6	845.1	841.0	845.0	837.2	848.2
29.00	806.3	810.0	802.4	812.8	807.7	813.0	802.1	817.1
31.77	769.9	774.4	764.8	778.3	772.3	778.7	764.5	783.8
34.53	731.3	736.9	724.0	741.7	734.5	742.6	724.3	748.9
37.29	690.9	697.8	680.7	703.9	695.1	705.1	681.1	713.0
40.05	648.5	657.1	634.9	664.3	654.0	666.1	635.3	675.7
42.81	604.7	614.8	586.1	623.5	611.6	626.4	587.0	637.7
45.58	559.6	571.8	535.1	582.1	568.6	586.2	536.1	599.5
48.34	513.5	528.4	480.5	540.6	525.0	546.3	482.0	561.9
51.10	467.3	485.1	422.6	499.4	481.7	507.5	424.2	525.4
53.86	421.1	442.5	360.5	459.4	439.3	470.6	362.1	491.2
56.63	375.4	401.5	293.2	421.2	398.7	437.2	294.4	460.6
59.39	333.8	363.5	200.1	368.4	371.4	411.7	200.2	412.6
62.15	291.8	322.7	151.4	329.1	338.6	382.0	151.4	382.5
64.91	251.0	281.8	114.2	288.5	308.3	353.1	114.6	351.9
67.68	212.1	240.8	85.64	247.3	280.8	325.6	86.98	322.0
70.44	174.7	200.4	63.49	206.0	256.6	300.8	65.97	293.8
73.20	138.5	160.2	46.33	164.9	235.6	278.3	50.37	267.4
75.96	103.4	120.6	32.68	124.0	218.1	259.3	38.60	243.5
78.72	69.13	81.47	21.45	83.44	204.6	244.5	29.72	222.8

TABLE VII-3. Normalized Experimental Axial  $^{238}\text{U}$  Reaction Rate Data

Axial Distance, cm	Unreflected Assembly		Reflected Assembly	
	$^{238}\text{U}_f$	$^{238}\text{U}_c$	$^{238}\text{U}_f$	$^{238}\text{U}_c$
88.90	23.60	117.5	25.00	218.8
83.82	32.75	174.3	35.34	252.0
78.74	49.43	227.4	52.87	294.7
73.66	77.11	291.3	79.06	338.9
68.58	119.6	352.0	124.4	394.5
63.50	195.9	410.5	202.4	449.7
58.42	367.0	487.4	383.5	518.9
53.39	477.1	558.4	496.4	579.5
48.26	547.3	646.2	555.9	666.9
43.18	653.6	691.9	667.8	711.7
38.10	734.1	754.6	738.5	768.9
33.02	788.2	808.1	796.5	837.9
27.94	858.5	868.8	861.7	881.1
22.86	896.3	914.9	902.8	914.2
17.78	943.0	946.4	936.9	963.8
12.70	968.7	968.4	974.2	975.6
7.62	992.4	985.6	999.5	992.4
1.59	992.3	999.1	991.7	1000.0
-1.59	993.2	1012.2		
-7.62	993.4	981.5		
-12.70	972.5	976.3		
-17.78	944.9	954.5		
-22.86	919.5	921.5		
-27.94	860.1	871.1		
-33.02	809.4	837.5		
-38.10	735.7	758.8		
-43.18	666.4	707.5		
-48.26	554.0	675.5		
-53.34	490.5	572.5		
-58.42	382.8	506.1		
-62.79 <sup>a</sup>	231.8	440.9		
-68.58	139.2	368.4		
-74.45	86.35	292.9		
-77.87	70.44	259.9		
-83.66	45.05	183.5		
-89.54	27.38	115.3		

<sup>a</sup>Distances in the movable half ( $z < 0$ ) for  $|z| \geq 62.79$  cm are in the pin zone.

TABLE VII-4. Normalized Experimental Axial Fission Rate Data

Axial Distance, cm	Unreflected Assembly		Reflected Assembly
	$^{239}\text{Pu}_f$	$^{235}\text{U}_f$	$^{235}\text{U}_f$
86.36		147.2	246.6
76.20		255.0	314.5
66.04		374.8	406.6
55.88		503.2	519.1
53.98	515.8		
48.90	592.4		
45.72		646.4	652.9
43.82	662.7		
38.74	730.5		
35.56		785.2	777.4
33.66	791.0		
28.58	853.6		
25.40		885.5	883.2
23.50	897.0		
18.42	929.6		
15.24		957.5	954.5
13.34	966.3		
8.25	988.6		
4.76		997.0	990.9
3.17	993.0		
-4.76		1003.7	
-15.24		963.4	
-25.40		890.2	
-35.56		787.1	
-45.72		691.6	
-55.88		517.3	
-62.79 <sup>a</sup>		392.4	
-74.45		258.2	
-84.59		164.3	

<sup>a</sup>Distances in the movable half ( $z < 0$ ) for  $|z| \geq 62.79$  cm are in the pin zone.

TABLE VII-5. Normalized Calculated Axial Reaction Rate Data

Axial Distance, cm	Unreflected Assembly				Reflected Assembly		
	$^{239}\text{Pu}_f$	$^{235}\text{U}_f$	$^{238}\text{U}_f$	$^{238}\text{U}_c$	$^{235}\text{U}_f$	$^{238}\text{U}_f$	$^{238}\text{U}_c$
1.02	1000.1	1000.2	999.7	1000.3	1000.2	999.7	1000.3
3.06	998.4	998.7	998.2	998.7	998.7	998.2	998.8
5.10	995.3	995.5	994.7	995.6	995.5	995.1	995.6
7.15	990.6	990.9	990.2	990.9	990.9	990.6	991.1
9.19	984.2	984.5	983.7	984.7	984.8	984.0	985.0
11.23	976.3	976.7	975.7	976.9	977.2	976.5	977.4
13.27	966.8	967.4	966.1	967.7	968.1	966.9	968.5
15.31	955.8	956.6	955.1	957.0	957.5	956.3	958.0
17.35	943.4	944.3	942.6	944.8	945.5	944.2	946.1
19.40	929.4	930.5	928.5	931.2	931.9	930.1	932.8
21.44	914.0	915.3	913.0	916.2	917.2	915.0	918.1
23.48	897.3	898.8	896.0	900.0	900.9	898.4	902.2
25.52	878.9	880.9	877.5	882.1	883.5	880.2	885.0
27.56	859.4	861.6	857.4	863.3	864.8	860.5	866.5
29.60	838.4	841.1	835.9	843.1	844.8	839.4	847.1
31.64	816.3	819.3	812.8	821.9	823.7	816.7	826.4
33.69	792.8	796.5	788.2	799.6	801.4	793.0	804.7
35.73	768.2	772.7	762.7	776.3	778.2	767.3	782.2
37.77	742.5	747.8	735.1	752.1	754.2	740.6	758.8
39.81	715.8	721.9	706.6	727.1	729.1	712.4	734.7
41.85	688.0	695.4	676.0	701.6	703.5	682.6	710.1
43.89	659.4	668.0	643.9	675.2	677.0	650.8	684.8
45.94	629.8	639.9	610.4	648.3	649.9	617.6	659.2
47.98	599.5	611.2	574.8	621.1	622.7	582.3	633.2
50.02	568.5	582.3	537.2	593.5	595.0	545.0	607.3
52.04	537.4	553.2	497.6	566.3	567.6	506.1	581.8
54.04	506.0	524.5	456.1	539.5	540.6	464.6	557.0
56.04	474.6	495.9	411.8	513.1	514.3	420.3	532.8
58.04	442.7	467.6	364.3	487.4	488.8	372.4	509.8
60.04	411.1	440.2	312.9	462.5	464.5	320.4	488.2
62.04	383.4	415.2	235.7	420.2	444.2	241.5	447.2
64.04	355.5	389.2	196.5	395.0	422.5	201.6	426.5
66.04	328.6	363.3	163.9	371.3	401.3	168.3	405.8
68.04	302.5	337.8	136.6	346.3	380.6	140.5	385.0
70.04	277.4	312.4	113.8	321.3	360.8	117.5	364.7
72.11	252.4	286.6	93.76	295.5	341.5	97.19	344.3
74.26	227.4	260.2	76.97	269.0	322.5	80.31	324.0
76.40	203.3	234.3	63.14	242.6	304.9	66.40	304.5
78.54	180.2	209.0	51.61	216.5	289.0	55.00	286.2
80.69	157.8	184.1	42.06	190.9	274.9	45.59	269.3
82.83	136.2	159.7	34.06	165.6	262.7	37.86	253.9
84.98	115.3	135.7	27.32	140.7	252.9	31.49	240.2
87.12	94.86	112.2	21.58	116.2	245.6	26.25	228.4
89.26	74.94	89.01	16.63	92.07	241.3	21.93	218.6
91.41	55.42	66.17	12.29	68.23	240.5	18.37	211.3

TABLE VIII-1. Absolute Reaction Rate Measurements

Matrix	Radial Position, cm	$^6\text{Li}(n, \alpha)$ , <sup>a</sup> $10^{+8}$ events/sec-g	$^{239}\text{Pu}(n, f)$ , <sup>b</sup> $10^{+7}$ events/sec-g
S23/23	0.000	9.928 ± 0.089	4.187 ± 0.037
S23/24	5.524	9.860 ± 0.089	4.138 ± 0.036
S23/25	11.049	-	4.027 ± 0.036
S23/26	16.574	9.286 ± 0.084	3.889 ± 0.034
S23/27	22.098	-	3.692 ± 0.033
S23/28	27.622	8.168 ± 0.074	3.451 ± 0.031
S23/29	33.147	-	3.172 ± 0.029
S23/30	38.672	6.782 ± 0.061	2.853 ± 0.026
S23/31	44.196	-	2.511 ± 0.023
S23/32	49.720	5.292 ± 0.048	2.149 ± 0.020

<sup>a</sup>Measured reaction rate times  $R_0/R$ ; for  $^6\text{Li}$ ,  $R_0/R = 1.0534$  at all positions.

<sup>b</sup>Measured reaction rate times  $R_0/R$ ; for  $^{239}\text{Pu}$ ,  $R_0/R = 1.0028$  at all positions.

TABLE VIII-2. Reactivity Worth Measurements

Sample	Matrix	Radial Position, cm	Principal Isotope i	$\rho$ , Ih/kg	$\rho_o/\rho$	$i_{\rho_o}/\rho_o$	$i_{\rho_o}$ , Ih/kg	C/E
Li-15	S23/23	0.000	$^6\text{Li}$	-2479.36 ± 7.88	1.06374	1.01634	-2680.49 ± 8.52	1.0794 ± 0.0037
"	S23/24	5.524	"	-2439.06 ± 14.69	"	1.01634	-2638.87 ± 15.88	1.0810 ± 0.0065
"	S23/26	16.574	"	-2166.54 ± 7.68	"	1.01636	-2342.34 ± 8.31	1.0765 ± 0.0038
"	S23/28	27.622	"	-1680.15 ± 5.88	"	1.01640	-1816.56 ± 6.36	1.0692 ± 0.0037
"	S23/30	38.672	"	-1121.11 ± 5.88	"	1.01649	-1212.24 ± 6.36	1.0456 ± 0.0055
"	S23/32	49.720	"	-593.35 ± 6.46	"	1.01671	-641.72 ± 6.99	1.023 ± 0.011
Th-3	S23/23	0.000	$^{232}\text{Th}$	-21.382 ± 0.206	1.02903	1.00000	-22.00 ± 0.21	1.169 ± 0.011
U-233-3	S23/23	0.000	$^{233}\text{U}$	-293.44 ± 1.78	1.00544	1.00493	-296.49 ± 1.80	1.1636 ± 0.0071
MB-21	S23/23	0.000	$^{235}\text{U}$	156.04 ± 0.49	1.01923	1.07675	171.25 ± 0.54	1.2033 ± 0.0038
MB-21	S23/25	11.049	"	146.53 ± 0.12	"	1.07635	160.75 ± 0.13	1.2110 ± 0.0010
MB-21	S23/27	22.098	"	123.53 ± 0.19	"	1.07607	135.48 ± 0.21	1.1997 ± 0.0019
MB-25	S23/23	0.000	$^{238}\text{U}$	-11.032 ± 0.34	1.00834	1.04044	-11.57 ± 0.36	1.106 ± 0.034
Pu-25	S23/23	0.000	$^{239}\text{Pu}$	229.69 ± 1.02	1.00144	1.02690	236.21 ± 1.04	1.1862 ± 0.0052
Pu-27	S23/23	0.000	"	234.85 ± 0.38	0.98255	1.02690	236.96 ± 0.38	1.1825 ± 0.0019
MB-06	S23/23	0.000	"	224.74 ± 1.87	1.00944	1.02984	233.64 ± 1.94	1.199 ± 0.010
MB-10	S23/23	0.000	"	229.31 ± 0.77	1.00304	1.02984	236.87 ± 0.80	1.1829 ± 0.0040
MB-10	S23/25	11.049	"	212.64 ± 0.34	"	1.02958	219.59 ± 0.35	1.2044 ± 0.0019
MB-10	S23/26	16.574	"	199.38 ± 0.95	"	1.02953	205.89 ± 0.98	1.1913 ± 0.0057
MB-10	S23/27	22.098	"	178.08 ± 0.41	"	1.02944	183.88 ± 0.42	1.1972 ± 0.0027
MB-10	S23/29	33.147	"	131.68 ± 0.63	"	1.02915	135.93 ± 0.65	1.1702 ± 0.0056
MB-10	S23/31	44.196	"	82.463 ± 0.103	"	1.02854	85.08 ± 0.11	1.1345 ± 0.0014
MB-10	S23/32	49.720	"	61.370 ± 0.441	"	1.02799	63.28 ± 0.46	1.0926 ± 0.0079
Pu-240-2D	S23/23	0.000	$^{240}\text{Pu}$	35.494 ± 0.183	1.02166	1.15978	42.06 ± 0.22	1.2209 ± 0.0063
Pu-50	S23/23	0.000	$^{241}\text{Pu}$	178.79 ± 8.29	1.01288	1.61169	291.86 ± 13.53	1.283 ± 0.059
Pu-242-4-1	S23/23	0.000	$^{242}\text{Pu}$	33.852 ± 0.265	0.95828	0.89447	29.02 ± 0.23	1.425 ± 0.011

NOTE: The errors in this table are statistical only. They do not include uncertainties in the autorod calibration nor in the sample-size correction factor.

TABLE VIII-3.  $^{252}\text{Cf}$  Worth Measurements and Calculations

Matrix	Radial Position, cm	$\rho', \text{Ih}$	$\overline{\phi}_f^* \times 10^{-7}$
S23/23	0.000	$0.03855 \pm 0.00018$	2.2686
S23/24	5.524	$0.03851 \pm 0.00016$	2.2528
S23/25	11.049	$0.03736 \pm 0.00029$	2.2029
S23/26	16.574	$0.03610 \pm 0.00026$	2.1200
S23/28	27.622	$0.03188 \pm 0.00017$	1.8643
S23/30	38.672	$0.02595 \pm 0.00029$	1.5108
S23/32	49.720	$0.02008 \pm 0.00010$	1.0930

NOTE: Source strength S on 10/8/75 was  $(1.3135 \pm 0.0093) \times 10^7 \text{ n/sec.}$

TABLE VIII-4. Spectrum-Averaged Calculated Quantities

Isotopic	Matrix	Radial Position, cm	$\overline{\phi}_f^* \times 10^{-7}$	$\overline{\phi}_a^* \times 10^{-7}$	$(1 + \overline{\alpha})$	$\overline{v}$	RCF <sup>a</sup>	FCF <sup>b</sup> $\times 10^4$
$^{232}\text{Th}$	S23/23	0.000	2.2666	1.8779	27.9048	2.3414	0.8054	-2168.1
$^{233}\text{U}$	S23/23	0.000	2.2947	1.9003	1.0891	2.4921	1.0098	-5.0608
$^{235}\text{U}$	S23/23	0.000	2.2793	1.8914	1.2626	2.4600	1.0156	-6.5894
"	S23/25	11.049	2.2133	1.8360	1.2628	2.4599	1.0145	-6.5852
"	S23/27	22.098	2.0156	1.6698	1.2634	2.4597	1.0108	-6.5664
$^{238}\text{U}$	S23/23	0.000	2.2839	1.9365	5.4923	2.7712	0.6236	-479.18
$^{239}\text{Pu}$	S23/23	0.000	2.2948	1.9304	1.2096	2.9484	1.0109	-2.7764
"	S23/25	11.049	2.2284	1.8739	1.2100	2.9483	1.0101	-2.7758
"	S23/26	16.574	2.1445	1.8026	1.2104	2.9483	1.0091	-2.7746
"	S23/27	22.098	2.0294	1.7045	1.2112	2.9482	1.0075	-2.7722
"	S23/29	33.147	1.7174	1.4374	1.2145	2.9475	1.0018	-2.7556
"	S23/31	44.196	1.3226	1.0952	1.2231	2.9454	0.9896	-2.6805
"	S23/32	49.720	1.1054	0.9029	1.2322	2.9426	0.9780	-2.563
$^{240}\text{Pu}$	S23/23	0.000	2.2886	2.0158	1.8668	3.0790	1.0632	-5.1605
$^{241}\text{Pu}$	S23/23	0.000	2.2876	1.9007	1.1662	2.9894	1.0108	-13.226
$^{242}\text{Pu}$	S23/23	0.000	2.2822	2.0627	1.7365	3.0456	1.0638	-26.320

<sup>a</sup>RCF = reactivity correction factor =  $\left[1 - (\rho_s + \rho_l)/\rho\right]$

<sup>b</sup>FCF = fission correction factor =  $(R_p + R_\alpha - R_{n2n})/R_f$

TABLE VIII-5. Unnormalized Perturbation Denominator

Matrix	Radial Position, cm	$D(^{252}\text{Cf}) \times 10^{-15}$
S23/23	0.000	$7.729 \pm 0.065$
S23/24	5.524	$7.684 \pm 0.063$
S23/25	11.049	$7.745 \pm 0.081$
S23/26	16.574	$7.714 \pm 0.078$
S23/28	27.622	$7.680 \pm 0.068$
S23/30	38.672	$7.647 \pm 0.100$
S23/32	49.720	$7.151 \pm 0.061^a$
	$\bar{D}$ :	$7.702 \pm 0.056$

<sup>a</sup>Data point omitted in the evaluation of  $\bar{D}$ .

TABLE VIII-6. Normalized Perturbation Denominator

Quantity	Value
$\bar{D}$ (Cf-252)	$(7.702 \pm 0.095)^a \times 10^{15}$
S (0)	$(7.191 \pm 0.077) \times 10^7$
S* (0)	$2.2923 \times 10^7$
$I_h/(\delta k/k)$	$9.74779 \times 10^4$
$NP = S(0) S^*(0)/I_h/(\delta k/k)$	$(1.692 \pm 0.018) \times 10^{10}$
$\bar{D}/NP$ , normalized mean (E)	$(4.552 \pm 0.074) \times 10^5$
Calculated (C)	$3.8690 \times 10^5$
C/E	$0.850 \pm 0.014$

<sup>a</sup>Error includes a 1.0% uncertainty in the autorod calibration.

TABLE VIII-7. Thin-Sample  $(1 + \bar{\alpha})$  Values

Isotope	Matrix	Radial Position, cm	Calculated $(1 + \bar{\alpha})$	Measured $(1 + \bar{\alpha})$	C/E
<sup>232</sup> Th	S23/23	0.000	27.905	$26.120 \pm 1.312$	$1.068 \pm 0.054$
<sup>233</sup> U	S23/23	0.000	1.089	$1.075 \pm 0.046$	$1.013 \pm 0.043$
<sup>235</sup> U	S23/23	0.000	1.263	$1.289 \pm 0.032$	$0.980 \pm 0.024$
<sup>235</sup> U	S23/25	11.049	1.263	$1.282 \pm 0.032$	$0.985 \pm 0.024$
<sup>235</sup> U	S23/27	22.098	1.263	$1.274 \pm 0.032$	$0.992 \pm 0.025$
<sup>238</sup> U	S23/23	0.000	5.492	$5.526 \pm 0.083$	$0.994 \pm 0.015$
<sup>239</sup> Pu	S23/23	0.000	1.210	$1.224 \pm 0.034$	$0.988 \pm 0.028$
<sup>239</sup> Pu	S23/25	11.049	1.210	$1.243 \pm 0.034$	$0.974 \pm 0.026$
<sup>239</sup> Pu	S23/26	16.574	1.210	$1.225 \pm 0.035$	$0.988 \pm 0.028$
<sup>239</sup> Pu	S23/27	22.098	1.211	$1.243 \pm 0.034$	$0.974 \pm 0.027$
<sup>239</sup> Pu	S23/29	33.147	1.214	$1.222 \pm 0.036$	$0.994 \pm 0.029$
<sup>239</sup> Pu	S23/31	44.196	1.223	$1.199 \pm 0.035$	$1.020 \pm 0.030$
<sup>240</sup> Pu	S23/23	0.000	1.867	$1.875 \pm 0.074$	$0.996 \pm 0.039$
<sup>241</sup> Pu	S23/23	0.000	1.166	$1.293 \pm 0.117$	$0.902 \pm 0.082$

TABLE VIII-8. Errors in  $(1 + \bar{\alpha})$  From Uncertainties in Measured Quantities

Isotope	$(1 + \bar{\alpha})$		$\delta p$	$\delta R_f$	$\delta \bar{v}$	Total Error (1 $\sigma$ )
	Exp.	$\delta D(\text{Cf})$				
<sup>232</sup> Th	26.120	0.167	-0.223	-1.281	0.071	1.312
<sup>233</sup> U	1.075	-0.014	-0.012	0.036	0.021	0.046
<sup>235</sup> U	1.289	-0.012	-0.005	0.025	0.015	0.032
<sup>238</sup> U	5.526	0.016	-0.068	-0.029	0.033	0.083
<sup>239</sup> Pu	1.224	-0.017	-0.008	0.020	0.021	0.034
<sup>240</sup> Pu	1.875	-0.012	-0.008	0.019	0.070	0.074
<sup>241</sup> Pu	1.293	-0.017	-0.017	0.039	0.022	0.117



TABLE VIII-9. Error Sensitivities

A 1.0% Increase In	Causes Percent Increase In $(1 + \bar{\alpha})$						
	$^{239}\text{Pu}$	$^{240}\text{Pu}$	$^{241}\text{Pu}$	$^{233}\text{U}$	$^{235}\text{U}$	$^{238}\text{U}$	$^{232}\text{Th}$
$\bar{\phi}_a^*$	-1.000	-1.000	-1.000	-1.000	-1.000	-0.991	-0.992
$\bar{v} \bar{\phi}_f^*$	2.864	1.864	2.784	2.799	2.300	0.592	0.108
$\bar{D}(\text{Cf}) \rho(\text{RCF})/R_f$	-1.864	-0.865	-1.784	-1.799	-1.300	0.400	0.884
$D(\text{Cf}) = S \bar{\phi}_f^* (\text{Cf}) / \bar{\rho}'(\text{Cf})$	-1.864	-0.865	-1.784	-1.799	-1.300	0.400	0.884

TABLE VIII-10. Central-Point Breeding Ratio Measurement

Quantity	Measured	Calculated	C/E
$^{49}\text{N} \times 10^{-21} \text{ (cm}^{-3}\text{)}$	1.1832		
$^{40}\text{N} \times 10^{-21} \text{ (cm}^{-3}\text{)}$	0.1569		
$^{41}\text{N} \times 10^{-21} \text{ (cm}^{-3}\text{)}$	0.0163		
$^{28}\text{N} \times 10^{-21} \text{ (cm}^{-3}\text{)}$	5.5421		
$^{25}\text{N} \times 10^{-21} \text{ (cm}^{-3}\text{)}$	0.0122		
$(1 + ^{49}\bar{\alpha})$ cell avg.	$1.208 \pm 0.034$	1.1961	$0.990 \pm 0.028$
$(1 + ^{40}\bar{\alpha})$ " "	$1.769 \pm 0.070$	1.7613	$0.996 \pm 0.039$
$(1 + ^{41}\bar{\alpha})$ " "	$1.288 \pm 0.117$	1.1620	$0.902 \pm 0.082$
$(1 + ^{25}\bar{\alpha})$ " "	$1.278 \pm 0.032$	1.2594	$0.985 \pm 0.024$
$^{28}\text{C}/^{49}\text{f}$ " "	$0.1196 \pm 0.0008$	0.1301	$1.0878 \pm 0.0073$
$^{40}\text{f}/^{49}\text{f}$	$0.2527 \pm 0.0020$	0.2582	$1.0218 \pm 0.0081$
$^{41}\text{f}/^{49}\text{f}$	$1.248 \pm 0.018$	1.2859	$1.030 \pm 0.015$
$^{25}\text{f}/^{49}\text{f}$ cell avg.	$0.9864 \pm 0.0067$	0.9707	$0.9841 \pm 0.0067$
$(^{28}\text{C}/^{49}\text{f}) / (1 + ^{49}\bar{\alpha})$	$0.0990 \pm 0.0029$	0.1088	$1.099 \pm 0.032$
$C = \frac{^{28}\text{N}^{28}\text{C}/^{49}\text{f}}{^{49}\text{N}(1 + ^{49}\bar{\alpha})}$	$0.464 \pm 0.014$	0.5095	$1.099 \pm 0.032$
$[\text{N}]^a$	$1.0460 \pm 0.0042$	1.0428	$0.9969 \pm 0.0040$
$[\text{D}]^b$	$1.0291 \pm 0.0018$	1.0279	$0.9988 \pm 0.0018$
$\text{BR}_p = C [\text{N}] / [\text{D}]$	$0.471 \pm 0.014$	0.5169	$1.097 \pm 0.032$

$$^a [\text{N}] \equiv 1 + (^{40}\text{N}^{40}\bar{\alpha}^{40}\text{f}/^{49}\text{f}) / (^{28}\text{N}^{28}\text{C}/^{49}\text{f})$$

$$^b [\text{D}] \equiv \frac{^{41}\text{N}(1 + ^{41}\bar{\alpha})^{41}\text{f}}{^{49}\text{N}(1 + ^{49}\bar{\alpha})^{49}\text{f}} + \frac{^{25}\text{N}(1 + ^{25}\bar{\alpha})^{25}\text{f}}{^{49}\text{N}(1 + ^{49}\bar{\alpha})^{49}\text{f}} + 1$$

TABLE IX-1. Average Atom Densities for Control Rod Compositions,<sup>a</sup>  
10<sup>21</sup> atoms/cm<sup>3</sup>

Nuclide	Core Type 2	Control Rod Composition			
		#0	#1	#2	#3
Fe	18.0097	14.1169	14.1551	14.1932	14.0675
Ni	1.3367	1.3445	1.3481	1.3516	1.3350
Cr	2.9038	2.9127	2.9196	2.9265	2.8942
Mn	0.2296	0.2272	0.2278	0.2283	0.2259
Mo	0.4651	0.2374	0.2374	0.2374	0.2374
C	0.0306	0.0304	4.7266	9.4228	9.4467
Si	0.1788	0.1817	0.1894	0.1970	0.1878
Cu	0.0193	0.0198	0.0198	0.0199	0.0197
S	0.0020	0.0019	0.0019	0.0019	0.0019
P	0.0052	0.0052	0.0052	0.0052	0.0052
Co	0.0093	0.0091	0.0091	0.0091	0.0091
Al	0.0073	0.0063	0.0064	0.0064	0.0062
O	15.7637	5.6820	5.6820	5.6820	5.6820
<sup>235</sup> U	0.0147	0.0056	0.0056	0.0056	0.0056
<sup>238</sup> U	6.6559	2.5036	2.5036	2.5036	2.5036
<sup>238</sup> Pu	0.0008	0.0004	0.0004	0.0004	0.0004
<sup>239</sup> Pu	1.7812	0.8906	0.8906	0.8906	0.8906
<sup>240</sup> Pu <sup>b</sup>	0.2364	0.1182	0.1182	0.1182	0.1182
<sup>241</sup> Pu <sup>b</sup>	0.0228	0.0114	0.0114	0.0114	0.0114
<sup>242</sup> Pu <sup>b</sup>	0.0032	0.0016	0.0016	0.0016	0.0016
<sup>241</sup> Am <sup>c</sup>	0.0177	0.0088	0.0088	0.0088	0.0088
<sup>10</sup> B <sup>c</sup>	-	-	3.5854	7.1708	12.5368
<sup>11</sup> B	-	-	14.5389	29.0778	19.9930

<sup>a</sup> Estimated uncertainty of  $\pm 10\%$  for densities  $< 0.1 \times 10^{21}$  atoms/cm<sup>3</sup> and  $\pm 1\%$  for densities  $\geq 0.1 \times 10^{21}$  atoms/cm<sup>3</sup>.

<sup>b</sup> Decay of <sup>241</sup>Pu  $\rightarrow$  <sup>241</sup>Am adjusted to June 30, 1975.

<sup>c</sup> Axial <sup>10</sup>B per linear inch: #1 - 4.6272 g; #2 - 9.2544 g; #3 - 16.1796 g.

TABLE IX-2. GCFR Control Rod Worths

Measurement	Reactivity <sup>a</sup> , 1h		Exchange Worth, 1h		C/E
	Calculated	Experimental <sup>b</sup>	Calculated	Experimental	
GCFR reference configuration <sup>c</sup>	-183.11	+117.44 $\pm$ 0.10			
Control rod composition #0 <sup>d</sup>	-382.24	-73.15 $\pm$ 1.02	-99.13	-190.59 $\pm$ 1.35	1.045 $\pm$ 0.007
Control rod composition #1	-863.14	-527.17 $\pm$ 1.20	-480.90	-454.02 $\pm$ 1.79	1.059 $\pm$ 0.004
Control rod composition #2	-1301.92	-919.77 $\pm$ 1.85	-919.68	-846.62 $\pm$ 2.28	1.086 $\pm$ 0.003
Control rod composition #3	-1735.44	-1223.25 $\pm$ 16.76	-1353.20	-1150.10 $\pm$ 16.81	1.177 $\pm$ 0.017

<sup>a</sup>  $1\% \Delta k/k = 974.779$  1h.

<sup>b</sup> Data corrected to 25°C.

<sup>c</sup> Reference for composition #0 exchange worth.

<sup>d</sup> Reference for composition #1, #2, and #3 exchange worths.

TABLE X-1. Measured Central Neutron Spectrum

ENERGY	FLUX	ERROR	RES	ENERGY	FLUX	ERROR	RES
1969.100	.3953E 05	.118E 04	.093	1873.068	.4265E 05	.115E 04	.093
1781.719	.4307E 05	.113E 04	.093	1694.625	.4718E 05	.110E 04	.093
1612.169	.4950E 05	.124E 04	.093	1533.545	.4978E 05	.142E 04	.093
1458.754	.4977E 05	.134E 04	.093	1387.611	.4939E 05	.127E 04	.093
1319.936	.5425E 05	.893E 03	.093	1255.565	.5683E 05	.924E 03	.093
1194.332	.5814E 05	.984E 03	.093	1136.085	.5509E 05	.925E 03	.093
1080.679	.5042E 05	.906E 03	.093	1027.974	.5167E 05	.102E 04	.093
977.840	.5195E 05	.942E 03	.093	930.152	.5618E 05	.878E 03	.093
884.788	.6386E 05	.821E 03	.094	841.638	.7179E 05	.862E 03	.094
800.591	.8001E 05	.816E 03	.094	761.547	.8354E 05	.906E 03	.094
724.407	.9074E 05	.665E 03	.094	689.078	.9220E 05	.123E 04	.094
655.471	.1003E 06	.139E 04	.094	623.504	.1036E 06	.158E 04	.094
593.096	.1020E 06	.149E 04	.094	564.171	.1003E 06	.114E 04	.094
536.657	.9825E 05	.130E 04	.094	510.484	.9721E 05	.153E 04	.094
485.586	.9196E 05	.141E 04	.094	461.906	.8359E 05	.103E 04	.094
439.379	.7470E 05	.947E 03	.094	417.951	.6608E 05	.145E 04	.094
397.568	.6313E 05	.994E 03	.094	378.178	.6746E 05	.856E 03	.094
359.735	.6986E 05	.101E 04	.094	342.191	.7838E 05	.932E 03	.094
325.502	.7243E 05	.211E 04	.094	309.628	.8750E 05	.250E 04	.094
294.527	.9160E 05	.202E 04	.095	280.163	.9099E 05	.214E 04	.095
266.500	.9698E 05	.229E 04	.095	253.503	.9607E 05	.212E 04	.095
241.140	.9578E 05	.229E 04	.095	229.379	.9644E 05	.213E 04	.095
218.193	.9258E 05	.195E 04	.095	207.551	.9402E 05	.216E 04	.095
197.429	.9232E 05	.199E 04	.095	187.801	.9125E 05	.183E 04	.095
178.642	.9507E 05	.170E 04	.095	169.929	.9446E 05	.157E 04	.096
161.642	.9205E 05	.177E 04	.096	153.759	.9526E 05	.149E 04	.096
146.260	.9515E 05	.141E 04	.096	139.127	.9553E 05	.129E 04	.096
132.342	.9779E 05	.119E 04	.096	125.888	.1004E 06	.138E 04	.096
119.748	.9749E 05	.162E 04	.097	113.908	.9717E 05	.150E 04	.097
106.353	.1012E 06	.110E 04	.097	103.068	.9886E 05	.131E 04	.097
98.042	.9157E 05	.349E 04	.097	93.260	.8491E 05	.321E 04	.098
88.712	.7911E 05	.293E 04	.098	84.386	.8787E 05	.270E 04	.098
80.270	.8910E 05	.248E 04	.098	76.355	.8781E 05	.274E 04	.099
72.632	.8472E 05	.307E 04	.099	69.089	.8516E 05	.283E 04	.099
65.720	.7753E 05	.212E 04	.099	62.515	.7693E 05	.238E 04	.100
59.466	.7706E 05	.182E 04	.100	56.566	.6961E 05	.195E 04	.100
53.807	.6401E 05	.180E 04	.101	51.183	.6277E 05	.178E 04	.101
48.667	.6489E 05	.163E 04	.101	46.312	.6807E 05	.155E 04	.102
44.054	.6326E 05	.143E 04	.102	41.905	.5744E 05	.167E 04	.103
39.862	.5987E 05	.154E 04	.103	37.918	.5179E 05	.253E 04	.104
36.068	.4744E 05	.272E 04	.105	34.309	.3904E 05	.248E 04	.107
32.636	.4004E 05	.227E 04	.108	31.044	.3094E 05	.207E 04	.109
29.530	.2851E 05	.224E 04	.110	28.090	.3491E 05	.205E 04	.112
26.720	.4647E 05	.189E 04	.113	25.417	.5756E 05	.212E 04	.114
24.178	.5566E 05	.195E 04	.116	22.998	.4891E 05	.150E 04	.117
21.877	.4515E 05	.138E 04	.119	20.810	.4335E 05	.126E 04	.121
19.795	.4191E 05	.120E 04	.122	18.830	.3896E 05	.129E 04	.124
17.911	.3715E 05	.124E 04	.126	17.038	.3517E 05	.118E 04	.128
16.207	.3556E 05	.131E 04	.130	15.416	.3092E 05	.222E 04	.132
14.665	.2962E 05	.204E 04	.134	13.949	.3572E 05	.219E 04	.136
13.269	.3520E 05	.171E 04	.139	12.622	.2958E 05	.185E 04	.141
12.006	.3322E 05	.170E 04	.143	11.421	.3501E 05	.156E 04	.146
10.864	.3043E 05	.144E 04	.148	10.334	.2870E 05	.158E 04	.151
9.830	.2525E 05	.145E 04	.154	9.351	.2253E 05	.163E 04	.157
8.895	.2230E 05	.149E 04	.160	8.461	.1986E 05	.105E 04	.163
8.048	.1952E 05	.115E 04	.166	7.656	.1938E 05	.110E 04	.169
7.282	.1913E 05	.101E 04	.172	6.927	.1963E 05	.965E 03	.176
6.589	.1957E 05	.924E 03	.179	6.268	.1942E 05	.808E 03	.183
5.962	.1404E 05	.136E 04	.187	5.672	.1508E 05	.124E 04	.191
5.395	.1321E 05	.129E 04	.195	5.132	.1166E 05	.118E 04	.199
4.882	.1290E 05	.125E 04	.203	4.643	.1414E 05	.114E 04	.207
4.417	.1382E 05	.123E 04	.212	4.202	.9855E 04	.112E 04	.216
3.997	.1053E 05	.103E 04	.221	3.802	.1192E 05	.938E 03	.226
3.616	.1065E 05	.696E 03	.231	3.440	.1060E 05	.710E 03	.236
3.272	.1111E 05	.676E 03	.242	3.113	.1161E 05	.620E 03	.247
2.961	.1269E 05	.589E 03	.253	2.816	.1332E 05	.541E 03	.258
2.679	.1310E 05	.497E 03	.264	2.548	.1438E 05	.540E 03	.270
2.424	.1489E 05	.495E 03	.277	2.306	.1438E 05	.520E 03	.283
2.193	.1034E 05	.743E 03	.290	2.086	.9551E 04	.768E 03	.296
1.985	.9624E 04	.707E 03	.303	1.888	.1019E 05	.649E 03	.311
1.796	.8656E 04	.593E 03	.318	1.708	.8071E 04	.619E 03	.325
1.625	.9171E 04	.571E 03	.333	1.546	.8107E 04	.598E 03	.341
1.470	.5320E 04	.550E 03	.349	1.399	.3541E 04	.503E 03	.358
1.336	.4270E 04	.536E 03	.366	1.266	.3099E 04	.488E 03	.375
1.204	.3500E 04	.444E 03	.384	1.145	.3297E 04	.405E 03	.394
1.089	.3912E 04	.370E 03	.403	1.036	.3723E 04	.402E 03	.413
.986	.4244E 04	.367E 03	.423				

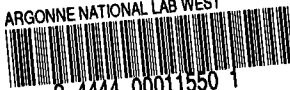
Distribution for ANL-76-108Internal:

J. A. Kyger	H. O. Monson	B. Toppel
A. Amorosi	R. Sevy	A. Travelli
R. Avery	P. Amundson	D. C. Wade
L. Burris	W. P. Barthold	S. K. Bhattacharyya
D. W. Cissel	E. F. Bennett	R. G. Bucher
S. A. Davis	S. Carpenter	K. E. Freese
B. R. T. Frost	R. Forrester	J. A. Morman
D. C. Rardin	H. H. Hummel	R. B. Pond (20)
R. G. Staker	L. G. LeSage	W. R. Robinson
R. J. Teunis	M. Lineberry	D. M. Smith
C. E. Till	F. H. Martens	T. Wei
R. S. Zeno	G. K. Rusch	W. Woodruff
C. E. Dickerman	G. Simons	J. B. van Erp
H. K. Fauske	A. B. Smith	A. B. Krisciunas
S. Fistedis	W. M. Stacey	ANL Contract File
B. D. LaMar	W. J. Sturm	ANL Libraries (5)
J. F. Marchaterre	F. W. Thalgot	TIS Files (6)

External:

ERDA-TIC, for distribution per UC-77 (177)  
 Manager, Chicago Operations Office  
 Chief, Chicago Patent Group  
 Director, ERDA-NRA (2)  
 Director, Reactor Programs Div., ERDA-CH  
 Director, CH-INEL  
 President, Argonne Universities Association  
 Applied Physics Division Review Committee:  
   R. B. Brugger, Univ. Missouri, Columbia  
   P. Greebler, General Electric Co., Sunnyvale  
   R. L. Hellens, Combustion Engineering  
   J. M. Hendrie, Brookhaven National Lab.  
   J. S. King, Univ. Michigan  
   W. B. Loewenstein, Electric Power Research Inst.

ARGONNE NATIONAL LAB WEST



3 4444 00011550 1